

ABSTRACT

Title of dissertation: CHARACTERIZATION OF THE BEHAVIOR OF
ULTRA-HIGH PERFORMANCE CONCRETE

Benjamin A. Graybeal, Doctor of Philosophy, 2005

Dissertation directed by: Professor Pedro A. Albrecht
Department of Civil and Environmental Engineering

In the past decade significant advances have been made in the field of high performance concretes. The next generation of concrete, Ultra-High Performance Concrete (UHPC), exhibits exceptional strength and durability characteristics that make it well suited for use in highway bridge structures. This material can exhibit compressive strength of 28 ksi, tensile strength of 1.3 ksi, significant tensile toughness, elastic modulus of 7600 ksi, and minimal long-term creep or shrinkage. It can also resist freeze-thaw and scaling conditions with virtually no damage and is nearly impermeable to chloride ions.

Prestressed highway bridge girders were cast from this material and tested under flexure and shear loadings. The testing of these AASHTO Type II girders containing no mild steel reinforcement indicated that UHPC, with its internal passive fiber reinforcement, could effectively be used in highway bridge girders. A large suite of material characterization tests was also completed. Based on this research, a basic structural design philosophy for bridge girder design is proposed.

**CHARACTERIZATION OF THE BEHAVIOR OF
ULTRA-HIGH PERFORMANCE CONCRETE**

by

Benjamin A. Graybeal

Dissertation submitted to the Faculty of the Graduate School of the
University of Maryland, College Park in partial fulfillment
of the requirements for the degree of
Doctor of Philosophy
2005

Advisory Committee:

Professor Pedro A. Albrecht, Chair
Professor Amde M. Amde
Professor William Fourney
Professor Chung C. Fu
Professor Ricardo A. Medina

©Copyright by

Benjamin Allen Graybeal

2005

ACKNOWLEDGEMENTS

This investigation was funded by the Federal Highway Administration through the Turner-Fairbank Highway Research Center. Prestress Services of Kentucky, Inc. and Lafarge, Inc. also provided noteworthy contributions to the research.

The author would like to thank Dr. Pedro Albrecht at the University of Maryland as well as Joseph Hartmann and Dr. William Wright at the Federal Highway Administration for their guidance throughout this research. He would also like to acknowledge his colleagues at the Turner-Fairbank Highway Research Center, who provided invaluable insight and assistance throughout the planning and experimental testing phases of this work.

Finally, the author wishes to express his gratitude to his wife, Christy, and to his entire family for their love, guidance, support, and encouragement.

TABLE OF CONTENTS

List of Tables	v
List of Figures	vii
CHAPTER 1 INTRODUCTION	1
1.1 Introduction	1
1.2 Objective	2
1.3 Summary of Approach	2
1.4 Outline of Report	3
CHAPTER 2 BACKGROUND AND PREVIOUS WORK	5
2.1 UHPC Constituent Materials	5
2.2 Manufacturer Supplied UHPC Material Properties	6
2.3 Steel Fiber Material Properties	7
2.4 Relevant Material Property Characterization Studies	9
2.4.1 Fiber Orientation Effect on Mechanical Properties by Stiel et al.	9
2.4.2 Prestressing Strand Development Length by Steinberg and Lubbers	10
2.4.3 Permeability of Cracked Concrete by Rapoport et al.	10
2.4.4 Creep and Shrinkage of UHPC by Acker	11
2.4.5 Abrasion Resistance of HSC via ASTM C944 by Horszczaruk	12
2.5 Relevant Girder Testing	13
2.5.1 Shear Capacity of AASHTO Type II Girders by Tawfig	13
2.5.2 Shear Capacity of Small UHPC Beams by Hegger et al.	14
2.5.3 Flexural Capacity of High Strength Concrete Girders by Russell and Burns	15
CHAPTER 3 UHPC MATERIAL CHARACTERIZATION	16
3.1 Research Plan	16
3.1.1 Batch and Specimen Nomenclature	17
3.1.2 Test Matrix	19
3.2 Batching, Casting, and Curing of UHPC	24
3.3 Compression Testing	36
3.3.1 Strength	40
3.3.2 Strength, Modulus of Elasticity, and Strain Capacity with Time	44
3.3.3 Linearity of UHPC Compressive Response	54
3.3.4 Compression Specimen Geometry	61
3.3.5 Demolding Age Effect on Compressive Strength	64
3.3.6 Long-term Delayed Steam Effect on Compressive Strength	65
3.3.7 Fiber Effect on Compression Failure	67
3.3.8 Load Rate Effect on Compression Testing Results	70
3.4 Tension Testing	71
3.4.1 Flexural Prism	72
3.4.1.1 Strength	84
3.4.1.2 Toughness	90

3.4.2	Split Cylinder	96
3.4.3	Mortar Briquette	105
3.4.3.1	Strength	112
3.4.3.2	Toughness	113
3.4.4	Direct Tension	119
3.5	Fracture Testing.....	125
3.6	Penetration Resistance Testing.....	140
3.7	Shrinkage Testing.....	141
3.7.1	Long-term Shrinkage Testing.....	141
3.7.2	Early Age Shrinkage Testing	144
3.8	Creep Testing.....	146
3.8.1	Long-term Creep Testing	146
3.8.2	Early Age High Stress Creep Testing	151
3.9	Coefficient of Thermal Expansion	154
3.10	Heat of Hydration	156
3.11	Air Void Testing.....	159
3.12	Steel Fiber Dispersion Testing	163
3.13	Durability Testing.....	164
3.13.1	Rapid Chloride Ion Penetrability Testing.....	165
3.13.2	Chloride Penetration.....	167
3.13.3	Scaling Resistance.....	170
3.13.4	Abrasion Resistance	174
3.13.5	Freeze-Thaw Resistance.....	180
3.13.6	Alkali-Silica Reaction	189
3.14	Split Cylinder Tension Testing on Cracked Cylinders.....	192
CHAPTER 4 GIRDER MATERIAL PROPERTIES		198
4.1	Test Specimen Casting, Harvesting, and Preparation	198
4.2	UHPC Compression Testing	199
4.3	UHPC Flexural Prism Testing.....	202
CHAPTER 5 GIRDER FABRICATION AND EXPERIMENTAL METHODS.....		206
5.1	Girder Fabrication	206
5.2	Test Matrix	207
5.3	Test Setup and Specimen Details	208
5.4	Instrumentation.....	212
5.4.1	Girder 80F	212
5.4.2	Girder 28S	213
5.4.3	Girder 24S	216
5.4.4	Girder 14S	217
5.5	Loading Procedure.....	220
CHAPTER 6 UHPC GIRDER TESTING RESULTS.....		222
6.1	Static Flexural Testing.....	222
6.2	Static Shear Testing.....	233
6.2.1	Girder 28S	233

6.2.2	Girder 24S	243
6.2.3	Girder 14S	249
CHAPTER 7 DISCUSSION OF RESULTS		261
7.1	Tensile Behavior of UHPC.....	261
7.1.1	Summary of Experimental Results.....	261
7.1.2	Summary of Experimental Test Methods.....	266
7.2	Local and Global Mechanical Failure Modes of UHPC	269
7.3	Effect of Curing Procedure on UHPC Properties.....	274
7.4	Early Age Strength Gain of UHPC	276
7.5	Comparison of Cylinder and Cube Compression Strength Results.....	279
7.7	Shrinkage Behavior of UHPC	281
7.8	Long-term Stability of UHPC	282
7.9	Modulus of Elasticity of UHPC	284
7.10	Compressive Stress-Strain Behavior of UHPC	289
7.11	Development Length of Prestressing Strand in UHPC	295
7.12	Estimation of Prestress Losses in UHPC Girders.....	298
7.13	Flexural Behavior of Prestressed UHPC Girders	302
7.13.1	Analytical Predictions of Global Behavior	302
7.13.2	Cracking Behavior.....	305
7.13.3	Effective Moment of Inertia.....	310
7.13.4	Flexural Stiffness Under Flexural Loading.....	313
7.13.5	Uniaxial Stress-Strain Model of Girder Flexural Behavior	319
7.14	Shear Behavior of Prestressed UHPC Girders Containing No Mild Steel.....	328
7.14.1	Predicted vs. Actual Global Behavior	328
7.14.2	Cracking Behavior.....	331
7.14.3	Simplified Model of UHPC Girder Shear Failure.....	333
7.14.4	Strut-and-Tie Model of Girder 28S Failure.....	336
CHAPTER 8 DESIGN PHILOSOPHY FOR UHPC BRIDGE GIRDERS		339
8.1	Introduction	339
8.2	Flexure	339
8.3	Shear	341
CHAPTER 9 CONCLUSIONS AND FUTURE RESEARCH		344
9.1	Introduction	344
9.2	Conclusions	345
9.2.1	General	345
9.2.2	Highway Bridge Girders	346
9.2.3	Material Property Characterization	348
9.3	Ongoing and Future Research	354
REFERENCES		355

LIST OF TABLES

Table 2.1-A:	Typical UHPC composition.....	6
Table 2.2-A:	Manufacturer supplied material characteristics	6
Table 2.3-A:	Chemical composition of steel fibers.....	7
Table 3.1.2-A:	Batching descriptions with associated specimens and curing regimes.....	20
Table 3.1.2-B:	Batching descriptions with associated specimens and curing regimes for non-standardized batches.....	23
Table 3.2-A:	Batching and casting properties of Steam and Air treated UHPC. Batching and casting properties of Tempered Steam and Delayed Steam treated UHPC.....	32
Table 3.2-B:	Batching and casting properties of batches cast to complete the study by addressing special issues	34
Table 3.3.1-A:	Control cylinder compressive strength results.....	41
Table 3.3.1-B:	More control cylinder compressive strength results	42
Table 3.3.2-A:	Strength, modulus of elasticity, and strain at peak stress results at various ages after casting (Part I)	52
Table 3.3.2-A:	Strength, modulus of elasticity, and strain at peak stress results at various ages after casting (Part II).....	53
Table 3.3.3-A:	Compressive stress-strain response linearity at various ages after casting (Part I)	57
Table 3.3.3-A:	Compressive stress-strain response linearity at various ages after casting (Part II)	58
Table 3.3.4-A:	Cylinder and cube compressive strength results.....	63
Table 3.3.5-A:	Demolding age effect on 28-day compressive strength results	65
Table 3.3.6-A:	Long-term delayed steam effect on compressive strength.....	66
Table 3.3.8-A:	Load rate effect on compression testing results.....	71
Table 3.4.1.1-A:	ASTM C1018 strength results	89
Table 3.4.1.2-A:	Definition of Toughness Indices (From ASTM C1018 FIG. X1.1) ...	91
Table 3.4.1.2-B:	ASTM C1018 toughness results	93
Table 3.4.2-A:	Split tensile strength normalized by 28 day compressive strength....	104
Table 3.4.2-B:	First crack parameters determined by instantaneous lateral expansion of cylinder and aural observations.....	104
Table 3.4.3.2-A:	Fiber influence on post-cracking behavior	118
Table 3.4.4-A:	Direct tension test results	124
Table 3.6-A:	Penetration resistance results	141
Table 3.7.1-A:	Long-term shrinkage.....	142
Table 3.7.2-A:	Early age shrinkage rate.....	147
Table 3.8.1-A:	Long-term creep results	149
Table 3.8.2-A:	Early age creep results	153
Table 3.9-A:	Coefficient of thermal expansion results	156
Table 3.11-A:	Air void analysis results.....	162
Table 3.13.1-A:	Rapid chloride ion penetrability results	167
Table 3.13.5-A:	Effect of a water bath on the compressive strength of Steam and Air treated UHPC.....	188

Table 3.13.6-A:	Timetable for ASTM C1260 specimens	191
Table 3.13.6-B:	ASTM C1260 alkali-silica reactivity expansion results	192
Table 3.14-A:	Crack width and split cylinder peak strength results for ponded cylinders.....	196
Table 4.2-A:	Compression test results	201
Table 4.3-A:	Prism flexure test results.....	205
Table 5.2-A:	Test matrix.....	208
Table 7.1.1-A:	UHPC material characterization results for average tensile properties of UHPC.....	262
Table 7.3-A:	Average UHPC material properties presented according to curing treatment	277
Table 7.9-A:	Compressive strength and modulus of elasticity results.....	284
Table 7.10-A:	Constants for Equation 7.10-A	294

LIST OF FIGURES

Figure 2.3-A:	Three tensile stress-strain responses for steel fiber reinforcement	8
Figure 3.2-A:	Mixing of UHPC including (clockwise from left) water addition, HRWA addition, pre-paste consistency, fiber addition, and finished mix	27
Figure 3.2-B:	Mix time as affected by premix age.....	35
Figure 3.2-C:	Final flow diameter as affected by premix age.....	35
Figure 3.3-A:	(a) Grinding and (b) measuring of 3-in. diameter cylinders	38
Figure 3.3-B:	3-in. diameter cylinders (a) before and (b) after compression testing.....	39
Figure 3.3.1-A:	Compressive strength and density of control cylinders	43
Figure 3.3.1-B:	Compressive strength and cylinder end planeness of control cylinders.....	43
Figure 3.3.2-A:	Modulus ring attachment (a) before and (b) during testing	48
Figure 3.3.2-B:	Selected stress-strain responses for Steam treated UHPC (N1A)	48
Figure 3.3.2-C:	Selected stress-strain responses for Steam treated UHPC (N1AxxA)	49
Figure 3.3.2-D:	Selected stress-strain responses for Air treated UHPC.....	49
Figure 3.3.2-E:	Selected stress-strain responses for Tempered Steam treated UHPC	50
Figure 3.3.2-F:	Selected stress-strain responses for Delayed Steam treated UHPC	50
Figure 3.3.2-G:	Compressive strength gain from casting up to 8 weeks of age.....	51
Figure 3.3.2-H:	Modulus of elasticity gain from casting up to 8 weeks of age.....	51
Figure 3.3.2-I:	Strain at peak compressive stress from casting up to 8 weeks of age.....	51
Figure 3.3.3-A:	Sample Air treated stress-strain curve with linearity descriptors	55
Figure 3.3.3-B:	Secant modulus from casting up to 8 weeks of age	59
Figure 3.3.3-C:	Ratio of elastic to secant modulus from casting up to 8 weeks of age.....	59
Figure 3.3.3-D:	Compressive stress to strength ratio at 1% stress drop from linear elastic	60
Figure 3.3.3-E:	Compressive stress to strength ratio at 5% stress drop from linear elastic	60
Figure 3.3.4-A:	Compression cubes and cylinders including (clockwise from upper left) 4-in., 3-in. overlength, 3-in., and 2-in. diameter cylinders and 2 in. and 4 in. cubes.....	62
Figure 3.3.4-B:	(a) Cylinder and (b) cube compression testing	62
Figure 3.3.7-A:	Compression failure of a Steam treated UHPC cylinder containing no fiber reinforcement. (a) 1/6 th of a second before failure. (b) 1/30 th of a second before failure. (c) At failure. (d) 1/10 th of a second after failure.....	69
Figure 3.4.1-A:	Prism flexural test setup for a (a) 9 in. span and a (b) 12 in. span.....	73

Figure 3.4.1-B:	Examples of first crack shown on load-deflection response curves	78
Figure 3.4.1-C:	ASTM C1018 load-deflection response results for 2x2 prisms over a 6 in. span with third point loading	79
Figure 3.4.1-D:	ASTM C1018 load-deflection response results for 3x4 prisms over a 12 in. span with third point loading	80
Figure 3.4.1-E:	ASTM C1018 load-deflection response results for 2x2 prisms over a 9 in. span with third point loading	81
Figure 3.4.1-F:	ASTM C1018 load-deflection response results for 2x2 prisms over a 12 in. span with third point loading	82
Figure 3.4.1-G:	ASTM C1018 load-deflection response results for 2x2 prisms over a 15 in. span with 3 in. between loads	83
Figure 3.4.1.1-A:	Ratio of shear to flexural deflection for a third-point loaded prism	88
Figure 3.4.1.2-A:	ASTM C1018 toughness results	94
Figure 3.4.1.2-B:	ASTM C1018 residual strength results	95
Figure 3.4.2-A:	Split cylinder tensile test including (a) standard test setup, (b) lateral expansion measuring apparatus, and (c) UHPC cylinder during test	98
Figure 3.4.3-B:	Typical response for a UHPC cylinder during the ASTM C496 test	99
Figure 3.4.3-C:	Average tensile cracking results from the ASTM C496 test	101
Figure 3.4.2-D:	Average split cylinder peak strength from the ASTM C496 test.....	103
Figure 3.4.3-A:	AASHTO T132 setup including (a) test grips and (b) specimen.....	106
Figure 3.4.3-B:	Load-displacement response for Steam treated briquette tests	108
Figure 3.4.3-C:	Load-displacement response for Air treated briquette tests.....	109
Figure 3.4.3-D:	Load-displacement response for Tempered Steam treated briquette tests	110
Figure 3.4.3-E:	Load-displacement response for Delayed Steam treated briquette tests	111
Figure 3.4.3.1-A:	Tensile cracking strength of UHPC briquettes	112
Figure 3.4.3.1-B:	Post-cracking peak strength of UHPC briquettes	114
Figure 3.4.3.2-A:	Area under the load-displacement response curve after cracking.....	116
Figure 3.4.3.2-B:	Ratio of post-cracking to pre-cracking areas under the load-displacement curve.....	117
Figure 3.4.4-A:	(a) Notched cylinder and (b) testing of an unnotched cylinder	121
Figure 3.5-A:	Test setup for 4 in. by 2 in. notched prisms loaded on a 16 in. span	127
Figure 3.5-B:	Resistance foil gage to monitor crack propagation.....	128
Figure 3.5-C:	Prism M1P00 after (a) 3.4 in. and (b) 3.85 in. of crack extension.....	129
Figure 3.5-D:	Prism M2P03 after 3.65 in. of crack extension.....	130
Figure 3.5-E:	Load-CMOD response for Steam treated prism M1P00 (a.) Overall response including periodic unloadings. (b.) Initial response including elastic stiffness and 95% of elastic stiffness curves.	132

Figure 3.5-F:	Load-CMOD response for Steam treated prism M1P01 (a.) Overall response including periodic unloadings. (b.) Initial response including elastic stiffness and 95% of elastic stiffness curves.	133
Figure 3.5-G:	Load-CMOD response for Steam treated prism M1P02 (a.) Overall response including periodic unloadings and crack length from tension flange. (b.) Initial response including elastic stiffness and 95% of elastic stiffness curves. ...	134
Figure 3.5-H:	Load-CMOD response for Steam treated prism M1P03 (a.) Overall response including periodic unloadings and crack length from tension flange. (b.) Initial response including elastic stiffness and 95% of elastic stiffness curves. ...	135
Figure 3.5-I:	Load-CMOD response for Steam treated prism M2P00 (a.) Overall response including periodic unloadings. (b.) Initial response including elastic stiffness and 95% of elastic stiffness curves.	136
Figure 3.5-J:	Load-CMOD response for Steam treated prism M2P01 (a.) Overall response including periodic unloadings. (b.) Initial response including elastic stiffness and 95% of elastic stiffness curves.	137
Figure 3.5-K:	Load-CMOD response for Steam treated prism M2P02 (a.) Overall response including periodic unloadings and crack length from tension flange. (b.) Initial response including elastic stiffness and 95% of elastic stiffness curves.....	138
Figure 3.5-L:	Load-CMOD response for Steam treated prism M2P03 (a.) Overall response including periodic unloadings and crack length from tension flange. (b.) Initial response including elastic stiffness and 95% of elastic stiffness curves.....	139
Figure 3.7.1-A:	Long-term shrinkage results	143
Figure 3.7.2-A:	Embeddable vibrating wire gage	145
Figure 3.7.2-B:	Early age shrinkage.....	146
Figure 3.8.1-A:	(a) Creep cylinders in load frame and (b) measurement of creep.....	148
Figure 3.8.1-B:	Long-term creep results	151
Figure 3.8.2-A:	Short-term creep test setup.....	152
Figure 3.8.2-B:	Early age creep behavior of 8 ksi to 9.5 ksi UHPC	154
Figure 3.8.2-C:	Early age creep behavior of 12.5 ksi UHPC	155
Figure 3.10-A:	Heat generated in 6-in. diameter cylinders during initial curing	157
Figure 3.10-B:	Heat generated in 6-in. diameter cylinders from casting through steaming	158
Figure 3.10-C:	Heat signature for 6-in. diameter cylinders in a well insulated calorimeter	159
Figure 3.12-A:	Fiber dispersion analysis results for cylinders impacted on an ASTM C230 flow table.....	164
Figure 3.12-B:	Fiber dispersion analysis photographs for a 1 in. ² area in the (a) bottom, (b) lower middle, (c) upper middle, and (d) top of a cast cylinder	164

Figure 3.13.1-A:	(a) Cylinder and (b) setup for rapid chloride ion penetrability test.....	166
Table 3.13.1-A:	Rapid chloride ion penetrability results	
Figure 3.13.1-B:	Average current passed versus time results for three sets of cylinders.....	167
Figure 3.13.2-A:	Chloride ion content results after 90 days of ponding.....	170
Figure 3.13.2-B:	(a) Cylinder prior to and (b) after 90 days of chloride ponding.....	170
Figure 3.13.3-A:	Scaling slab prior to the initiation of ASTM C672 testing.....	172
Figure 3.13.3-B:	Scaling slab after ASTM C672 testing	173
Figure 3.13.3-C:	Surface deterioration of a vertical surface after 70 plus 145 cycles of wetting/drying with a chloride solution in a freezing/thawing environment	174
Figure 3.13.4-A:	ASTM C944 abrasion test setup	175
Figure 3.13.4-B:	Steel cast surface Air and Steam Treated abrasion specimens after 8 and 10 minutes of abrading, respectively	177
Figure 3.13.4-C:	ASTM C944 weight loss (grams) per abrading.....	178
Figure 3.13.4-D:	Average weight loss (grams) per abrading	178
Figure 3.13.4-D:	Linear best-fit weight loss (grams) per abrading	179
Figure 3.13.5-A:	Resonant frequency testing of a freeze/thaw prism	182
Figure 3.13.5-B:	Freeze-thaw prism (a) before testing and (b) after 564 cycles.....	182
Figure 3.13.5-C:	Resonant frequency of freeze/thaw prisms	183
Figure 3.13.5-D:	Relative dynamic modulus of elasticity of freeze/thaw prisms	184
Figure 3.13.5-E:	Mass change of prisms during freeze-thaw testing.....	185
Figure 3.13.5-F:	Resonant frequency of prisms maintained at room temperature in a laboratory environment or in a water bath.....	186
Figure 3.13.5-G:	Relative dynamic modulus of elasticity of prisms maintained at room temperature in a laboratory environment or in a water bath.....	187
Figure 3.13.5-H:	Mass change of prisms maintained at room temperature in a laboratory environment or in a water bath.....	187
Figure 3.13.6-A:	Length comparator for ASR measurements.....	190
Figure 3.13.6-B:	ASTM C1260 alkali-silica reactivity expansion results	192
Figure 3.14-A:	Crack in a split cylinder tensile specimen.....	195
Figure 3.14-B:	Crack in a split cylinder tensile specimen under 350x magnification	196
Figure 3.14-C:	Split cylinder peak strength results.....	197
Figure 4.3-A:	Third-point loading response of a 2 in. by 2 in. prism on a 9 in. span.....	204
Figure 5.3-A:	Origin of the four girder specimens, with the south elevation of the tested configuration shown.....	209
Figure 5.3-B:	AASHTO Type II cross-section and strand pattern.....	211
Figure 5.4.1-A:	Instrumentation plan for Girder 80F.....	214
Figure 5.4.2-A:	Instrumentation plan for Girder 28	215
Figure 5.4.3-A:	Instrumentation plan for Girder 24S.....	218
Figure 5.4.4-A:	Instrumentation plan for Girder 14S.....	219

Figure 6.1-A:	Load-deflection response of Girder 80F. (a.) Deflection measured at midspan. (b.) Average deflections measured at load and quarter points.....	223
Figure 6.1-B:	Load-rotation response of Girder 80F.....	224
Figure 6.1-C:	Deflected shape of Girder 80F at selected load levels.....	224
Figure 6.1-D:	Moment-curvature response of Girder 80F.....	225
Figure 6.1-E:	Midspan neutral axis depth from the top of Girder 80F	226
Figure 6.1-F:	Principal strains in the web near the west support of Girder 80F	227
Figure 6.1-G:	Principal strain angles in the web near the west support of Girder 80F	227
Figure 6.1-H:	Crack spacing on the bottom flange of Girder 80F at 12 in. midspan overall girder deflection.....	229
Figure 6.1-I:	Girder 80F after approximately 17 in. of deflection.....	231
Figure 6.1-J:	Girder 80F immediately after failure	231
Figure 6.1-K:	Failure surface of Girder 80F including (a) overall west failure surface and (b) close-up of west failure surface showing pulled-out fibers and necked strands.....	232
Figure 6.2.1-A:	Load-deflection response of Girder 28S	234
Figure 6.2.1-B:	Bearing rotation response of Girder 28S	235
Figure 6.2.1-C:	Deflected shape of Girder 28S.....	235
Figure 6.2.1-D:	Strand slip in Girder 28S.....	236
Figure 6.2.1-E:	Principal tensile strain in the web of Girder 28S	237
Figure 6.2.1-F:	Principal tensile strain angle in the web of Girder 28S	237
Figure 6.2.1-G:	Principal compressive strain in the web of Girder 28S.....	238
Figure 6.2.1-H:	Principal compressive strain angle in the web of Girder 28S.....	238
Figure 6.2.1-I:	Crack at south base of Girder 28S web at a load of 450 kips	239
Figure 6.2.1-J:	Tension failure of top flange and crushing of web at conclusion of test	241
Figure 6.2.1-K:	Crack pattern at failure in Girder 28S.....	242
Figure 6.2.2-A:	Load-deflection response of Girder 24S.....	244
Figure 6.2.2-B:	Bearing rotation of Girder 24S	244
Figure 6.2.2-C:	Deflected shape of Girder 24S.....	245
Figure 6.2.2-D:	Principal tensile strain in the web of Girder 24S	247
Figure 6.2.2-E:	Principal tensile strain angle in the web of Girder 24S	247
Figure 6.2.2-F:	Principal compressive strain in the web of Girder 24S.....	248
Figure 6.2.2-G:	Principal compressive strain angle in the web of Girder 24S.....	248
Figure 6.2.2-H:	Failure of Girder 24S. (a) 1/15 th second before failure. (b) 1/30 th second before failure. (c) At failure. (d) 1/30 th second after failure.....	250
Figure 6.2.2-I:	Failed Girder 24S (a) south elevation and (b) bottom flange near bearing.....	251
Figure 6.2.2-J:	Crack pattern at failure in Girder 24S.....	252

Figure 6.2.3-A:	Load-deflection response for Girder 14S.....	253
Figure 6.2.3-B:	Bearing rotation for Girder 14S.....	253
Figure 6.2.3-C:	Deflected shape for Girder 14S.....	254
Figure 6.2.3-D:	Strand slip in Girder 14S.....	255
Figure 6.2.3-E:	Principal tensile strain in the web of Girder 14S.....	256
Figure 6.2.3-F:	Principal tensile strain angle in the web of Girder 14S.....	256
Figure 6.2.3-G:	Principal compressive strain in the web of Girder 14S.....	257
Figure 6.2.3-H:	Principal compressive strain angle in the web of Girder 14S.....	257
Figure 6.2.3-I:	Girder 14S at (a) peak load and (b) post-peak load of 595 kips.....	259
Figure 6.2.3-J:	Crack pattern at failure in Girder 14S.....	260
Figure 7.4-A:	Compressive strength gain as a function of time after casting.....	278
Figure 7.9-A:	Modulus of elasticity as a function of 28-day compressive strength.....	288
Figure 7.9-B:	Modulus of elasticity as a function of compressive strength.....	289
Figure 7.10-A:	Compressive stress-strain behavior compared with linear elastic response.....	292
Figure 7.10-B:	Normalized compressive stress-strain results for Steam treated UHPC.....	293
Figure 7.10-C:	Deviation from linear elastic compressive behavior for Steam treated UHPC.....	293
Table 7.10-A:	Constants for Equation 7.10-A.....	294
Figure 7.10-D:	Compressive stress-strain response approximations.....	295
Figure 7.13.1-A:	Predicted behavior of girders tested in the configuration of Girder 80F.....	306
Figure 7.13.2-A:	Girder 80F midspan bottom flange strain throughout testing.....	308
Figure 7.13.2-B:	Flexural crack spacing observed on the bottom flange of Girder 80F at a total applied load of 155 kips.....	308
Figure 7.13.2-C:	Flexural crack spacing related to tensile strain.....	309
Figure 7.13.2-D:	Tensile strain related to flexural crack spacing.....	310
Figure 7.13.3-A:	Effective moment of inertia of Girder 80F.....	312
Figure 7.13.4-A:	Flexural stiffness of an AASHTO Type II girder.....	316
Figure 7.13.4-B:	Ratio of predicted deflections and rotations to experimental results.....	317
Figure 7.13.4-C:	Predicted and observed midspan deflection results.....	317
Figure 7.13.4-D:	Predicted and observed load point deflection results.....	318
Figure 7.13.4-E:	Predicted and observed quarter point deflection results.....	318
Figure 7.13.4-F:	Predicted and observed end rotation results.....	318
Figure 7.13.5-A:	Experimental strain profile results for midspan of Girder 80F.....	320
Figure 7.13.5-B:	Analytically derived uniaxial stress-strain behavior of UHPC.....	324
Figure 7.13.5-C:	Summation of forces on cross-section during loading steps.....	325
Figure 7.13.5-D:	External and internal moments on midspan cross-section.....	327
Figure 7.13.5-E:	Internally and externally determined moment of inertia.....	327
Figure 7.14.4-A:	Truss model for failure of Girder 28S.....	337
Figure 8.2-A:	Sample uniaxial stress-strain behavior for I-girder flexural design.....	341

CHAPTER 1

INTRODUCTION

1.1 Introduction

Ultra-High Performance Concrete (UHPC) is a new class of concrete that has been developed in recent decades. When compared with High Performance Concrete (HPC), UHPC tends to exhibit superior properties such as advanced strength, durability, and long-term stability.

Many researchers around the world have developed concretes that could be classified as UHPC. Although there are differences among types of UHPC, there are also many overall similarities. The Association Française de Génie Civil (AFGC) *Interim Recommendations for Ultra High Performance Fibre-Reinforced Concretes* (2002) indicates that UHPC tends to have the following properties: compressive strength that is greater than 21.7 ksi, internal fiber reinforcement to ensure non-brittle behavior, and a high binder content with special aggregates. Furthermore, UHPC tends to have a very low water content and can achieve sufficient rheological properties through a combination of optimized granular packing and the addition of high-range water reducing admixtures.

Characterization of the material behaviors of UHPC has progressed to such an extent that the full-scale structural use of this concrete is on the horizon. To date, UHPC has been used in the construction of two public highway bridges (Hajar et al. 2003, Cavill and

Chirgwin 2004), numerous pedestrian bridges (Blais and Couture 1999, Behloul et al. 2004), and a wide variety of other projects (Semioli 2001, Acker and Behloul 2004, Buitelaar 2004). Research and observations to date indicate that UHPC has the potential to expand the use of concrete into new forms that have heretofore been impossible.

This research program focused on determining the behaviors of UHPC because this information is relevant to the highway bridge industry in the United States. Currently, the only UHPC that is commercially available in the United States is Ductal[®], which is a product of Lafarge, Inc. Therefore, Ductal[®] was the UHPC product used in this research program.

1.2 Objective

The objective of this research is to evaluate the potential use of UHPC in highway bridge girders by characterizing material behaviors through small-scale specimen testing and by characterizing structural behaviors through full-scale girder testing.

1.3 Summary of Approach

The research included two experimental phases and one analytical phase. The experimental phases focused on determining the material behavior from small-scale testing and the structural behavior from full-scale prestressed bridge girder tests. The material characterization of UHPC included the testing of over 1000 individual specimens, with an emphasis toward determining the compressive and tensile behaviors, the long-term stability, and the durability of UHPC. Many of the material characterization

tests were completed according to ASTM and AASHTO standard test procedures; however, in some instances these tests were modified or new tests were devised to accurately capture the relevant behaviors of the concrete.

The full-scale bridge girder testing was conducted on AASHTO Type II prestressed girders. The tests that were conducted include one flexure test on an 80-foot span girder and three shear tests on shorter span girders. These girders did not contain any mild steel reinforcement, thus the UHPC was required to carry all secondary (i.e., shear, temperature, shrinkage) tensile forces.

The analytical phase of this research combined, analyzed, and elaborated upon the results from the experimental phases. This phase included developing predictor equations for basic properties of UHPC and developing a rational philosophy for the flexure and shear design of prestressed UHPC I-girders.

1.4 Outline of Report

This report is divided into nine chapters. Chapters 1 and 2 provide an introduction and relevant background information. Chapter 3 presents the results of the material characterization study. Chapter 4 presents the results of the material tests performed on the specimens from the full-scale UHPC girders. Information regarding the fabrication of and experimental method associated with those girders is presented in Chapter 5. The full-scale girder test results are presented in Chapter 6. Chapter 7 analyzes and discusses the experimental results presented in Chapters 3 through 6. A design philosophy for the

flexural and shear design of prestressed UHPC I-girders is presented in Chapter 8.

Finally, Chapter 9 presents the conclusions of this research program.

CHAPTER 2

BACKGROUND AND PREVIOUS WORK

2.1 UHPC Constituent Materials

The UHPC used in this study is a patented product of a major worldwide concrete manufacturer. The product is a reactive powder concrete that is marketed under the name Ductal[®]. This product has a number of different material compositions depending on the particular application. A typical composition is provided in Table 2.1-A.

The constituent material proportions were determined, in part, based on an optimization of the granular mixture. This method allows for a finely graded and highly homogeneous concrete matrix. Fine sand, generally between 150 and 600 μm , is dimensionally the largest granular material. The next largest particle is cement with an average diameter of approximately 15 μm . Of similar size is the crushed quartz with an average diameter of 10 μm . The smallest particle, the silica fume, has a diameter small enough to fill the interstitial voids between the cement and the crushed quartz particles.

Dimensionally, the largest constituent in the mix is the steel fibers. In this study, the fibers in the mix had a diameter of 0.008 in. and a length of 0.5 in. Given the relative sizes of the sand and the fibers, the steel fibers are able to reinforce the concrete matrix on the micro level. A further discussion of the properties of the steel fibers is provided in Section 2.4.

Table 2.1-A: Typical UHPC composition

Material	Amount (lb/yd ³)	Percent by Weight
Portland Cement	1200	28.5
Fine Sand	1720	40.8
Silica Fume	390	9.3
Ground Quartz	355	8.4
Superplasticizer	51.8	1.2
Accelerator	50.5	1.2
Steel Fibers	263	6.2
Water	184	4.4

2.2 Manufacturer Supplied UHPC Material Properties

As previously discussed, the UHPC used in this study is a proprietary product. The manufacturer has performed significant material property testing and has reported typical characteristics. Table 2.2-A provides some of the material properties relevant to using this material in bridge applications. In general, these properties have not been verified and are provided here solely for completeness.

Table 2.2-A: Manufacturer supplied material characteristics

Material Characteristic	Range
Compressive Strength (ksi)	26 – 33
Modulus of Elasticity (ksi)	8000 – 8500
Flexural Strength (ksi)	5.8 – 7.2
Chloride Ion Diffusion (ft ² /s)	0.02 x 10 ⁻¹¹
Carbonation Penetration Depth (in)	<0.02
Freeze-Thaw Resistance (RDM)	100%
Salt-Scaling Resistance (lb/ft ²)	<0.0025
Entrapped Air Content	2 – 4%
Post-Cure Shrinkage (microstrain)	0
Creep Coefficient (x10 ⁻⁶ in/in/°C)	0.2 – 0.5
Density (lb/ft ³)	152 - 159

2.3 Steel Fiber Material Properties

The steel fibers used in this test program were straight steel wire fibers manufactured by Bekaert Corporation. The fibers have a nominal diameter of 0.008 in. (0.20 mm) and a nominal length of 0.5 in. (13 mm). The chemical composition of the fibers is shown in Table 2.3-A. Note that a thin brass coating is applied to the fibers during the drawing process; therefore, virgin fibers may be gold-colored. This coating disappears during the mixing process and is no longer clearly visible during the casting of the UHPC.

The intended function of these fibers within UHPC requires that the fibers have a very high tensile strength. The manufacturer's specified minimum tensile strength is 377 ksi (2600 MPa), and tension tests are performed as a means of quality control on the fiber production. The results from three of these tests are presented in Figure 2.3-A. The average yield strength of these fibers as calculated by the 0.2% offset method is 457.7 ksi. The modulus of elasticity is 29790 ksi, and the ultimate strength is 474.0 ksi. These results clearly show that these high strength steel wires have little reserve strength or ductility capacity beyond yield.

Table 2.3-A: Chemical composition of steel fibers

Element	Composition (percent)
Carbon	0.69 – 0.76
Silicon	0.15 – 0.30
Manganese	0.40 – 0.60
Phosphorus	≤ 0.025
Sulfur	≤ 0.025
Chromium	≤ 0.08
Aluminum	≤ 0.003

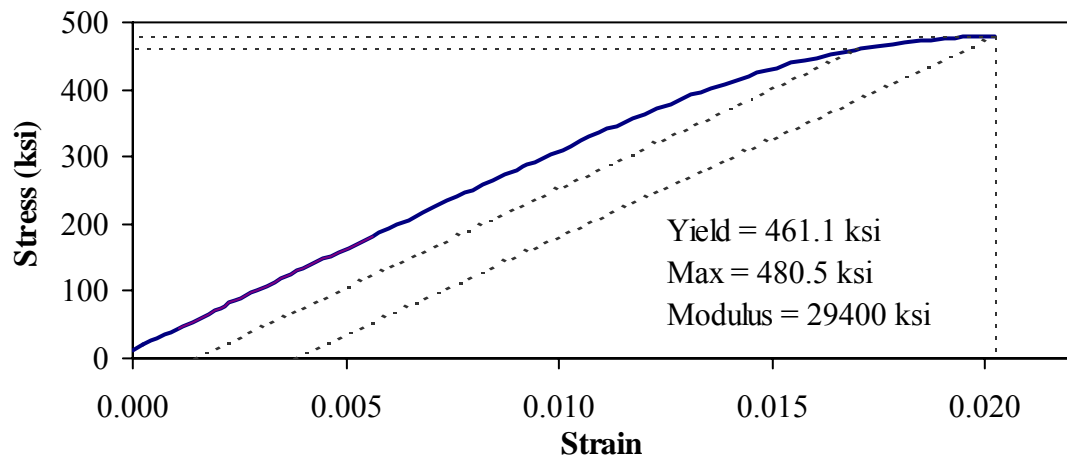
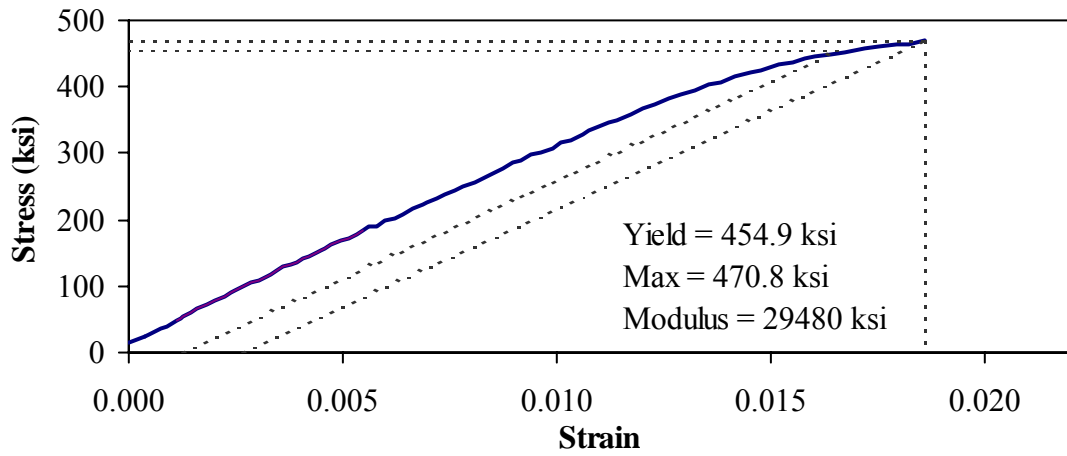
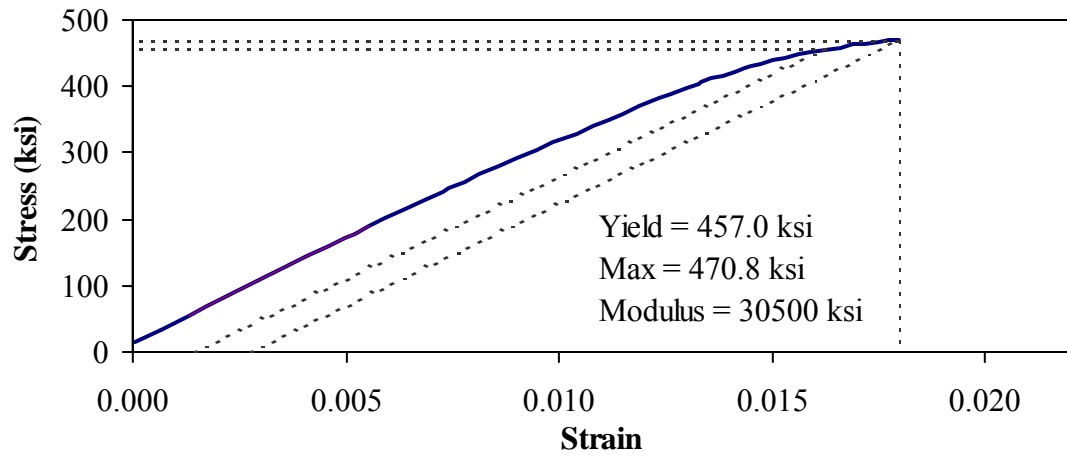


Figure 2.3-A: Three tensile stress-strain responses for steel fiber reinforcement

2.4 Relevant Material Property Characterization Studies

2.4.1 Fiber Orientation Effect on Mechanical Properties by Stiel et al.

Stiel, Kariloo, and Fehling (2004) have conducted a research program investigating the effect of fiber orientation on the mechanical properties of UHPC. These researchers focused on a patented UHPC marketed under the name CARDIFRC[®]. This UHPC is composed of similar constituent materials and in similar proportions to the UHPC investigated in the present study. One primary difference is that CARDIFRC[®] contains two lengths of steel fibers and a total fiber volumetric percentage of 6 percent.

This research program focused on the effect of UHPC flow direction during casting on the compressive and flexural tensile behaviors of the concrete. Fiber reinforcement tends to align with the direction of flow during casting. This research program investigated the tensile and compressive behaviors of UHPC when loaded parallel to and perpendicular to the direction of flow during casting. The compression tests were performed on 100 mm cubes. The three-point bending flexure tests were performed on 100 mm by 100 mm prisms with a 500 mm length.

The cube compression tests indicated that preferential fiber alignment has no significant effect on either the compressive strength or the modulus of elasticity of UHPC. However, the three-point flexure tests showed that the peak equivalent flexural strength of the UHPC prisms was decreased by a factor of more than three when the fibers were preferentially aligned perpendicular to the principal flexural tensile forces. This preferential fiber alignment was clearly apparent on failure surfaces of the prisms. These

prisms also did not exhibit the traditional post-cracking toughness behaviors normally associated with UHPC and frequently exhibited an abrupt load decrease immediately after first cracking. All of these findings point to the importance of understanding the structural loadings that will be carried by a UHPC member and following correct placement techniques when casting UHPC members.

2.4.2 Prestressing Strand Development Length by Steinberg and Lubbers

Researchers at Ohio University (Steinberg and Lubbers 2003) recently completed a study of the force transfer behavior of prestressing strand in UHPC. This research program focused on determining the development length of 0.5-in. 270-ksi low relaxation prestressing strands in UHPC similar to that studied in the present research program. Predefined lengths of strands were cast into blocks of UHPC, then the strands were pulled until slip or strand rupture occurred. Embedment lengths of 12, 18, and 24 in. were investigated. In all tests, fracture of the strand occurred before significant slip of the strand could occur. These results indicate that the development length of this type of strand in UHPC is less than 12 in.

2.4.3 Permeability of Cracked Concrete by Rapoport et al.

Rapoport et al. (2002) investigated the permeability of steel fiber reinforced concrete as compared to normal concrete. The research focused on creating small cracks in 0.5 percent and 1.0 percent steel fiber reinforced concrete, then determining the permeability of the concrete. The two primary findings of interest from this study are as follows. First, this study confirmed the findings of other researchers (Aldea et al. 1999) that cracks less

than 0.004 in. wide have little impact on the permeability of normal concrete. Second, this study confirmed that steel fiber reinforcement reduces the total permeability of a strained section of concrete by changing the cracking mechanism from a few large width cracks to many small width cracks. As would be expected, the concrete with the higher volume percentage of fiber reinforcement displayed more distributed cracking and had a lower permeability.

2.4.4 Creep and Shrinkage of UHPC by Acker

Recall the very low post-steam treatment creep and shrinkage values presented in Table 2.2-A. Lafarge, the manufacturer and distributor of the UHPC discussed in this report, has performed significant research focusing on the creep and shrinkage behaviors of this concrete. Some results of this research were presented in Acker (2004), wherein the microstructural behaviors leading to creep and shrinkage of UHPC, HPC, and normal concrete are discussed. Additional discussion with further experimental results are presented in Acker (2001).

Acker argues that creep and shrinkage are closely related behaviors that cannot generally be uncoupled and studied separately. He indicates that shrinkage is primarily caused by self-desiccation of the concrete binder resulting in the irreversible collapse of calcium-silicate-hydrate (CSH) sheets. As UHPC contains a very low water-to-cementitious ratio, this concrete completely self-desiccates between casting and the conclusion of Steam treatment. Thus, UHPC exhibits no post-treatment shrinkage.

In regard to creep, Acker restates previous research indicating that the CSH phase is the only constituent in UHPC that exhibits creep. Also, he points out that concrete creep tends to be much more pronounced when it occurs as the concrete is desiccating. Thus, the collapsed CSH microstructure and the lack of internal water both work to reduce the creep of UHPC.

2.4.5 Abrasion Resistance of HSC via ASTM C944 by Horszczaruk

Horszczaruk (2004) studied the abrasion resistance of high strength fiber reinforced concrete using the ASTM C944 standard procedure. This is the same procedure that the abrasion tests discussed in Section 3.13.4 of the present report followed. Horszczaruk's study focused on 12 ksi to 14.5 ksi compressive strength concretes containing basalt aggregates (0.1 in. to 0.5 in. diameter) and natural river sands (less than 0.1 in. diameter). The testing followed ASTM C944, except that the duration of test was increased from 2 minutes to 40 minutes to allow for differentiation between concretes.

The relevant results from this study include the following. The linear best-fit approximation of the concrete mass loss per 2 minute abrading cycle ranged from 0.14 grams to 0.78 grams. Of the ten concretes tested, six of them ranged from 0.14 grams to 0.25 grams. Horszczaruk also indicates that the rate of mass loss was relatively consistent throughout the abrading, with no clear increased abrasion resistance during the abrading of the smooth exterior face of the concrete.

2.5 Relevant Girder Testing

2.5.1 Shear Capacity of AASHTO Type II Girders by Tawfig

In the early 1990's the Florida Department of Transportation sponsored a research program focused on determining the shear capacity of high strength concrete bridge girders. This research, performed by Tawfig (1995, 1996), experimentally determined the shear capacity of AASHTO Type II girders composed of 8, 10, and 12 ksi concrete. The AASHTO Type II girder cross-section tested included 16 strands in the bottom flange, 2 in the top flange, and an 8-in. by 42-in. composite deck cast onto the top of the girder.

Six tests were completed, with two at each compressive strength level. The loading arrangement for the test included offset three-point loading with a shear span-to-depth ratio of approximately 2.5. The shear reinforcement in these girders was designed according the AASHTO *Standard Specifications for Highway Bridges* (1992). Two #4 stirrups were spaced every 6 in. for the first 4 feet from the bearing, then two #4 stirrups for spaced every 8 in. for the next four feet. The remainder of the span had single #4 stirrups spaced at 8 and 12 in. spacings.

The overall shear capacity of these girders is the primary result from these tests that is applicable to the UHPC girder tests performed as part of the current research program. On average, the shear capacity exhibited in each of the six tests was approximately 270 kips. The shear capacity was not significantly influenced by the compressive strength of the concrete.

2.5.2 Shear Capacity of Small UHPC Beams by Hegger et al.

Researchers at the Institute of Structural Concrete at RWTH Aachen University have recently completed several tests investigating the shear capacity of UHPC beams. This research (Hegger et al. 2004) focused on determining the shear capacity of a 12 in. deep prestressed concrete beam containing no mild steel shear reinforcement. The UHPC used in this research program was similar to the UHPC discussed throughout this report, although it did contain a slightly larger percentage of steel fiber reinforcement (2.5 percent).

The cross-section of the I-beams tested in this research program contained eight 7-wire 0.6-in. prestressing strands in the bottom flange. The bottom flange of the beam was 11.5 in. wide and the top flange was 8.7 in. wide. The web of the beam was 5.9 in. tall and 2.8 in. thick. The overall beam length was 11.5 ft. and each beam was loaded in four-point bending.

The average ultimate shear capacity of these UHPC beams was 61.4 kips. Given the size of these beams, this result is very similar to the shear capacities that were observed in the full-scale AASHTO Type II shear tests that are presented in Chapters 6 and 7. The analytical procedure presented in Section 7.14.3 indicates that the average tensile stress carried by the UHPC across the shear failure plane was approximately 2 ksi.

2.5.3 Flexural Capacity of High-Strength Concrete Girders by Russell and Burns

Russell and Burns (1993) investigated the behavior of prestressed concrete girders composed of high-strength concrete. In particular, this study focused on the static and fatigue behavior of composite bridge girders under flexure and shear loadings. The girder flexural test completed in this research is of most interest to the present study.

This research was completed on Texas Type C girders, which are of similar shape but slightly shallower than AASHTO Type III girders. The tested girder was 40 in. deep, with an 8 in. deep composite deck cast on top. The deck was 72 in. wide and composed of 6 ksi concrete. The girder was composed of 10 ksi concrete and spanned 48 ft. The flexural test girder contained twenty-eight 0.5-in. 270-ksi low-relaxation prestressing strands, each stressed to 31 kips. Twelve of the strands were draped.

The flexural testing of this girder included both static and fatigue loadings. Initially, sufficient load was applied to crack the girder in flexure and shear. Flexural loading was then repeated for 225,000 cycles, after which the girder was loaded to flexural failure. The flexural capacity of this 48 in. deep composite girder was 38300 k-in. of applied load. Russell and Burns note that “[t]he girder failed in pure flexure with yielding of the strands and large plastic rotations. Cracking extended into the deck slab.” The load-deflection response of the girder indicates that the midspan deflection at failure was approximately 7 in.

CHAPTER 3

UHPC MATERIAL CHARACTERIZATION

3.1 Research Plan

The stated goal of the UHPC material characterization study is to determine the basic behaviors of UHPC with the intent of using UHPC in highway bridges. Many material behaviors are critical to the successful use of concrete in a highway bridge. These behaviors include strength, durability, and long-term stability. Each of these behaviors will be discussed in depth in this chapter.

The curing treatment applied to concrete—which is always important—is even more important in the case of UHPC. The UHPC studied in this research program is normally steam treated once it has reached sufficient strength to undergo the process. However, steam treatment of UHPC in a controlled environment may not always be feasible or even desirable. For this reason, the focus of the research, which is discussed in this chapter, is on characterizing UHPC that had been treated to one of four curing conditions. The four curing conditions included the standard steam treatment, a delayed version, a lower temperature version of the same steam treatment, and an air treatment wherein no steaming was conducted. These curing regimes will be described in more detail later in this chapter.

This chapter describes the results of the material characterization study. The chapter starts by introducing specimen nomenclature and test matrix information. Next, the

batching, casting, and curing procedures and results are presented. Results from individual tests that focused on specific aspects of UHPC behavior are discussed in the remainder of this chapter.

3.1.1 Batch and Specimen Nomenclature

The material characterization study detailed in this chapter included over well 1000 individual UHPC specimens. A naming scheme was created to allow for easy, unique identification of each specimen. The large majority of specimens cast for this study were part of the standardized set of batches designed to investigate the behavior of UHPC cured under various curing conditions. The other specimens were cast in extraneous batches that focused on specific behaviors of UHPC, primarily as related to compression testing.

For clarity, the nomenclature discussed here will not be mentioned throughout most of this chapter. In most instances, the presentation and discussion of results can be completed without naming individual specimens. However, in some instances, the naming system has to be used because of the large amount of similar specimens and testing procedures.

The nomenclature used to describe the specimens in the standardized batches is based on a five-digit alphanumeric identifier. A letter that identifies the premix delivery fills the first digit in the identifier. This letter is 'L,' 'M,' or 'N' for the first, second, or third delivery, respectively. The second digit in the identifier is filled by an integer that

identifies the curing treatment applied to the specimen. This number ranges from one to four for the Steam, Air, Tempered Steam, and Delayed Steam treatments, respectively. The third digit in the identifier is reserved for a letter that identifies the tests performed on that batch of specimens. These letters and the associated tests will be discussed further in the following section. A two-digit number indicating the particular specimen within the batch occupies the fourth and fifth digits. In the few cases in which a batch was repeated, the second batch was named identically to the first batch, except that an 'A' was placed at the end of the identifier for each specimen.

An example of this alphanumeric identification scheme is as follows. The first three digits in the name M1F01 indicate that this specimen was from the second premix delivery that was first Steam treated and then subjected to testing within the general durability batches. The '01' in the fourth and fifth digits indicates that this specimen was a prism subjected to freeze-thaw testing.

A simpler naming scheme was used for the extraneous batches. These batches were named sequentially based on the premix delivery. For example, the 10th batch cast from the 'L' delivery focused on the effect of varying the load rate on compression test results. Thus, the specimens from this batch are identified as L10-xx, with the 'xx' being an integer identifier for each of the cylinders cast. In general, 30 or more cylinders populated these batches, and the associated testing was designed to indicate the effect of some external action on compressive behavior. The primary exception to this rule is batch N06, which focused on the early age shrinkage behavior of UHPC.

3.1.2 Test Matrix

The test matrix devised for the material characterization study was intended to cover a wide range of the basic behaviors of UHPC. The types of tests performed can generally be grouped into three classes. First, strength tests focused on the compressive and tensile behaviors of UHPC at various ages and under various curing conditions. Second, durability tests focused on the durability of UHPC under conditions with standardized aggressors. Finally, stability tests focused on the long-term ability of UHPC to maintain dimensional stability under various loading and environmental conditions.

Table 3.1.2-A lists the standardized batches that were used throughout this study. The batch letter listed in the first column is the same letter that would reside in the third digit of the alphanumeric identifier in a specimen's name. A simplified description of the batch along with the associated testing is included in the next column. The specimens cast for each particular batch are included in the third column. Finally, the last two columns include the volume of material that was in an individual batch as well as the curing regimes for which each batch was cast. A batch of the size indicated was cast for each curing regime listed. Note that this large table continues over three pages.

Table 3.1.2-B provides similar information for the extraneous batches that were cast. The only difference between this table and Table 3.1.2-A is that the batches were not cast for each curing regime listed. Because the first column lists individual batches of concrete, the curing regimes listed were applied to some of the specimens in each batch.

Table 3.1.2-A: Batching descriptions with associated specimens and curing regimes

Batch	Batch Description	Test Completed	Specimens Cast †	Batch Size (ft³)	Curing Regimes ‡
A	Compressive Strength			1.15	1,2,3,4
		<i>Compressive Strength, Stress-Strain</i>	36 3x6 cylinders		
		<i>Penetration Resistance</i>	1 6x6 cylinder		
B	Cubes/Cylinders Compression			0.9	1,2
		<i>28 day Compressive Strength</i>	6 3x6 cylinders		
		<i>28 day Compressive Strength</i>	3 3x6.5 cylinders		
		<i>28 day Compressive Strength</i>	6 2x4 cylinders		
		<i>28 day Compressive Strength</i>	5 4x8 cylinders		
		<i>28 day Compressive Strength</i>	6 2" cubes		
		<i>28 day Compressive Strength</i>	5 4" cubes		
C	Split Tensile			0.95	1,2,3,4
		<i>Split Tensile</i>	12 4x8 cylinders		
		<i>28 day Compressive Strength</i>	6 3x6 cylinders		
D	Direct Tension			1.0	1,2,3,4
		<i>Direct Tension</i>	12 4x8 cylinders		
		<i>Mortar Briquette</i>	18 briquettes		
		<i>28 day Compressive Strength</i>	6 3x6 cylinders		
E	Prism Flexure			1.1	1,2,3,4
		<i>Prism Flexure</i>	3 3x4x16 prisms		
		<i>Prism Flexure</i>	8 2x2x11 prisms		
		<i>Prism Flexure</i>	8 2x2x17 prisms		
		<i>28 day Compressive Strength</i>	6 3x6 prism		
P	Fracture/Fatigue of Prisms			1.05	1,2
		<i>Notched Prism Fracture</i>	4 2x4x18 prisms		
		<i>Flexural Toughness</i>	5 2x2x17 prisms		
		<i>Flexural Fatigue</i>	7 2x2x17 prisms		
		<i>28 day Compressive Strength</i>	6 3x6 cylinders		

Table 3.1.2-A (continued): Batching descriptions with associated specimens and curing regimes

Batch	Batch Description	Test Completed	Specimens Cast[†]	Batch Size (ft³)	Curing Regimes[‡]
F	Durability (Cl ⁻ Pen, FT, etc.)			1.0	1,2,3,4
		<i>Rapid Chloride Penetrability</i>	3 4x3 cylinders		
		<i>Chloride Penetration</i>	3 4x3 cylinders		
		<i>Freeze-Thaw</i>	3 3x4x16 prisms		
		<i>Abrasion</i>	3 6x3 cylinders		
		<i>ASR</i>	6 1x1x11 prisms		
		<i>28 day Compressive Strength</i>	6 3x6 cylinders		
Q	Freeze-Thaw Supplemental			1.1	1,2,3,4
		<i>Frequency Response</i>	4 3x4x16 prisms		
		<i>28 day Compressive Strength</i>	6 3x6 cylinders		
G	Scaling Slabs			0.9	1,2,3,4
		<i>Scaling</i>	2 3x14x14 slabs		
		<i>28 day Compressive Strength</i>	6 3x6 cylinders		
R	Split Tensile Crack Corrosion			1.05	1,2
		<i>Split Tensile</i>	9 4x8 cylinders		
		<i>Split Tensile w/ Ponding</i>	6 4x8 cylinders		
		<i>28 day Compressive Strength</i>	6 3x6 cylinders		
H	Creep, Shrinkage, Thermal Expansion			1.05	1,2,3,4
		<i>Creep</i>	5 4x8 cylinders		
		<i>Shrinkage</i>	3 3x3x11 prisms		
		<i>Thermal Expansion</i>	3 4x8 cylinders		
		<i>28 day Compressive Strength</i>	6 3x6 cylinders		
S	Early-Age Sustained Compressive Stress			0.95	1,2
		<i>Compressive Strength</i>	25 3x6 cylinders		
		<i>28 day Compressive Strength</i>	8 3x6 cylinders		

Table 3.1.2-A (continued): Batching descriptions with associated specimens and curing regimes

Batch	Batch Description	Test Completed	Specimens Cast [†]	Batch Size (ft³)	Curing Regimes [‡]
J	Air Content, Fiber Dispersion			0.7	1
		<i>Air Content, Fiber Dispersion</i>	8 4x8 cylinders		
		<i>28 day Compressive Strength</i>	6 3x6 cylinders		
K [*]	Air Content, Fiber Dispersion			0.7	1
		<i>Air Content, Fiber Dispersion</i>	8 4x8 cylinders		
		<i>28 day Compressive Strength</i>	6 3x6 cylinders		
M	Heat of Hydration			0.9	1,2
		<i>Heat of Hydration</i>	3 6x12 cylinders		
		<i>Heat of Hydration</i>	2 3x6 cylinders		
		<i>28 day Compressive Strength</i>	6 3x6 cylinders		
N [*]	Heat of Hydration			0.9	1,2
		<i>Heat of Hydration</i>	3 6x12 cylinders		
		<i>Heat of Hydration</i>	2 3x6 cylinders		
		<i>28 day Compressive Strength</i>	6 3x6 cylinders		

[†] Cylinders listed as *diameter x height*. Prisms listed as *depth x width x length* in tested configuration.

[‡] 1 = Steam, 2 = Air, 3 = Tempered Steam, 4 = Delayed Steam

^{*} Batch mix design did not contain any accelerator.

Table 3.1.2-B: Batching descriptions with associated specimens and curing regimes for non-standardized batches

Batch	Batch Description	Test Completed	Specimens Cast [†]	Batch Size (ft³)	Curing Regimes [‡]
L10	Load Rate Effect	<i>Compressive Strength</i>	24 3x6 cylinders	1.0	1
L12	Fiber Effect on Compression	<i>Compressive Strength</i>	3 3x6 cylinders	0.15	1
L21	Long-Term Delayed Steam	<i>Compressive Strength</i>	36 3x6 cylinders	1.0	1,2
L22	Long-Term Delayed Steam	<i>Compressive Strength</i>	36 3x6 cylinders	1.0	1,2
L23	Demolding Time Effect	<i>Compressive Strength</i>	36 3x6 cylinders	1.05	1,2
N06	Early Age Shrinkage	<i>Shrinkage</i>	2 3x3x11 prisms	0.17	1,2
		<i>Compressive Strength</i>	2 3x6 cylinders		

[†] Cylinders listed as *diameter x height*. Prisms listed as *depth x width x length*.

[‡] 1 = Steam, 2 = Air

3.2 Batching, Casting, and Curing of UHPC

The first phase of the material characterization study described in this chapter is to determine the properties of fresh UHPC. To achieve consistent results throughout the entire study, a series of specific, standardized procedures were implemented for the creation of the specimens described in the previous section. The casting of these specimens allowed for the mixing, associated testing, and observation of over 50 batches of UHPC.

The UHPC used in this study can be divided into three parts—premix, fibers, and liquids. The premix consists of all of the cementitious, aggregate, and filler materials (described in Chapter 2). The premix was batched and blended by the manufacturer and delivered in bulk to the researchers. All of the UHPC testing described in this chapter consists of specimens created from one of the three premix deliveries made to the researchers over the course of 18 months. As described in the previous section, these deliveries were designated as the ‘L,’ ‘M,’ and ‘N’ premixes. For the purpose of this study, all of the premixes are assumed to be identical; however, it is realized that manufacturing processes can vary with time and the final premix product could show slight variations.

The liquids that were mixed with the UHPC included water, accelerator, and a high-range water-reducing admixture (HRWA). The accelerator used in this study was Rheocrete CNI. The HRWA was Glenium 3000NS.

The fibers included in the UHPC were always undeformed cylindrical steel fibers that were 0.5 in. long and had a 0.008-in. diameter. These fibers were included in the mix at a concentration of 2% by volume.

The mix proportions used throughout this study included the following:

- Premix 137.0 lb/ft³ of concrete
- Water 6.81 lb/ft³ of concrete
- HRWA 1.92 lb/ft³ of concrete
- Accelerator 1.87 lb/ft³ of concrete
- Steel Fibers 9.74 lb/ft³ of concrete

These mix proportions were followed for all except three batches. Those three batches followed a slightly different mix design as required by the material property being investigated. In two batches, namely M1K and M1N, the accelerator was replaced by an additional 1.80 lb/ft³ of water. In the remaining batch, L12, the fibers were not included in the mix so that compression test behavior in unreinforced UHPC could be studied.

A 2.0 ft³ capacity pan mixer was used for nearly all of the UHPC mixing. This 1934 vintage mixer was somewhat underpowered for this application, resulting in extended mix times as compared to mixing UHPC in modern mixers. Regardless, this mixer was able to impart enough energy into the mix to obtain sufficient rheology for the casting of laboratory specimens. A 0.3 ft³ mixer was used for the two batches that only required a small volume of material.

Key points in the mixing procedure are graphically shown in Figure 3.2-A. The mixing procedure for UHPC included the following steps:

- Weigh all constituent materials. Add $\frac{1}{2}$ of HRWA to water.
- Place premix in mixer pan, and mix for 2 minutes.
- Add water (with $\frac{1}{2}$ of HRWA) to premix slowly over the course of 2 minutes.
- Wait 1 minute then add remaining HRWA to premix over the course of 30 seconds.
- Wait 1 minute then add accelerator over the span of 1 minute.
- Continue mixing as the UHPC changes from a dry powder to a thick paste.

The time for this process will vary.

- Add fibers to the mix slowly over the course of 2 minutes.
- After the fibers have been added, continue running mixer for 1 minute to ensure that the fibers are well dispersed.



Figure 3.2-A: Mixing of UHPC including (clockwise from left) water addition, HRWA addition, pre-paste consistency, fiber addition, and finished mix

As soon as mixing was completed, the casting of specimens and the measurement of the rheological properties of the UHPC commenced. The rheology of the UHPC was measured via a flow table test similar to that described in ASTM C1437. In the test that was implemented in this study, the mini slump cone is filled then removed to allow the concrete to flow outward. Once the concrete reaches a steady state, the average diameter is determined by measuring the concrete at three locations. Next, the flow table is dropped 20 times in approximately 20 seconds. Again, the concrete is allowed to settle then its average diameter is recorded.

The casting of all UHPC specimens used in this material characterization study was completed within 20 minutes after the completion of mixing. All specimens were cast on a vibrating table and were allowed to remain on the table for approximately 30 seconds after filling. The filling of molds was completed via scoops used to move the UHPC from the mixing pan into the mold. In prisms specimens for flexure tests, the UHPC was always placed in one end of the mold and allowed to flow to the other end in order to complete the filling. As was discussed in Section 2.4.1, the tensile properties of UHPC are dependent on fiber reinforcement orientation, which is a direct result of casting procedure.

After filling, specimens were removed from the vibrating table and were screeded. Although screeding is not normally recommended for UHPC and is very difficult to complete on a large-scale cast, it was implemented here to make the later preparation of cured specimens easier. After screeding, each specimen had its exposed surface covered

in plastic to prevent moisture loss. The specimens then sat undisturbed until final set had occurred.

The demolding of the specimens occurred approximately 24 hours after casting. As will be discussed later in this chapter, this timetable sometimes resulted in the demolding of specimens that were marginally ready and had only very recently achieved set.

Demolding of larger specimens that would have needed sufficient strength to support their greater self-weight would not have been possible in all cases on this timetable.

As previously mentioned, four curing regimes were implemented in order to study UHPC characteristics under different curing conditions. The standard, manufacturer recommended curing treatment included steaming the UHPC at 90°C and 95% relative humidity (RH) for 48 hours. In practice, this procedure included 2 hours of increasing steam and 2 hours of decreasing steam, leaving 44 total hours of constant steaming at 90°C and 95% RH. This treatment was initiated within 4 hours after demolding. This curing condition will henceforth be referred to as Steam treatment.

The remaining three regimes include Air treatment, Tempered Steam treatment, and Delayed Steam treatment. The Air treatment allowed the specimens to remain in a standard laboratory environment from demolding until testing. The Tempered Steam treatment is very similar to the Steam treatment, except that the temperature inside the steam chamber was limited to 60°C. Finally, the Delayed Steam treatment is a curing regime wherein the Steam treatment described above is followed, but it is not initiated

until the 15th day after casting. Until the 15th day, Delayed Steam specimens are equivalent to Air treated specimens.

Tables 3.2-A and 3.2-B provide information relating to the casting and curing of each of the batches included in this material characterization study. Table 3.2-A focuses on the primary sets of specimens that were implemented across most curing regimes. These batches were all cast with premix from the ‘M’ or ‘N’ deliveries. Table 3.2-B provides the results from other batches cast and primarily focuses on material cast from the ‘L’ premix delivery.

The tables include a listing of the age of the UHPC premix at the time of casting along with the total mixing time for each batch. Observation of the mixing and casting procedure throughout all the mixes completed in this study indicated that the behavior of the mix changed as the premix aged. This qualitative observation is confirmed by the results as shown in Figure 3.2-B. The total mixing time for each mix in the ‘M’ and ‘N’ premixes is plotted against the premix age at casting. This figure shows a clear trend in which younger premixes could mix within 15 minutes while older mixes could take twice as long. Although not verified, it is likely that these increased times result from the agglomeration of fine particles within the premix as it ages. It must be noted that these mix times are relative and are only specifically applicable to the pan mixer used in this study.

The rheology measures are also listed in Tables 3.2-A and 3.2-B. The final values ranged from 6.5 to 8.25 in. This wide range is indicative of large differences in rheology. The UHPC exhibiting the stiffer results was much more difficult to cast and would definitely have been problematic outside of a laboratory setting. Alternatively, a flow measure that was near or above 8 in. was consistent with UHPC that was easy to place.

Figure 3.2-C shows the final rheology values for the ‘M’ and ‘N’ premixes. The first castings of the ‘M’ premix were completed during a time period when the laboratory conditions included very low humidity. For this reason, the results are shown in two series that indicate whether the humidity was low or normal during casting. Very stiff rheology results were obtained for a few mixes just before the rectification of the humidity situation. It is expected that the large diameter of the pan in the pan mixer combined with the low air moisture content worked to sap a small amount of moisture from the UHPC. This moisture loss was sufficient to adversely affect the rheological properties.

Table 3.2-A: Batching and casting properties of Steam and Air treated UHPC

Batch	Batch Description	Age at Casting	Batch Size (ft ³)	Mixing Time (min)	Flow (in.)		Demolded (hours)	Curing Regime
					Initial	Final		
N1A	Compressive Strength	4 months	1.15	24	6.75	7.75	22.5	Steam
N1A _{xx} A	Compressive Strength	5 months	0.95	28	6.75	7.5	28	Steam
M1B	Cubes/Cylinders Compression	6 weeks	0.9	20	6	6.75	26	Steam
N1C	Split Tensile	2 weeks	0.95	20	6.5	7.5	22	Steam
M1D	Direct Tension	9 weeks	1	22	6.5	7.5	28	Steam
N1E	Prism Flexure	4 weeks	1.1	21	6.75	7.75	23	Steam
M1F	Durability (CI Pen, FT, etc.)	4 weeks	1	15	6.5	7.5	26	Steam
M1G	Scaling Slabs	4 weeks	0.9	14	7	7.5	26	Steam
N1H	Creep and Shrinkage	15 weeks	1.05	23	6.75	7.75	22.5	Steam
M1J	Air Content, Fiber Dispersion	6 weeks	0.7	21.5	5.5	6.5	26	Steam
M1J _{xx} A	Air Content, Fiber Dispersion	8 weeks	0.7	23	6.25	7.5	26	Steam
M1K [†]	Air Content, Fiber Dispersion	7 weeks	0.7	20	6.5	7.5	72	Steam
M1M	Heat of Hydration	6 weeks	0.9	21.5	5.5	6.75	26	Steam
M1M _{xx} A	Heat of Hydration	7 weeks	0.5	23.5	5.75	6.75	26	Steam
M1M _{xx} B	Heat of Hydration	8 weeks	0.9	20	6.25	7.25	26	Steam
M1N [†]	Heat of Hydration	7 weeks	0.9	16.5	7.25	8.25	72	Steam
M1P	Fracture/Fatigue of Prisms	7 weeks	1.05	20	6.25	7.5	26	Steam
M1Q	Freeze-Thaw Supplemental	12 weeks	1.1	20	6	7	29	Steam
N2A	Compressive Strength	8 weeks	1.15	22	6.75	8	20	Air
N2C	Split Tensile	3 weeks	0.95	21	7	8.25	24	Air
M2D	Direct Tension	9 weeks	1	21	6	7	26	Air
N2E	Prism Flexure	3 weeks	1.1	20	6.75	7.75	24	Air
M2F	Durability (CI Pen, FT, etc.)	5 weeks	1.05	17.5	6	7	26	Air
M2G	Scaling Slabs	5 weeks	0.9	17	6.25	7.25	26	Air
N2H	Creep and Shrinkage	8 weeks	1.05	21.5	6.5	7.5	22	Air
M2P	Fracture/Fatigue of Prisms	12 weeks	1.05	20	6	7.25	29	Air
M2Q	Freeze-Thaw Supplemental	12 weeks	1.1	19.5	6.25	7.5	29	Air

[†] Batch mix design did not contain any accelerator.

Table 3.2-A (continued): Batching and casting properties of Tempered Steam and Delayed Steam treated UHPC

Batch	Batch Description	Age at Casting	Batch Size (ft ³)	Mixing Time (min)	Flow (in.)		Demolded (hours)	Curing Regime
					Initial	Final		
N3A	Compressive Strength	8 weeks	1.15	20	6.5	7.5	21	T. Steam
N3C	Split Tensile	3 weeks	0.95	21	7	8	23	T. Steam
M3D	Direct Tension	8 weeks	1	20	6.5	7.5	26	T. Steam
N3E	Prism Flexure	5 weeks	1.1	21	6.75	7.75	25	T. Steam
M3F	Durability (CI Pen, FT, etc.)	5 weeks	1.05	15	6.25	7.25	26	T. Steam
M3G	Scaling Slabs	5 weeks	0.9	14	6.5	7.25	26	T. Steam
N3H	Creep and Shrinkage	7 weeks	1.05	20	6.5	7.75	22	T. Steam
M3Q	Freeze-Thaw Supplemental	12 weeks	1.1	19.5	6.25	7.5	29	T. Steam
N4A	Compressive Strength	2 weeks	1.15	16	6.5	7.75	24	D. Steam
N4C	Split Tensile	2 weeks	0.95	20	6.75	8	23	D. Steam
M4D	Direct Tension	7 weeks	1	20	6.25	7.5	26	D. Steam
N4E	Prism Flexure	2 weeks	1.1	20	6.75	8	22	D. Steam
M4F	Durability (CI Pen, FT, etc.)	4 weeks	1	16	6.75	7.75	26	D. Steam
M4G	Scaling Slabs	4 weeks	0.9	15	6.5	7.25	26	D. Steam
N4H	Creep and Shrinkage	7 weeks	1.05	21	7.25	8.25	23	D. Steam
M4Q	Freeze-Thaw Supplemental	12 weeks	1.1	20	6	7	29	D. Steam

Table 3.2-B: Batching and casting properties of batches cast to complete the study by addressing special issues

Batch	Batch Description	Age at Casting	Batch Size (ft ³)	Mixing Time (min)	Flow (in.)		Demolded (hours)	Curing Regime
					Initial	Final		
L1B	Cubes/Cylinders Compression	16 months	0.9	26	6	7	48	Steam
L1F	Durability (CI Pen, FT, etc.)	11 months	0.9	20	6.25	7	41	Steam
L1G	Scaling Slabs	11 months	1.0	23	6.25	7.25	44	Steam
L1R	Split Tensile Cracked Corrosion	16 months	1.1	22	6.5	7.5	48	Steam
L2B	Cubes/Cylinders Compression	8 months	0.9	34	6	7	114	Air
L2F	Durability (CI Pen, FT, etc.)	11 months	1.0	17	5.75	6.75	50	Air
L2G	Scaling Slabs	11 months	0.9	20	5.75	6.75	43	Air
L2R	Split Tensile Cracked Corrosion	16 months	1.1	24	6.75	7.75	47	Air
L2S	Early-Age Sustained Compressive Stress	26 months	1.0	23	6.75	7.75	–	Steam & Air
L03 †	Fiber Dispersion	8 months	1.0	19	8.25	9.25	139	Air
L10	Load Rate Effect	10 months	1.0	27	6.5	7.25	47	Steam
L12	Fiber Effect on Compression	11 months	0.15	18	7.25	8.0	42	Steam
L21	Long-Term Delayed Steam	25 months	1.0	22	7.25	8.25	44	Steam & Air
L22	Long-Term Delayed Steam	25 months	1.0	22	7.25	8	43	Steam & Air
L23	Demolding Time Effect	25 months	1.0	22	6.5	7.5	various	Steam & Air
N06	Early Age Shrinkage	5 months	0.17	23	N/A	N/A	–	Steam & Air

† Batch mix design did not contain any accelerator.

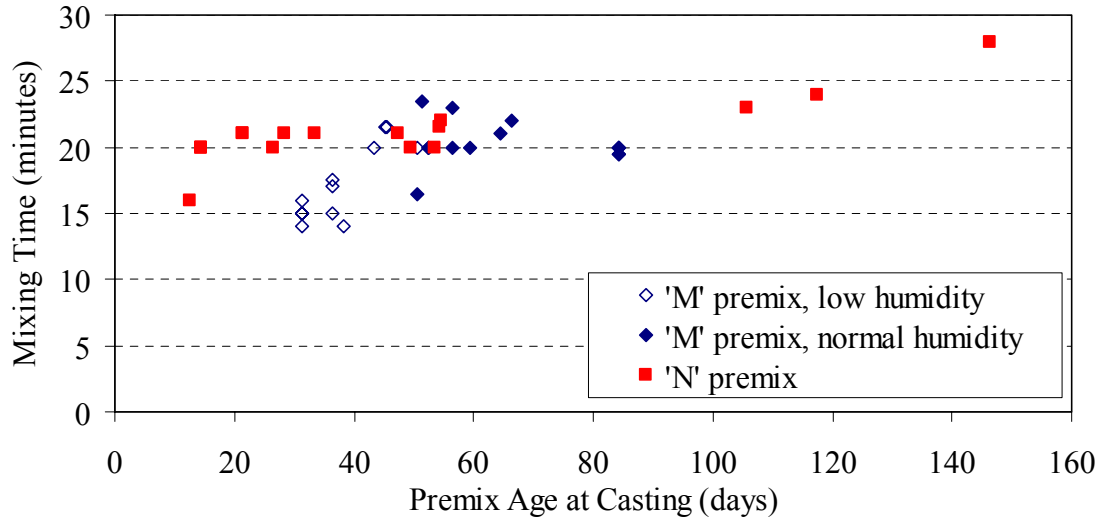


Figure 3.2-B: Mix time as affected by premix age

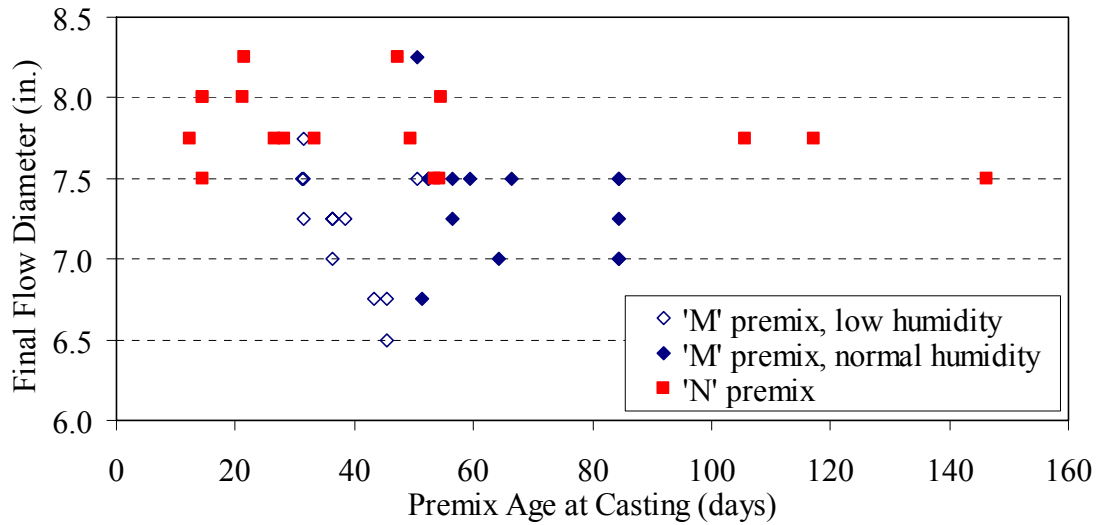


Figure 3.2-C: Final flow diameter as affected by premix age

3.3 Compression Testing

A significant portion of this study focused on the behaviors of molded UHPC cylinders under compressive loading. The compressive tests discussed in this section were all completed nominally according to the ASTM C39 standard test method for cylinders and the ASTM C109 standard test method for cubes. Throughout the entire material characterization study, nearly 1000 compression specimens were tested. Although the load configuration and basic test setup remained constant, various properties were investigated through the use of different data collection techniques and different specimen geometries.

The basic compression test on UHPC was the ASTM C39 test on a 3-in. diameter cylinder. This test was used as a control test throughout the material characterization study to ensure that consistent batching, mixing, and curing of the UHPC had occurred. The 3 in. cylinders were cast on a vibrating table in 6 in. tall plastic molds. The concrete was scooped into the molds and was not rodded due to the presence of the fibers. Once full, the molds were held on the vibrating table for a few extra seconds before being removed and having their top surfaces screeded. After the molds were set, curing treatments were applied according to each of the four curing regimes.

The preparation of the cylinders for testing was somewhat more involved than that normally used for cylinder testing. The largest difference is that the end planeness of the cylinders was ensured through the use of an end grinder. Figure 3.3-A shows a picture of the end grinding procedure. All cylinders that were projected to have strengths above 12

ksi were subjected to grinding. UHPC cylinders with strengths under this level were sulfur capped as grinding tends to pull out the fibers and create a non-uniform end surface at these lower strengths.

After grinding, the cylinders were measured to verify end planeness and to determine length, diameter, and density. The end planeness was verified through the use of a flat steel plate and a dial gage as shown in Figure 3.3-A. Sliding the cylinder under the dial gage allowed for determination of the longest and shortest lengths of the cylinder to an accuracy of 0.001 in. The out-of-planeness of the cylinder ends could be determined from this information. Each cylinder had to exhibit under 1 degree of out-of-planeness or the ends were reground. Next, the length was measured at four points around the circumference of the cylinder, and the average was calculated. The diameter was then measured at six locations—at the top, middle, and bottom of the cylinder on two perpendicular diameters. The average value was then used to calculate the area of the cylinder. Finally, the mass of the cylinder was determined, and the density was calculated. The entire grinding and measuring procedure was completed after any steam-based treatment was applied to the cylinder or at least 2 weeks after casting for the Air treated specimens, unless the testing timetable required otherwise. In this case, a cylinder was prepared for testing within 1 day of performing the test.

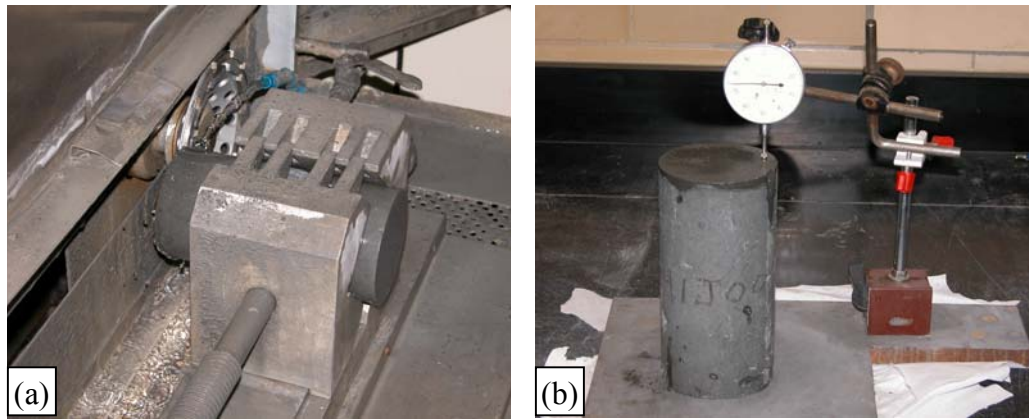


Figure 3.3-A: (a) Grinding and (b) measuring of 3-in. diameter cylinders

The testing of all cylinders was completed in a Forney 1000 kip capacity compression testing machine. The operator of this hydraulically operated machine uses a needle valve to set and control the loading rate. Aside from some preliminary testing that will be discussed later, the load rate for all cylinder and cube compression tests was set at 150 psi/sec. This load rate is higher than the load rates recommended in ASTM C39 and C109. The increased load rate was necessary, as the high strengths of UHPC would mean that a UHPC cylinder tested at the ASTM C39 load rate might take 15 to 20 minutes to reach failure. A small study, completed to determine if the higher load rate would have any adverse effect on results, indicated that the higher load rate was acceptable. A further discussion of this set of tests is presented subsequently in this chapter.

A 6.5-in. diameter spherical bearing was used as the upper loading platen for all cylinder and cube tests. Although this bearing would normally only be used for 4-in. diameter cylinders, it was used for all of the tests because of the high stress levels placed on the

bearing by this high strength concrete. The lower test platen was always either the machine's lower platen or a machined steel plate resting on the machine's platen.

Figure 3.3-B shows a cylinder that is prepared for testing. All specimens were loaded via the hydraulically controlled constant load rate from approximately 5 kips through failure. The cylinders and cubes exhibited very little decrease in stiffness throughout testing, thus the load rate remained relatively constant. Figure 3.3-B also shows a picture of a cylinder after testing. Notice that the cylinder remains intact. This is due to the presence of the fibers as will be discussed more fully later in this chapter.

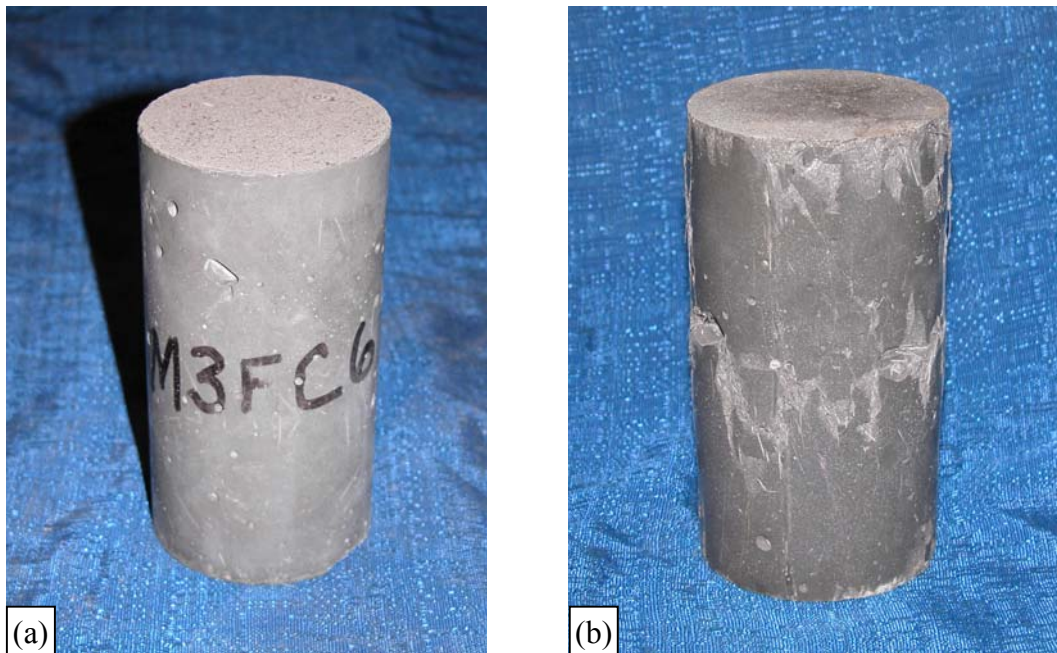


Figure 3.3-B: 3-in. diameter cylinders (a) before and (b) after compression testing

3.3.1 Strength

The compressive strength results from 44 batches of UHPC are presented in Table 3.3.1-A. These results are from the control cylinders cast with each batch from the ‘M’ and ‘N’ deliveries of UHPC premix. Control cylinder results from the ‘L’ delivery are shown in Figure 3.3.1-B. All tests were performed on the corresponding day that is listed in the table. In general, six cylinders were tested for each batch, and the results were averaged to obtain the result shown in the table.

Based on these tests, the average 28-day compressive strength of UHPC has been determined. Steam treated UHPC was found to have a compressive strength of 28.0 ksi with a 95% confidence interval of 27.7 to 28.3 ksi. Air treated UHPC has a compressive strength of 18.3 ksi with a 95% confidence interval of 17.9 to 18.7 ksi. Tempered Steam treated UHPC has a compressive strength of 24.8 ksi with a 95% confidence interval of 24.3 to 25.3 ksi. Finally, Delayed Steam treated UHPC has a compressive strength of 24.8 ksi with a 95% confidence interval of 24.3 to 25.3 ksi.

Table 3.3.1-A: Control cylinder compressive strength results

Batch	Curing	Batch Description	Compressive Strength (ksi)			
			Day	No.	Average	St. Dev.
N1A	Steam	Compressive Strength	28	6	26.2	1.02
N1A _{xx} A	Steam	Compressive Strength	30	6	28.4	2.08
M1B	Steam	Cubes/Cylinders Compression	29	6	29.4	0.61
N1C	Steam	Split Tensile	28	6	26.3	1.76
M1D	Steam	Direct Tension	28	6	24.3	0.95
N1E	Steam	Prism Flexure	28	6	27.4	1.25
M1F	Steam	Durability (CI Pen, FT, etc.)	28	6	29.3	1.59
M1G	Steam	Scaling Slabs	28	6	29.2	1.53
N1H	Steam	Creep and Shrinkage	28	6	27.3	1.33
M1J	Steam	Air Content, Fiber Dispersion	28	6	27.7	1.24
M1J _{xx} A	Steam	Air Content, Fiber Dispersion	28	6	25.6	1.07
M1K	Steam	Air Content, Fiber Dispersion	28	6	27.3	1.34
M1M	Steam	Heat of Hydration	28	6	28.2	1.00
M1M _{xx} A	Steam	Heat of Hydration	28	6	27.7	2.18
M1M _{xx} B	Steam	Heat of Hydration	28	6	28.5	1.09
M1N	Steam	Heat of Hydration	28	6	28.3	1.37
M1P	Steam	Fracture/Fatigue of Prisms	28	6	25.7	2.53
M1Q	Steam	Freeze-Thaw Supplemental	28	4	20.8	0.72
N2A	Air	Compressive Strength	28	6	16.2	0.72
N2C	Air	Split Tensile	28	6	17.5	0.65
M2D	Air	Direct Tension	28	6	15.4	0.50
N2E	Air	Prism Flexure	28	6	17.6	0.69
M2F	Air	Durability (CI Pen, FT, etc.)	28	6	19.0	0.76
M2G	Air	Scaling Slabs	28	6	16.9	0.48
N2H	Air	Creep and Shrinkage	28	6	16.5	0.50
M2P	Air	Fracture/Fatigue of Prisms	28	6	15.5	0.62
M2Q	Air	Freeze-Thaw Supplemental	28	4	15.3	0.20
N3A	T.Steam	Compressive Strength	28	6	22.3	0.91
N3C	T.Steam	Split Tensile	28	6	24.4	0.66
M3D	T.Steam	Direct Tension	28	6	25.2	0.72
N3E	T.Steam	Prism Flexure	28	6	25.1	0.61
M3F	T.Steam	Durability (CI Pen, FT, etc.)	28	6	26.5	1.21
M3G	T.Steam	Scaling Slabs	28	6	24.6	1.37
N3H	T.Steam	Creep and Shrinkage	28	5	25.7	0.31
M3Q	T.Steam	Freeze-Thaw Supplemental	28	5	21.6	0.73
N4A	D.Steam	Compressive Strength	30	6	25.1	1.05
N4C	D.Steam	Split Tensile	28	6	24.6	0.89
M4D	D.Steam	Direct Tension	28	6	22.9	1.72
N4E	D.Steam	Prism Flexure	28	5	25.0	0.62
M4F	D.Steam	Durability (CI Pen, FT, etc.)	28	6	25.9	1.08
M4G	D.Steam	Scaling Slabs	28	6	25.9	1.04
N4H	D.Steam	Creep and Shrinkage	28	5	24.4	1.20
M4Q	D.Steam	Freeze-Thaw Supplemental	28	5	17.8	0.93

Table 3.3.1-B: More control cylinder compressive strength results

Batch	Curing	Batch Description	Compressive Strength (ksi)			
			Day	No.	Average	St. Dev.
L1B	Steam	Cubes/Cylinders Compression	28	6	30.5	1.02
L2B	Air	Cubes/Cylinders Compression	28	8	21.6	0.55
L1R	Steam	Split Tensile Ponding	28	6	29.9	0.75
L2R	Air	Split Tensile Ponding	28	6	20.6	0.59

These results, although quite high for concrete, are likely lower than would normally be observed with this UHPC. Two factors that have been found to clearly influence the compressive strength are the environment that UHPC is kept in prior to any steam-based treatment and the steaming environmental conditions. In this study, the UHPC was demolded as soon as it had sufficient strength to maintain its geometric integrity. At this age, the UHPC is still rather permeable and is susceptible to moisture loss and resulting lower strength values. This factor will be discussed in more depth later in this chapter. Second, the UHPC manufacturer recommends 48 hours of steam treatment, whereas in this study the UHPC only actually received 44 hours at the steam treatment level with 2 hours of ramping up and down from room temperature.

The results from the individual compression tests listed in Table 3.3.1-A are shown in Figures 3.3.1-A and 3.3.1-B relative to density and cylinder end planeness, respectively. The density results show that this concrete ranges from around 150 to 156 lb/ft³. An estimate of 155 lb/ft³ is reasonable regardless of the type of curing treatment applied. Also, within each curing regime there seems to be a slight increase in compressive strength as the density increases. The cylinder end planeness results show that the out-of-planeness of the cylinders had little impact on the compressive strength. The spherical

bearing used in these tests clearly was able to accommodate for these differences in planeness.

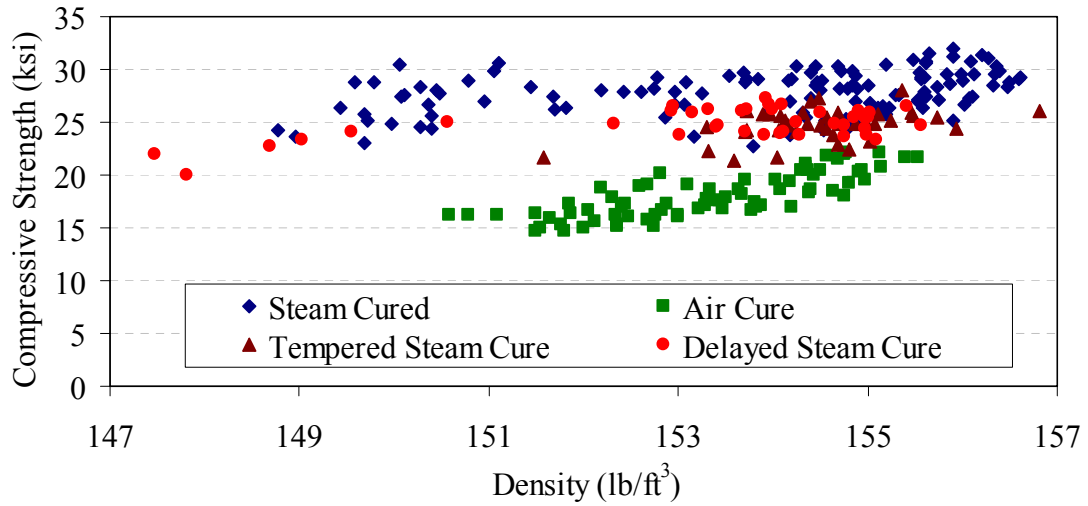


Figure 3.3.1-A: Compressive strength and density of control cylinders

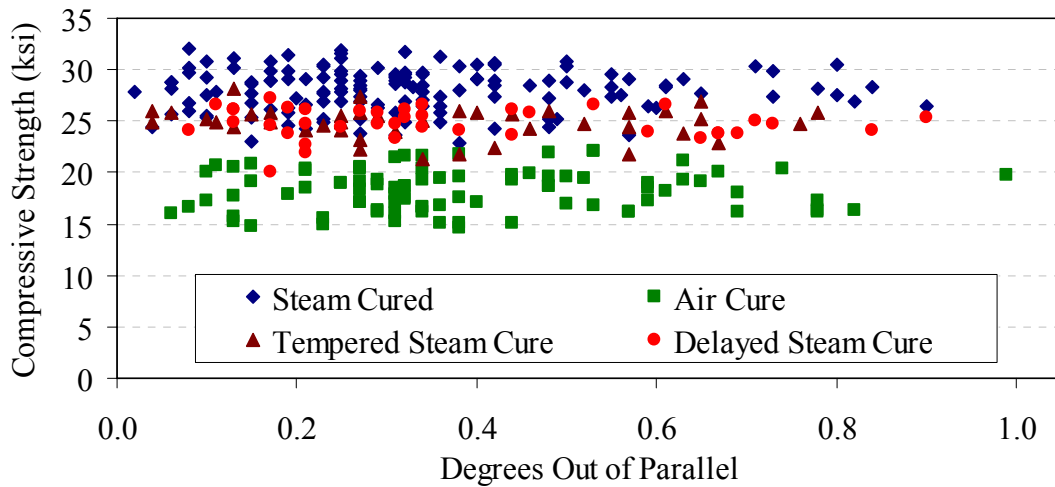


Figure 3.3.1-B: Compressive strength and cylinder end planeness of control cylinders

3.3.2 Strength, Modulus of Elasticity, and Strain Capacity With Time

The age dependent compressive behavior of UHPC was investigated through a series of compression tests completed from 1 day to 8 weeks after casting. This testing provided results related to strength, modulus of elasticity, and compressive strain capacity both before and after the application of any curing treatment.

These tests were also completed in the 1000 kip Forney test machine following the same procedures discussed previously. However, in these tests, a deformation measuring device was attached to each cylinder to capture the axial movement. These tests were completed nominally in accordance with ASTM C469 with one exception: A number of the allowances made by this test method for the collection of data via simplified systems were bypassed in favor of more robust methodologies.

The test setup included the specially designed axial deformation measuring device shown in Figure 3.3.2-A. The two parallel rings are both rigidly attached to the cylinder with a 2 in. gage length between attachment points. The upper ring holds three LVDTs whose ends bear on the lower ring. Thus, the axial deformation of the cylinder can be accurately measured from initiation of loading through failure. The load and the output from the three LVDTs were digitally recorded at approximately 4 Hz throughout the test.

The testing of each cylinder was completed in a single constant load application from start to failure. This procedure runs counter to the standard procedure presented in ASTM C469 but is consistent with both ASTM C39 and the alternate loading procedure

presented in ASTM C469. It is expected that the normal ASTM C469 procedure was designed to allow for assurance of seating by repeatedly loading and unloading the cylinder and to allow for removal of the deformation measuring apparatus by stopping the test well before reaching failure. In this test program, proper seating of the cylinder could be assured by monitoring the load-deformation response during the test. Removal of the deformation measuring device was not necessary as a loose-fitting plastic sleeve was sufficient to stop any UHPC chips from damaging the LVDTs during cylinder failure.

As previously mentioned, the preparation of specimens for tests at early ages was completed within 1 day prior to the test. Also, cylinders with projected strengths below 12 ksi were sulfur capped instead of ground.

Selected results from these tests are compiled in Figures 3.3.2-B through 3.3.2-F. These figures show one stress-strain curve for each of the ages at which compression responses were collected. Note that a replicate (N1AxxA) was completed for the Steam treated portion of the testing as the compressive strength results from the initial set (N1A) were somewhat below the anticipated value. Unfortunately, the replicate compressive strength results were also somewhat lower than anticipated.

The stress-strain responses obtained from these tests will be the focus of the remainder of this section as well as the next section. In a qualitative sense, note the change in the overall shape of the curves in Figures 3.3.2-B through 3.3.2-F. At 1, 2, or even 3 days

after casting if no steam-based curing is applied, the UHPC exhibits a ductile stress-strain response. The rounded curve and the steady decrease after peak stress illustrate that the UHPC can sustain some load-carrying capacity through large deformations without brittle failure. The overall behavior changed dramatically after the steam-based treatment or after 2 weeks of Air treatment. In this case, the UHPC exhibits more of a brittle response wherein the attainment of the peak compressive load results in a rapid, uncontrolled decrease in load-carrying capacity. As time progresses or as the steam-based treatment becomes more acute, the brittle nature of the compressive failure response also becomes more acute.

Figure 3.3.2-G shows the strength results for five sets of specimens. The results presented in the figure are also shown in Table 3.3.2-B along with standard deviation values and the numbers of cylinders tested. In a similar fashion, Figure 3.3.2-H shows the modulus of elasticity results for the five sets of specimens. The modulus of elasticity was calculated based on the average LVDT-based deformation measurements and the load reading. A best-fit linear approximation of the stress-strain results from 10% to 30% of the compressive strength of each individual cylinder was used. Again, Table 3.3.2-B presents further information relating to these results.

Additional modulus of elasticity tests were also completed on spare cylinders from various batches of UHPC cast for this research program. These tests were completed following the same procedures discussed above and were all completed at 1 month of age. In general, between 20 and 30 cylinders were tested at this age for each curing

regime. The overall modulus of elasticity results include a stiffness of 7650 ksi for Steam treated, 6200 ksi for Air treated, 7400 ksi for Tempered Steam treated, and 7300 for Delayed Steam treated UHPC.

Finally, the axial strain carried by each cylinder at peak compressive loading was also determined based on the load-deformation results from each cylinder. This strain value was calculated as the average deformation exhibited by the cylinder over the 2 in. gage length of the deformation measuring system. These results are presented in Figure 3.3.2-I and Table 3.3.2-B. The additional modulus of elasticity tests discussed above also provided extra information related to strain at peak stress. The overall strain at peak stress results include 0.0041 for Steam, 0.0035 for Air, 0.0035 for Tempered Steam, and 0.0039 for Delayed Steam treated UHPC.

The results presented thus far in this section illustrate three primary findings. First, after Steam or Delayed Steam treatment, the UHPC is stabilized. In terms of strength, stiffness, and strain at peak load, the UHPC shows very little change after a steam-based treatment has been applied. Second, Air treated UHPC continues to gain strength for at least 8 weeks after casting, but its increase in stiffness and decrease in strain at peak load seem to be curtailed at 1 month. Finally, UHPC gains strength and stiffness very quickly at early ages, while also becoming much less ductile with a large decrease in strain at peak load. Specifically, the compressive strength and stiffness after 24 hours are around 1.5 and 1500 ksi, respectively. After 3 days, however, these values have increased to over 10 and 5000 ksi, respectively, without any curing treatment.

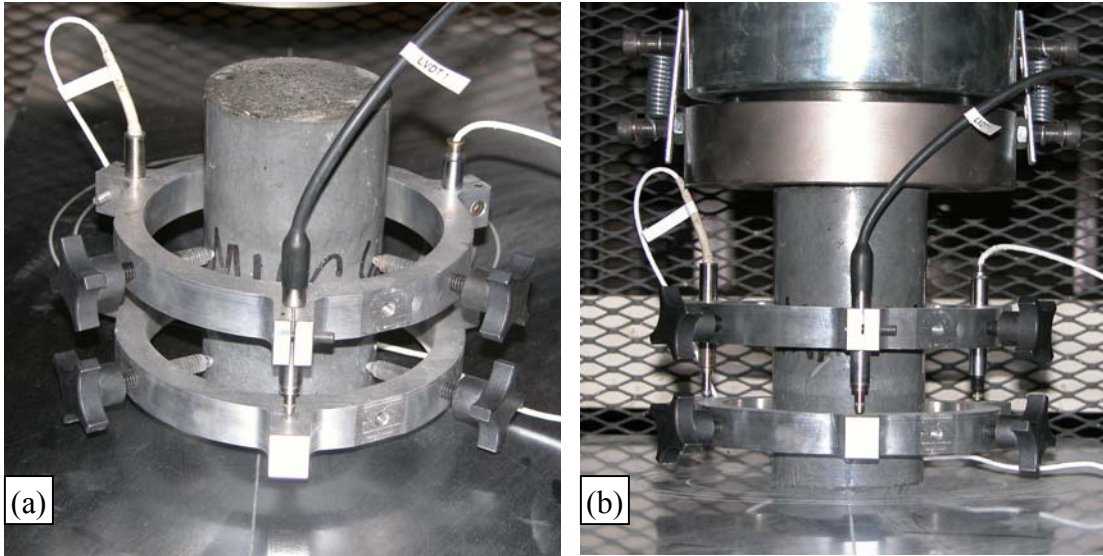


Figure 3.3.2-A: Modulus ring attachment (a) before and (b) during testing

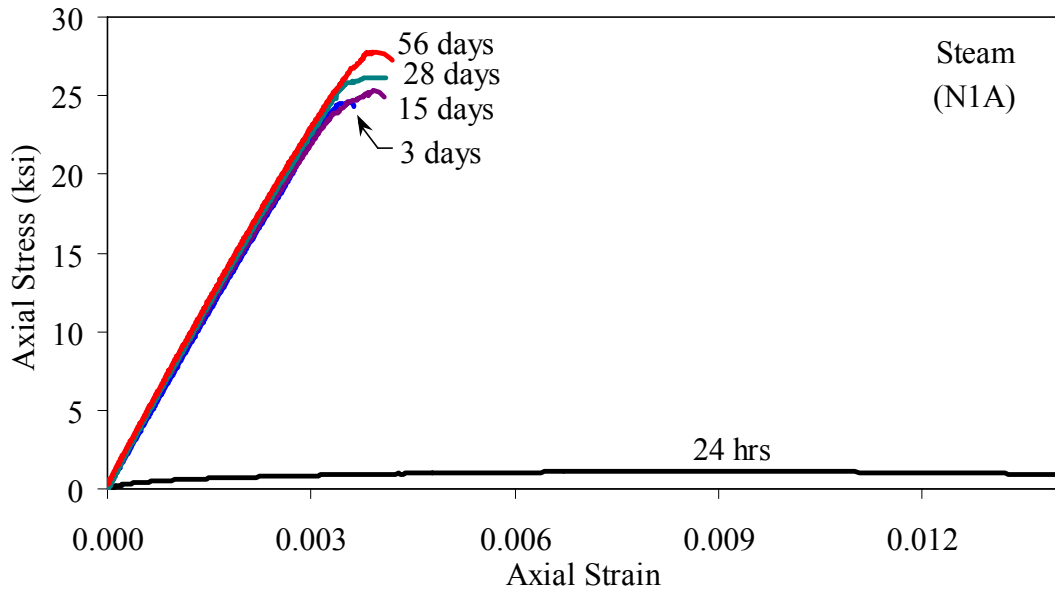


Figure 3.3.2-B: Selected stress-strain responses for Steam treated UHPC (N1A)

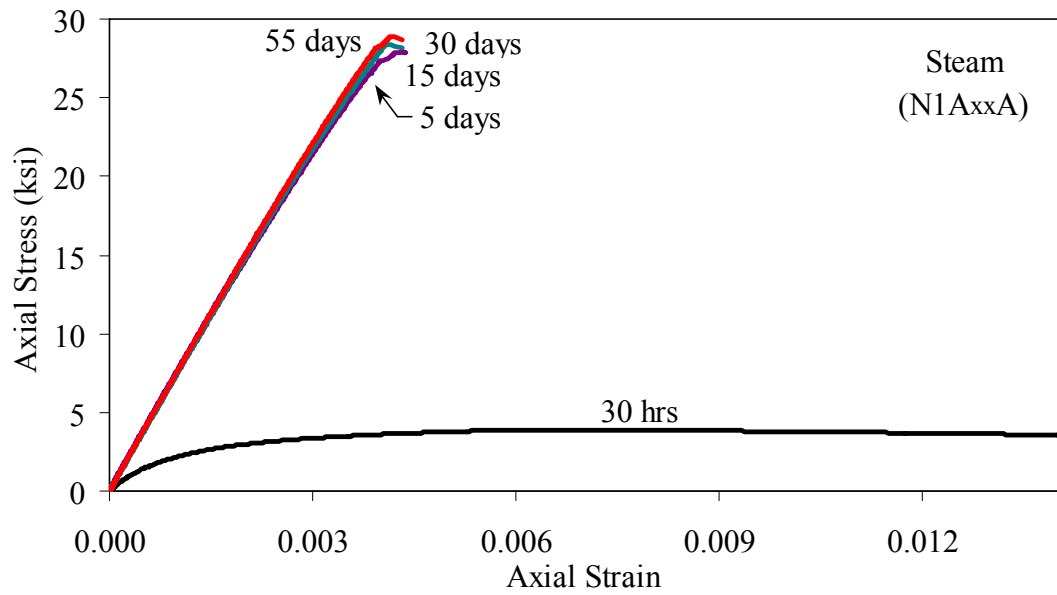


Figure 3.3.2-C: Selected stress-strain responses for Steam treated UHPC (N1AxxA)

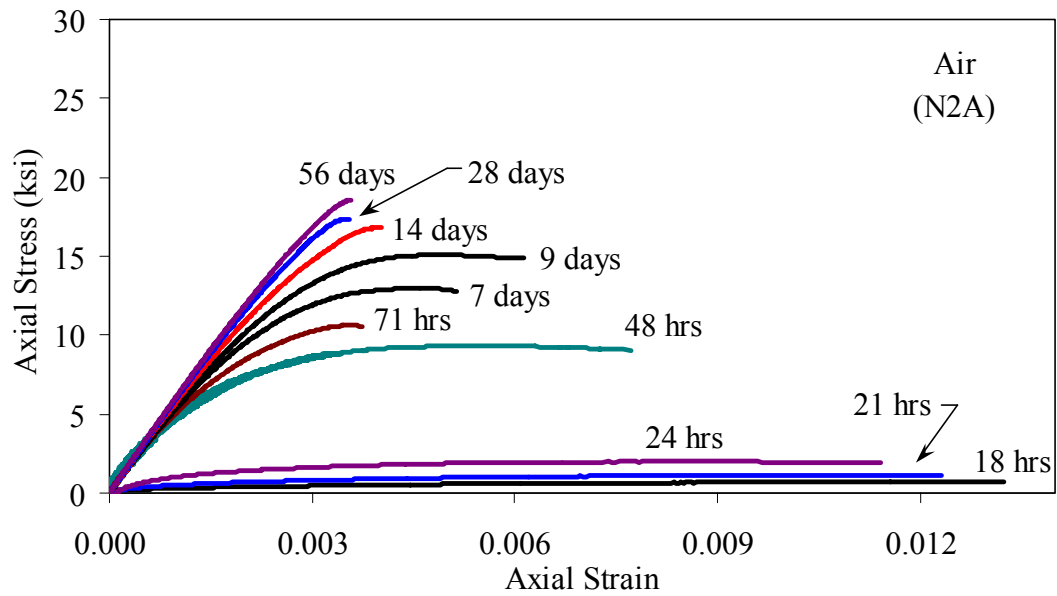


Figure 3.3.2-D: Selected stress-strain responses for Air treated UHPC

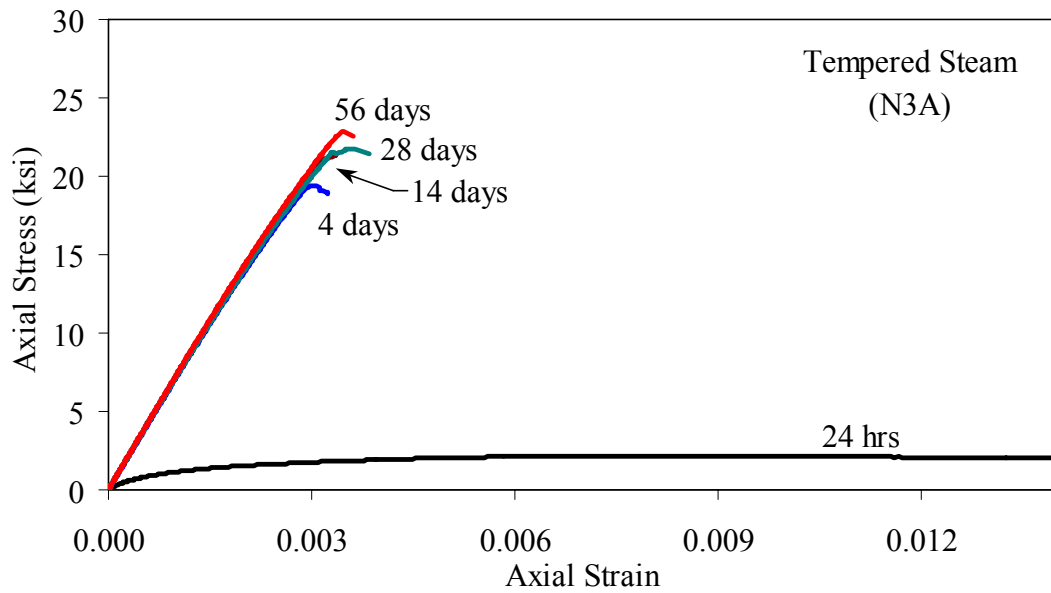


Figure 3.3.2-E: Selected stress-strain responses for Tempered Steam treated UHPC

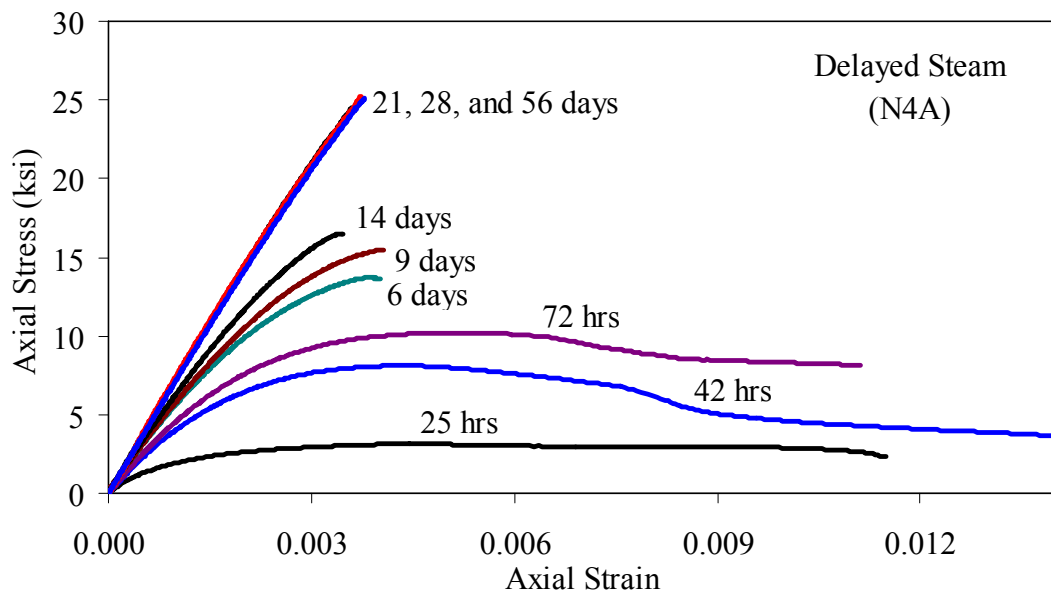


Figure 3.3.2-F: Selected stress-strain responses for Delayed Steam treated UHPC

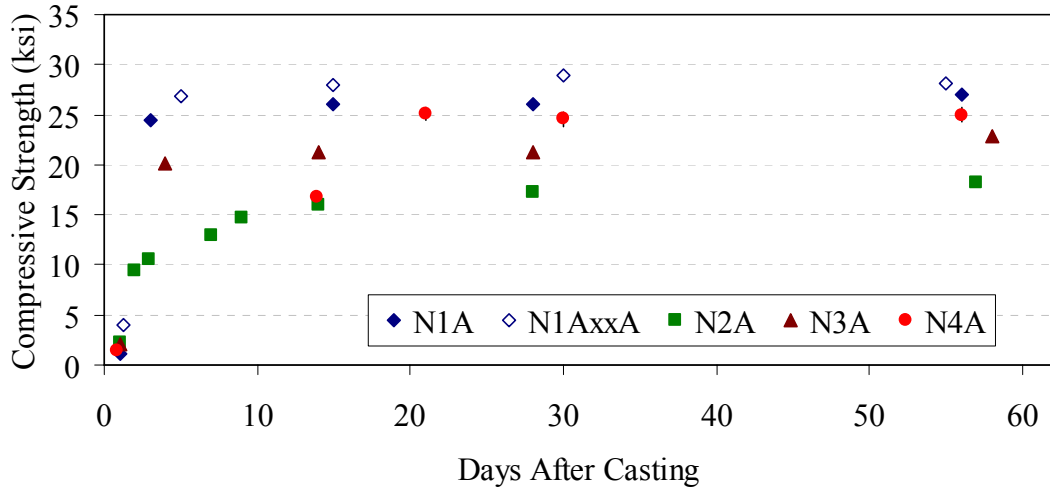


Figure 3.3.2-G: Compressive strength gain from casting up to 8 weeks of age

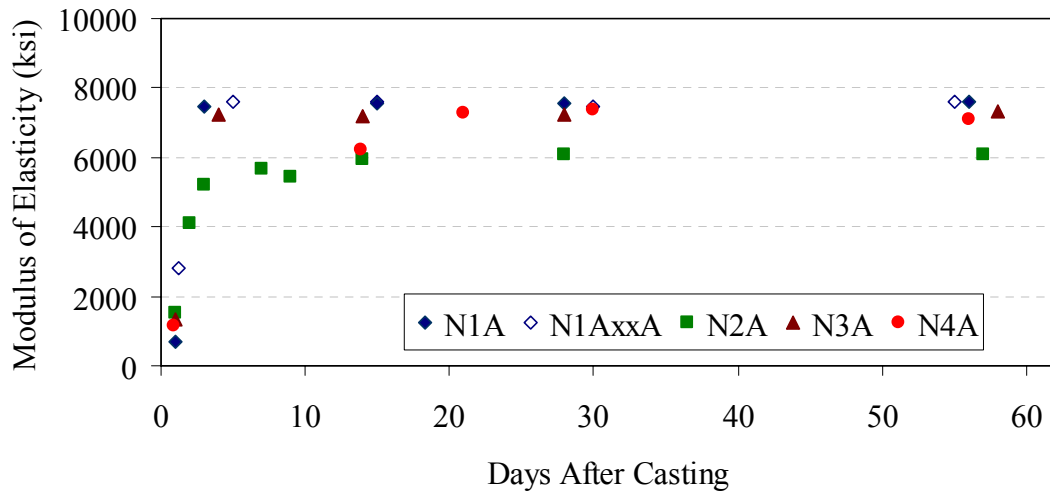


Figure 3.3.2-H: Modulus of elasticity gain from casting up to 8 weeks of age

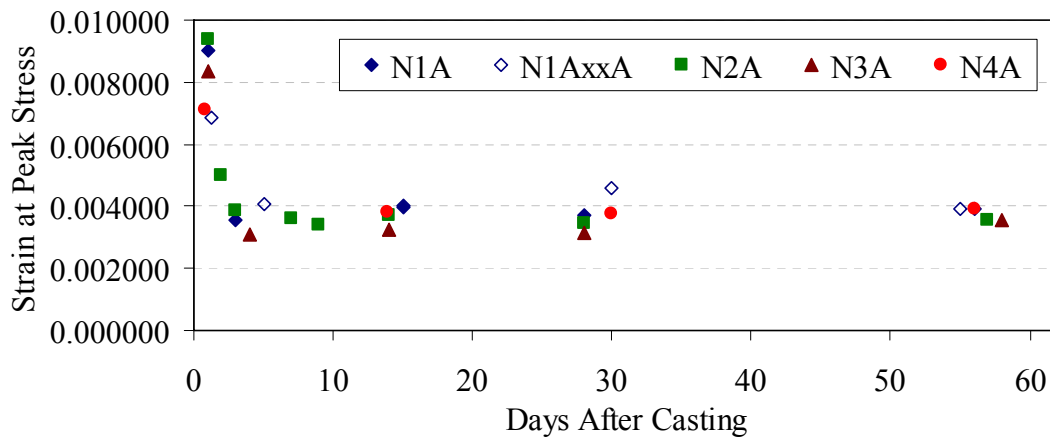


Figure 3.3.2-I: Strain at peak compressive stress from casting up to 8 weeks of age

Table 3.3.2-A: Strength, modulus of elasticity, and strain at peak stress results at various ages after casting (Part I)

Test Age (Days)	<u>Compressive Strength (ksi)</u>			<u>Modulus of Elasticity (ksi)</u>			<u>Strain at Peak Stress</u>		
	No.	Ave.	St. Dev.	No.	Ave.	St. Dev.	No.	Ave.	St. Dev.
Steam (N1A)									
1.0	6	1.1	0.09	6	670	151	6	0.009020	0.001740
3	6	24.5	0.58	6	7470	220	1	0.003580	—
15	6	26.0	0.69	6	7570	196	1	0.003970	—
28	6	26.1	0.50	6	7580	147	2	0.003740	0.000080
56	6	27.0	0.83	5	7620	182	2	0.003900	0.000080
Steam (N1A _{xx} A)									
1.3	5	3.9	0.36	5	2820	278	5	0.006830	0.000840
5	5	26.8	0.92	5	7600	109	4	0.004080	0.000470
15	6	28.0	0.75	6	7620	162	4	0.004020	0.000250
30	6	28.9	0.97	6	7460	167	4	0.004580	0.000300
55	6	28.1	1.20	6	7610	99	4	0.003920	0.000300
Air (N2A)									
1.0	3	2.2	0.20	3	1520	312	3	0.009360	0.001930
2.0	2	9.4	0.10	2	4100	76	3	0.005020	0.000530
3	2	10.6	0.08	2	5220	43	3	0.003850	0.000340
7	3	12.9	0.09	3	5660	111	3	0.003620	0.000800
9	2	14.7	0.59	2	5450	112	3	0.003400	0.001640
14	6	16.0	0.61	6	5970	172	6	0.003710	0.000590
28	6	17.2	0.53	6	6070	164	4	0.003430	0.000130
57	6	18.1	0.69	6	6090	146	3	0.003570	0.000240

Table 3.3.2-A: Strength, modulus of elasticity, and strain at peak stress results at various ages after casting (Part II)

Test Age (Days)	<u>Compressive Strength (ksi)</u>			<u>Modulus of Elasticity (ksi)</u>			<u>Strain at Peak Stress</u>		
	No.	Ave.	St. Dev.	No.	Ave.	St. Dev.	No.	Ave.	St. Dev.
Tempered Steam (N3A)									
1.0	6	2.1	0.17	6	1350	262	6	0.008380	0.001430
4	6	20.2	0.58	4	7240	133	2	0.003100	0.000200
14	6	21.2	0.99	6	7210	107	3	0.003260	0.000080
28	6	21.3	0.78	6	7240	165	1	0.003150	–
58	6	22.8	0.75	6	7310	127	3	0.003550	0.000220
Delayed Steam (N4A)									
0.8	2	1.4	0.06	2	1140	521	3	0.007120	0.003600
14	4	16.7	0.41	4	6220	253	3	0.003810	0.000280
21	6	25.2	0.64	5	7300	146	0	–	–
30	6	24.6	0.70	6	7350	105	1	0.003760	–
56	6	25.0	0.65	6	7120	214	3	0.003890	0.000150

3.3.3 Linearity of UHPC Compressive Response

It is normally assumed that concrete begins to develop internal microcracking and exhibit an associated reduction in stiffness at high stresses. The stress level varies depending on the composition of the concrete. The linearity of the compressive stress-strain response of UHPC was investigated through the elastic modulus testing results that were described in the previous section.

Two methods are used to describe the linearity of the compressive stress-strain response of concrete. The first is the secant modulus. The secant modulus, E_0 , is defined as the compressive strength of the concrete divided by the strain at the peak strength. The second method involves determining the proportion of the strength at which the observed stress is some percentage below the elastic modulus predicted stress. Figure 3.3.3-A shows an example of both of these linearity descriptors in conjunction with an Air treated UHPC cylinder tested at 57 days after casting. Both of these linearity descriptors relate to the elastic modulus, also known as the tangent modulus, that was defined previously as being the linear best-fit approximation of the stress-strain response between 10% and 30% of the compressive strength.

The linearity to peak strength results, as defined by the secant modulus, are presented in Table 3.3.3-A and Figures 3.3.3-B and 3.3.3-C. The secant modulus shows very similar qualitative behaviors compared with the elastic modulus behaviors described in the previous section. More importantly, the ratio of the tangent to secant modulus values illustrates how the UHPC behavior changes as curing progresses. At 1 day after casting

this ratio ranges from 5 to 7, but by 3 days it is under 2 even without any supplemental curing. The ratio tends to stabilize around 1.1 for the steam-based specimens and around 1.2 for the Air treated specimens. For reference, this value is normally approximately 4 for normal weight 1000 psi compressive strength concrete and approximately 1.3 for 10 ksi compressive strength concrete (Popovics 1998).

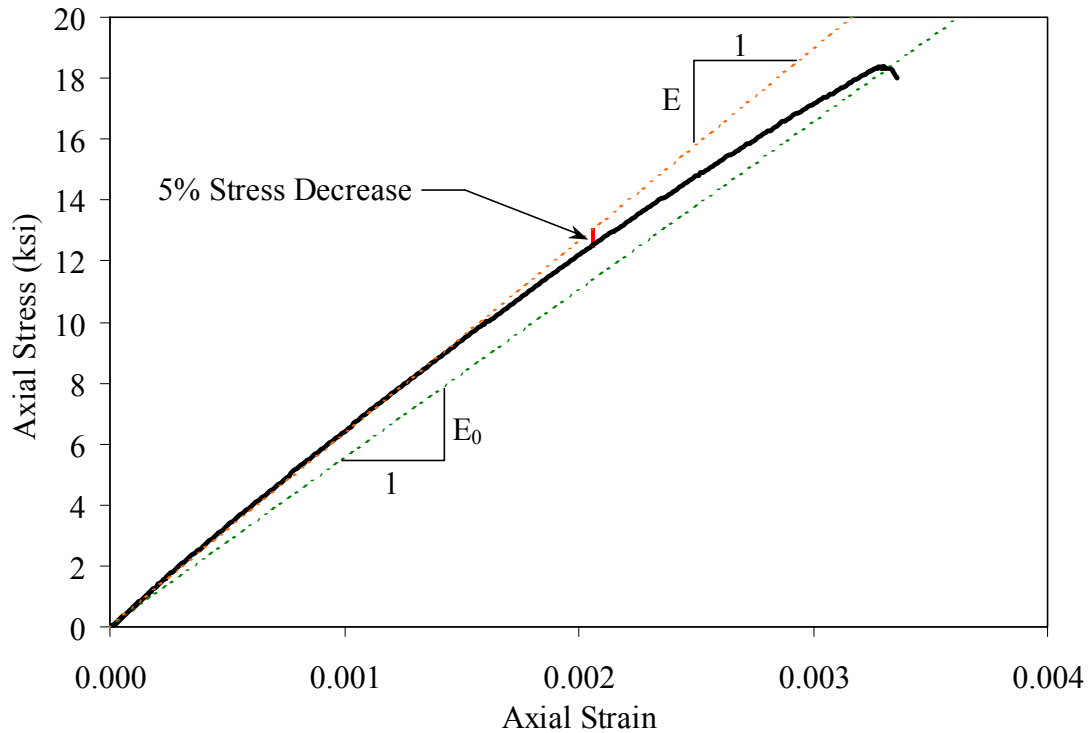


Figure 3.3.3-A: Sample Air treated stress-strain curve with linearity descriptors

The linearity results—in terms of the stress at which the stress will have dropped some percentage from the linear elastic expected value—are presented in Table 3.3.3-A and Figures 3.3.3-D and 3.3.3-E. The research program focused on stress drops of 1%, 3%, and 5%. The results from the 1% drop are highly dependent on the predefined range for calculation of the elastic modulus and as such are of less interest. The results from the 5%

drop clearly show that UHPC exhibits nearly linear behavior up to high stress levels. Figure 3.3.3-E shows that the cylinders that underwent steam-based treatment reach between 80% and 90% of their compressive strength before diverging 5% from linear elastic behavior. The Air treated cylinders seem to be asymptotically approaching the same type of response by 8 weeks after casting, having reached 70% of their compressive strength before diverging 5% from the linear elastic behavior.

Table 3.3.3-A: Compressive stress-strain response linearity at various ages after casting (Part I)

Test Age (days)	Compressive Strength (ksi)	Strain at Peak Stress	E / E ₀	No.	Linearity (1%)		Linearity (3%)		Linearity (5%)	
					Strain	Stress (ksi)	Strain	Stress (ksi)	Strain	Stress (ksi)
Steam (N1A)										
1.0	1.1	0.009020	5.53	6	0.000440	0.28	0.000490	0.31	0.000530	0.32
3	24.5	0.003580	1.09	6	0.001540	11.4	0.002520	18.3	0.003070	21.7
15	26.0	0.003970	1.16	6	0.001470	11.0	0.002620	19.2	0.003380	24.1
28	26.1	0.003740	1.08	6	0.001570	11.8	0.002570	18.9	0.003290	23.8
56	27.0	0.003900	1.10	5	0.001610	12.1	0.002670	19.8	0.003360	24.4
Steam (N1A _{xx} A)										
1.3	3.9	0.006830	4.90	5	0.000340	0.94	0.000420	1.1	0.000470	1.2
5	26.8	0.004080	1.16	5	0.001730	13.0	0.002790	20.5	0.003400	24.5
15	28.0	0.004020	1.09	6	0.001830	13.8	0.002890	21.3	0.003440	24.9
30	28.9	0.004580	1.18	5	0.001930	14.4	0.002960	21.6	0.003620	25.7
55	28.1	0.003920	1.06	6	0.001870	14.1	0.002960	21.9	0.003700	26.7
Air (N2A)										
1.0	2.2	0.009360	6.49	2	0.000330	0.43	0.000380	0.55	0.000410	0.59
2.0	9.4	0.005020	2.20	0	—	—	—	—	—	—
3	10.6	0.003850	1.90	2	0.000590	3.0	0.000740	3.7	0.000870	4.3
7	12.9	0.003620	1.59	3	0.000680	3.8	0.000930	5.1	0.001140	6.1
9	14.7	0.003400	1.26	2	0.000920	5.0	0.001250	6.6	0.001520	7.9
14	16.0	0.003710	1.39	6	0.000860	5.0	0.001200	6.9	0.001490	8.4
28	17.2	0.003430	1.21	6	0.001040	6.2	0.001530	9.0	0.001930	11.1
57	18.1	0.003570	1.20	6	0.001180	7.1	0.001760	10.4	0.002220	12.8

Table 3.3.3-A: Compressive stress-strain response linearity at various ages after casting (Part II)

Test Age (days)	Compressive Strength (ksi)	Strain at Peak Stress	E / E ₀	No.	Linearity (1%)		Linearity (3%)		Linearity (5%)	
					Strain	Stress (ksi)	Strain	Stress (ksi)	Strain	Stress (ksi)
Tempered Steam (N3A)										
1.0	2.1	0.008380	5.34	6	0.000390	0.51	0.000460	0.59	0.000520	0.66
4	20.2	0.003100	1.11	4	0.001310	9.4	0.001940	13.6	0.002400	16.5
14	21.2	0.003260	1.11	6	0.001380	9.9	0.002110	14.8	0.002630	18.0
28	21.3	0.003150	1.07	6	0.001180	8.4	0.002070	14.5	0.002580	17.8
58	22.8	0.003550	1.14	6	0.001360	9.8	0.002150	15.2	0.002710	18.8
Delayed Steam (N4A)										
0.8	1.4	0.007120	5.61	1	0.000480	0.36	0.000550	0.41	0.000380	0.34
14	16.7	0.003810	1.42	4	0.000870	5.3	0.001190	7.1	0.001480	8.7
21	25.2			5	0.001490	10.8	0.002250	15.9	0.002900	20.1
30	24.6	0.003760	1.13	6	0.001630	11.9	0.002420	17.3	0.003000	21.0
56	25.0	0.003890	1.11	6	0.001700	12.0	0.002630	18.2	0.003280	22.2

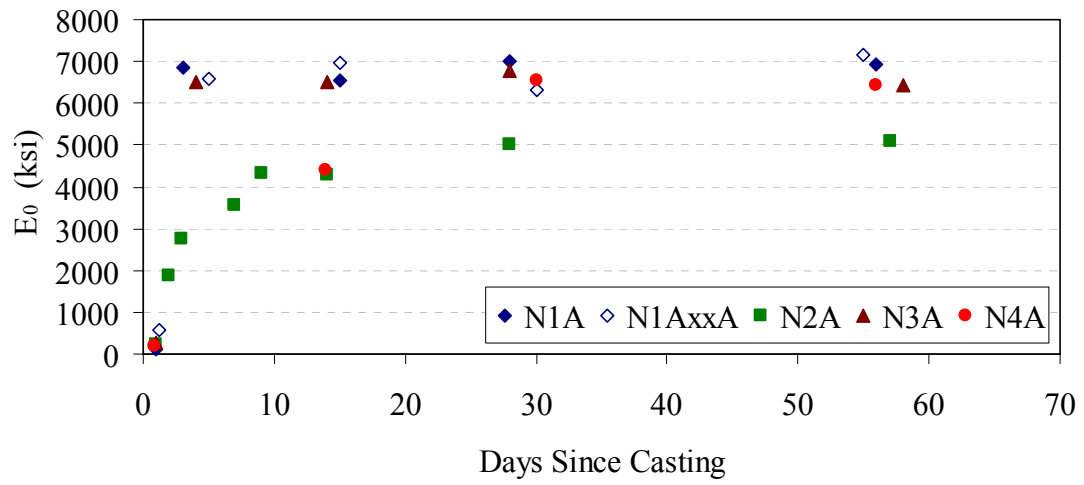


Figure 3.3.3-B: Secant modulus from casting up to 8 weeks of age

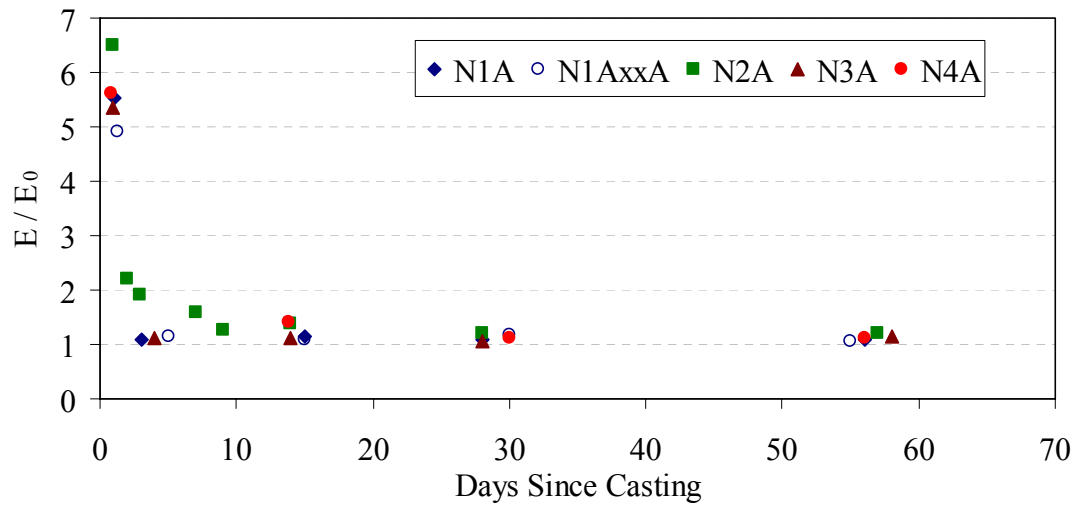


Figure 3.3.3-C: Ratio of elastic to secant modulus from casting up to 8 weeks of age

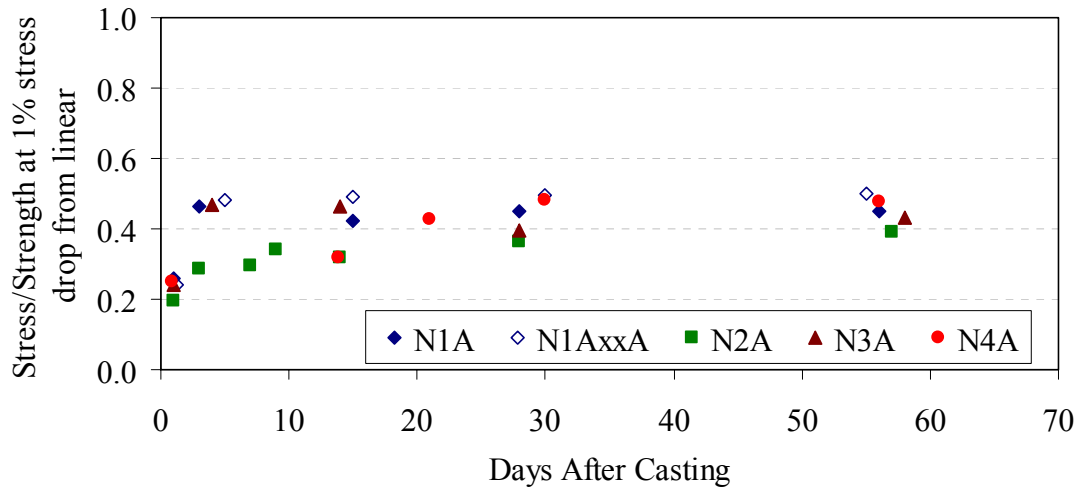


Figure 3.3.3-D: Compressive stress to strength ratio at 1% stress drop from linear elastic

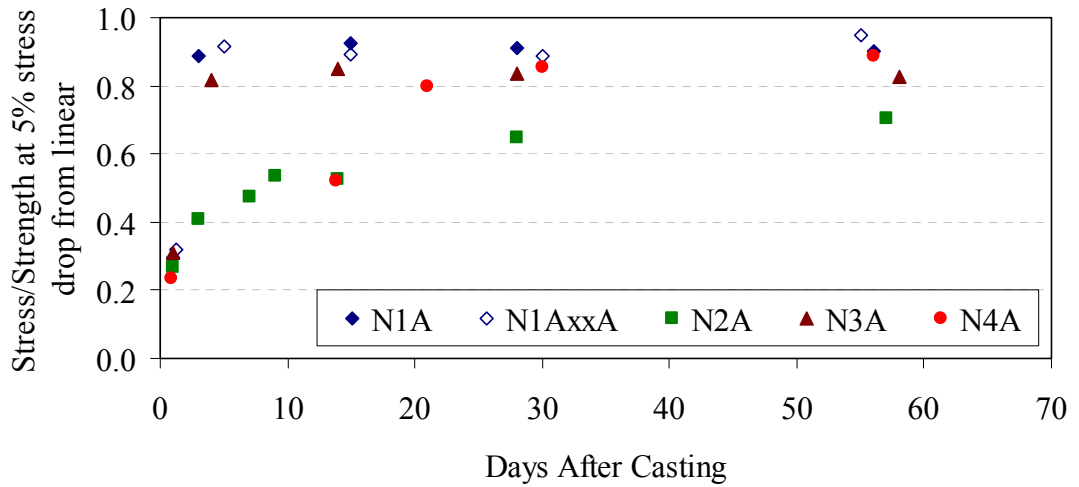


Figure 3.3.3-E: Compressive stress to strength ratio at 5% stress drop from linear elastic

3.3.4 Compression Specimen Geometry

In the United States, the cylinder is the standard concrete compression test specimen. Conversely, the cube is the standard specimen in parts of Europe. It is generally accepted that with normal strength concrete the cube will result in a higher compressive strength due to its shorter aspect ratio and the proportionally larger lateral confinement provided by the machine platens.

A series of tests were completed to determine the effect of various specimen geometries on the compressive strength of UHPC. Compression tests were completed according to ASTM C39 on 2-in., 3-in., and 4-in. diameter cylinders with cast lengths of twice their diameters. ASTM C39 compression tests were also performed on overlength 3 in. diameter cylinders that had a cast length of 6.5 in. Cube compression tests were completed according to ASTM C109 on 2 in. and 4 in. cubes. Figure 3.3.4-A shows the range of sizes and geometries of the specimens tested. Figure 3.3.4-B shows the cylinder and cube specimens in the compression testing machine. Note that all specimens were tested in a hydraulically actuated 1000 kip Forney test machine with a load rate equivalent to 150 psi/sec.

The test program described above was repeated three times. Each time, the set of cylinder and cube specimens was cast from a single batch. Two of the batches were Steam treated while the third batch was Air treated. Table 3.3.4-A provides the results from the compression tests. The 3-in. diameter cylinder—used as the control specimen throughout the entire study—was also the control specimen for this series of tests.



Figure 3.3.4-A: Compression cubes and cylinders including (clockwise from upper left) 4-in., 3-in. overlength, 3-in., and 2-in. diameter cylinders and 2 in. and 4 in. cubes

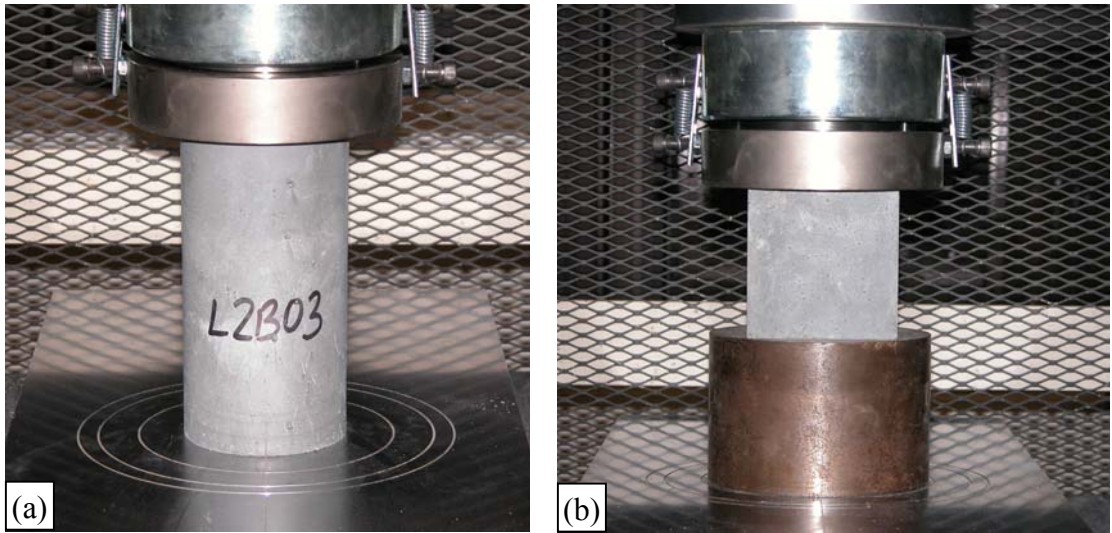


Figure 3.3.4-B: (a) Cylinder and (b) cube compression testing

The combined results from the three sets of tests indicate that the compressive strength of UHPC can be measured, relatively accurately, through various sizes of cubes and cylinders. Results were never more than 8% removed from the control cylinder result.

The cubes tended to exhibit slightly higher strengths on the order of 5%. In addition, the 2-in. diameter cylinders tended to exhibit slightly lower strengths. The smaller cubes and cylinders tended to exhibit larger standard deviations. Conversely, the large specimens tended to exhibit smaller standard deviations. These results were expected because heterogeneities in the concrete would likely remain in a uniform size range but would be proportionally larger in smaller specimens.

Table 3.3.4-A: Cylinder and cube compressive strength results

Specimen	No.	Compressive Strength (ksi)		% Difference From Control
		Average	St. Dev.	
Steam (M1B)				
3 in. Cylinder †	6	29.4	0.61	–
4 in. Cylinder	5	29.3	0.91	-0.3
Overlength 3 in. Cylinder	3	27.2	1.29	-7.5
2 in. Cylinder	6	29.5	1.00	0.3
100 mm Cube	5	29.1	1.75	-1.2
2 in. Cube	6	31.1	1.70	5.8
Steam (L1B)				
3 in. Cylinder †	6	30.5	1.02	–
4 in. Cylinder	5	31.2	0.78	2.2
Overlength 3 in. Cylinder	3	28.2	1.19	-7.5
2 in. Cylinder	6	29.0	1.79	-5.0
100 mm Cube	5	31.9	0.73	4.6
2 in. Cube	6	31.9	1.56	4.6
Air (L2B)				
3 in. Cylinder †	8	21.6	0.55	–
4 in. Cylinder	5	22.4	0.30	3.7
Overlength 3 in. Cylinder	3	21.8	0.22	1.1
2 in. Cylinder	6	20.3	2.15	-5.9
100 mm Cube	3	23.3	0.42	8.0
2 in. Cube	6	22.9	1.28	6.1

† Considered to be the control specimen.

3.3.5 Demolding Age Effect on Compressive Strength

Throughout this test program, control cylinder compressive strengths were sometimes below the anticipated value. As previously mentioned, the mix design, constituent materials, and mixing procedure were always the same. For this reason, the deviations in strength were troubling. Two observations were made during the early stages of the test program: (1) the set time of the UHPC sometimes varied and (2) in general, the older the premix, the longer the set time. Regardless of these observations, the cylinders were nearly always demolded at approximately 24 hours after casting. This delayed setting sometimes resulted in the cylinders barely having enough strength to remain intact throughout the demolding process.

After the bulk of the test program was complete, an additional batch was added to the test program. This batch included two sets of 3-in. diameter cylinders that were demolded at various ages after casting. One of the sets was then Steam treated while the other was Air treated. The earliest that any cylinders could be stripped was determined to be 28 hours after casting because of the advanced age of the premix by this point in the test program. The other cylinders were stripped at 47 and 55 hours after casting. Otherwise, the cylinders in each set were treated identically up through compression testing at 28 days.

Table 3.3.5-A presents the results from this set of compression tests. These results clearly indicate that the age of the UHPC at stripping has a major impact on the compressive strength. The cylinders that were stripped as soon as their integrity allowed had a 25% to 30% lower compressive strength at 28 days compared with the cylinders that were

stripped approximately 20 hours later. Once the cylinder has gained sufficient integrity to support itself, the primary role of the cylinder mold is to retain moisture within the cylinder. The loss of that moisture barrier clearly resulted in a decrease in the moisture that was available for hydration and a resulting decrease in compressive strength.

Table 3.3.5-A: Demolding age effect on 28-day compressive strength results

Specimen Group	No.	Compressive Strength (ksi)	
		Average	St. Dev.
Steam			
Stripped at 28 hours after casting	6	20.8	1.25
Stripped at 47 hours after casting	6	29.4	0.85
Stripped at 55 hours after casting	6	30.2	1.89
Air			
Stripped at 28 hours after casting	6	14.4	0.49
Stripped at 47 hours after casting	6	18.7	0.51
Stripped at 55 hours after casting	6	19.7	0.75

3.3.6 Long-Term Delayed Steam Effect on Compressive Strength

Although the Delayed Steam curing regime was designed to mimic the postponed steam curing of UHPC, it is anticipated that longer delays prior to steam treatment could occur. For this reason, two batches of UHPC were cast to focus on the compressive strength level that UHPC can attain if the steam treatment is significantly delayed. Each of these batches included 36 cylinders, half of which were air treated and half of which had a steam treatment applied at a time distant from casting. The steam treatment was the same as the standard Steam treatment except for the start date. The steam treatment always started 6 days prior to the date of the compression testing.

Table 3.3.6-A presents the results of these tests. The first batch, L21, was tested at 8, 12, and 16 weeks after casting. The second batch, L22, was tested at 8, 20, and 32 weeks after casting. In both cases, the Air treated cylinders and the cylinders that underwent the long-term delayed steam treatment showed consistent compressive strengths over the months of testing. The diminishing impact of the steam treatment, delayed from 1 day to 2 weeks after casting, does not seem to continue indefinitely. By 2 months, the impact seems to have leveled off such that steaming at this time is as effective as steaming at up to 32 weeks after casting. Additionally, it is important to note that the application of the steam treatment increased the compressive strength by 30%, regardless of when it was applied.

Table 3.3.6-A: Long-term delayed steam effect on compressive strength

Batch	Curing	Steam Days	Test Day	No.	Compressive Strength (ksi)	
					Average	St. Dev.
L21	Air		56 days	6	20.6	0.56
	Air		84 days	6	20.0	0.67
	Air		112 days	6	19.5	0.33
	Steam	50 to 52	56 days	6	26.2	1.04
	Steam	78 to 80	84 days	6	25.2	0.59
	Steam	106 to 108	112 days	6	25.8	0.74
L22	Air		56 days	6	18.9	0.35
	Air		140 days	6	18.6	0.82
	Air		224 days	6	19.0	0.89
	Steam	50 to 52	56 days	6	25.1	0.91
	Steam	134 to 136	140 days	6	24.2	1.25
	Steam	218 to 220	224 days	7	24.8	0.69

3.3.7 Fiber Effect on Compression Failure

The steel fiber reinforcement included in UHPC provides a number of advantages, most notably in terms of tensile structural behavior. Normally, a compression test on high strength concrete would result in a very brittle, dramatic failure. As noted earlier in the discussion of UHPC compression behavior, the UHPC that is reinforced with steel fibers does not exhibit explosive failures during compression tests. Recalling Figure 3.3-B, a compression test on Steam treated UHPC would likely result in a rapid load drop, but the cylinder would remain intact.

A few UHPC cylinders were cast according to the normal mix design and procedures except that the steel fiber reinforcement was not added. Thus, the high compressive strength abilities of the UHPC matrix are present, but the restraining and confining effects of the fibers are absent. The test results from these cylinders indicated a dramatic change in the compression failure behavior.

Figure 3.3.7-A shows four still pictures of the failure of one of these cylinders. These pictures were captured from a digital video recording. The video was captured at a frame rate of 30 per second, thus the smallest increment of time over which to observe changes in behavior is $1/30^{\text{th}}$ of a second. The failure of this cylinder began when small chips of UHPC began to fly off the top and bottom of the cylinder at its intersection with the platens. This chipping continued for a few seconds until a larger chip exited the top of the cylinder just $1/6^{\text{th}}$ of a second before failure. The cylinder then rapidly and dramatically

failed: Over the course of $1/30^{\text{th}}$ of a second, the intact cylinder shattered into many small pieces of UHPC.

Although this experiment was not controlled with fiber reinforced and unreinforced UHPC tested in parallel, the compressive strength results are still of interest. The cylinders tested averaged 29 ksi, with the cylinder shown in the video reaching 31 ksi. Note that these strengths correspond to loads of approximately 200 kips; therefore, the Forney 1000 kip capacity testing machine was only at 20% of its capacity and would not have held an inordinately high level of strain energy prior to failure.



(a)



(b)



(c)



(d)

Figure 3.3.7-A: Compression failure of a Steam treated UHPC cylinder containing no fiber reinforcement. (a) $1/6^{\text{th}}$ of a second before failure. (b) $1/30^{\text{th}}$ of a second before failure. (c) At failure. (d) $1/10^{\text{th}}$ of a second after failure.

3.3.8 Load Rate Effect on Compression Testing Results

The compression testing discussed so far in Section 3.3 was all completed with a load rate of 150 psi/sec during the initial elastic portion of the stress-strain response. As previously mentioned, this load rate is outside the bounds recommended by the ASTM C39 test method. Prior to the initiation of the compression testing portion of the UHPC material characterization work, a set of UHPC cylinders was cast with the focus being on the effect of various load rates on standard compression testing results.

It is normally accepted that higher load rates will result in higher compression strength and modulus of elasticity results. For this reason, using the ASTM C39 load rate of 35 +/- 15 psi/sec is recommended for any standardized compression testing of concrete.

However, the high strength results expected from UHPC mean that a single compression test on a concrete cylinder could take 15 to 20 minutes or more. This objectionably long time for a single data point led to the testing discussed below.

Twenty-four cylinders with a 3-in. diameter were cast within a single batch of UHPC for this testing. The cylinders were all cast and Steam treated according to normal procedures. The cylinders were then divided into four groups, each of which was tested at a different load rate ranging from 35 psi/sec to 250 psi/sec. Within each group of six cylinders, three were tested in compression according to ASTM C39. The remaining three were tested according to ASTM C469, including multiple unloads/reloads, before being tested according to ASTM C39. This testing differed from the previously discussed modulus testing because the axial deformations were measured via a standard

compressometer as described in the test method, and data on Poisson’s ratio was also collected.

Table 3.3.8-A presents the results of these tests. The results do not clearly indicate a change in behavior caused by the increasing load rate. For this particular batch, the compressive strength remained around 29 ksi, the modulus of elasticity remained around 8200 ksi, and Poisson’s ratio was quite consistent at 0.19. These results indicate that an increase in the load rate would not be detrimental. From a practical standpoint, a compression test run at 150 psi/sec can be completed within 5 minutes on a Steam treated cylinder and more quickly on lower strengths of UHPC. For these reasons, a load rate of 150 psi/sec was chosen for all of the UHPC compression testing.

Table 3.3.8-A: Load rate effect on compression testing results

Load Rate (psi/sec)	Compressive Strength (ksi)			Modulus of Elasticity (ksi)			Poisson’s Ratio		
	No.	Ave.	St. Dev.	No.	Ave.	St. Dev.	No.	Ave.	St. Dev.
35	6	28.2	1.62	3	8090	303	3	0.195	0.018
50	6	29.1	1.00	3	8401	212	3	0.193	0.011
150	6	29.2	0.99	3	8256	262	3	0.199	0.007
250	6	29.2	0.48	3	8011	149	3	0.184	0.011

3.4 Tension Testing

Four types of tension tests were implemented in this research program to experimentally determine the tensile properties of UHPC. These tests included flexural testing of prismatic sections, split tensile testing of cylinders, axial tensile testing of mortar

briquettes, and axial tensile testing of cylinders. The following sections discuss the test procedures and the test results.

3.4.1 Flexural Prism

The ASTM C1018 *Standard Test Method for Flexural Toughness and First-Crack Strength of Fiber-Reinforced Concrete (Using a Beam With Third-Point Loading)* was one test used to determine the tensile properties of UHPC. This test involves the four-point flexural loading of small-scale concrete prisms. During the test, the load on and the deflection of the prism are monitored. These data are then used to determine the cracking strength and post-cracking toughness response of the concrete.

This test method requires specialized equipment in order to correctly load the specimen and accurately monitor the response. First, the test setup requires that the deflection measuring system must measure “net values exclusive of any extraneous effects due to seating or twisting of the specimen on its supports or deformation of the support system.” Second, the loading of the prism must be completed through a “testing arrangement where specimen net mid-span deflection is used to control the rate of increase of deflection using a closed-loop, servo-controlled testing system.”

To meet these requirements, a specialized test setup was devised. In this setup, a yoke similar to that shown in Figure 2 of ASTM C1018 was used to measure the midspan deflections. LVDTs were attached to the yoke on each side of the specimen at midspan, and the yoke was attached to the specimen at mid-depth over the support points. The

LVDTs bore on a plate that was epoxied to the compression face and extended to hang over the sides of the prism. Figure 3.4.1-A shows two examples of the deflection measurement setup for this four-point bending test.

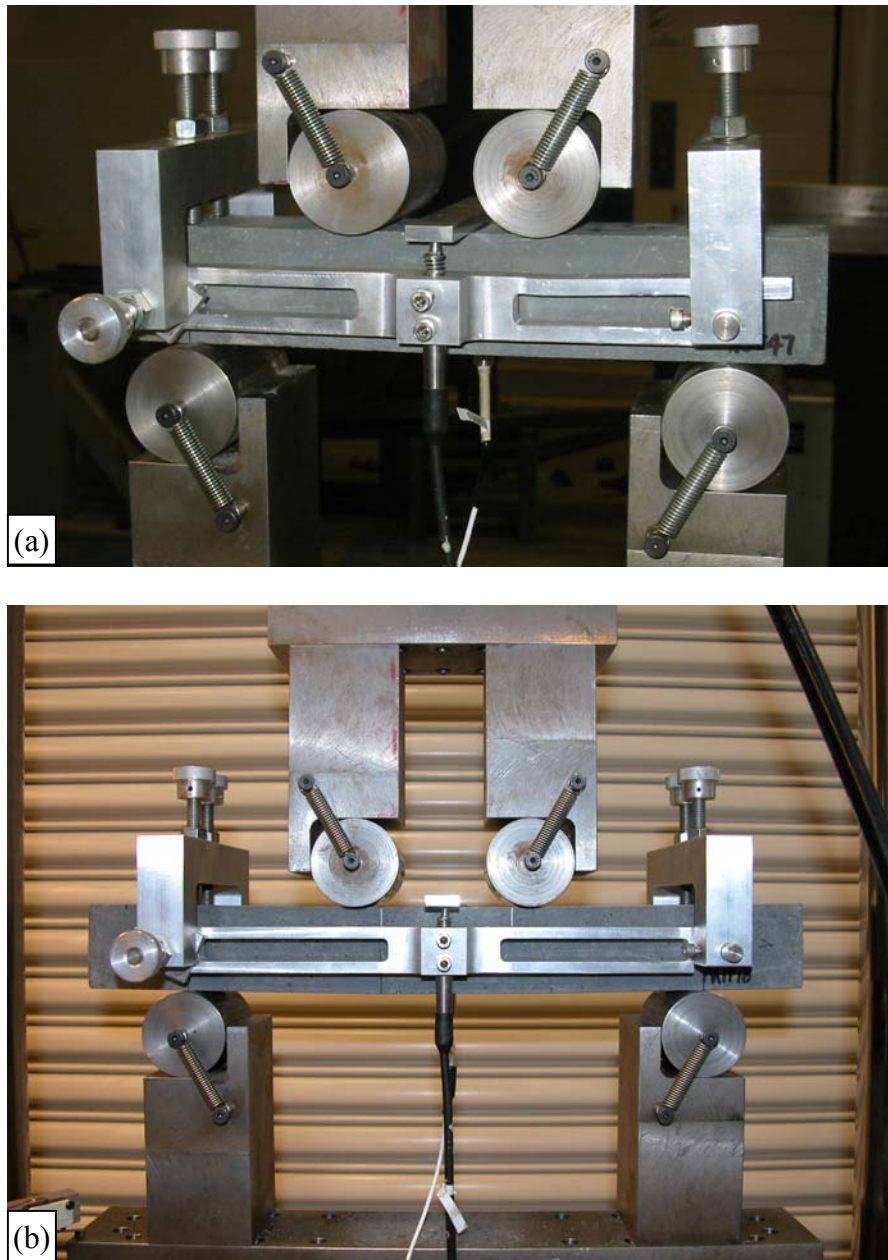


Figure 3.4.1-A: Prism flexural test setup for a (a) 9 in. span and a (b) 12 in. span

The loading control of the test was accomplished by completing the test in an MTS load frame. The control signal for the MTS was the midspan net deflection of the specimen as captured by the LVDTs. The signals from the two LVDTs were electronically averaged then submitted to the MTS control panel. In this way, the deflection rate of the prism was accurately and consistently maintained at the correct level. This loading technique also limited the amount of potential energy stored in the load frame that could be transmitted into the concrete prism during the temporary stiffness loss associated with cracking.

The loading apparatus used to test the prisms was reconfigurable to allow for testing of multiple sizes of prisms. The rollers and their support blocks are movable to allow for lower support spans from 6 in. to 16 in. and upper loading spans from 2 in. to 6 in. As shown in Figure 3.4.1-A, the two upper load points and the two lower support points are steel rollers that impart no axial restraint on the prism. Torsional effects caused by misalignment between the planes of the prism faces and the rollers were overcome by placing individual shims between each roller and its bearing block. The bearing blocks under the rollers are supported by 6 in. deep solid steel beams that are connected to the heads of the MTS machine. These deep steel beams reduce flexibility in the loading apparatus thus allowing for easier and more refined control of the test during cracking of the prism.

The ASTM C1018 test was performed on prisms from all four curing regimes. The casting and curing of the prisms was completed following normal procedures. During

casting of each prism, special care was taken to ensure that the UHPC flowed from one end of the prism to the other, thus ensuring a fiber distribution and alignment system that was similar to that which would occur in the large-scale casting of a beam or plate type flexural member.

The test specification recommends a preferred standard size of molded specimen of 14 in. by 4 in. by 4 in., resulting in a third-point loading configuration with a 12 in. lower span. This specimen size was not used for a number of reasons. First, this depth of prism is on the high end of the likely thickness of UHPC plate members subject to flexural forces. Second, a shear span to prism depth ratio equal to one, as recommended by the specification, will create a stress field and deflection response in the prism that is substantially both flexural and shear. A larger shear span to prism depth ratio would much more accurately represent the flexural response of UHPC. Finally, the specification indicates that the prism cross-sectional dimensions must only be at least three times the length of a fiber. This requirement can easily be met by smaller cross-sectional sizes.

The test program included two prism cross-sections and a total of four loading configurations. The cross-sections investigated were 2 in. by 2 in. prisms and 3 in. deep by 4 in. wide prisms. The 2 in. by 2 in. prisms were cast in lengths of 11 in. and 17 in. The 3 in. by 4 in. prisms were cast 16 in. long. Four loading configurations were used to test the 2 in. by 2 in. prisms. These included third-point loading on 6 in., 9 in., and 12 in. lower spans, as well as loading on a 15 in. lower span with 3 in. between the upper load points. The third-point loading with a 12 in. lower span was also used for the 3 in. by 4

in. cross-section prisms. These various cross-sections and loading configurations allow for the comparison of observed tensile behaviors because the 2 in. by 2 in. prism on a 6 in. span is a scaled model of the ASTM C1018 recommended prism. Other test setups provide more realistic representations of flexural tensile material behaviors.

The following procedure was used to complete the test:

1. The prism was centered in the load frame with the screeded face of the prism oriented toward the front and the vertical molded faces placed as the compression and tension faces.
2. The load was manually increased to approximately 50 lbs.
3. The setup was checked to ensure that all rollers were bearing on the prism.
4. The LVDTs were then set in place, and control of the machine was transferred to the averaging circuit attached to the LVDTs.
5. The MTS Microprofiler was then used to apply a constant deflection rate to the prism.
6. The deflection rate was set so that the expected first crack deflection would occur approximately 1 minute into the test. This rate varied depending on the prism cross-section and loading configuration.
7. The test was stopped after a deflection of at least 16 times the cracking deflection was reached.
8. The collection of the data for the test was completed through an analog data acquisition system. It was set to record data at 10 Hz until well after first cracking of the prism had clearly occurred.

9. The record rate was then manually decreased to 4 Hz for the remainder of the test. The time, load, deflection from both LVDTs, and electronic circuit averaged deflection values were all recorded.

The strength and toughness results and analysis presented in the next two sections are highly dependent on the correct identification of first cracking in each prism test. Plain concrete and fiber reinforced concrete may begin to behave nonlinearly due primarily to internal microcracking prior to the first overall cracking of the prism; therefore, determining first cracking can be somewhat subjective. The behavior of UHPC is such that the first cracking is tensile stress cracking on the bottom flange of the prism. Thus, first cracking—recorded by the data acquisition system and physically observed on the specimen—is usually quite clear. Figure 3.4.1-B shows the early parts of load-deflection response curves for both a Steam and an Air treated prism. This figure shows that the prism response is linear until first cracking when a clearly defined decrease in load carrying capacity occurs. Soon thereafter the load again begins to increase. The sawtooth pattern visible in the response is indicative of additional individual cracks forming throughout the highly stressed tension face of the prism.

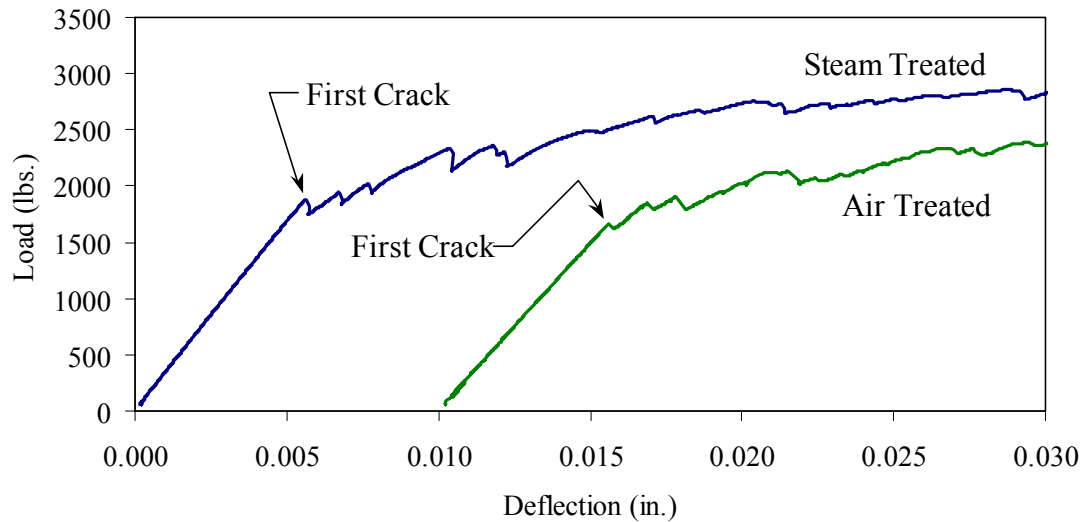


Figure 3.4.1-B: Examples of first crack shown on load-deflection response curves

A total of 76 prisms were tested over the five loading/cross-section configurations. Seventy-one prisms were tested successfully out of this group. The load-deflection results are presented in Figures 3.4.1-C through 3.4.1-G. Figure 3.4.1-C presents the results from the scaled standard ASTM C1018 test on 2 in. by 2 in. prisms with third-point loading over a 6 in. span. Figure 3.4.1-D presents the results from the 3 in. by 4 in. prisms tested with third-point loading over a 12 in. span. Figures 3.4.1-E and 3.4.1-F present the results from 2 in. by 2 in. prisms tested with third-point loading on 9 in. and 12 in. spans, respectively. Finally, Figure 3.4.1-G presents the results from the 2 in. by 2 in. prisms tested over a 15 in. span with 3 in. between the load points. Sequential results in each set have been offset by 0.005 in. to allow for clear presentation. The curing regime applied to each set of prisms is listed in the lower right corner of each set of results.

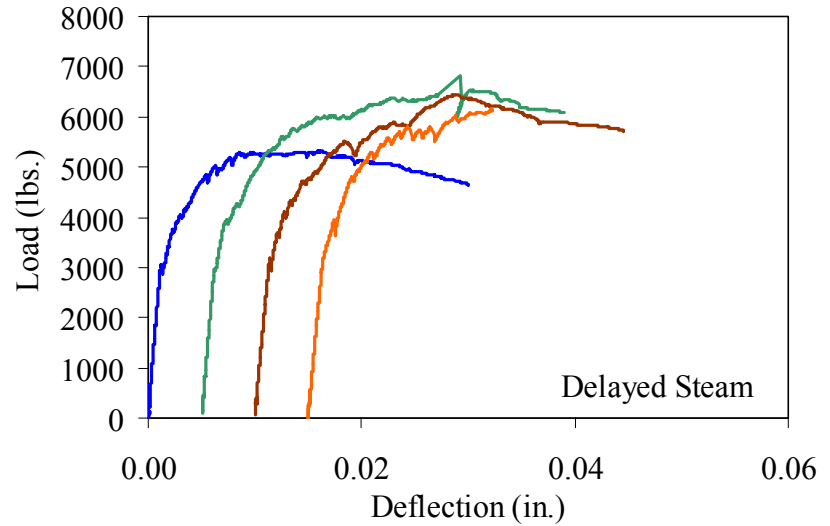
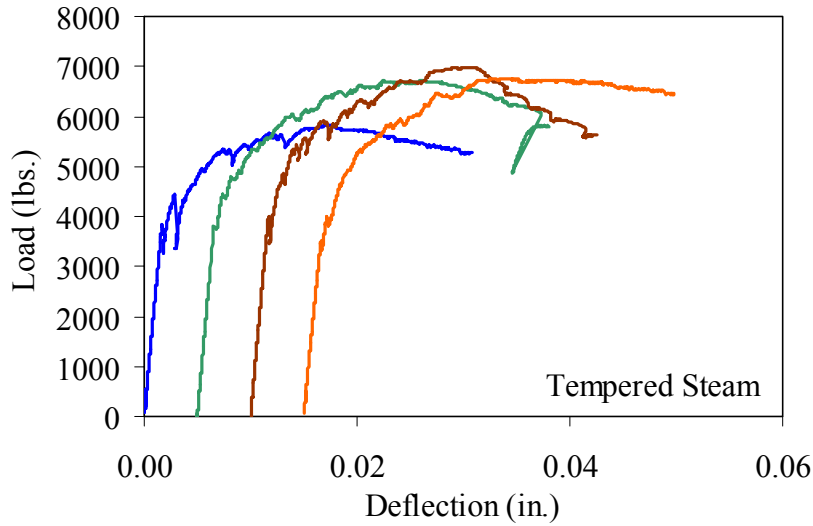
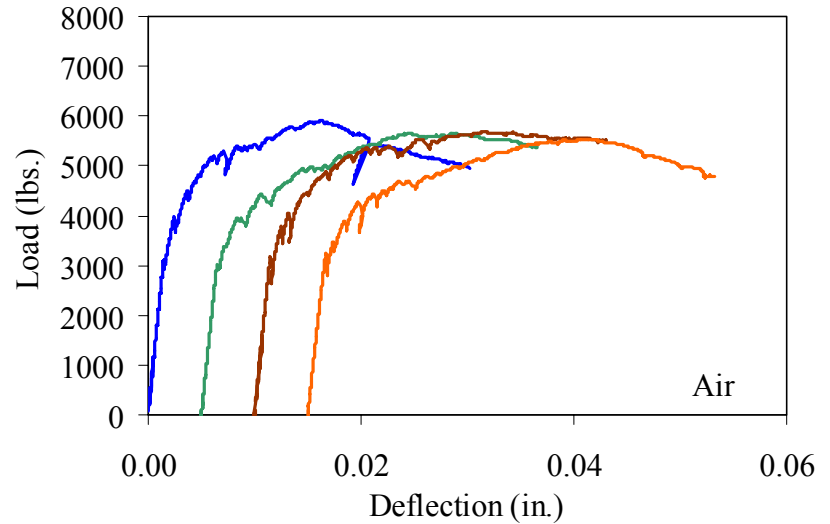
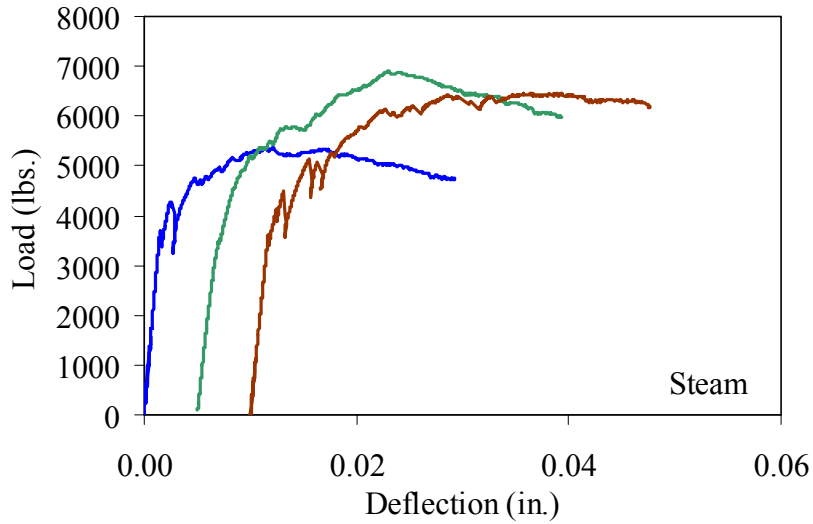


Figure 3.4.1-C: ASTM C1018 load-deflection response results for 2x2 prisms over a 6 in. span with third point loading

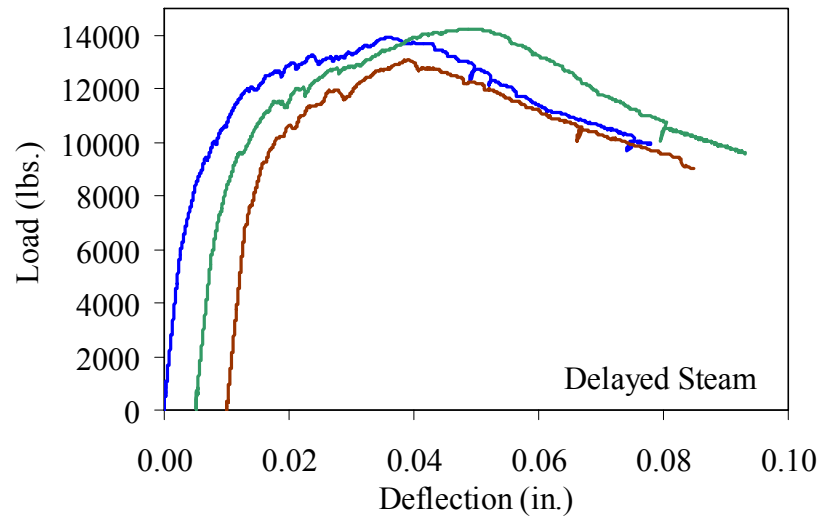
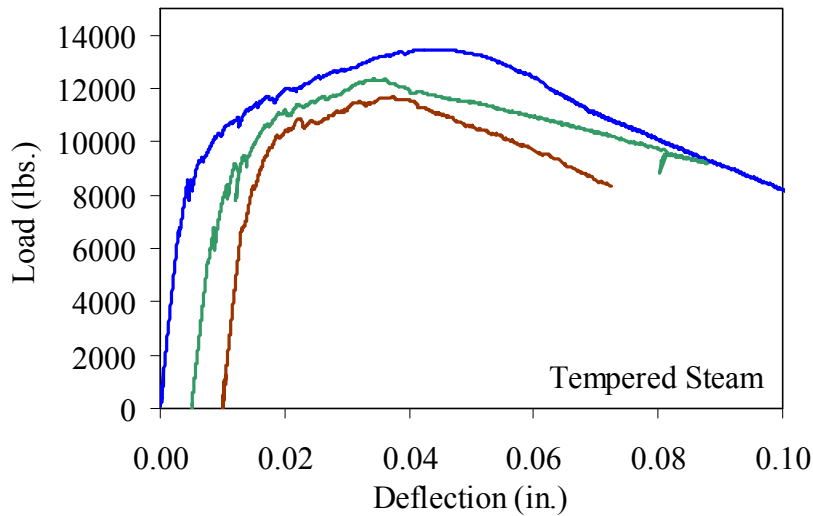
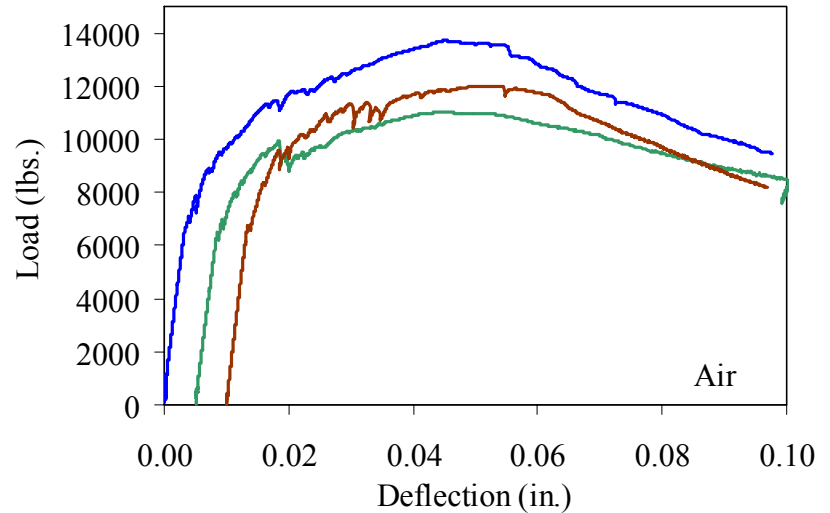
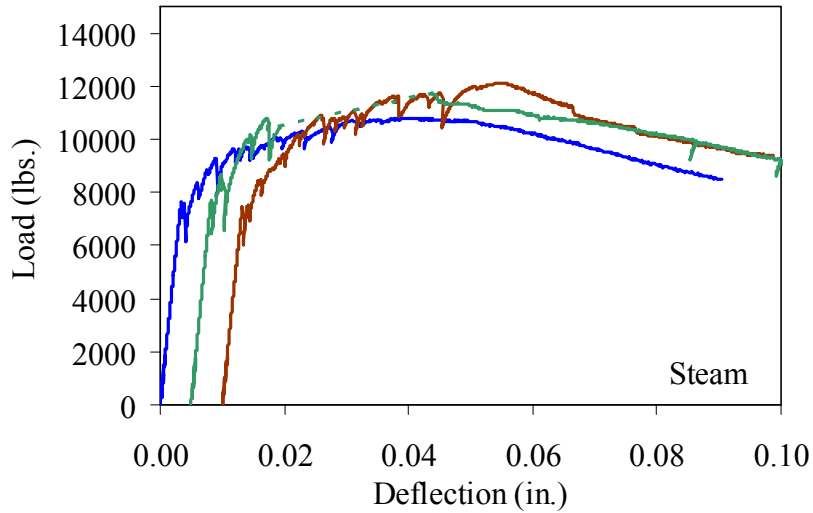


Figure 3.4.1-D: ASTM C1018 load-deflection response results for 3x4 prisms over a 12 in. span with third point loading

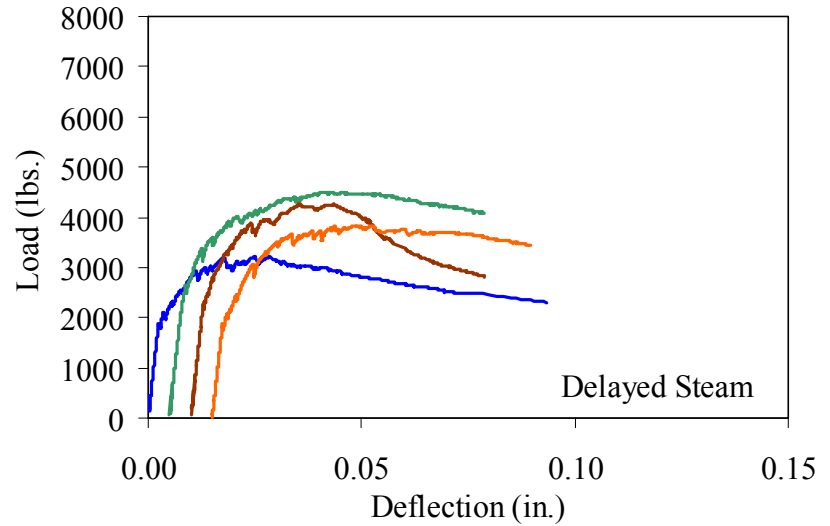
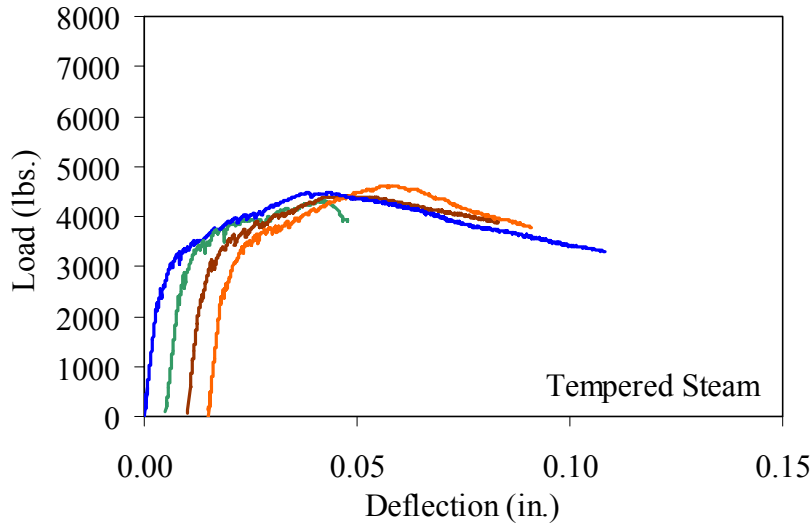
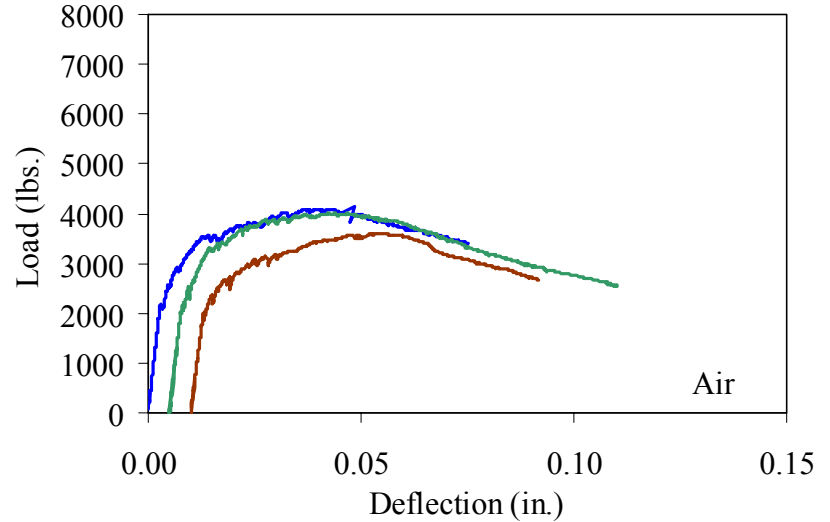
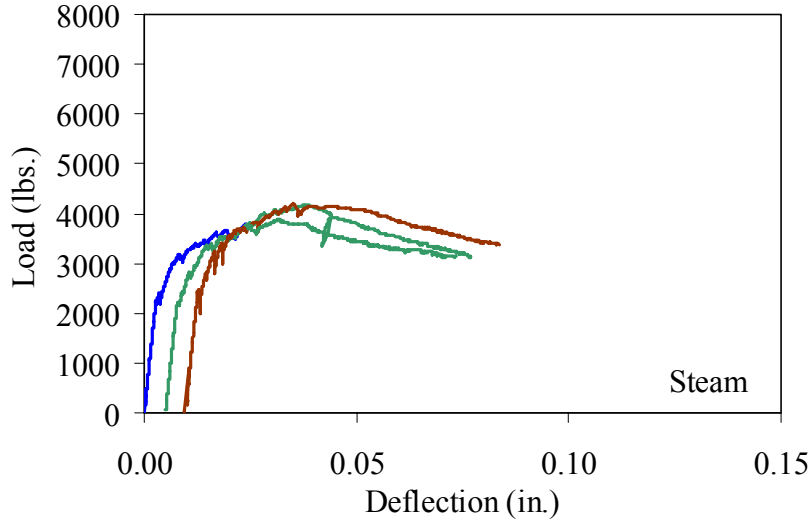


Figure 3.4.1-E: ASTM C1018 load-deflection response results for 2x2 prisms over a 9 in. span with third point loading

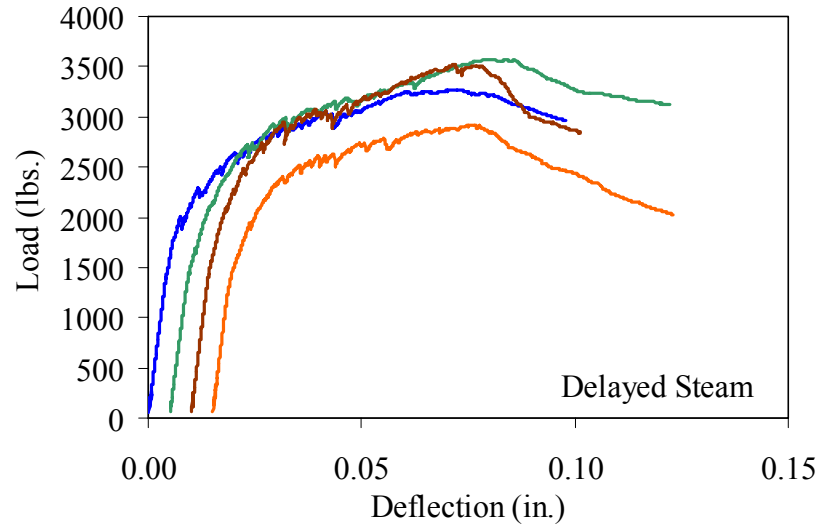
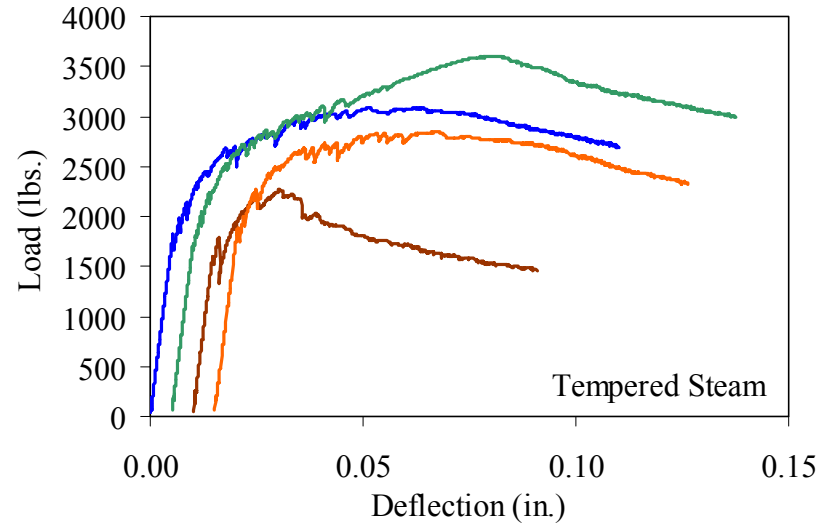
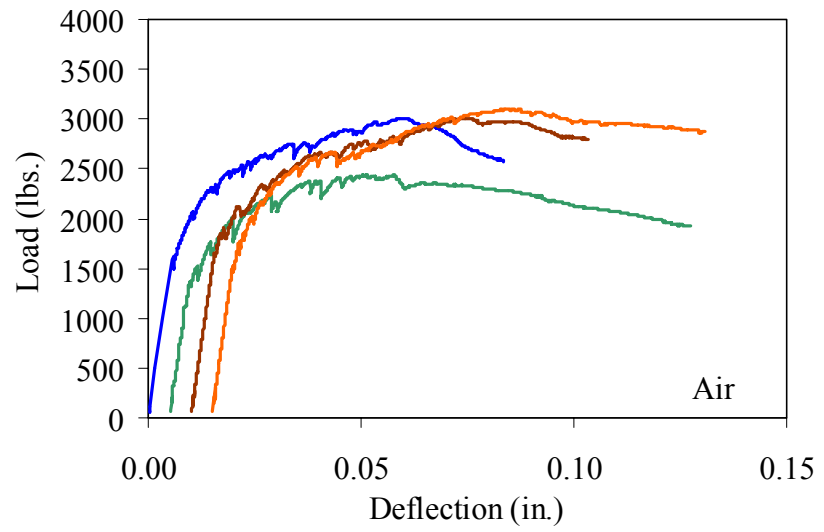
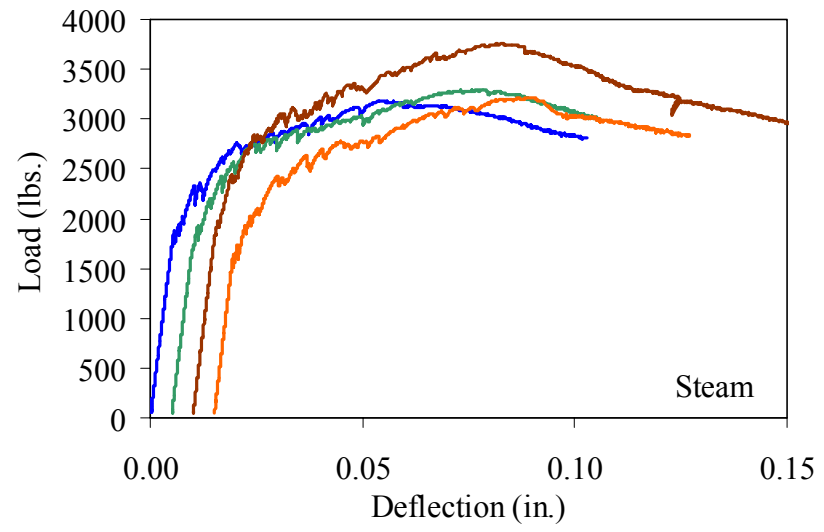


Figure 3.4.1-F: ASTM C1018 load-deflection response results for 2x2 prisms over a 12 in. span with third point loading

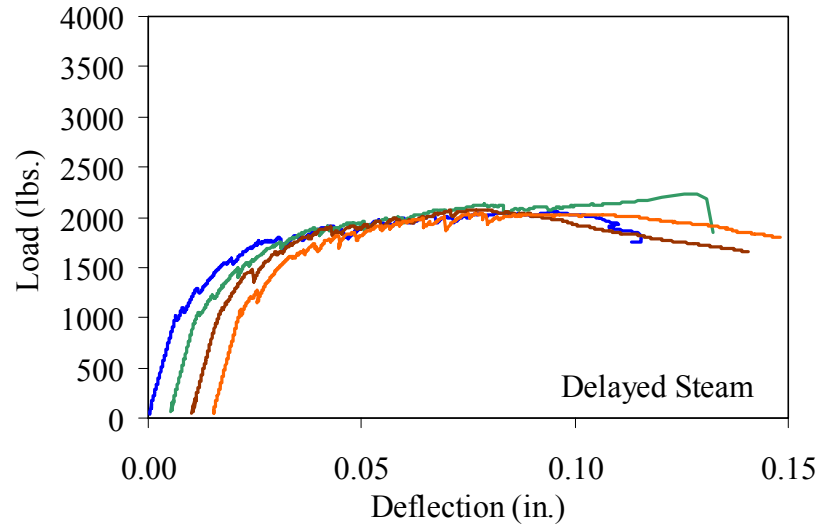
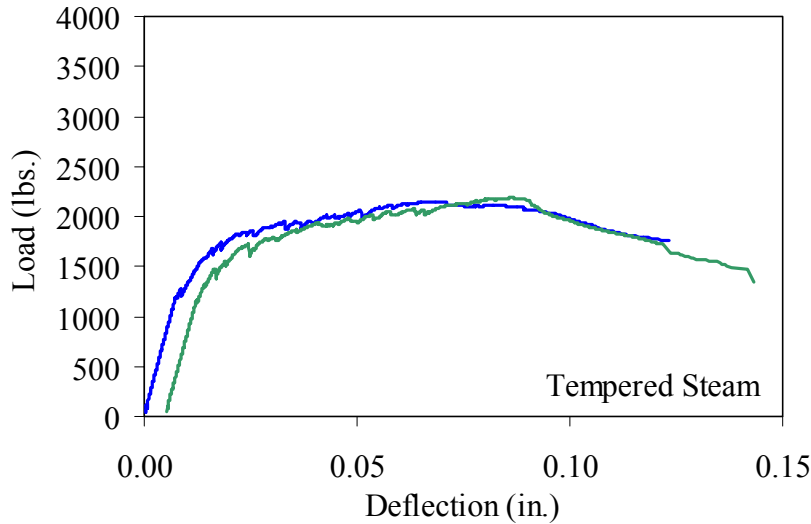
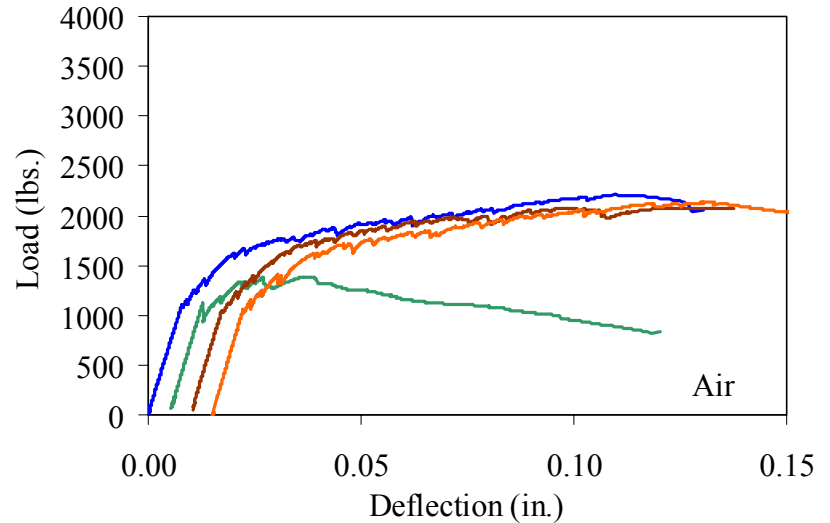
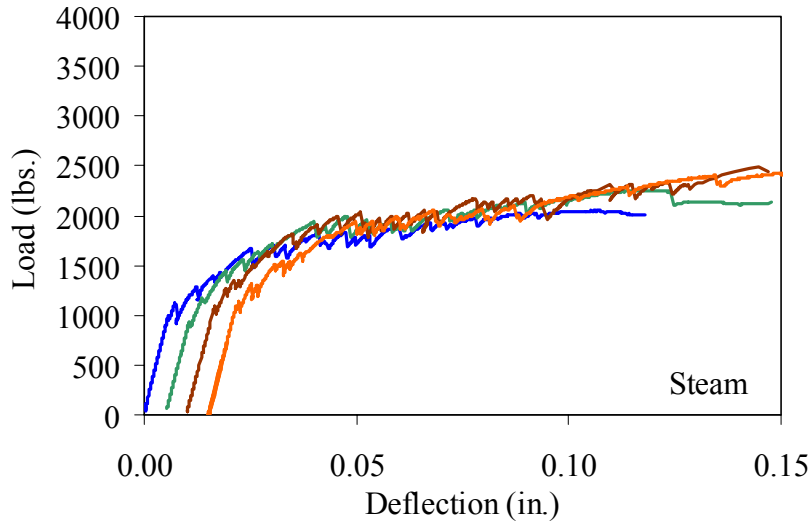


Figure 3.4.1-G: ASTM C1018 load-deflection response results for 2x2 prisms over a 15 in. span with 3 in. between loads

3.4.1.1 Strength

The procedure implemented for the ASTM C1018 prism flexure tests allowed for accurate recording of the flexural behavior of UHPC from initial elastic behavior through tensile cracking to tensile fiber pullout. The strength-based results from these tests are presented in Table 3.4.1.1-A. The table provides the averaged results from the prisms in each set. The first and most important result from these tests is behavior at first cracking of the UHPC matrix. As previously discussed, the first crack is an indication of the tensile cracking strength of UHPC. The load, strength, and deflection at first cracking are all listed in the table. The first crack strength is based on Equation 3.4.1.1-A, which is referenced in ASTM C1018, provided in ASTM C78, and based on mechanics of materials principles assuming pure bending. In Equation 3.4.1.1-A, $f_{ct,flexure}$ is the flexural tensile cracking strength, P is the total load applied to the prism, l is the span, b is the width of the prism, and d is the depth. The variable η equals 1.0 for third point loading and 1.2 for the loading configuration with a 15 in. span and 3 in. between load points. This factor accounts for the difference in the bending moment at midspan on the prism under the differing loading configurations.

$$f_{ct,flexure} = \eta \frac{Pl}{bd^2} \quad (3.4.1.1-A)$$

It has been widely observed that the actual tensile cracking strength of concrete, f_{ct} , is overestimated by the tensile cracking strength results of a small-scale flexural test, $f_{ct,flexure}$. Carpinteri and Chiaia (2002) summarized extensive amounts of previous research on this topic. They indicated that the overestimation is usually caused by depth and strain

gradient effects on the flexural cross-section. Chanvillard and Rigaud (2003) indicate that the concrete ahead of the crack front tends to microcrack, thus reducing stress concentrations. They performed research on the UHPC that is the subject of this report. Their results indicated that the overestimation of the tensile strength is caused by the fiber reinforcement.

Various correction factors have been suggested to account for this overestimation. The Association Française de Génie Civil (AFGC) *Interim Recommendations for Ultra High Performance Fibre-Reinforced Concretes* (2002) recommends Equation 3.4.1.1-B, which varies depending on the depth of the cross-section in millimeters, d , as compared to a reference depth, d_0 , of 100 mm. Note that this empirical equation is based on experimental data, but it has been verified for UHPC by Chanvillard and Rigaud (2003). The first crack tensile strength results as modified by this correction factor are provided in Table 3.4.1.1-A.

$$f_{ct} = f_{ct,flexure} \left(\frac{2.0 \left(\frac{d}{d_0} \right)^{0.7}}{1 + 2.0 \left(\frac{d}{d_0} \right)^{0.7}} \right) \quad (3.4.1.1-B)$$

Table 3.4.1.1-A also includes results related to the average peak load carried by each set of prisms. The peak load values tended to be between 170 and 200 percent of the cracking load values. The equivalent flexural strength corresponding with the peak load is listed. This strength is based on Equation 3.4.1.1-A and substitutes the peak load for

the cracking load. This calculation is presented purely for comparative purposes, as this equivalent flexural strength has no physical meaning. At peak loading, the UHPC prism is exhibiting extensive cracking, and its midspan neutral axis no longer resides at mid-depth. Thus, the assumptions of pure bending on a uniform, elastic cross-section, which are inherent in this equation, are not met.

Finally, this table includes the average effective modulus of elasticity of each set of prisms. Equation 3.4.1.1-C provides the relationship between the centerline deflection of a simply-supported beam with two point loads and the cross-sectional and material properties of the beam. This equation accounts for both the flexural and shear responses in the beam. In Equation 3.4.1.1-C, Δ_{cl} is the centerline deflection, P is the total load applied to the prism, L is the span, a is the shear span, E is the modulus of elasticity, and I is the moment of inertia. In the shear term, A' is the effective shear area (i.e., 80% of the cross-sectional area for a prism) and G is the shear modulus. To calculate the shear modulus, it is assumed that the Poisson's ratio of UHPC is 0.18. Manipulation of this equation shows that the modulus of elasticity can be calculated based on the elastic slope of the load-deflection curve and a constant term representing the load configuration and beam cross-section.

$$\Delta_{cl} = \frac{Pa}{48EI}(3L^2 - 4a^2) + \frac{Pa}{2GA'} \quad (3.4.1.1-C)$$

The load-deflection responses presented previously were analyzed to determine the average elastic response between 20% and 50% of the load at first cracking. These

stiffness values, which are dependent on the test setup, were then used in conjunction with Equation 3.4.1.1-C to determine the effective modulus of elasticity. The effective modulus results tend to be higher than those based on the compression tests presented earlier in this chapter. The exception to this tendency is in the prisms where lower modulus values were observed with a span to depth ratio of 3.

The lower modulus value in the smaller span to depth ratio prisms is likely due to the effects of local disturbed regions near the load application points. With this short span and these close load points, nearly the entire prism could be considered to be locally disturbed, including deformations that could add to the flexure and shear deformations. Any additional deformation would result in a lower calculated effective modulus of elasticity.

Prism flexure testing of five different loading configurations for each curing regime was intended to identify the benefits and detriments of varying the prism span and cross-section. From a qualitative standpoint, the easiest completion was of the 9 in. and 12 in. span tests on the 2 in. x 2 in. cross-section. The behavior of the prisms in these loading configurations was observed to be more consistent than in other configurations. Also in these configurations, the moderate elastic load-displacement response decreased the difficulty encountered with the stiffer and more flexible configurations in the test setups. Quantitatively, the results from the 9 in., 12 in., and 15 in. spans for the 2 in. x 2 in. cross-section prisms were most consistent.

Also, it must be mentioned that the basic intent of the ASTM C1018 test seems to be to create a state of pure bending in a concrete prism to allow for quantification of the tensile properties. As the span to depth ratio of the beam decreases, the proportion of the behavior that is shear based increases. Figure 3.4.1.1-A shows the ratio of the shear to flexural deflection of a 2 in. deep prism. This prism was assumed to be loaded at its third-points, and it has a shear modulus equal to 61% of its elastic modulus based on a Poisson's ratio of 0.18. With a span to depth ratio of 3, the shear deflections are 17.1% of the flexural deflections, thus the assumption of flexural behavior is questionable. As the span increases toward 12 in., the assumption of flexural behavior becomes much more reasonable. In the longer spans, the state of stress on the cross-section in the constant moment region is primarily composed of stresses normal to the face of the cross-section. However, the same does not hold true for the shorter spans and the more influential shear forces.

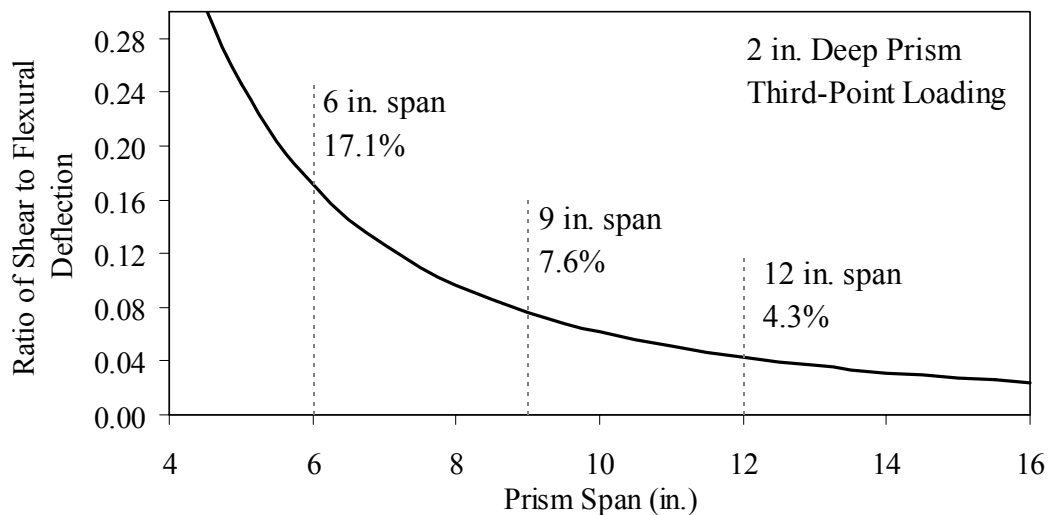


Figure 3.4.1.1-A: Ratio of shear to flexural deflection for a third-point loaded prism

Table 3.4.1.1-A: ASTM C1018 strength results

	Prism Cross-Section and Setup*	No.	First Crack Deflection (in.)	First Crack Strength [†] (ksi)	Corrected First Crack Strength [‡] (ksi)	Modulus of Elasticity [§] (ksi)	Peak Load Deflection (in.)	Peak Load Equivalent Strength [†] (ksi)
Steam	2x2, 6, 2	3	0.00172	2.70	1.50	7410	0.01979	4.68
	3x4, 12, 4	3	0.00325	2.54	1.58	8780	0.04154	3.85
	2x2, 9, 3	3	0.00273	2.57	1.43	8670	0.02997	4.60
	2x2, 12, 4	4	0.00460	2.42	1.34	8540	0.07315	5.14
	2x2, 15, 3	4	0.00614	2.31	1.28	8560	0.12498	5.21
Air	2x2, 6, 2	4	0.00153	2.35	1.30	6920	0.02093	4.27
	3x4, 12, 4	3	0.00362	2.26	1.41	7220	0.04265	4.08
	2x2, 9, 3	3	0.00290	2.31	1.28	7590	0.04284	4.40
	2x2, 12, 4	4	0.00527	2.31	1.28	7150	0.06014	4.33
	2x2, 15, 3	4	0.00760	2.43	1.35	7350	0.08726	4.39
Tempered Steam	2x2, 6, 2	4	0.00163	2.84	1.57	7830	0.01913	4.93
	3x4, 12, 4	3	0.00296	2.12	1.32	8180	0.03366	4.17
	2x2, 9, 3	4	0.00298	2.57	1.43	8050	0.03898	5.01
	2x2, 12, 4	4	0.00515	2.64	1.46	8160	0.04982	4.43
	2x2, 15, 3	2	0.00730	2.64	1.46	8130	0.07611	4.88
Delayed Steam	2x2, 6, 2	4	0.00157	2.50	1.39	8140	0.01914	4.64
	3x4, 12, 4	3	0.00420	2.57	1.60	8470	0.03615	4.58
	2x2, 9, 3	4	0.00270	2.34	1.30	8060	0.03068	4.45
	2x2, 12, 4	4	0.00544	2.45	1.36	8100	0.06774	4.98
	2x2, 15, 3	4	0.00659	2.33	1.29	8140	0.08818	4.73

* Prism depth x width, span length, distance between upper load points

† Calculated using Eqn 3.4.1.1-A, which assumes pure bending on a uniform, elastic, uncracked cross-section

‡ Calculated using Eqn 3.4.1.1-B

§ Calculated using Eqn 3.4.1.1-C, which allows for bending and shear on a uniform, elastic, uncracked cross-section

3.4.1.2 Toughness

Within concrete materials characterization testing, toughness is a term that provides some indication of the concrete's energy absorption capability. Usually, toughness is quantified in terms of the area under a load-deflection response curve. Toughness values are specific to the testing procedure implemented.

The ASTM C1018 test method presents one means of determining the toughness of fiber-reinforced concrete. The test results are analyzed in terms of the area under the load-deflection curve up to specific deflection levels. The toughness results are then normalized by dividing the total area under the curve up to the specified deflection by the area under the curve up to the deflection at first cracking.

ASTM C1018 defines a set of toughness indices in terms of the behavior that might be expected from a material that exhibits an elastic-plastic flexural load-deflection response. (Although not clearly stated in the test method, note that this reference response does not correspond to the response that would be observed for a material that exhibits elastic-plastic uniaxial stress-strain behavior.) Table 3.4.1.2-A is reproduced from the appendix of the test method. The table provides basic information relating to the calculation of toughness indices and the expected results from various materials. Additional indices can be created in a similar fashion. Results for I_{30} and I_{40} are also presented in the following discussion.

Table 3.4.1.2-A: Definition of Toughness Indices (From ASTM C1018 FIG. X1.1)

Index Designation	Deflection Criterion*	Values of Toughness Indices		
		Plain Concrete	Elastic-Plastic Material†	Observed Range for Fibrous Concrete
I ₅	3δ	1.0	5.0	1 to 6
I ₁₀	5.5δ	1.0	10.0	1 to 12
I ₂₀	10.5δ	1.0	20.0	1 to 25

* δ is the deflection at first cracking.

† This refers to a material that exhibits an elastic-plastic flexural response.

Table 3.4.1.2-B presents the toughness results for the sets of prismatic flexural tests. The information layout in the table is similar to Table 3.4.1.1-A. Note that some results are missing for I₄₀. In addition, some other results for I₄₀ are from fewer than the total number of prisms listed. This is due to some prisms exhibiting fiber pullout and subsequent failure prior to reaching 20.5 times the cracking deflection.

Residual strength factors are also presented in the table. These values are calculated by subtracting one toughness index from a subsequent index then multiplying the result by a normalizing factor related to the idealized elastic-plastic flexural response. Regardless of the toughness indices chosen, the residual strength factor for the idealized elastic-plastic flexural material will equal 100. For example, the residual strength factor, R_{10,20}, equals 10(I₂₀-I₁₀).

The toughness exhibited by the UHPC is quite impressive, regardless of the curing regime or test configuration. The results all tend to be at the upper end or above the ASTM C1018 predicted range for toughness of fiber-reinforced concrete. The UHPC also exhibits residual strength values that tend to increase at least through I₃₀, and these values

through this deflection level are all above the 100 reference level for elastic-plastic flexural behavior. The poorest results, although still quite good, are shown by the 3 in. by 4 in. prisms from each curing regime.

Table 3.4.1.2-B: ASTM C1018 toughness results

	Prism Cross-Section and Setup*	No.	First Crack Deflection (in.)	First Crack Strength [†] (ksi)	Toughness Index					Residual Strength Index			
					I ₅	I ₁₀	I ₂₀	I ₃₀	I ₄₀	R _{5,10}	R _{10,20}	R _{20,30}	R _{30,40}
Steam	2x2, 6, 2	3	0.00172	1.50	5.6	12.5	28.3	44.2	62.8	138	158	159	172
	3x4, 12, 4	3	0.00325	1.58	5.3	11.8	25.9	40.6	54.4	129	141	147	138
	2x2, 9, 3	3	0.00273	1.43	5.6	12.7	28.7	45.3	60.6	143	160	166	153
	2x2, 12, 4	4	0.00460	1.34	6.2	14.4	32.8	53.0	77.4	165	183	202	218
	2x2, 15, 3	4	0.00614	1.28	5.8	13.9	32.0	51.6	72.6	162	180	197	210
Air	2x2, 6, 2	4	0.00153	1.30	5.7	12.9	29.0	46.3	63.0	144	161	173	167
	3x4, 12, 4	3	0.00362	1.41	5.7	12.8	28.5	45.0	59.9	142	158	165	148
	2x2, 9, 3	3	0.00290	1.28	5.7	13.1	29.5	46.8	64.2	147	165	173	174
	2x2, 12, 4	4	0.00527	1.28	5.6	12.8	28.8	48.3	65.5	143	160	179	171
	2x2, 15, 3	4	0.00760	1.35	5.8	13.1	28.7	50.1	67.6	147	156	189	186
Tempered Steam	2x2, 6, 2	4	0.00163	1.57	5.8	12.9	28.2	44.2	65.5	141	153	160	176
	3x4, 12, 4	3	0.00296	1.32	6.1	14.1	31.9	53.7	73.0	161	178	134	128
	2x2, 9, 3	4	0.00298	1.43	6.0	13.8	31.1	50.8	69.6	155	173	194	188
	2x2, 12, 4	4	0.00515	1.46	5.8	13.0	28.0	43.1	–	144	150	151	–
	2x2, 15, 3	2	0.00730	1.46	6.1	13.9	31.1	47.6	–	156	172	165	–
Delayed Steam	2x2, 6, 2	4	0.00157	1.39	5.5	12.6	28.5	43.2	63.7	143	159	157	169
	3x4, 12, 4	3	0.00420	1.60	5.5	12.4	27.6	31.1	40.7	138	151	111	95
	2x2, 9, 3	4	0.00270	1.30	5.8	13.5	30.9	48.9	65.6	153	175	180	167
	2x2, 12, 4	4	0.00544	1.36	5.8	13.4	30.3	48.3	61.7	152	169	180	146
	2x2, 15, 3	4	0.00659	1.29	6.0	14.1	32.2	50.8	74.6	162	181	186	193

* Prism depth x width, span length, distance between upper load points

† Corrected tensile cracking strength based on Eqn. 3.4.1.1-B

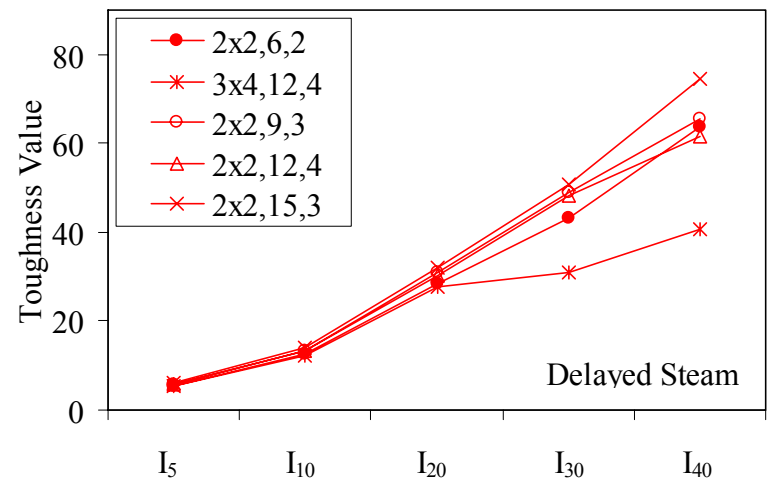
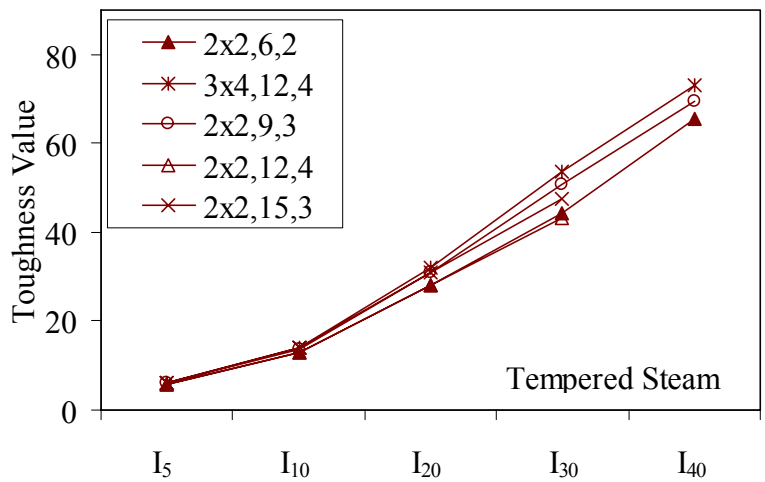
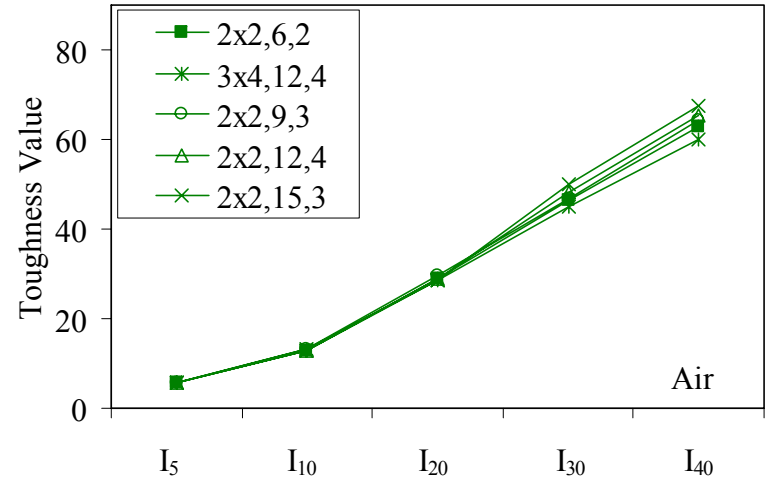
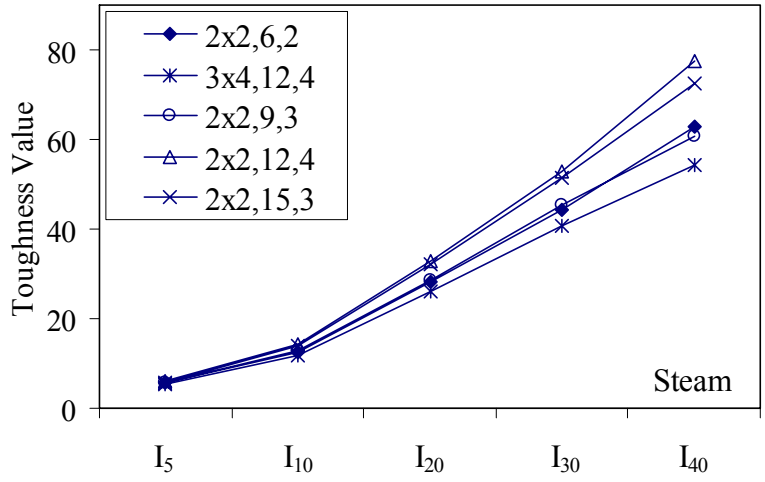


Figure 3.4.1.2-A: ASTM C1018 toughness results

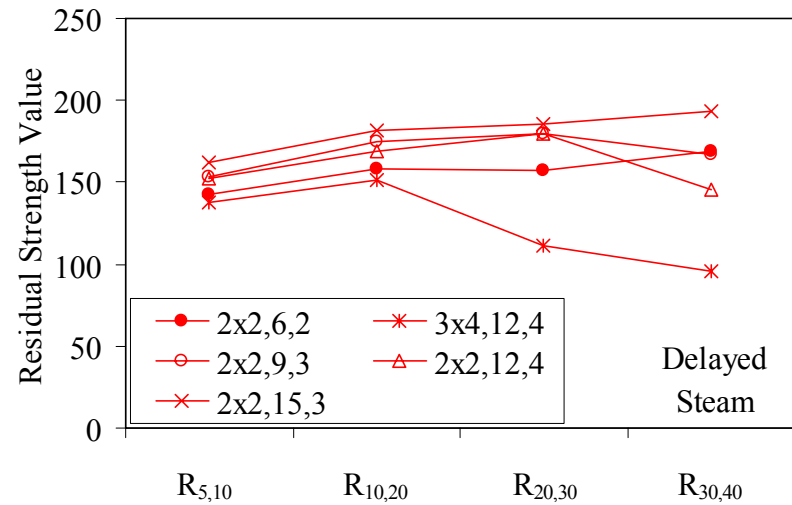
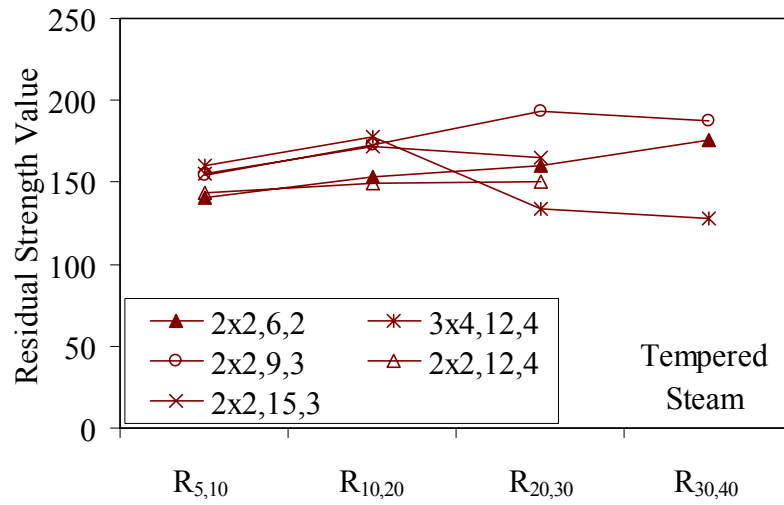
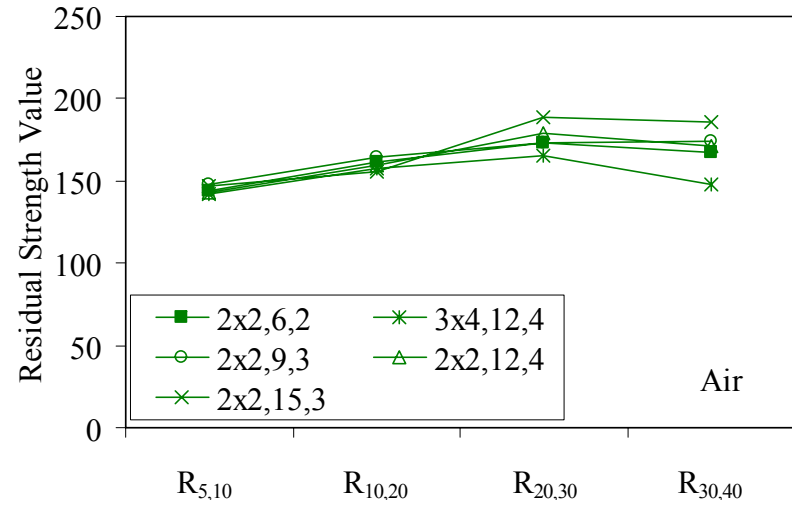
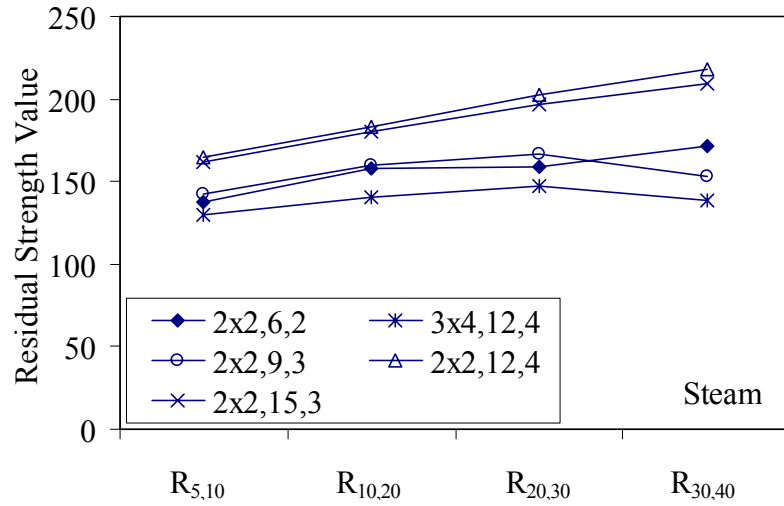


Figure 3.4.1.2-B: ASTM C1018 residual strength results

3.4.2 Split Cylinder

The tensile strength of UHPC was also measured through the ASTM C496 *Standard Test Method for Splitting Tensile Strength of Cylindrical Concrete Specimens*. This test, often referred to as the split cylinder test, indirectly measures the tensile strength of concrete by compressing a cylinder through a line load applied along its length. This test can be completed in a standard concrete compression testing machine, with only one special requirement: the hinged bearing that loads the specimen.

This load configuration creates a lateral tensile stress in the cylinder across the vertical plane of loading. A relatively uniform tensile stress field is created over the middle 75% of the cylinder's diameter along the plane of loading, and the maximum tensile stress occurs at the center of the cylinder. ASTM C496 indicates that the maximum tensile stress can be calculated based on Equation 3.4.2-A. In this equation, P is the load applied to the cylinder, l and d are the length and diameter, and f_{θ} is the tensile stress.

$$f_{\theta} = \frac{2P}{\pi ld} \quad (3.4.2-A)$$

The split cylinder test does not determine the uniaxial tensile cracking strength of concrete. The loading configuration used in this test actually creates a biaxial stress state inside the cylinder that has been described many times (Timoshenko and Goodier 1951, Petroski and Ojdrovic 1987). For the purposes of this report, it is sufficient to indicate that the vertical compressive stress in the center of the cylinder is approximately three times the lateral tensile stress.

This test is normally completed on standard concrete that does not contain fiber reinforcement. As such, the tensile strength results are normally clear. The cylinder will fail when its tensile strength is reached; therefore, the peak load carried by the cylinder can be used to determine the splitting tensile strength through Equation 3.4.2-A. Fiber reinforced concrete, and in particular UHPC, tends to behave differently. In these concretes, the initiation of cracking signifies the beginning of a new phase in the material's behavior, but does not signify failure of the material. With UHPC in particular, the load will continue to increase after cracking, and the cracks that form during cracking will be so small that identification without microscopic investigation may not be possible.

An additional feature was added to the ASTM 496 test because the cracking strength is the material property of interest. As the UHPC cylinder cracks, the measured length of the lateral diameter of the cylinder will show a marked increase. A lateral expansion measuring apparatus was devised and is shown in Figure 3.4.2-A. This spring-loaded device clamps across the cylinder and measures the lateral expansion of the cylinder from load initiation through failure. The small lateral compressive force exerted by the apparatus on the specimen (less than 2 psi) is considered negligible. Two LVDTs located near the front and back of the cylinder electronically capture the displacements, which are sent to a data acquisition system along with the load. This lateral expansion measuring apparatus is similar to a device used by Nanni in work that he completed on fiber reinforced concrete (1988).

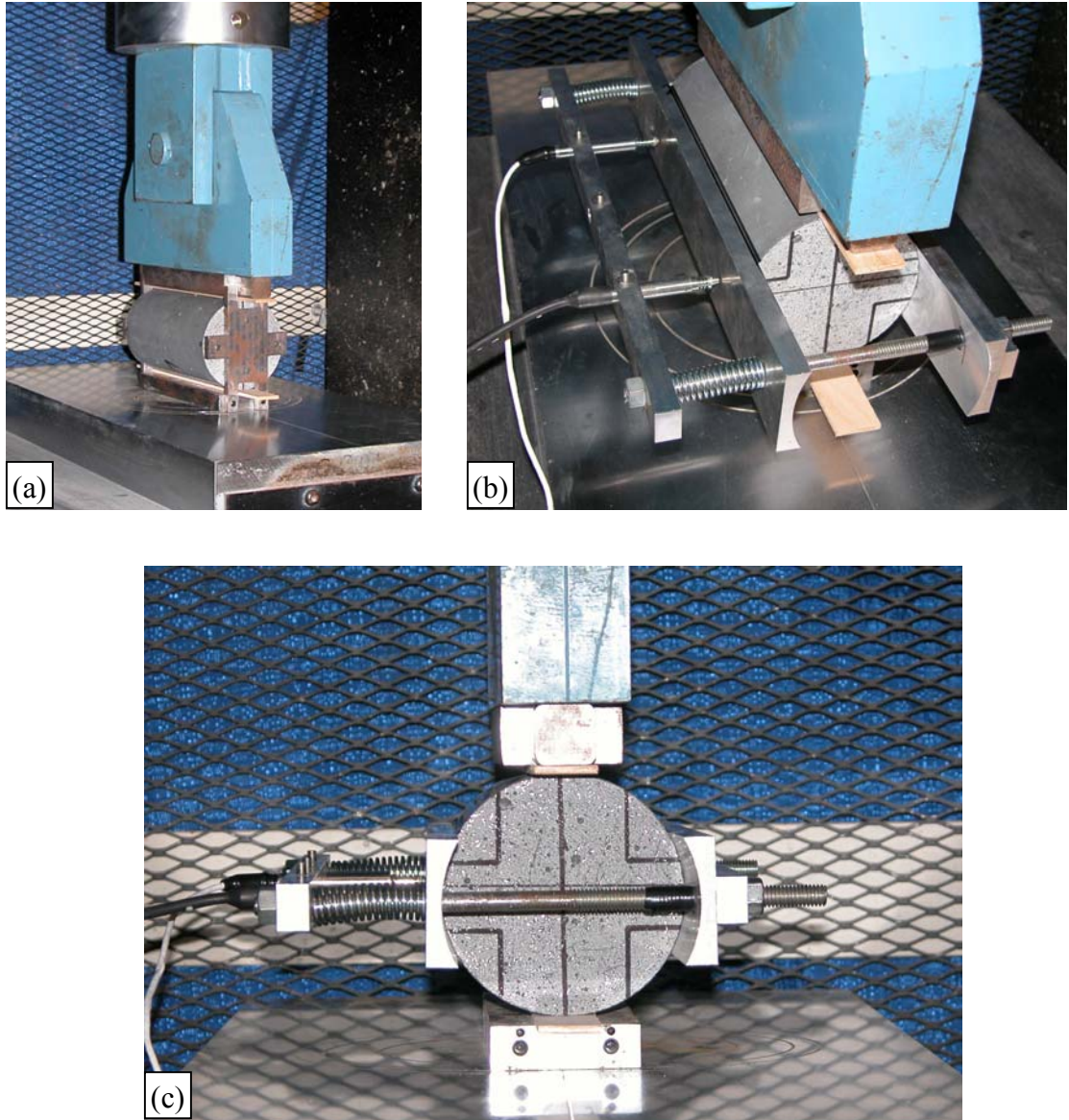


Figure 3.4.2-A: Split cylinder tensile test including (a) standard test setup, (b) lateral expansion measuring apparatus, and (c) UHPC cylinder during test

The typical load versus lateral displacement response for a UHPC cylinder is presented in Figure 3.4.2-B. The curve shown is the average of the results from the two LVDTs. The lateral deflection behavior is basically linear until the UHPC cracks. At cracking, a discontinuity occurs in the displacement response while the load level remains relatively

constant. The total jump in displacement is usually less than 0.001 in. and could be nonexistent in a specimen that has not undergone a steam-based treatment. After cracking, a clear change occurs in the slope of the response curve. The load then continues to increase at a decreasing rate until the peak load is reached.

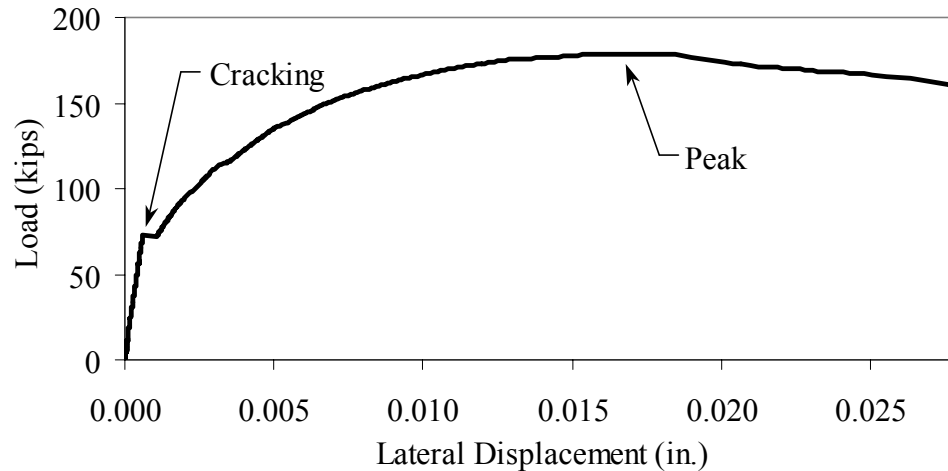


Figure 3.4.3-B: Typical response for a UHPC cylinder during the ASTM C496 test

Normal UHPC mix design and casting procedures were used for this series of tests.

Twelve 4 in. diameter cylinders were cast for each curing regime. The screeded end of the cylinder was ground prior to testing, and the length of each cylinder was approximately 7.9 in. The cylinders were tested in groups of four at three different ages for each curing regime. The Steam, Air, and Tempered Steam regimes were tested at 5, 14, and 28 days after casting. The Delayed Steam regime was tested at 14, 21, and 28 days after casting. Note that at 14 days, the Delayed Steam specimen results are more comparable to the Air treated specimens than to the other Delayed Steam treated specimens because the steam treatment did not occur until days 15 through 17.

The initial load rate for these tests was set at 500 psi/min of tensile stress according to Equation 3.4.2-A. The rate was set above the ASTM specified rate of 100 to 200 psi/min because of three reasons: (1) the higher tensile cracking strength of the UHPC, (2) the significant displacement that must be traversed before the peak load is reached, and (3) the reluctance to change the load rate after test initiation. Preliminary testing on UHPC prior to the initiation of these tests indicated that this increased load rate should not cause significant changes in material behaviors.

Figure 3.4.2-C presents the average tensile cracking results from the split cylinder tests. As previously mentioned, cracking is defined to occur when an abrupt or semi-abrupt change in specimen lateral stiffness occurs. The number of days after casting is indicated in parentheses after the curing regime's name. The figure shows both the average stress and the plus/minus one standard deviation from the average.

All of the groups that underwent a steam-based curing regime exhibited a split cylinder tensile cracking strength of between 1.6 ksi and 1.8 ksi. The Air treated group exhibited decidedly lower strength values, along with a clear increase in strength over time. At 5 days, the Air treated group had a tensile cracking strength of 1.0 ksi and by 28 days this strength had increased to over 1.3 ksi.

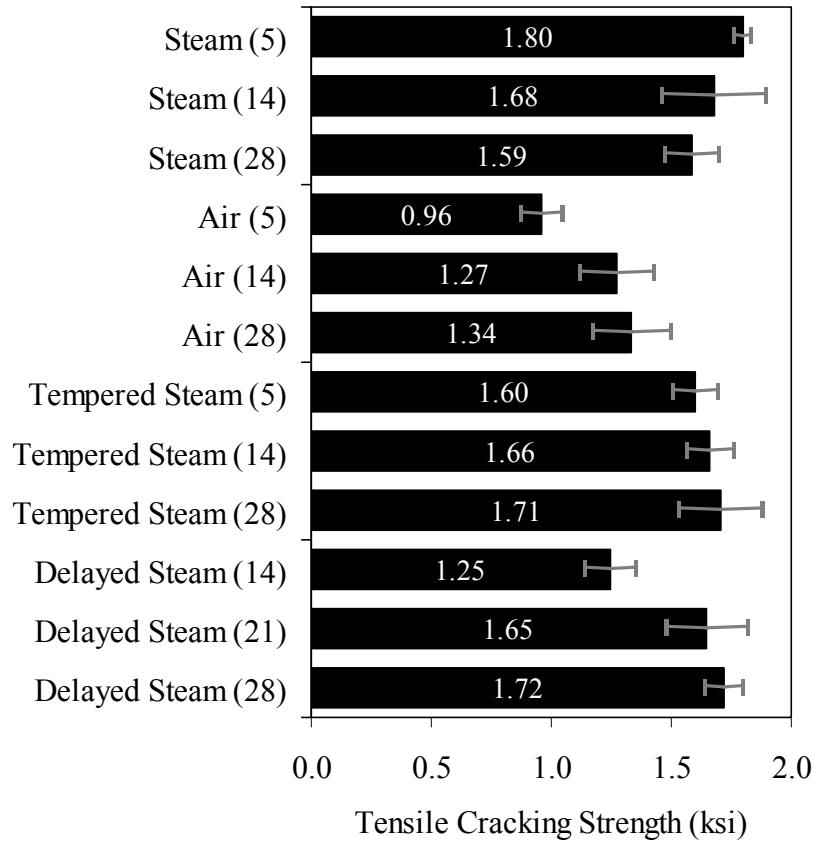


Figure 3.4.3-C: Average tensile cracking results from the ASTM C496 test

The split cylinder loading configuration causes vertical compressive stress and lateral tensile stress in the cylinder. This biaxial stress state has a definite effect on the post-cracking behavior. The vertical compressive stresses that are parallel to any cracks cause the fiber reinforcement bridging the cracks to carry higher loads prior to pulling out of the UHPC matrix. For this reason, results derived from the peak load carried by a cylinder and passed through Equation 3.4.2-A are not accurate general representations of the tensile strength of UHPC.

However, these peak load results may be useful for comparing fiber pullout behavior following different curing treatments. These variations in peak load results may be useful in determining whether curing was properly applied to a UHPC specimen. The average peak stress carried by these groups of specimens is presented in Figure 3.4.2-D. This stress is calculated based on both the peak load reached and Equation 3.4.2-A. The results show that fibers in Air treated cylinders pull out earlier under this stress state, and the cylinder as a whole can only carry an equivalent stress of around 2.8 ksi. The steam treatment in the Tempered Steam regime enhances the behavior such that 3.1 ksi of equivalent stress can be carried. The Steam and Delayed Steam regimes carried the largest peak loads with average equivalent stresses of around 3.5 ksi.

Frequently, the tensile strength of concrete is discussed as a percentage of the compressive strength. The results from the split cylinder tests have been normalized by the 28 day compressive strength of their control cylinders and are presented in Table 3.4.2-A. Only the post-curing treatment results are presented because only the 28 day compressive strengths are known for these particular batches of UHPC. The cracking stress tends to be between 5% and 7% of the compressive strength. The equivalent peak stress carried by the cylinders is higher, with values ranging from 12% to 16%.

The cracking behavior must be monitored for the ASTM C496 test to provide useful results in terms of tensile cracking strength. The lateral expansion measuring apparatus (described above) allowed for quantification of this cracking behavior. Monitoring of the cracking behavior may also be possible in certain instances via audible observations.

Table 3.4.2-B presents the first crack parameters for each group of specimens. Aural monitoring throughout the test allowed the load at first cracking to be estimated in nearly all of the cylinders that had undergone a steam-based curing treatment. As discussed previously, the data collection during the test allowed for a specific determination of the load at first crack. The size of the first crack was also estimated based on the instantaneous lateral expansion of the cylinder at first cracking. The values presented in the table are the crack size (measured by the front or back LVDT, whichever displayed a larger instantaneous increase). These results provide a clear sense of the width of UHPC tensile stress cracks when they first occur as well as the type of instrumentation that is required to monitor or capture this behavior.

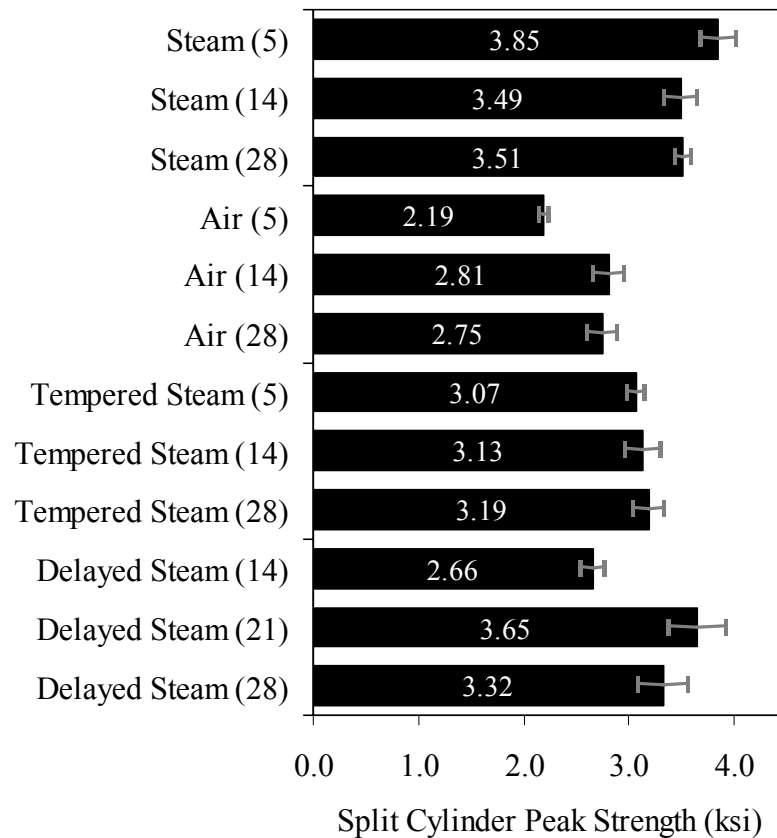


Figure 3.4.2-D: Average split cylinder peak strength from the ASTM C496 test

Table 3.4.2-A: Split tensile strength normalized by 28 day compressive strength

Group	28 day Compression Strength (ksi)	Normalized by 28 day Compressive Strength	
		ASTM C496 Cracking Stress	ASTM C496 Peak Stress
Steam (5)	26.3	0.051	0.148
Steam (14)	26.3	0.064	0.132
Steam (28)	26.3	0.060	0.134
Air (28)	17.5	0.076	0.161
Tempered Steam (5)	24.4	0.066	0.125
Tempered Steam (14)	24.4	0.068	0.127
Tempered Steam (28)	24.4	0.070	0.133
Delayed Steam (21)	24.6	0.067	0.147
Delayed Steam (28)	24.6	0.070	0.133

Table 3.4.2-B: First crack parameters determined by instantaneous lateral expansion of cylinder and aural observations

Group	Sound (Audible/Inaudible)	First Crack Size (in.)		
		Average	Minimum	Maximum
Steam (5)	Audible	0.00083	0.00067	0.00098
Steam (14)	Audible	0.00087	0.00050	0.00114
Steam (28)	Audible	0.00093	0.00062	0.00154
Air (5)	Inaudible	0.00031	0.00015	0.00048
Air (14)	Inaudible	0.00036	0.00000	0.00085
Air (28)	Inaudible	0.00071	0.00028	0.00109
Tempered Steam (5)	Audible	0.00081	0.00064	0.00101
Tempered Steam (14)	Audible	0.00070	0.00033	0.00146
Tempered Steam (28)	Audible	0.00076	0.00059	0.00110
Delayed Steam (14)	Inaudible	0.00058	0.00026	0.00085
Delayed Steam (21)	Audible	0.00071	0.00034	0.00093
Delayed Steam (28)	Audible	0.00033	0.00003	0.00073

3.4.3 Mortar Briquette

Another means of concrete tensile strength determination is the briquette tension test.

This test method, described in AASHTO T132, normally involves the direct tension testing of a small briquette cast from cement mortar. The dogbone-shaped briquette is 3 in. long, 1 in. thick, and has a 1 in.² cross-section at midlength. Special self-aligning grips allow for passive gripping of the specimen in the test machine and ensure uniform loading.

The standard UHPC mix was used, including the steel fibers, in this test program. The casting of the briquettes is assumed to have caused some preferential alignment of the fibers because the minimum cross-section of the briquette is only 1 in.². This preferential alignment would be expected to be parallel to the walls of the mold; therefore, the fiber percentage aligned across the anticipated failure plane would be higher than normal.

The normal UHPC mix design and casting procedures were used. Eighteen briquettes were cast for each of the four curing regimes: three sets of six briquettes that were tested at 28, 56, and 84 days after casting. Figure 3.4.3-A shows both the grips that were used to test the briquettes as well as a briquette in the grips.

The testing was completed in a 22 kip capacity MTS testing machine. The tests were controlled based on the displacement of the crosshead of the testing machine to enable the observation of the post-peak load-displacement response. AASHTO T132 recommends loading the briquettes at 600 lb/min. This portion of the test method was

modified, and the tests were conducted at a displacement rate of 0.001 in./sec. Given the stiffness of the load carrying apparatus between the crossheads, this displacement rate equates to approximately 900 lb/min throughout the initial elastic loading portion of each briquette's response.

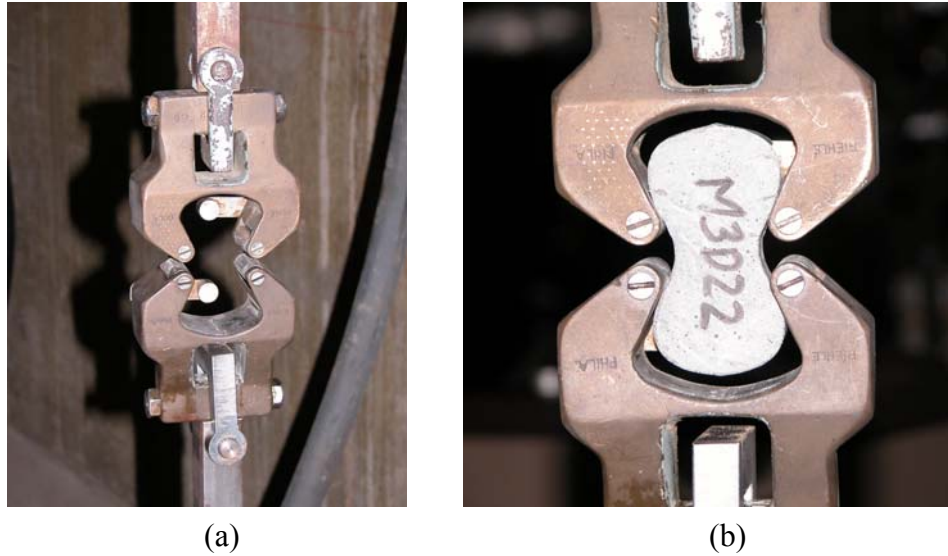


Figure 3.4.3-A: AASHTO T132 setup including (a) test grips and (b) specimen

Figure 3.4.3-B through 3.4.3-E present the results from the eighteen tests for each curing regime. Six replicates are included in each plot, with the results shifted by 0.05 in. to allow for clarity. The curing regime and age (in days) at testing are included in the upper right corner of each plot. These results show that the UHPC behaved linear-elastically up to first cracking. After cracking, a slight decrease in load usually occurred followed by a load increase to a level near or above the cracking load. All of the results show a significant amount of post-cracking load carrying capacity. A more detailed discussion of

these test results that focuses on strength and toughness is included in the following two sections.

Similar to all batches of UHPC cast for this research program, compression tests on 3-in. diameter control cylinders were completed. The results from the control cylinders for the four batches associated with the briquette testing indicate that three of these batches exhibited strengths below the average values. The Steam treated and Air treated batches showed compressive strengths 15% below the overall test program average, and the Delayed Steam treated batch was 8% below the average. These results should be kept in mind as the results in the remainder of this section are discussed.

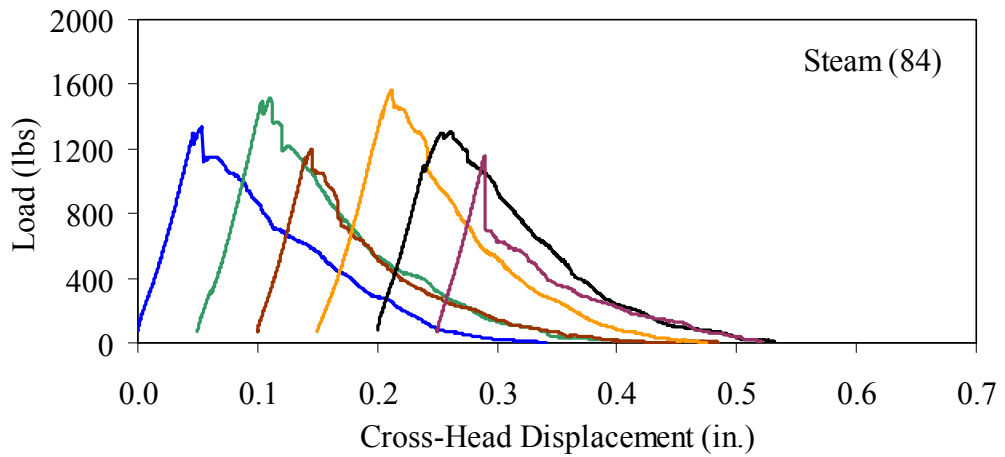
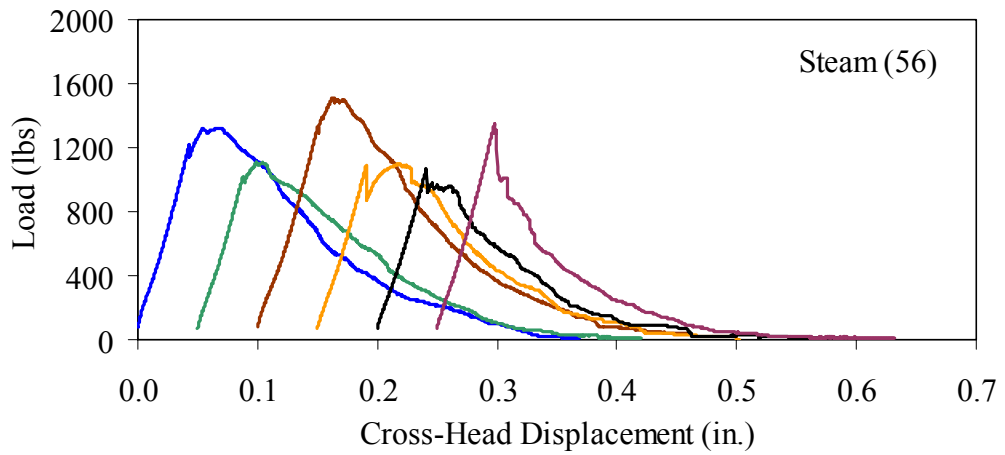
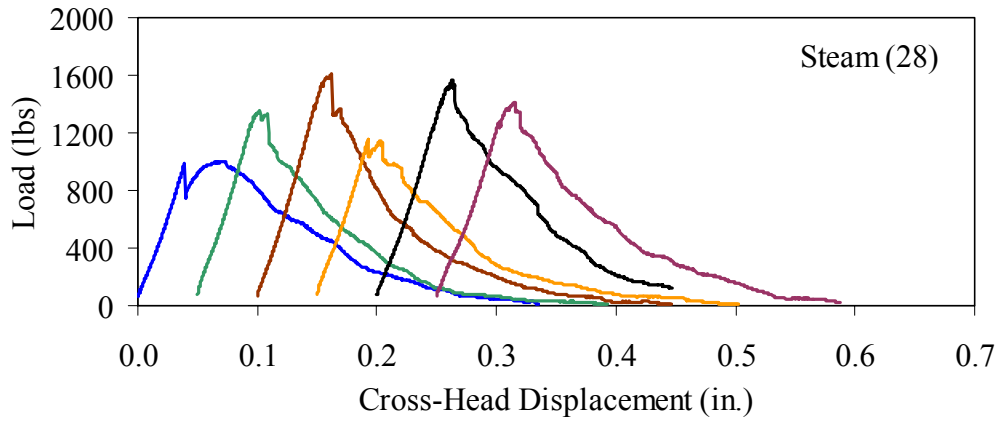


Figure 3.4.3-B: Load-displacement response for Steam treated briquette tests

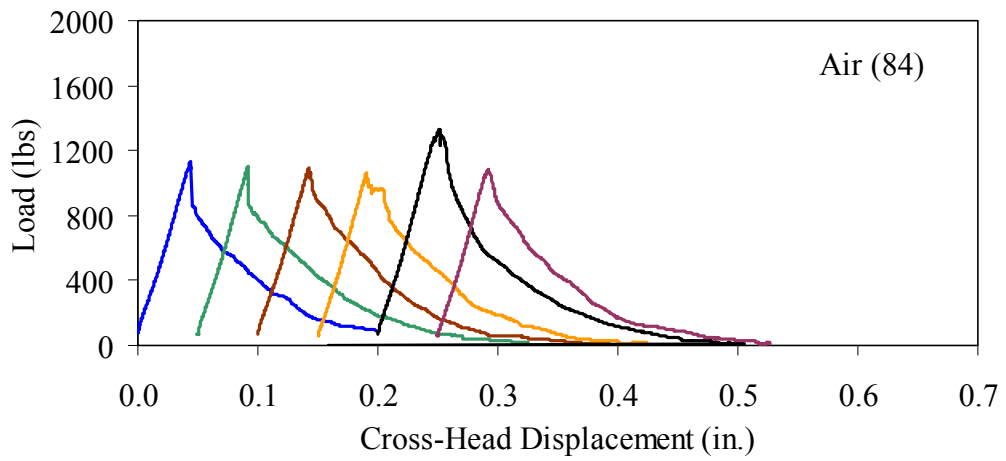
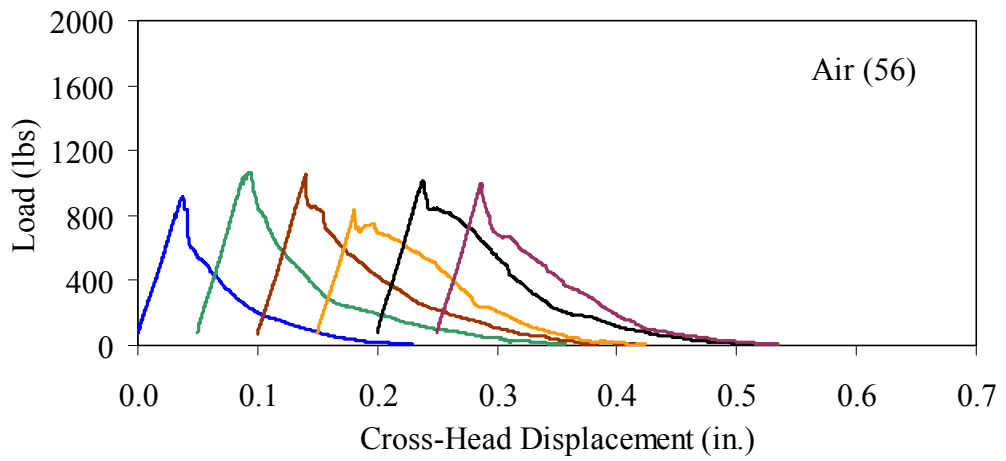
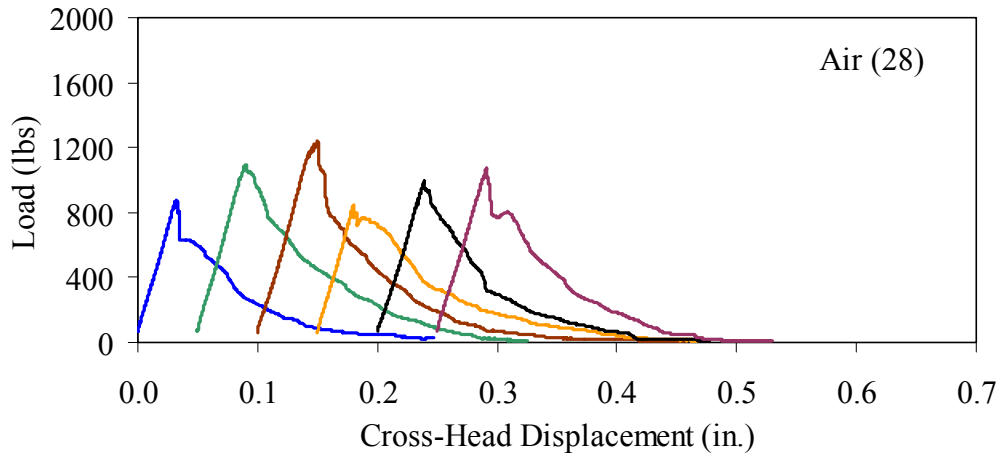


Figure 3.4.3-C: Load-displacement response for Air treated briquette tests

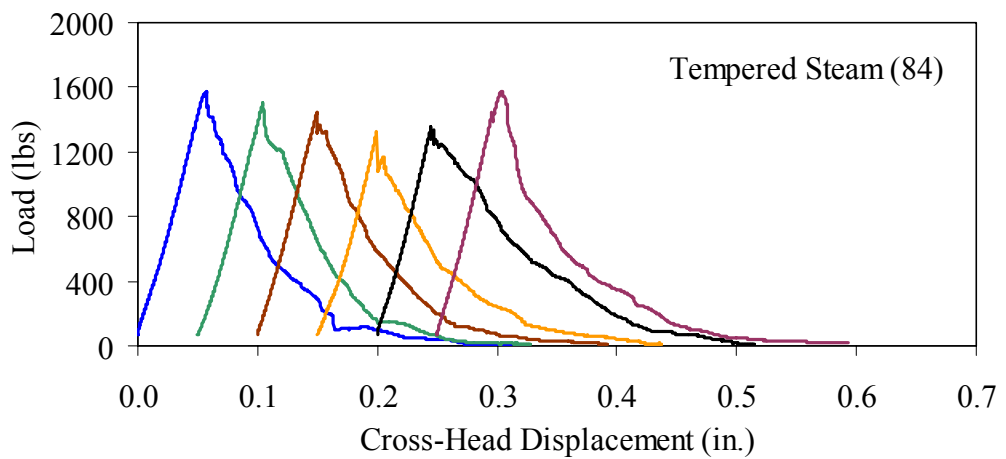
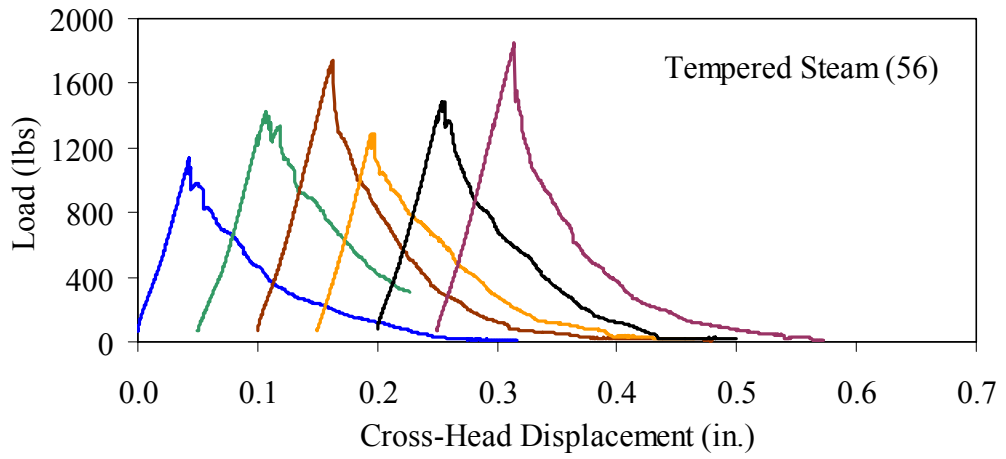
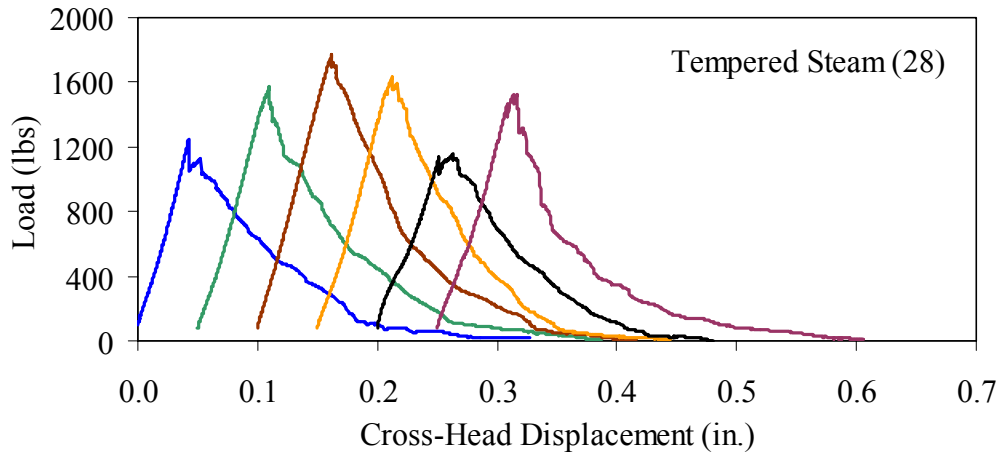


Figure 3.4.3-D: Load-displacement response for Tempered Steam treated briquette tests

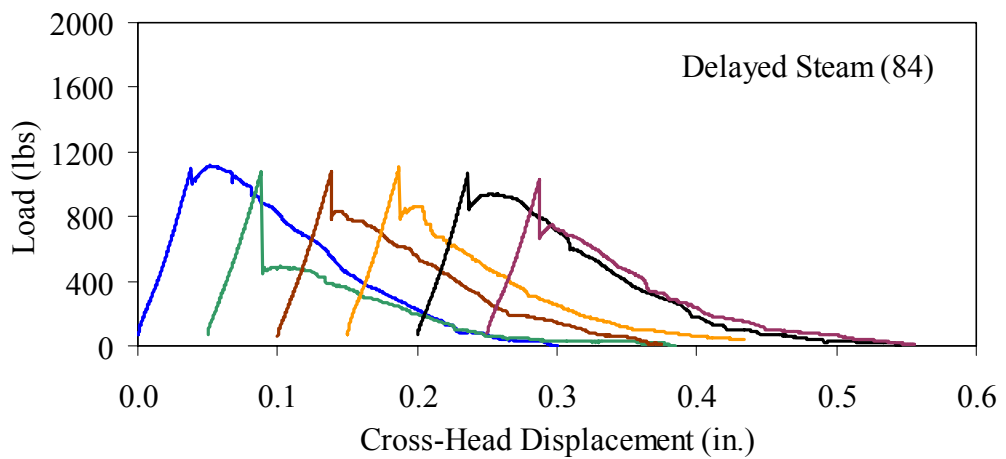
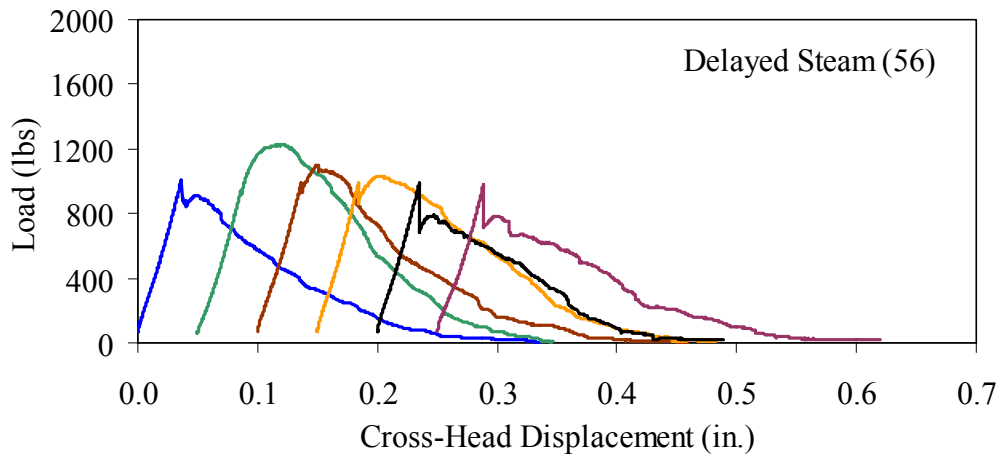
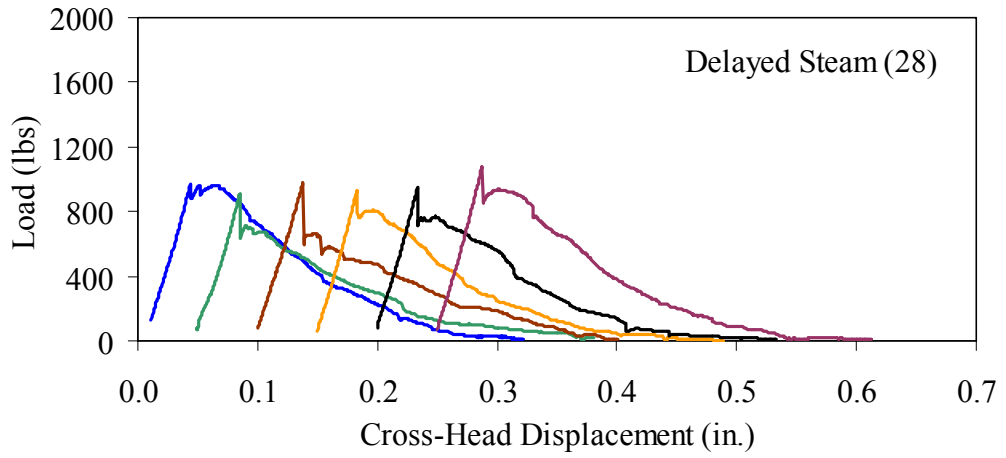


Figure 3.4.3-E: Load-displacement response for Delayed Steam treated briquette tests

3.4.3.1 Strength

The tensile cracking strength results are presented in Figure 3.4.3.1-A. First cracking was defined as a discontinuity in the load-displacement curve caused by an instantaneous decrease in load. The results from the six replicates in each group have been averaged, and the average value is shown on the bar in the chart. The standard deviation within the results for each group is provided by the error bar, which indicates a plus or minus one standard deviation.

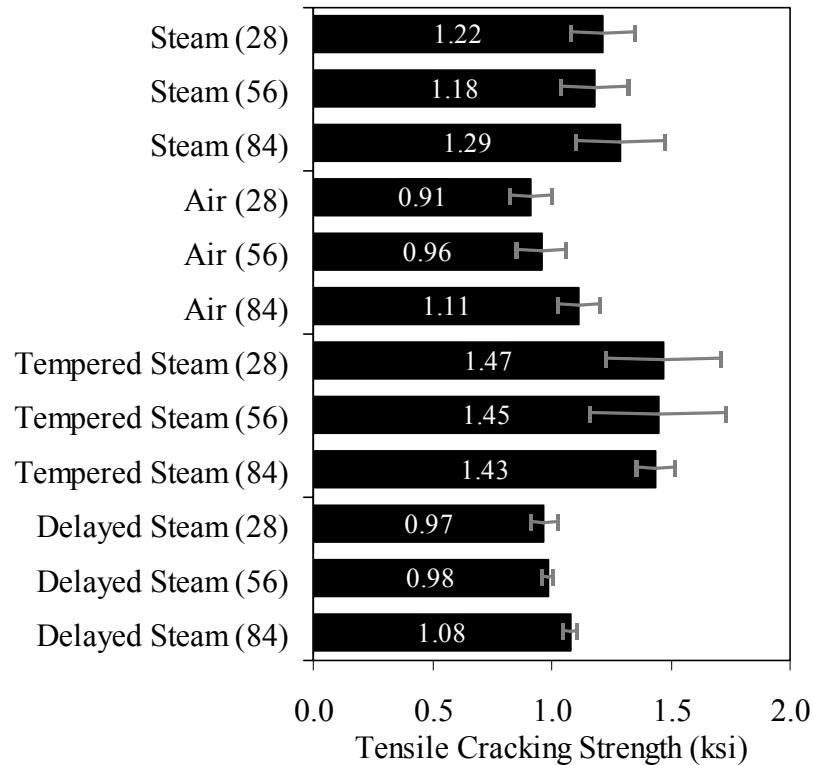


Figure 3.4.3.1-A: Tensile cracking strength of UHPC briquettes

The UHPC that underwent the steam-based curing treatment showed consistent strength levels from 1 to 3 months after casting. The Steam treated UHPC tensile cracking strength is approximately 1.2 ksi while the Tempered Steam treated UHPC is 1.4 ksi. The

Delayed Steam treated UHPC shows a lower value of around 1.0 ksi. The Air treated UHPC shows a steady increase in strength between the first and third months, with the cracking tensile strength increasing 20% to 1.1 ksi by 3 months. Again, recall that the compressive strength results for three of these curing regimes were lower than anticipated, thus the tensile strength results were likely affected as well.

The post-cracking strength results are presented in Figure 3.4.3.1-B, which has the same format as Figure 3.4.3.1-A. The post-cracking peak strength was defined as the highest load level reached after the tensile cracking load decreased. These results show significantly more scatter than the tensile cracking results. Of most importance, these results show that the post-cracking load-carrying capacity is very similar to the pre-cracking capacity. The fiber-reinforced nature of the UHPC matrix allows the fibers bridging a crack to carry a similar load level after cracking as the cement-based matrix did prior to cracking.

3.4.3.2 Toughness

The toughness exhibited by UHPC after cracking is of utmost importance if the UHPC will carry tensile forces after cracking. The UHPC needs to maintain load carrying capacity as multiple cracking occurs and as individual cracks widen. As discussed in Section 3.4.3.1, one means of measuring toughness is to calculate the area under the load-displacement curve. Frequently, the area under the curve after cracking is compared with the pre-cracking area. Using this means of comparison, normal concrete would have a toughness of nearly zero with no post-cracking load carrying capacity. On the other hand,

an elastic-plastic material such as mild steel would exhibit a high post-yield toughness result.

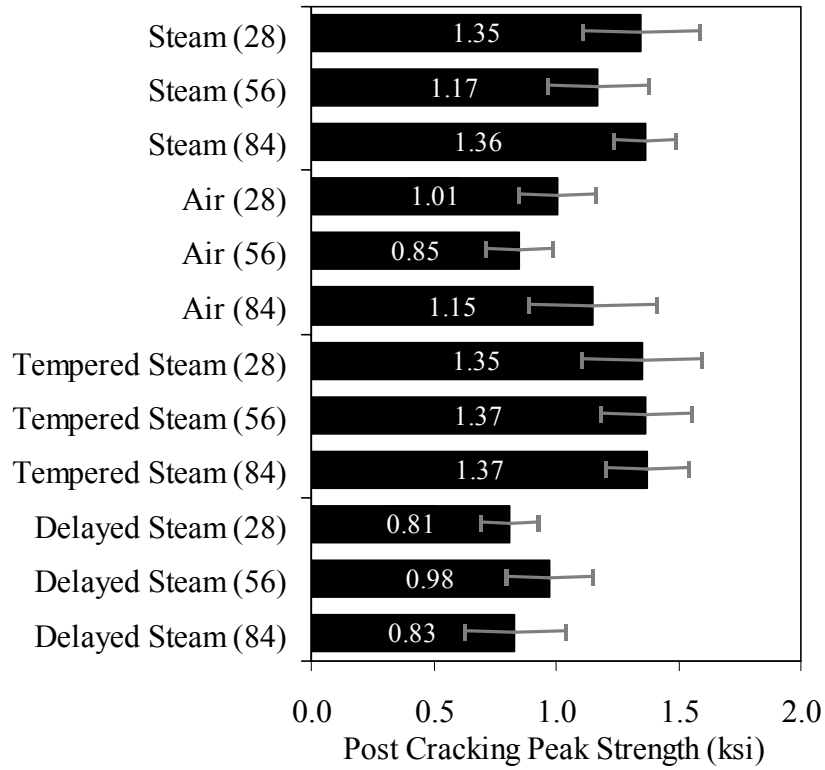


Figure 3.4.3.1-B: Post-cracking peak strength of UHPC briquettes

To compare toughness results from one test program to another, the means of measuring the displacement must accurately measure the actual displacement of the concrete in question. Given the nature of the AASHTO T132 test, measuring only the displacement of the UHPC briquette is not possible. Thus, the results presented here include the overall displacement of the loading system. A quantitative comparison of the areas contained under the load-displacement curves from this test program to other test programs is not

possible. However, a quantitative comparison within this test program and qualitative external comparisons are definitely warranted.

Figure 3.4.3.2-A presents the average calculated areas under the load-displacement curves after cracking for the twelve groups of briquettes tested. The area calculation includes the entire area under the curve from cracking until the load level dropped to 200 lbs, which is equivalent to a stress of 200 psi on the original minimum cross-section. These results show a much larger scatter, but the average results are relatively consistent within each curing regime. The larger area results in the Steam treated regime as compared with the Tempered Steam treated regime are quite instructive. Recall that the Tempered Steam briquettes in Figure 3.4.3-D show higher tensile strengths but that the shape of the post-cracking portion of the curve exhibits a more rapid decrease in load capacity. The Steam treated regime clearly exhibits the best post-cracking behavior, with almost twice the area as compared with the Air treated briquettes. The Tempered Steam and Delayed Steam treated regimes both show approximately 75% of the post-crack area as compared with the Steam treated regime.

For completeness, Figure 3.4.3.2-B presents the results for the ratio of the post-cracking area to the pre-cracking area under the load-deflection curve. As previously mentioned, this ratio is the standard means of measuring the toughness of a semi-brittle material like fiber reinforced concrete. The area under the curve before cracking is based on the linear elastic portion of the load-displacement response, thus eliminating the seating behaviors that occur early in each test. These results seem to indicate that the Tempered Steam

briquettes displayed the poorest toughness results while the Delayed Steam and Steam treated briquettes had the best results. However, these results are an artifact of the higher cracking strength exhibited by the Tempered Steam briquettes and not by their low post-cracking toughness.

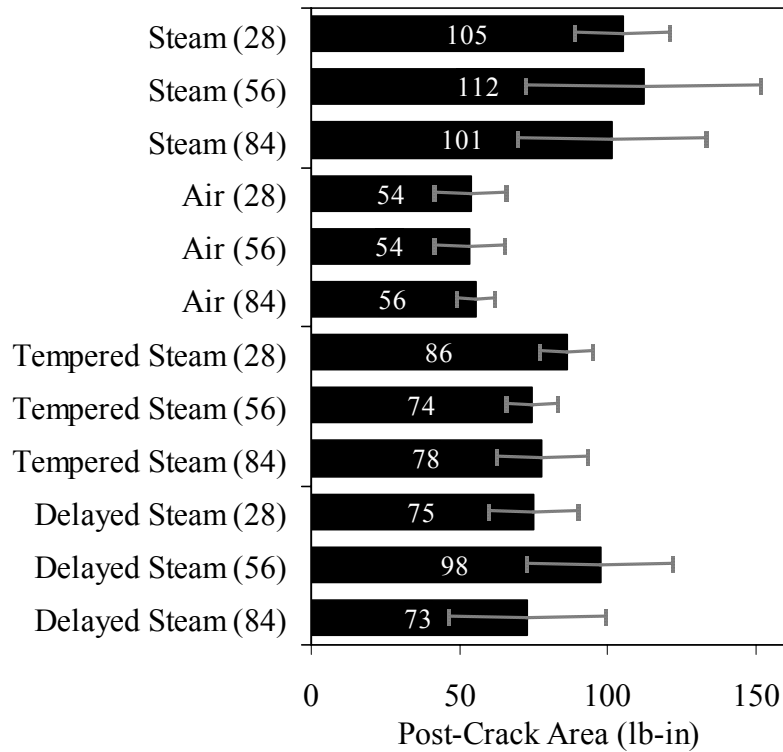


Figure 3.4.3.2-A: Area under the load-displacement response curve after cracking

The post-cracking behavior of UHPC is primarily dependent on the steel fibers and their attachment to the UHPC matrix. Clearly, a reduction in the number of fibers in the UHPC mix must eventually lead to a decrease in the sustained tensile load capacity after cracking. The curing treatment applied to the UHPC could likely have affected the bond between the fibers and the matrix.

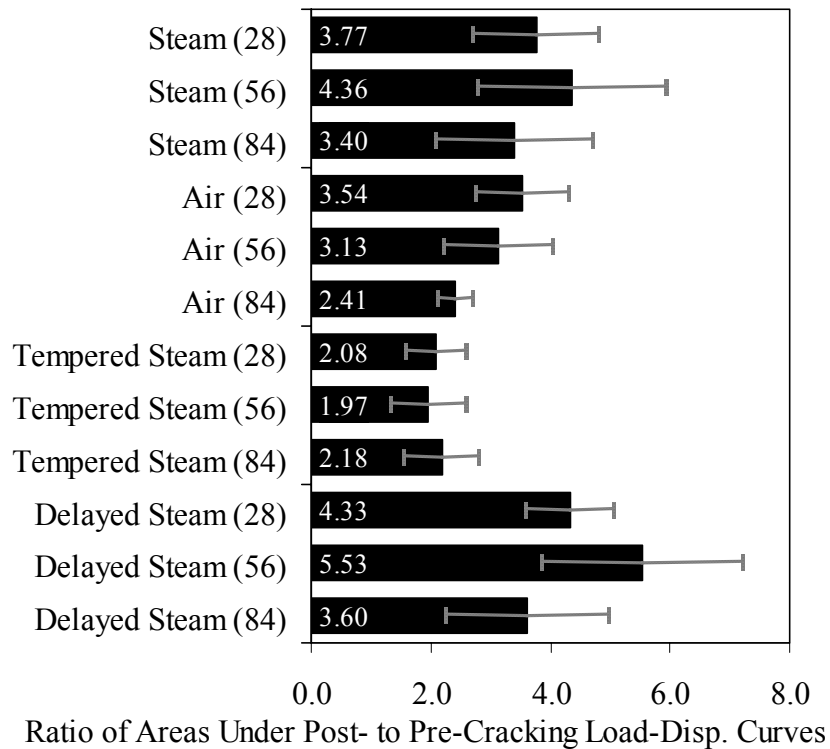


Figure 3.4.3.2-B: Ratio of post-cracking to pre-cracking areas under the load-displacement curve

Considering these two points, the failed specimens from the briquette tension tests were evaluated. A significant portion of the briquettes in 9 of the 12 briquette test groups were studied to determine the number of fibers that intersected the failure plane. The fibers extending from each of the failure surfaces in each briquette were counted. The totals are shown in Table 3.4.3.2-A. These results are then compared with the post-crack area under the load-displacement curve to determine what portion of the area could be attributed to each fiber. Obviously, this calculation glosses over many qualifying factors that would cause different fibers to carry different loads (i.e., fiber orientation relative to crack,

fibers extension on either side of crack). However, this calculation is instructive in providing some results related to the effect of curing and fiber percentages.

Aside from the Delayed Steam regime, these results indicate that the curing treatment seems to affect the ability of fibers to bond to the UHPC matrix. All of these groups contained similar numbers of fibers crossing the failure plane, but show three distinct levels of post-crack area per fiber. The Steam treated regime exhibits over twice the toughness as the Air treated regime on a per fiber basis. Additionally, the Delayed Steam treatment results show that these briquettes had distinctly fewer fibers crossing the failure plane. Although this result probably could not explain the lower pre-cracking tensile strength of these specimens, it definitely could explain the lower than expected post-cracking peak strength.

Table 3.4.3.2-A: Fiber influence on post-cracking behavior

Group	No. Samples	Fibers Crossing Failure Plane		Post-Crack Area per Fiber (lb-in/fiber)	
		Average	Standard Deviation	Average	Standard Deviation
Steam (56)	6	337	47	0.34	0.13
Steam (84)	5	276	46	0.35	0.10
Air (28)	5	370	45	0.15	0.03
Air (56)	6	356	42	0.15	0.04
Air (84)	6	329	77	0.17	0.03
Tempered Steam (56)	3	384	30	0.21	0.03
Tempered Steam (84)	6	321	35	0.25	0.08
Delayed Steam (56)	6	179	63	0.57	0.16
Delayed Steam (84)	6	149	19	0.48	0.12

3.4.4 Direct Tension

The fourth tension test used to quantify the material behaviors of UHPC was a direct tension test. Unlike the flexural or split cylinder tests, a direct tension test applies a uniaxial tensile stress onto the concrete and monitors tensile behaviors as tensile strains are increased. In this test program, 4-in. diameter concrete cylinders were subjected to a uniaxial tensile load applied through the flat end surfaces of each cylinder.

Direct tension tests are rarely performed on concrete due to the difficulties inherent in this test method. Among other things, direct tension tests generally require complicated test setups because of the tensile gripping of the concrete and the custom equipment required for the loading and data collection. However, many researchers have investigated this topic and have attempted to develop reliable and repeatable means of testing the tensile stress-strain properties of concrete (Boulay and Colson 1981, Boulay et al. 2004, V. Li 1997, V. Li et al. 1996, Z. Li et al. 1993, Z. Li et al. 1998, Lim et al. 1997, Morris and Garrett 1981, Phillips and Zhang 1993, RILEM TC 162-TDF 2001, Rossi 1997, Saito and Imai 1983, USBR 4914-92, Wang et al. 1990, J. Zhang et al. 2000, Zheng et al. 2001). The direct tension test setup and procedures used in this research program are an agglomeration of these testing techniques and rely most heavily on USBR 4914 *Procedure for Direct Tensile Strength, Static Modulus of Elasticity, and Poisson's Ratio of Cylindrical Concrete Specimens in Tension* and RILEM TC 162-TDF *Uniaxial Tension Test for Steel Fibre Reinforced Concrete*.

Concrete cylinders that had a 4-in. diameter and an 8-in. length were cast for the direct tension tests. These cylinders were cast following the normal casting and curing procedures detailed in Section 3.2. Six cylinders were prepared for each curing regime. Note that no special attention was given toward achieving the proper distribution and orientation of the fiber reinforcement within the cylinder, thus it is expected that the fibers were not necessarily randomly distributed and oriented within the cylinder. This topic will be discussed in further detail later in this section. The direct tension tests were completed between 2 and 4 months after casting. Finally, these cylinders were cast from the same four batches of UHPC as the mortar briquettes discussed in Section 3.4.3. To reiterate the discussion presented in this section, three of these four batches of cylinders exhibited somewhat low compressive strengths, which indicates that the tensile behaviors could be diminished as well.

Two loading configurations were used in this test program, each for half of the cylinders from each curing regime. In the first configuration, the cylinders were tested as cast. In the second configuration, the cylinders were circumferentially notched to create a plane of reduced cross-sectional area and thus higher stresses per applied load. The notch was created by milling a parabolic-shaped groove into the surface of the cylinder. This groove was 0.25 in. deep, thus resulting in a reduced cylinder diameter of 3.5 in. The total height of the groove was 0.5 in. Figure 3.4.4-A(a) shows a notched cylinder while Figure 3.4.4-A(b) shows an unnotched cylinder ready for testing.

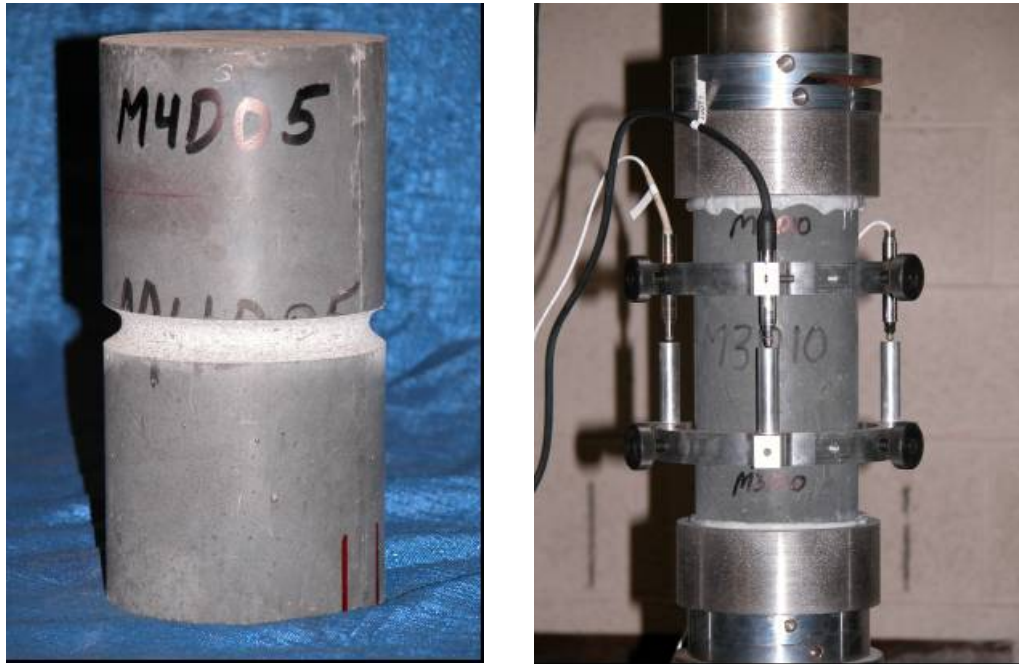


Figure 3.4.4-A: (a) Notched cylinder and (b) testing of an unnotched cylinder

These tests were completed in a 100-kip capacity MTS testing machine. The axial displacement rate of a portion of the cylinder was used as the control signal. This displacement rate was captured through three LVDTs mounted on a testing apparatus similar to the one that was discussed in Section 3.3.2 and shown in Figure 3.4.4-A(b). The signal from these LVDTs was electronically averaged and then was sent to the MTS controller. The unnotched cylinders used a 4 in. gage length centered on the specimen, and the notched cylinders used a 1.5 in. gage length centered over the notch. All cylinders were tested with a displacement rate of approximately 0.0002 in./min., which is the rate recommended in the RILEM test procedure.

Prior to testing, the cylinders had their ends ground and checked for planeness. The testing machine heads and the ends of the specimen were then lightly sandblasted. A high-strength, high-modulus, rapid setting epoxy was then applied to the testing machine heads as the cylinder was placed in the machine. A compressive load of approximately 5000 lbs. was then applied to the specimen until the epoxy had cured. Note that the epoxy required at least 8 hours of cure time; thus, testing was completed on a daily cycle.

The test setup and procedures discussed above were implemented in order to capture the full tensile stress-strain behavior of UHPC. Unfortunately, no behaviors after initial tensile cracking could be reliably observed and monitored. The MTS controller temporarily lost control of the cylinder during the brittle initiation of the first tensile crack. When control was regained, the cylinder had undergone some tensile fiber pullout across the crack, and the critical portion of the UHPC tensile behavior just after tensile cracking had been bypassed. This uncontrolled behavior was probably caused by a lack of sensitivity of the MTS control system due to its larger than necessary load capacity. However, accurate post-cracking results could probably not have been obtained anyway, because failure surfaces have indicated that the fiber distribution and orientation within the cylinders was not sufficiently random.

For these reasons, the test results presented in this section focus only on the tensile cracking strength and on the modulus of elasticity of the UHPC. Table 3.4.4-A provides the results from the six cylinders in each curing regime. The table indicates which specimens were notched, the location of the first tensile crack, the tensile cracking

strength, and the modulus of elasticity. The modulus of elasticity was determined based on the displacement readings across the 4 in. gage length between the applied stresses of 360 psi compressive and 360 psi tensile. Recall that the cylinders were initially compressed as the epoxy cured; thus, continuous data were recorded during the test over this transition from compressive to tensile behavior.

The table indicates that eleven of the twelve notched specimens failed within the notch. Aside from possible local stress concentrations caused by the notch, it is anticipated that these results accurately represent the tensile cracking strength of the UHPC. For the purposes of this research, local stress concentration effects are ignored, and these tensile cracking strengths are viewed to be accurate representations of pure tensile behavior. Only half of the unnotched cylinders failed remotely from the bearings; therefore, the unnotched specimen results are more limited. It is expected that the specimens that failed within 1 in. of the bearing had their strengths reduced by local bearing effects.

The limited total data set available from the direct tension tests precludes the presentation of definitive conclusions. However, the results do provide a range in which tensile cracking of UHPC can be anticipated. For Steam treated UHPC, tensile cracking likely occurs between 1.4 ksi and 1.6 ksi. For Air treated UHPC, the range is from 0.8 ksi to 1.0 ksi. For Tempered Steam specimens, the range was from 1.1 ksi to 1.3 ksi. And for Delayed Steam specimens, the range was from 1.3 ksi to 1.6 ksi.

Table 3.4.4-A: Direct tension test results

Specimen	Notched	Cracking Location	Cracking Strength (ksi)	Modulus of Elasticity (ksi)
Steam				
M1D00	Yes	Notch	1.56	N/A
M1D01	Yes	Notch	1.50	N/A
M1D02	Yes	Notch	1.75	N/A
M1D10	No	Within 1 in. of bearing	1.51 [†]	7525
M1D11	No	Center of specimen	1.44	7329
M1D12	No	Within 1 in. of bearing	1.36 [†]	7736
Air				
M2D00	Yes	Notch	0.82	N/A
M2D01	Yes	Notch	0.86 [‡]	N/A
M2D02	Yes	Notch	0.94 [‡]	N/A
M2D10	No	Within 1 in. of bearing	0.92 [†]	6723
M2D11	No	Within 1 in. of bearing	0.98 [†]	6946
M2D12	No	Within 1 in. of bearing	1.01 [†]	6942
Tempered Steam				
M3D00	Yes	Notch	1.05	N/A
M3D01	Yes	Notch	1.29	N/A
M3D02	Yes	Notch	1.09	N/A
M3D10	No	Center of specimen	1.13	7558
M3D11	No	Center of specimen	1.36	7674
M3D12	No	Center of specimen	1.39	7423
Delayed Steam				
M4D00	Yes	Unnotched section	1.19 [*]	N/A
M4D01	Yes	Notch	1.67	N/A
M4D02	Yes	Notch	1.58	N/A
M4D10	No	Within 1 in. of bearing	0.51 [†]	7383
M4D11	No	Center of specimen	1.32 [†]	7821
M4D12	No	Center of specimen	1.51	7460

[†] Cracking strength results may have been influenced by crack location.

[‡] Minimum cracking strength value due to difficulty with test apparatus leading to poor data resolution.

^{*} Cracking did not occur in the notch that had a peak tensile stress of 1.55 ksi.

The modulus of elasticity results are not affected by cracking or other localized behaviors. For this reason, three results are available for each curing regime. The Steam

treated UHPC modulus of elasticity averaged 7500 ksi. The Air treated UHPC averaged 6900 ksi. The Tempered Steam and the Delayed Steam treated UHPC specimens both averaged 7550 ksi. Note that aside from the Steam treated results, these results are somewhat higher than those presented in Section 3.3 that were obtained from purely compressive testing of cylinders.

Finally, the linearity of the tensile stress-strain response from minimal compressive load through tensile cracking was studied. The same stress-strain responses recorded from the testing of the unnotched cylinders that were used for the modulus of elasticity determination were also used to determine the nonlinearity of the response as cracking was approached. Overall, the results indicate that UHPC, regardless of the curing regime, exhibits very linear behavior up through tensile cracking. The theoretical linear elastic stress-strain response based on the calculated modulus of elasticity was used to determine the actual stress deviation (reduction) at any level of tensile strain. The decrease from the linear elastic predicted level was less than 20 psi for ten of the cylinders and was less than 30 psi for the remaining two specimens.

3.5 Fracture Testing

Understanding the cracking processes that occur when UHPC is stressed beyond its tensile strength is of great importance. Experience with UHPC structures has indicated that individual cracks tend to grow rapidly to a significant length, but that the width of any such crack is very small. However, it must be stated that this experience is based on

structural testing of UHPC members with loading configurations that were not intended to create and to propagate stable cracks.

A series of tests were completed on UHPC prisms to determine some of the basic behaviors of individual cracks. These tests focused on loading a prenotched prism in 3-point bending, with the load being incremented based on the opening at the mouth of the crack. The tests were loosely based on a portion of ASTM E1820 *Standard Test Method for Measurement of Fracture Toughness*.

The prisms and test setup conformed to the ASTM test method for the single edge beam test discussed in Annex A1 of the specification. The prism had a height of 4 in., a width of 2 in., and a span of 16 in. The only deviation from the ASTM test method was in the size and shape of the notch cut into the prism to act as the crack initiation point. In these tests, the crack was cut into the tension flange to a distance of approximately 1 in. The crack was cut with a 3/16th in. thick diamond tipped saw blade. The crack's tip had a rounded profile and was not sharpened through fatigue cycling or by any other means.

Four prisms were cast for both the Steam and Air treated curing regimes. These prisms were part of the M1P and M2P batches discussed in Section 3.1. The casting of these prisms followed normal procedures except that they were cast upside-down from the orientation in which they would be tested. These prisms were cast in special steel molds that allowed for partial enclosure of the top of the prism at the ends. Therefore, the only

non-molded surface on the finished prism was the center of the bottom or tension flange in the finished specimen.

These tests were completed in a 22-kip capacity MTS controlled load frame. The tests were controlled based on the crack mouth opening displacement (CMOD). The CMOD was measured via a 0.5 in. full range capacity clip gage that was attached to knife edges epoxied to the bottom flange on either side of the starter notch. The entire test loading protocol was preprogrammed into the MTS Microprofiler. The testing included an initial CMOD rate of approximately 0.0005 in./min, as well as a post-cracking rate 2.5 and 5.0 times larger. The protocol included periodic unloadings set to occur at predefined CMOD values. Unfortunately, for unknown reasons these unloadings frequently did not occur as planned. Tests were stopped after 0.1 in. of CMOD. Figure 3.5-A shows one of the prisms undergoing this fracture test.

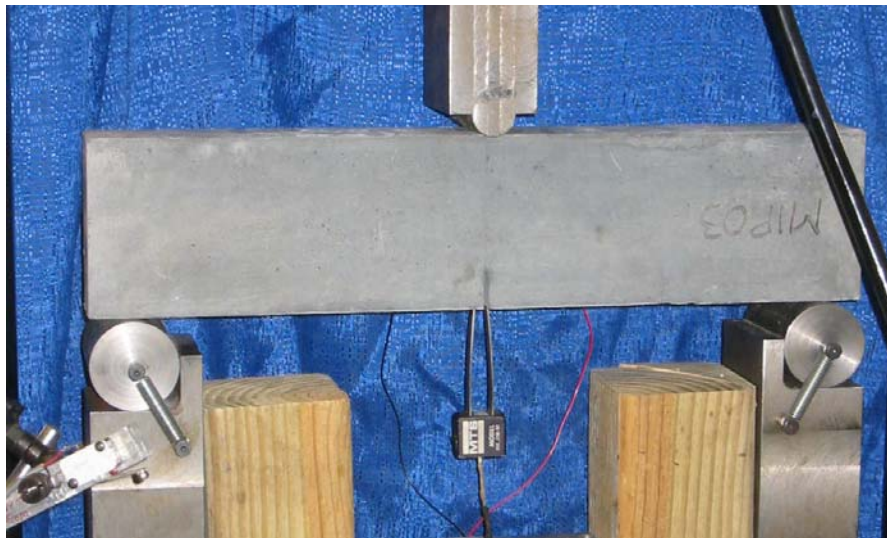


Figure 3.5-A: Test setup for 4 in. by 2 in. notched prisms loaded on a 16 in. span

Two methods were used to monitor the crack extension during the test. The primary method involved using an optical microscope to view the fracture process zone just ahead of the tip of the crack. This microscope had a field of view of 0.1 in., which allowed the crack tip to be located with relative ease. As the test progressed, alcohol was used as a volatile penetrant to help indicate the extent of cracking. The crack extension measurements were all taken from the bottom of the prism.

The second method used to monitor crack extension involved a crack propagation resistance gage. Figure 3.5-B shows one of these gages during a test as a crack is traversing the grid. The resistance across the gage changes as more of the lines are broken due to crack extension. This method of crack monitoring was used on two prisms from each of the Steam and Air treatment curing regimes.



Figure 3.5-B: Resistance foil gage to monitor crack propagation

Figures 3.5-C and 3.5-D show photographs of crack propagation on two prisms. Alcohol was used to help indicate the locations of the cracks in both figures. Some important findings observed throughout these tests are illustrated in the figures. First, a single crack formed initially in each prism because the starter notch had sufficient depth. The crack then extended up through the prism as shown in Figure 3.5-C(a). However, the fibers binding the initial crack together soon allowed for a redistribution of stresses resulting in the formation of other cracks that ran parallel to the first crack. Second, the cracks tended to extend very close to the compression flange. Figure 3.5-C(b) shows a crack extending to within 0.15 in. of the compression flange.

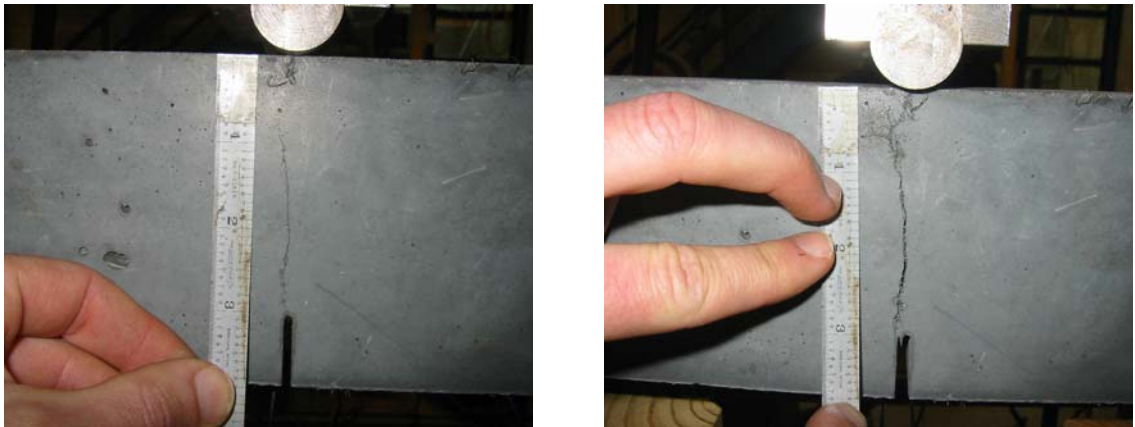


Figure 3.5-C: Prism M1P00 after (a) 3.4 in. and (b) 3.85 in. of crack extension

The load and crack extension results in terms of the CMOD for each specimen are presented in Figures 3.5-E through 3.5-L. In each figure, (a) shows the overall response of the prism with the load versus CMOD behavior plotted with regard to the left y-axis and the crack extension versus CMOD behavior plotted with regard to the right y-axis. In each figure, (b) shows the initial behavior and first cracking of the UHPC prisms.

Additionally, this plot shows the geometric construction used to determine when first cracking occurred.

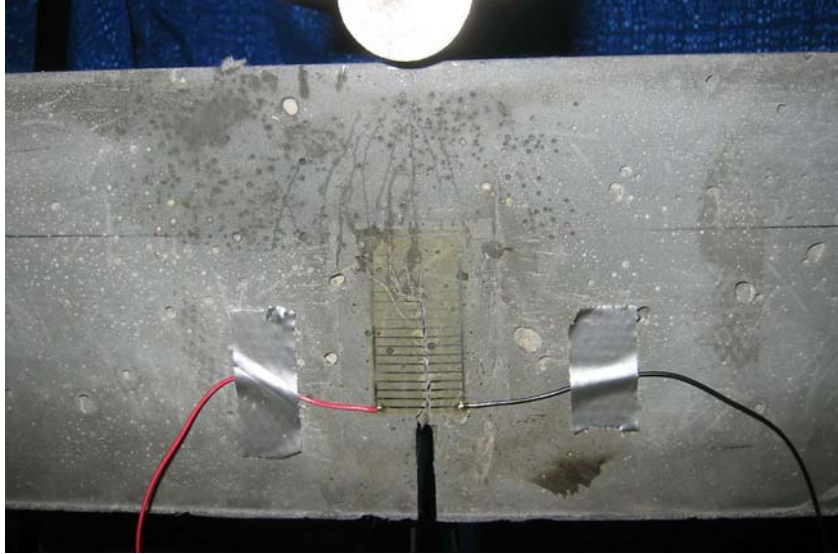


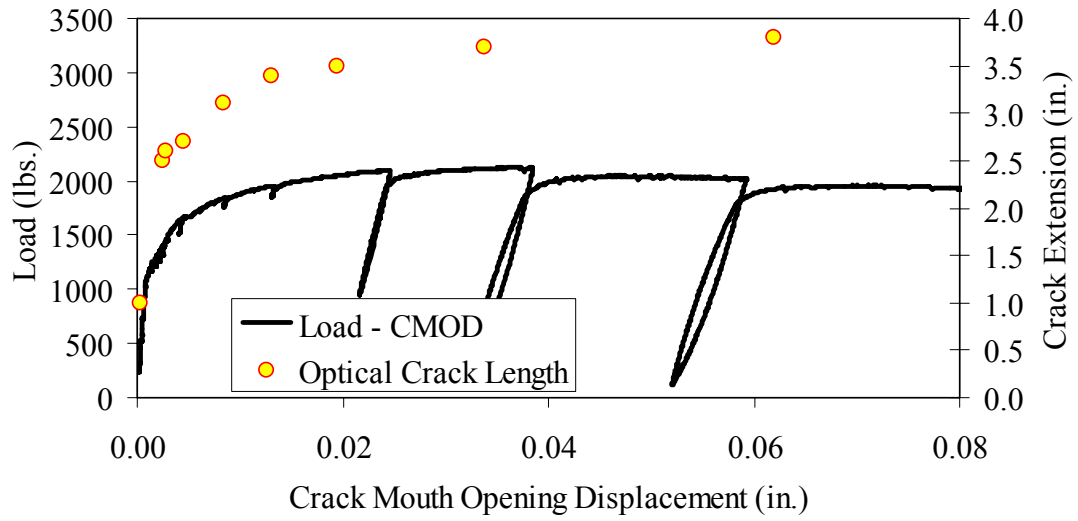
Figure 3.5-D: Prism M2P03 after 3.65 in. of crack extension

The ASTM E1820 specification defines cracking for materials that exhibit both stable and unstable first cracking. The data collected from these eight prisms indicate stable cracking behavior occurred with no clear evidence of a pop-in in any specimen. Thus, first cracking is defined by creating a linear best-fit line to the initial elastic portion of the load-CMOD response then decreasing the slope of this line by 5%. The intersection of the new line with the original data is defined as the load and CMOD at first cracking.

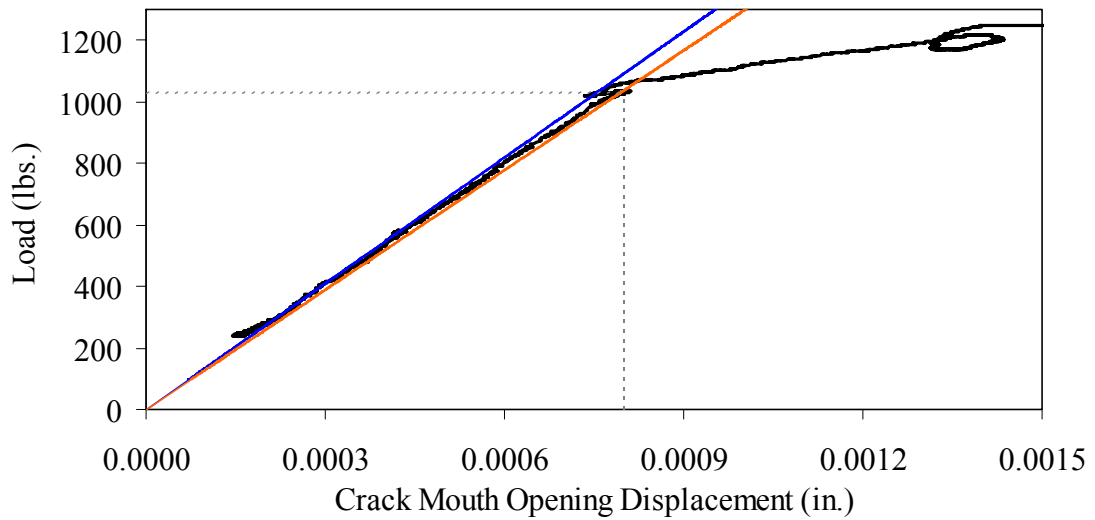
Part (b) of the referenced figures shows the required construction and the values at first cracking. Note that the initial load-CMOD response between 300 and 600 pounds was used to define the elastic portion of the behavior because it was beyond any initial

seating-based nonlinearities and was before the initiation of cracking-based nonlinearities.

The original intent of these tests had been to determine the fracture toughness, K_{Ic} , of Steam and Air treated UHPC according to ASTM E1820. Unfortunately, the calculations associated with this specification indicate that the test as performed did not meet the standards of a qualified and size-independent K_{Ic} test.

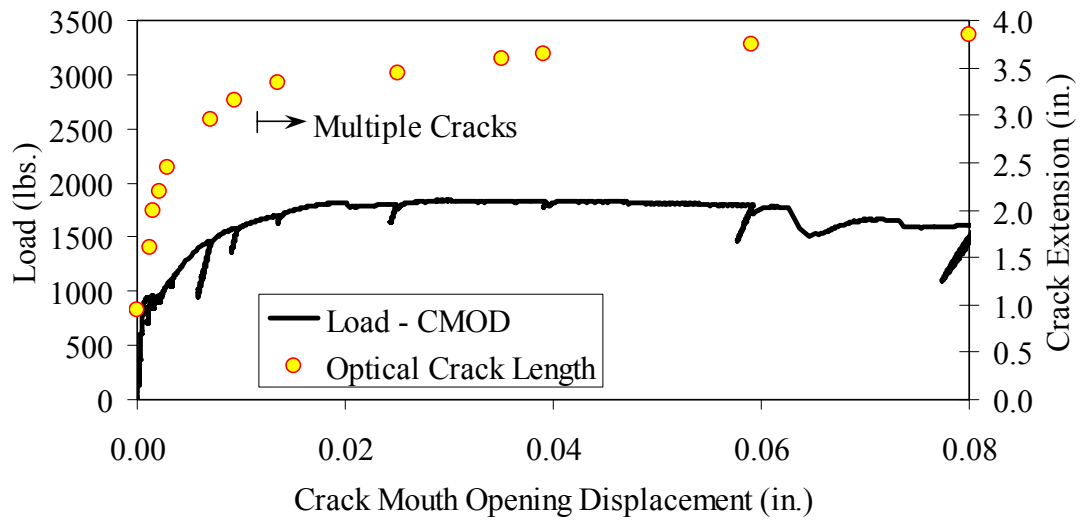


(a.) Overall response including periodic unloadings.

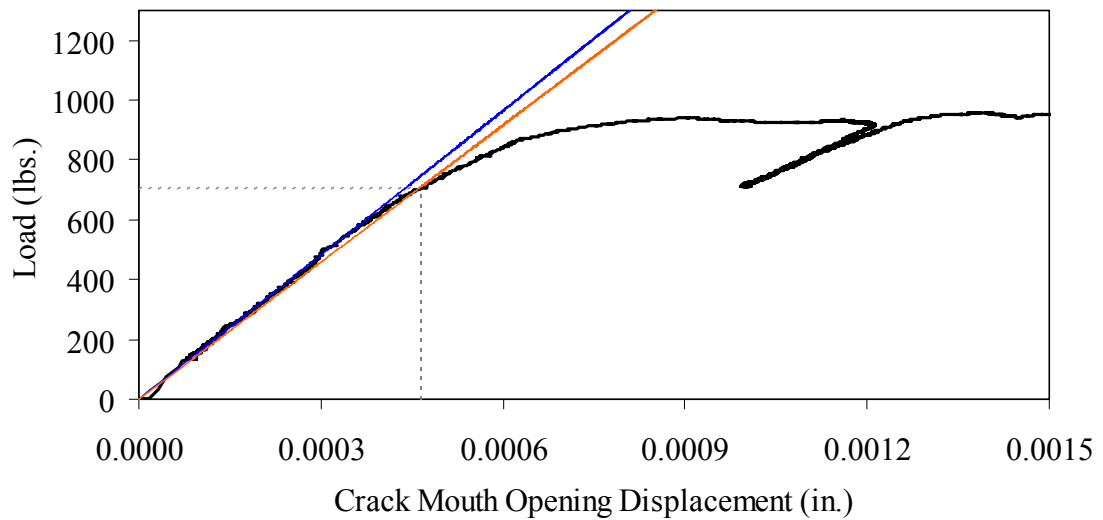


(b.) Initial response including elastic stiffness and 95% of elastic stiffness curves.

Figure 3.5-E: Load-CMOD response for Steam treated prism M1P00

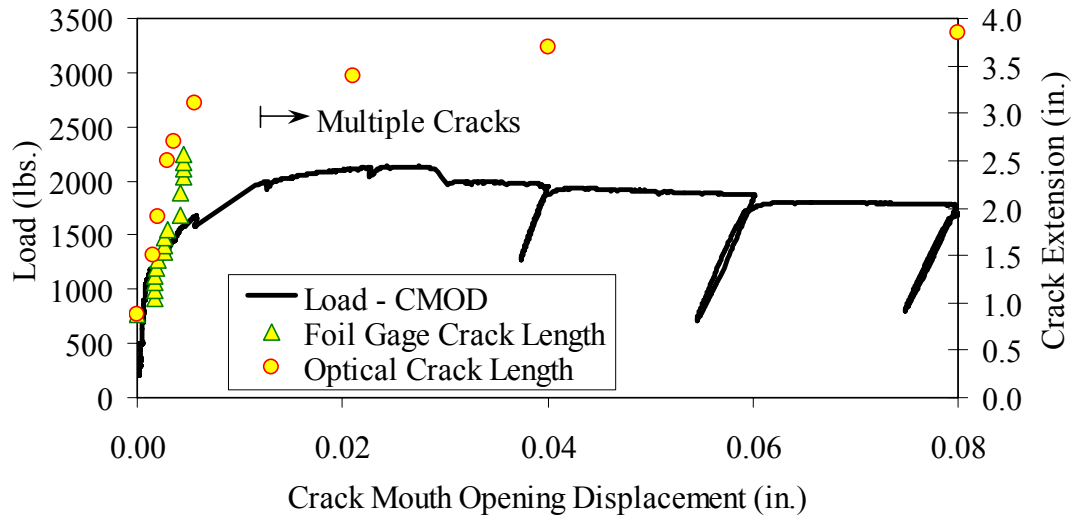


(a.) Overall response including periodic unloadings.

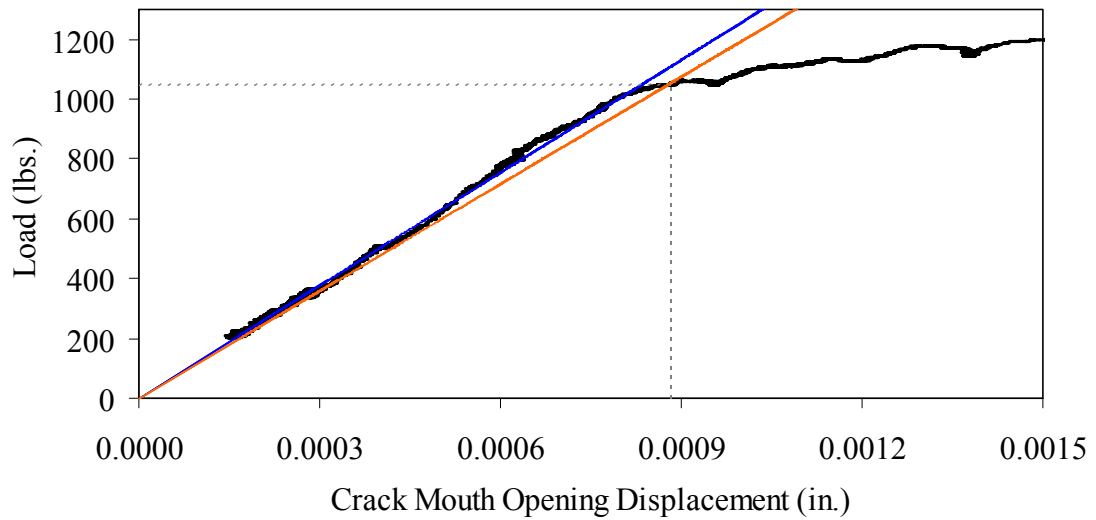


(b.) Initial response including elastic stiffness and 95% of elastic stiffness curves.

Figure 3.5-F: Load-CMOD response for Steam treated prism M1P01

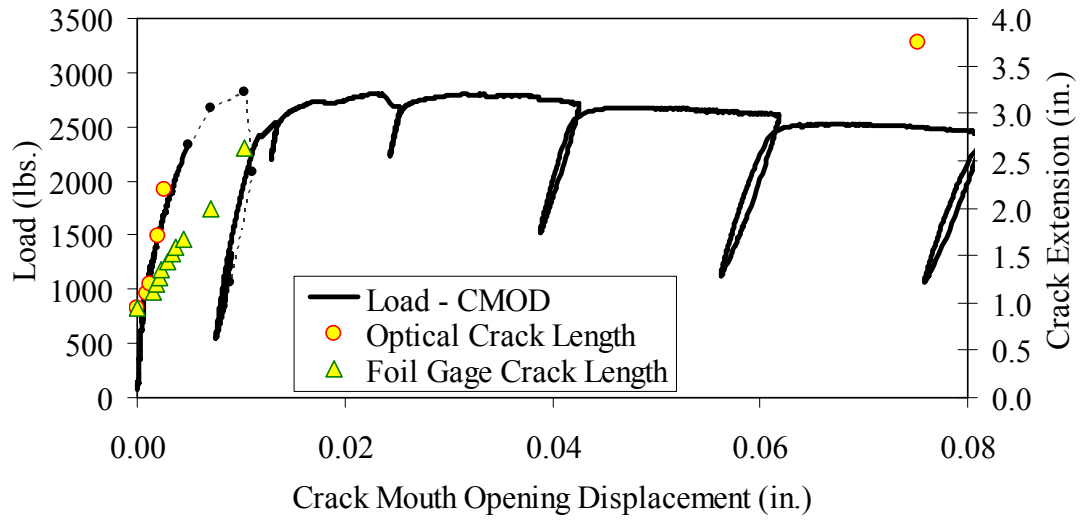


(a.) Overall response including periodic unloadings and crack length from tension flange.

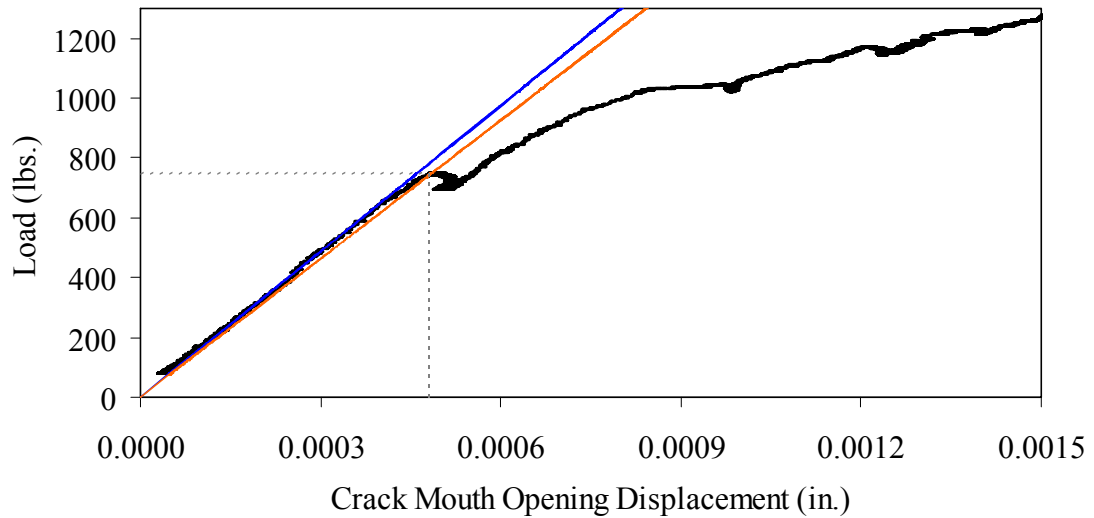


(b.) Initial response including elastic stiffness and 95% of elastic stiffness curves.

Figure 3.5-G: Load-CMOD response for Steam treated prism M1P02

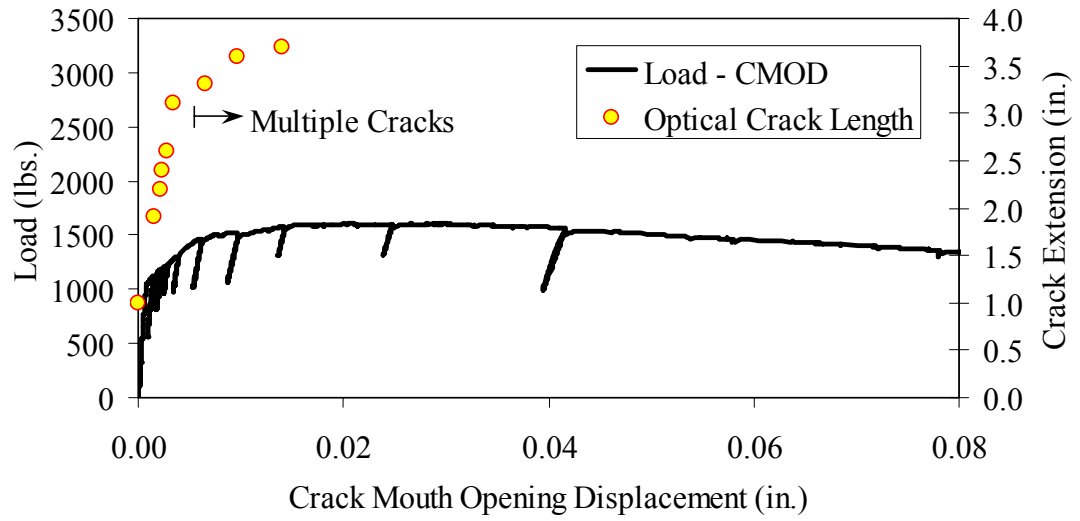


(a.) Overall response including periodic unloadings and crack length from tension flange.

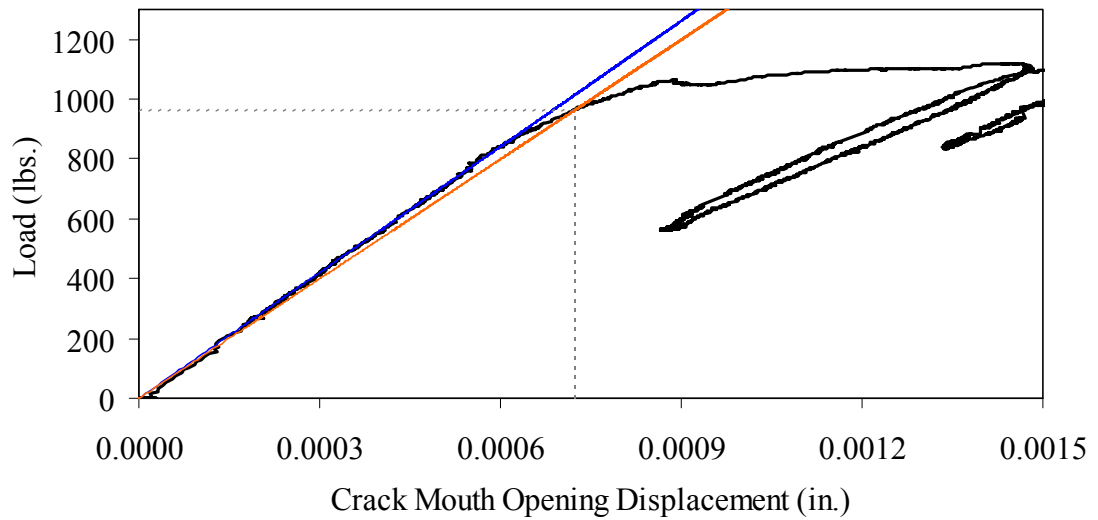


(b.) Initial response including elastic stiffness and 95% of elastic stiffness curves.

Figure 3.5-H: Load-CMOD response for Steam treated prism M1P03

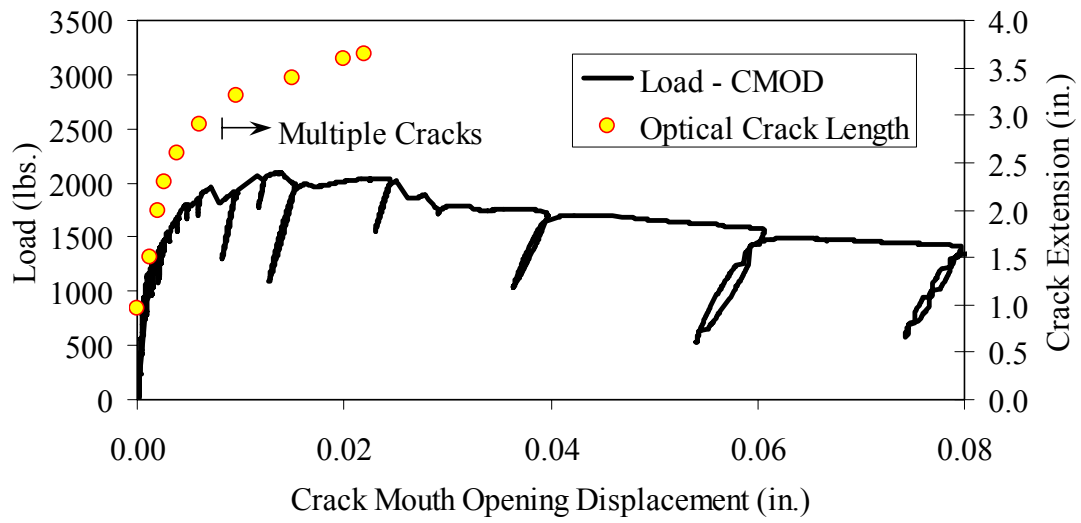


(a.) Overall response including periodic unloadings.

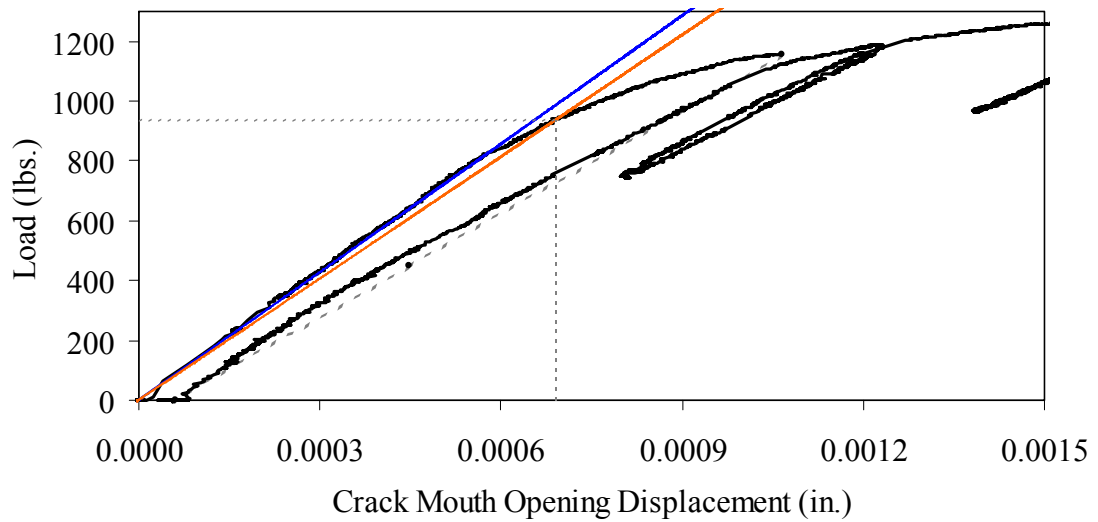


(b.) Initial response including elastic stiffness and 95% of elastic stiffness curves.

Figure 3.5-I: Load-CMOD response for Steam treated prism M2P00

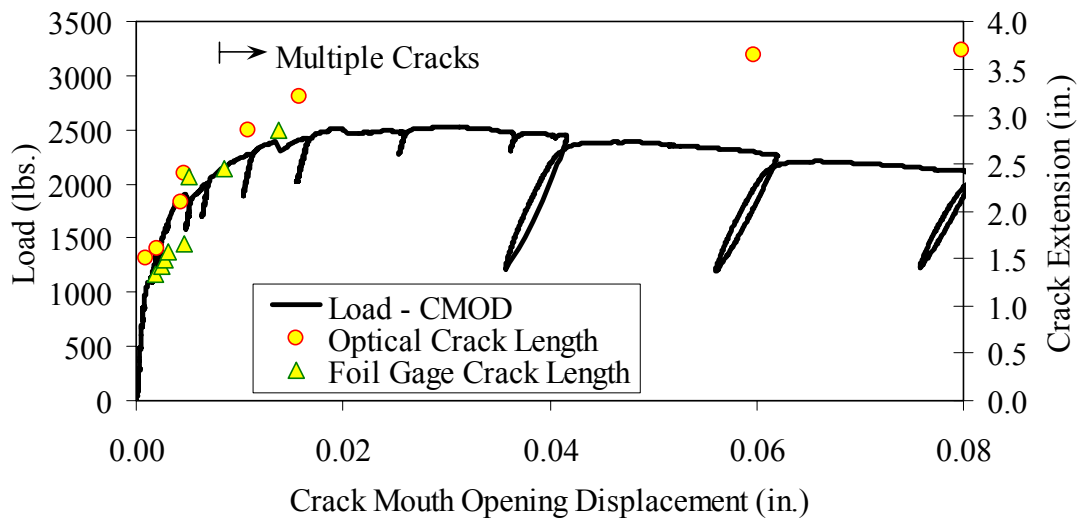


(a.) Overall response including periodic unloadings.

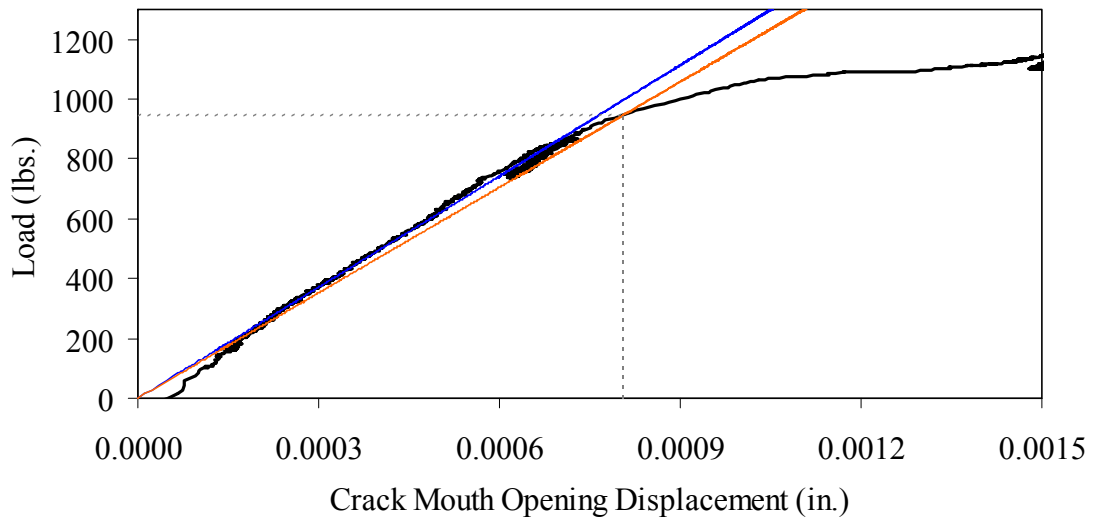


(b.) Initial response including elastic stiffness and 95% of elastic stiffness curves.

Figure 3.5-J: Load-CMOD response for Steam treated prism M2P01

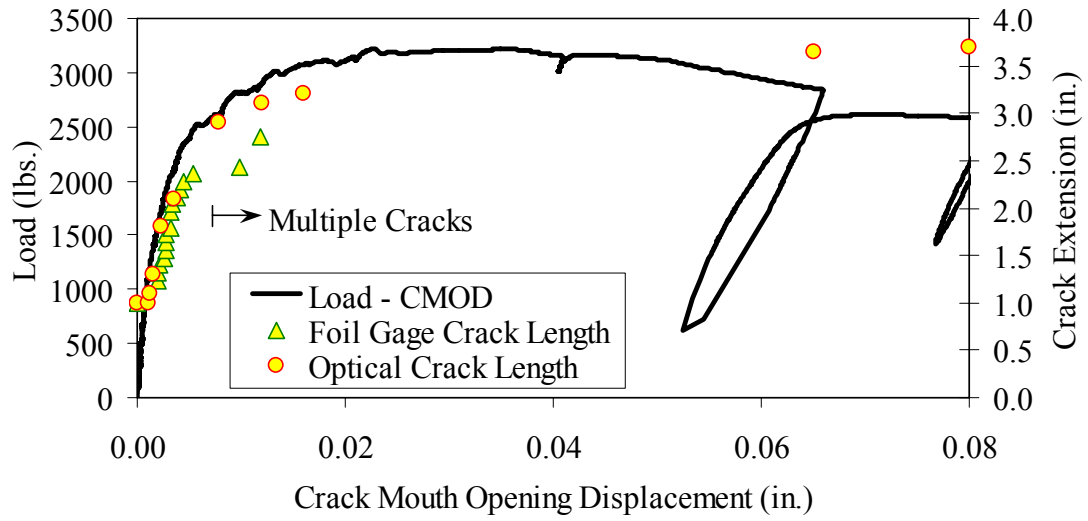


(a.) Overall response including periodic unloadings and crack length from tension flange.

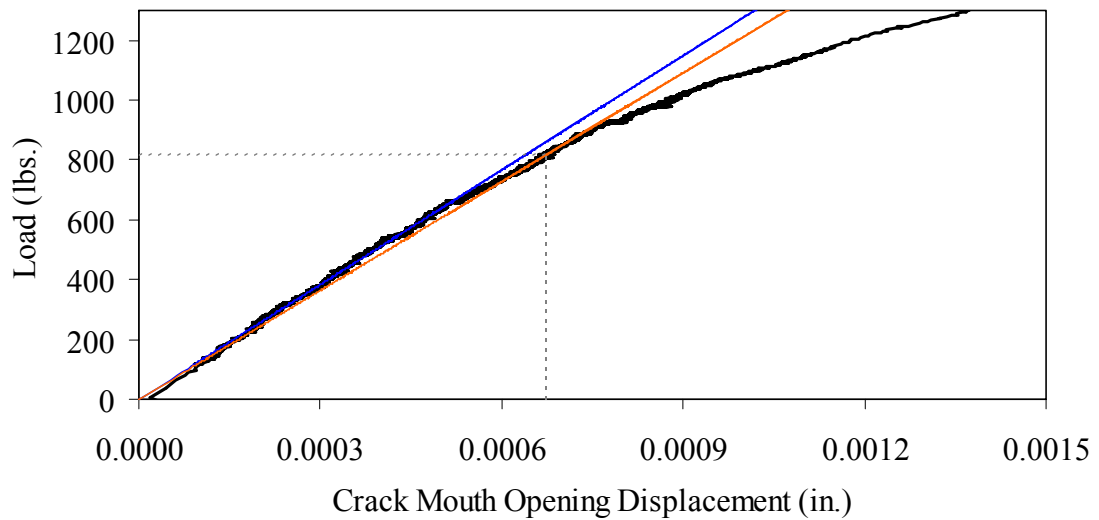


(b.) Initial response including elastic stiffness and 95% of elastic stiffness curves.

Figure 3.5-K: Load-CMOD response for Steam treated prism M2P02



(a.) Overall response including periodic unloadings and crack length from tension flange.



(b.) Initial response including elastic stiffness and 95% of elastic stiffness curves.

Figure 3.5-L: Load-CMOD response for Steam treated prism M2P03

3.6 Penetration Resistance Testing

Penetration resistance testing was completed on early age UHPC to determine the times of initial and final setting. The testing was completed nominally in accordance with the AASHTO T197 standard test method. The primary difference between the T197 test procedure and the one undertaken was that the UHPC was used as cast and was not sieved to obtain a mortar sample. The lack of coarse aggregate and the ease with which a penetration probe could be inserted into fresh UHPC allowed for this change in test procedure.

The T197 penetration resistance test is performed by forcing a flat-headed probe into a sample of fresh concrete. The surface area of the probe and the force required to insert it are used to determine the penetration resistance in psi. Initial setting is defined as when the concrete reaches a penetration resistance of 500 psi. Final setting is defined as when the concrete reaches a penetration resistance of 4000 psi. The probe sizes range from 1 in.² down to 0.025 in.². Preliminary testing indicated that the smallest probe could be used to provide consistent results in both the initial and final setting ranges. Additionally, the use of a single probe size eliminates one source of error within the results. For these reasons, the smallest probe was used exclusively in this study.

The penetration testing was performed in conjunction with the compression stress-strain response testing described in Section 3.3.2. The requirements of these test along with the delayed set times inherent in UHPC made the collection of penetration resistance data troublesome. In general, UHPC tends to exhibit virtually no setting for at least 12 hours.

Sometime thereafter, the concrete will begin to set and will then quickly reach both initial and final set. This timetable led to the collection of partial penetration resistance results from four different batches of concrete.

Table 3.6-A provides the penetration resistance results. The table indicates the batch from which the penetration resistance specimens came and the subsequent curing action which was applied to all other specimens in that batch. However, it must be reiterated that no curing actions were performed on any of the penetration resistance specimens. These results show that the initial set for this particular UHPC mix design, cast and maintained under laboratory conditions, occurred around 15 hours. The final set occurred a few hours later at approximately 17 hours after casting.

Table 3.6-A: Penetration resistance results

Subsequent Curing Regime	Batch Name	Initial Set (hours)	Final Set (hours)
Steam	N1A	15.25	18 to 20
Air	N2A	less than 14.5	16
Tempered Steam	N3A	less than 15	15.75
Delayed Steam	N4A	between 9.5 and 17.5	between 9.5 and 17.5

3.7 Shrinkage Testing

3.7.1 Long-term Shrinkage Testing

Long-term shrinkage testing of the unrestrained, hardened UHPC was completed according to ASTM C157. Three prisms, 3-in. by 3-in. by 11-in., were cast for each curing regime. Gage studs were cast into the end of each prism so that the length change

could be measured according to ASTM C490. After casting, the prisms were kept in a laboratory environment until demolding, which occurred at approximately 22.5 hours.

Table 3.7.1-A shows the demolding time for each curing regime.

Table 3.7.1-A: Long-term shrinkage

Curing Regime	Premix Age at Casting (days)	Demolding Time (hours)	Ultimate Shrinkage (microstrain)
Steam	105	22.5	766
Air	55	22	555
Tempered Steam	50	22	620
Delayed Steam	47	23	657

Each prism had its initial length reading recorded within 30 minutes after demolding. The time of this initial reading was set by the demolding time as shown in Table 3.7.1-A and was not precisely 24 hours as recommend by the specification. The reading also did not capture some of the early age shrinkage of the UHPC, which will be discussed in the following section. All prisms were stored and measured in a temperature and humidity controlled room per the specification except for the duration of any steam-based treatment.

Measurements of the changes in length were recorded on a daily, then weekly, then monthly basis for 1 year. A special emphasis was placed on recording a measurement both before and after any curing treatment was applied to any prism. Figure 3.7.1-A shows the results of these tests up to 250 days after demolding. After that time, very little change was observed in the recorded values.

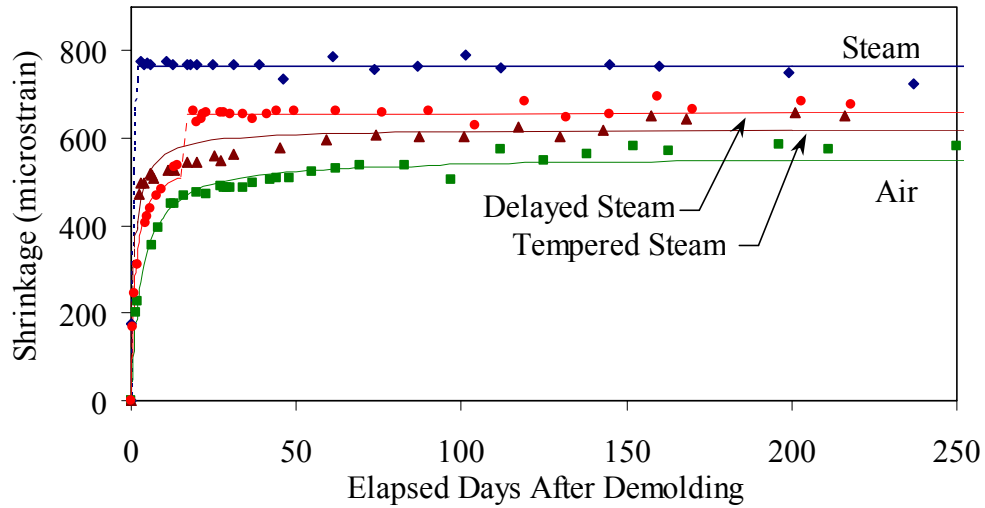


Figure 3.7.1-A: Long-term shrinkage results

Figure 3.7.1-A also provides best-fit approximations of the shrinkage behavior. The approximating equation, Equation 3.7.1-A (shown below), is a modification of the equation recommended in ACI 209R-92 wherein it is recommended that ‘A’ equal 35. In the research, s_t is the shrinkage at a given time, t is the time in days, s_{ult} is the ultimate shrinkage that the concrete will undergo, and A is a variable defining the shape of the curve.

$$s_t = \frac{t}{A + t} s_{ult} \quad (3.7.1-A)$$

The figure shows that the prisms that underwent Steam or Delayed Steam treatment exhibited no discernible post-treatment shrinkage. This result corroborates Acker’s (2004) shrinkage behavior theory presented in Chapter 2. In comparison, the Air and

Tempered Steam treated prisms show continued shrinkage past 4 months of age. Even so, all the prisms reached at least 95% of their ultimate shrinkage by 2 months after demolding. For comparison, the ACI 209R-92 recommended equation indicated that a normal concrete might have reached 60% of its ultimate shrinkage at this age.

3.7.2 Early Age Shrinkage Testing

The results presented in Section 3.7.1 show that this concrete can exhibit large unrestrained shrinkage strains regardless of the curing applied. More importantly, the shrinkage exhibited tends to occur much earlier in the overall behavior than would normally be expected. For these reasons, the ASTM C157 specification and its requirement that the concrete needs to have set prior to the recording of the initial measurement seems ill suited for determining the full unrestrained shrinkage behavior of this concrete.

To quantify this early age shrinkage behavior, a test was devised to measure the unrestrained shrinkage of a prism starting at casting. An embedded strain measuring device (Geokon 4202 Vibrating Wire Strain Gage) was cast into the center of a prism. This type of gage, shown in Figure 3.7.2-A, measures strain by monitoring the resonant frequency of a wire tensioned between two end blocks that are embedded in the concrete. Aside from the gage embedment, the mixing, casting, and demolding procedures were the same as the ones followed for the long-term shrinkage prisms discussed above. Vibrating wire gages were embedded into one prism that was receiving the Steam treatment and into another prism that was receiving the Air treatment. The gages monitored the

shrinkage for the first 17 days after casting. After demolding, standard ASTM C490 length change measurements were also recorded for verification purposes.



Figure 3.7.2-A: Embeddable vibrating wire gage

Figure 3.7.2-B shows the unrestrained shrinkage results from these embedded strain gages. The premix for this particular batch was over 150 days old, thus the initial setting was slower and the prisms were demolded at 28 hours. The Steam treated prism was steamed from hours 29 to 77 as shown in the figure, while the Air treated prism was maintained in a laboratory environment.

The figure shows that this concrete exhibits rapidly occurring, large-value early age shrinkage. The Steam treated prism reached a total of 850 microstrain, and the air treated prism was continuing to exhibit some shrinkage beyond the 790 microstrain recorded at 40 days after casting. Of greater interest is the rate at which the shrinkage occurs. Table 3.7.2-A provides shrinkage rates in microstrain per hour that were obtained at discrete times during the early age of these two prisms. In particular, note that the shrinkage rate is over 60 microstrain per hour at 1.18 days, which is just after the prisms are demolded.

This high rate of shrinkage soon drops off, but in total over 400 microstrain of shrinkage occurred in the Air treated prism in the 24 hours following the 20-hour mark when shrinkage started to occur. For reference, concrete usually has a tensile cracking strain of between 150 and 250 microstrain.

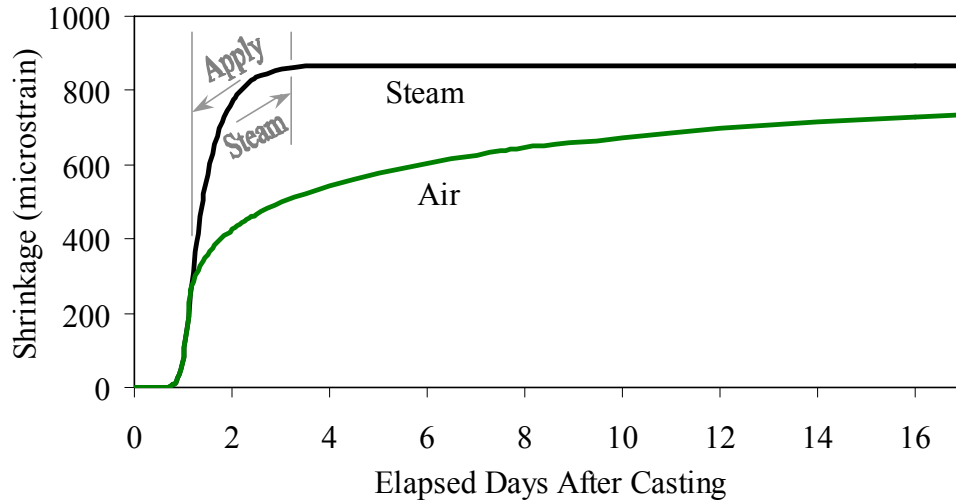


Figure 3.7.2-B: Early age shrinkage

3.8 Creep Testing

3.8.1 Long-Term Creep Testing

The long-term compressive creep testing of the UHPC was conducted according to ASTM C512. Four cylinders, 4-in. diameter by 8-in. long, were cast for each curing regime for these tests. Two additional half-height cylinders were cast for each curing regime to act as loading blocks. All cylinders had their ends ground to within 0.5 degree of parallel. The testing was completed using hydraulically actuated load frames in a room that was controlled for temperature and humidity. No attempt was made to retard moisture gain or loss from the cylinders either prior to or during the test.

Table 3.7.2-A: Early age shrinkage rate

Elapsed Time Since Casting (days)	Steam Treated Shrinkage Rate (microstrain per hour)	Air Treated Shrinkage Rate (microstrain per hour)
0.0	0	0
0.75	0	0
0.95	20	20
1.10	36	36
1.18	64	64
1.3	– *	18
1.5	34 *	3.5
1.7	11 *	3.5
2.0	6.5 *	2.9
2.5	2.8 *	2.4
3.0	1.2 *	0.8
3.5	0.0	0.7
4.5	0.2	1.9
6.0	0.1	1.3
8.0	0.0	0.8
10.0	0.0	0.5

* Prism was undergoing Steam treatment

The four cylinders for each curing regime were instrumented with Whittemore points prior to being stacked into a load frame. The Whittemore points were attached to each cylinder at three locations around the circumference with a 6 in. nominal gage length. Measurement of the points was completed prior to loading, immediately after loading, and periodically for 1 year. Figure 3.8.1-A shows creep cylinders in the load frame as well as the method used to measure the Whittemore points.

The creep testing was initiated for each curing regime after the curing treatment was applied. For the Steam and Tempered Steam cylinders, the creep loading was initiated 4 days after casting. Loading was initiated 21 days after casting for the Delayed Steam cylinders and 28 days after casting for the Air treated cylinders. The load level applied to

each set of cylinders was 11.2 ksi, which is 40% of 28 ksi, the anticipated compressive strength of a Steam treated cylinder.



Figure 3.8.1-A: (a) Creep cylinders in load frame and (b) measurement of creep

Table 3.8.1-A provides the creep testing results for the four curing regimes. The 28-day average compressive strength is also shown. Note that in all cases the load applied was in excess of the ASTM recommended load. The initial elastic strain was mechanically measured on the cylinders. The final creep strain is the estimated long-term value that the strain in the cylinders asymptotically approached. Intermediate creep strain values were calculated by subtracting the long-term shrinkage and the initial elastic strain from the overall measured strain. A best-fit approximation, discussed below, allowed for the determination of the final asymptotic value.

Note that the subtraction of the long-term shrinkage from the recorded creep strain assumes that creep and shrinkage are uncoupled behaviors. However, research has

indicated that these behaviors are dependent on one another in UHPC (Acker 2004). In this research, the shrinkage strain was subtracted from the creep strain for two reasons. First, some of the measured creep strain was necessarily due to shrinkage. Second, the overall shrinkage strains were small or nonexistent, thus the total error introduced was minimal. If the shrinkage strain were not subtracted from the creep strain for the Air and Tempered Steam treated specimens, the creep coefficients would have been less than 10% higher.

The creep coefficient, C_{cu} , is defined as the final asymptotic amount of additional creep strain that occurs over time divided by the initial elastic strain that occurs when load is first applied. The specific creep, δ_{cu} , is defined as the creep coefficient divided by the elastic modulus of the concrete. For reference, creep coefficients for concrete are normally in the range of 1.5 to 3.0, and specific creep values normally range from 250 to 1000 microstrain per ksi.

Table 3.8.1-A: Long-term creep results

Curing Regime	Control Strength (ksi)	Stress / Strength	Initial Elastic Strain ($\mu\epsilon$)	Final Creep Strain ($\mu\epsilon$)	C_{cu}	δ_{cu} ($\mu\epsilon/\text{ksi}$)
Steam	27.27	0.41	1500	440	0.29	39
Air	16.53	0.67	2057	1600	0.78	146
Tempered Steam	25.65	0.43	1670	1100	0.66	98
Delayed Steam	24.42	0.46	1580	485	0.31	44

Recall the discussion in Section 2.4.4 regarding the creep and shrinkage of UHPC. The results presented here correlate well with that discussion in that Steam and Delayed Steam treated UHPC exhibit extremely low creep coefficients, while the Tempered Steam and Air treated UHPC exhibits higher creep coefficients. Specifically, note that the Delayed and Tempered Steam specimens had similar compressive strengths and load levels, but that the Tempered Steam exhibited more than twice as much creep strain. The more severe steam treatments should cause more rapid and more complete self-desiccation of the UHPC, thus leading to less creep of the concrete.

A plot of the creep data acquired during the year of testing is shown in Figure 3.8.1-B. The creep strain shown is the additional strain observed after the initial loading of the cylinders. The data presented are the average results from the four cylinders in each curing regime. The figure also includes best-fit approximations for each dataset. The best-fit curves are based on Equation 3.8.1-A wherein t is the time in days since load initiation, ϵ_{ct} is the creep strain at that time, and A and B are variables that define the shape of the curve. This equation is loosely based on a creep equation suggested by Branson [1977].

$$\epsilon_{ct} = \frac{t^{0.6}}{A + t^{0.6}} B \quad (3.8.1-A)$$

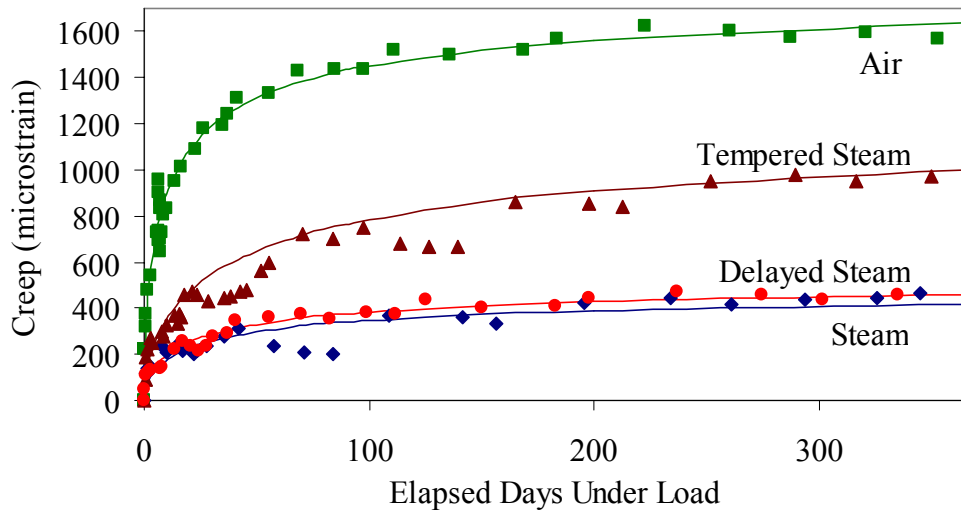


Figure 3.8.1-B: Long-term creep results

3.8.2 Early Age High Stress Creep Testing

A test program was initiated to investigate the dimensional stability of UHPC that was subjected to compression loading early in its strength gain. This test program was designed to answer questions related to the delay required prior to stressing a prestressed UHPC girder. Although the rapid strength gain of UHPC is beneficial with regard to the stressing of a girder, it is important to know what portion of that strength gain is actually useable.

Short-term creep tests were conducted on UHPC cylinders that were of moderate compressive strength. Two strength levels were investigated: 8.5 ksi and 12.5 ksi. Within one batch of UHPC, 4-in. diameter cylinders were cast for creep tests and 3-in. diameter cylinders were cast to determine the concurrent compressive strength of the UHPC. The specimen preparation procedures for the creep cylinders mimicked the procedures that

were followed for the ASTM C39 compression tests that were previously discussed, including sulfur capping of the cylinder ends due to the relatively low compressive strengths.

The creep testing was completed in a 100 kip capacity MTS testing machine. Each cylinder rested one end on a flat steel bearing and was loaded through the other end by a spherical bearing. Each cylinder was loaded at a computer controlled constant load rate of 150 psi/sec until the desired compressive load level was reached. This load level was then maintained for 30 minutes, after which the load was removed at 150 psi/sec. The deformation of the cylinder was monitored throughout the test via three LVDTs that were mounted on two parallel rings attached to the cylinders. This deformation measurement system was the same as the one used in the elastic modulus testing (previously discussed in Section 3.3.2). A photograph of the test setup is provided in Figure 3.8.2-A.

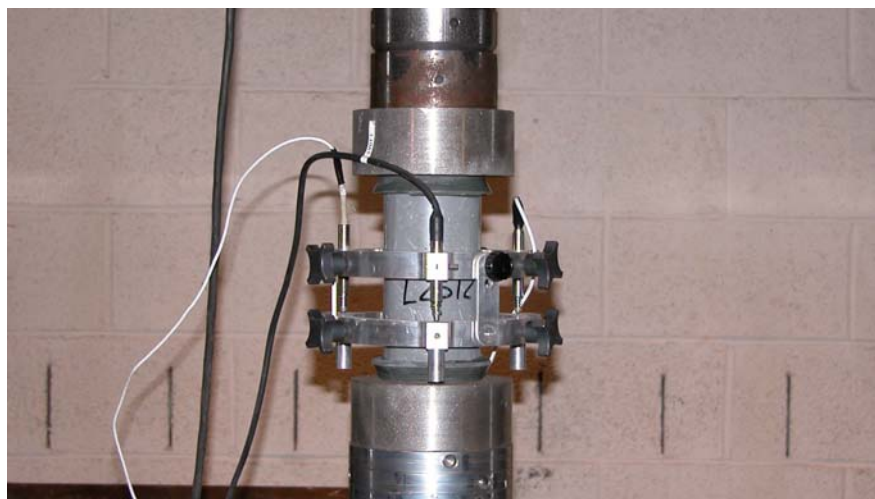


Figure 3.8.2-A: Short-term creep test setup

The early age creep results are presented in Table 3.8.2-A. The table provides the cylinder identifier, the compressive test at the time of creep testing based on concurrently tested 3-in. diameter cylinders, and the stress level maintained during the creep test. The stress levels tested ranged from 60% of the compressive strength to just over 90%.

Table 3.8.2-A lists the 30 min creep coefficient, C_{c-30} , for each of the cylinders that was able to carry the load through the end of the test. This creep coefficient is similar to the standard creep coefficient, except that here it equals the amount of additional creep strain that occurred during the 30 minutes divided by the initial elastic strain when the constant load level was reached. The two cylinders loaded to stress levels above 90% of the compressive strength both failed and thus no value of C_{c-30} is listed.

Table 3.8.2-A: Early age creep results

Cylinder Identifier	Compressive Strength (ksi)	Applied Stress (ksi)	Stress / Strength	C_{c-30}
8 to 9.5 ksi Compressive Strength				
A1	9.5	5.66	0.60	0.42
A2	8.5	6.34	0.75	0.66
A3	9.25	7.79	0.84	0.79
A4	8	7.07	0.88	0.80
12 to 13 ksi Compressive Strength				
B1	12.5	7.48	0.60	0.32
B2	12.25	8.79	0.72	0.39
B3	12.25	9.47	0.77	0.44
B4	12.25	10.15	0.83	0.52
B5	12.75	10.89	0.85	0.85
Failed Under Load				
A5	9.5	8.61	0.91	N/A
B6	12.25	11.22	0.92	N/A

Figures 3.8.2-B and 3.8.2-C show plots of the results of these tests. The observed strain values have been normalized on the strain when the constant stress level is first reached. In this way, the effect of stress level on early age creep is clearly visible. At both strength levels, stressing to above 85% causes twice the creep strain to occur and stressing above 90% caused failure. Even stressing to only 60% caused a significant amount of creep strain to accumulate in a short time.

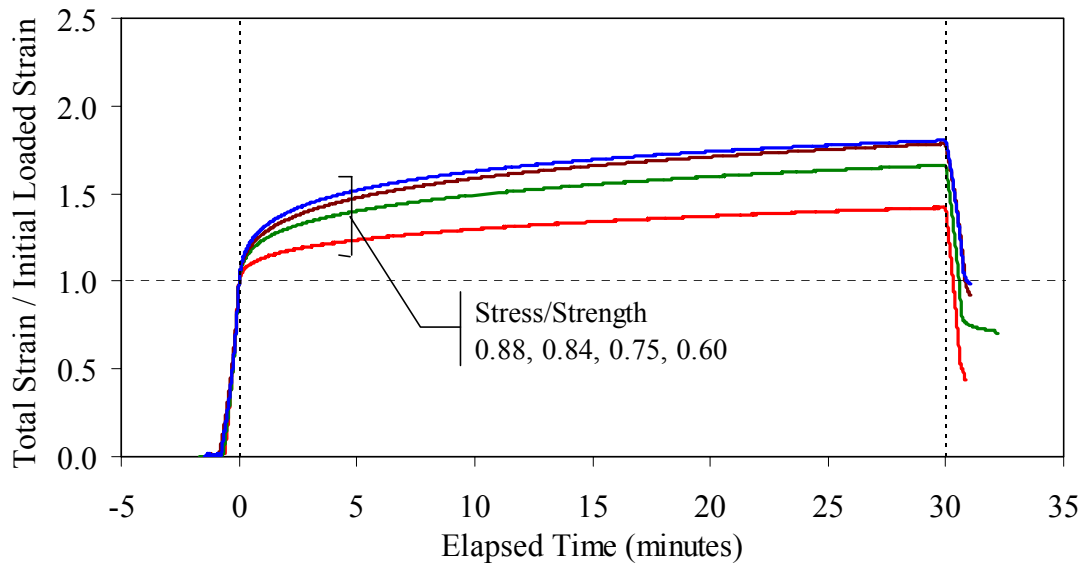


Figure 3.8.2-B: Early age creep behavior of 8 ksi to 9.5 ksi UHPC

3.9 Coefficient of Thermal Expansion

The coefficient of thermal expansion of UHPC was measured through the use of the provisional AASHTO test specification, TP60-00. The test method determines the coefficient of thermal expansion (CTE) by measuring the length change of a concrete cylinder in a variable temperature water bath. Three 4-in. diameter UHPC cylinders from each of the four curing regimes were tested.

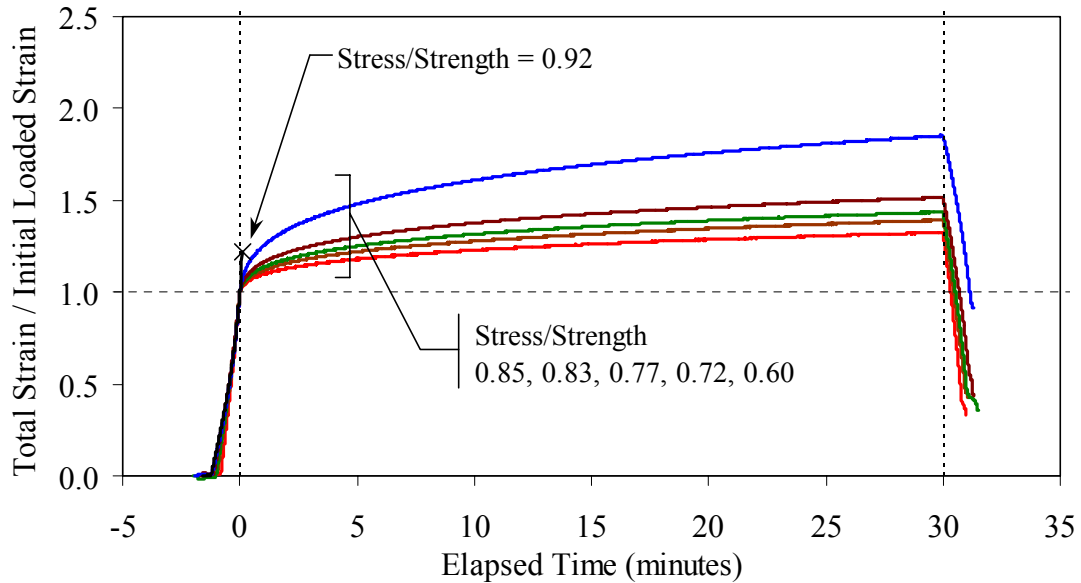


Figure 3.8.2-C: Early age creep behavior of 12.5 ksi UHPC

Normally, the degree of water saturation of a concrete will influence its CTE. To counteract this fact, the test method requires that the concrete needs to be in a saturated condition prior to testing. In the current testing of UHPC, the saturation of the cylinders prior to testing was considered to be detrimental to the final results for two reasons. First, one of the primary variables in the overall test program is the curing condition of the UHPC at the time of testing. Saturating the UHPC would change the condition of the UHPC by introducing more water into the matrix, which could then react with unhydrated cement. Second, because saturation of the UHPC is problematic due to its low permeability, determining when a specific degree of saturation was reached would be difficult. Thus, the exterior surfaces of the cylinders, aside from the bearing points of the supports and LVDT, were sealed with epoxy prior to testing.

The testing of the twelve cylinders was completed after they had undergone their complete curing treatment. All the cylinders were at least 2 months old. The Air treated cylinders were the oldest at 4.5 months at the time of testing.

The results from the CTE testing are shown in Table 3.9-A. In general, the CTE of UHPC is around 15×10^{-6} in./in./°C. This value is somewhat higher than the normally expected value for concrete of around 10×10^{-6} in./in./°C. However, recall that UHPC contains both a high cement content and no coarse aggregate. Hydrated Portland cement paste has been reported to have a CTE of between 11×10^{-6} and 16×10^{-6} in./in./°C, and aggregates tend to exhibit lower CTE values (Neville 1996).

Table 3.9-A: Coefficient of thermal expansion results

Curing Regime	Coefficient of Thermal Expansion			
	Results ($\times 10^{-6}$ in./in./°C)	No.	Average ($\times 10^{-6}$ in./in./°C)	Standard Deviation ($\times 10^{-6}$ in./in./°C)
Steam	15.3, 15.7, 15.8	3	15.6	0.3
Air	14.4, 14.6, 15.1	3	14.7	0.4
Tempered Steam	15.0, 15.5, 15.8	3	15.4	0.4
Delayed Steam	15.0, 15.2, 15.5	3	15.2	0.3

3.10 Heat of Hydration

The amount of heat that UHPC generates during initial curing is of interest for two reasons: (1) it can be used as an indicator of other behaviors and (2) it could cause detrimental behaviors if not accounted for in the design. Time-temperature data were gathered for 6-in. diameter cylinders during the first few days after casting. This testing was completed on two UHPC mixes. The first mix was the standard UHPC mix that has

been discussed throughout this report. The second mix included a slight modification of the mix design in that no accelerator was added. Specifically, 1.87 lb/ft³ of Rheocrete CNI was eliminated from the mix, and an extra 2.00 lb/ft³ of water was added.

The time-temperature results were collected for cylinders in three environments. Figure 3.10-A shows the heat that was generated by cylinders in a normal laboratory environment. These results indicate that the accelerator can have a significant effect on set time, but that the overall level of heat generation is not significantly different. Figure 3.10-B shows the heat that was generated by cylinders that were kept in a normal laboratory environment until setting began, after which the Steam treatment was applied. Again, the accelerator's primary impact seems to be in the rate of setting and not in the peak heat generated. Note that the Steam treatment of the accelerated mix was started earlier in the setting behavior, thus impacting the comparative level of the peak temperatures recorded.

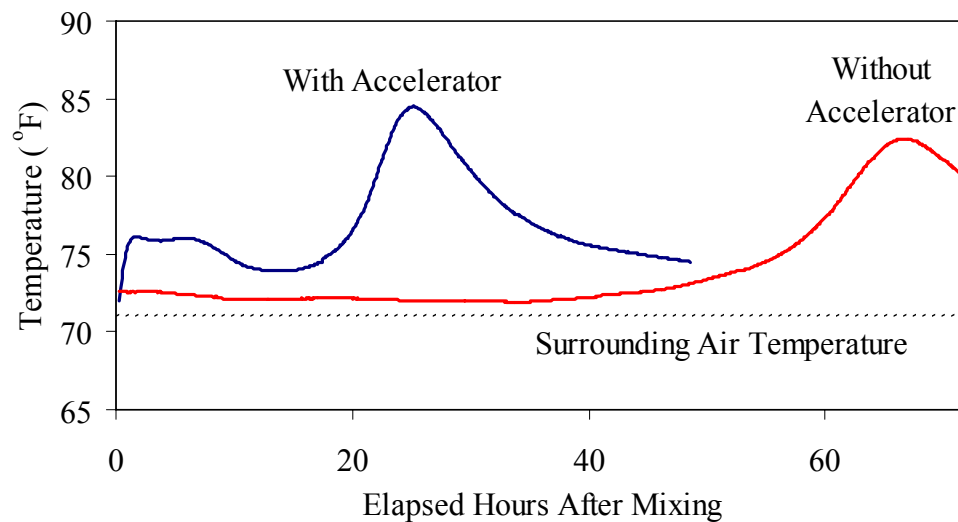


Figure 3.10-A: Heat generated in 6-in. diameter cylinders during initial curing

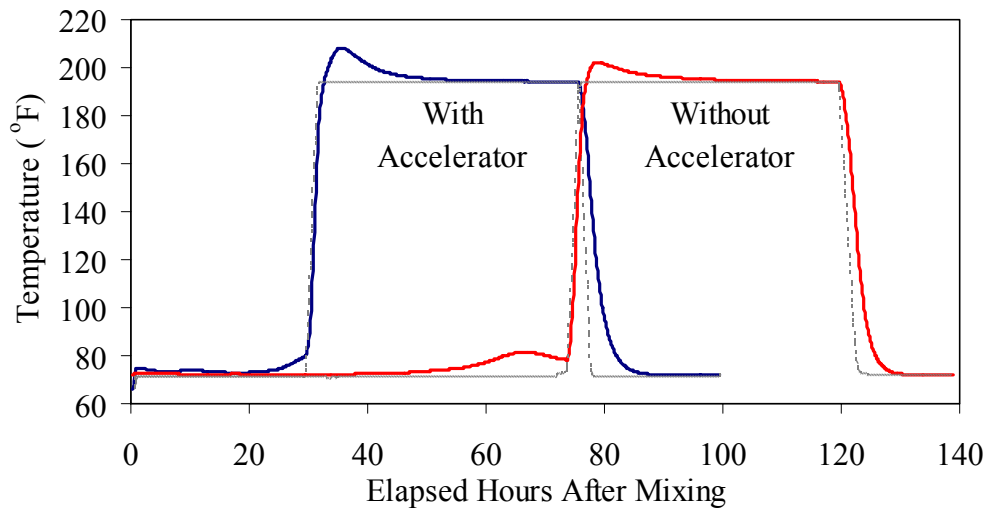


Figure 3.10-B: Heat generated in 6-in. diameter cylinders from casting through steaming

The difficulty with the previously discussed methods of measuring the heat generated by the UHPC is that local conditions within a laboratory environment can vary. Air currents that aid in the dissipation of heat can have a significant impact on final results. To address this issue, time-temperature data were also collected using a well-insulated calorimeter. For these tests, each 6-in. diameter cylinder was placed in a Quadrel iQdrumTM heat signature calorimeter and monitored for 6 days. The results are shown in Figure 3.10-C. Through the use of the calorimeter the effect of the accelerator becomes very clear. The accelerator causes a slow temperature rise to occur prior to setting and caused setting to begin over 1 day earlier. Heat was generated more quickly during setting, but the peak temperature reached by the cylinder was only 5°F higher than in the unaccelerated mix. Note that these relative changes between mix designs are instructive; however, the actual time-temperature and setting behaviors of any UHPC mix will depend on many other factors as well (i.e., age of premix, precise environmental conditions, quantity of accelerator).

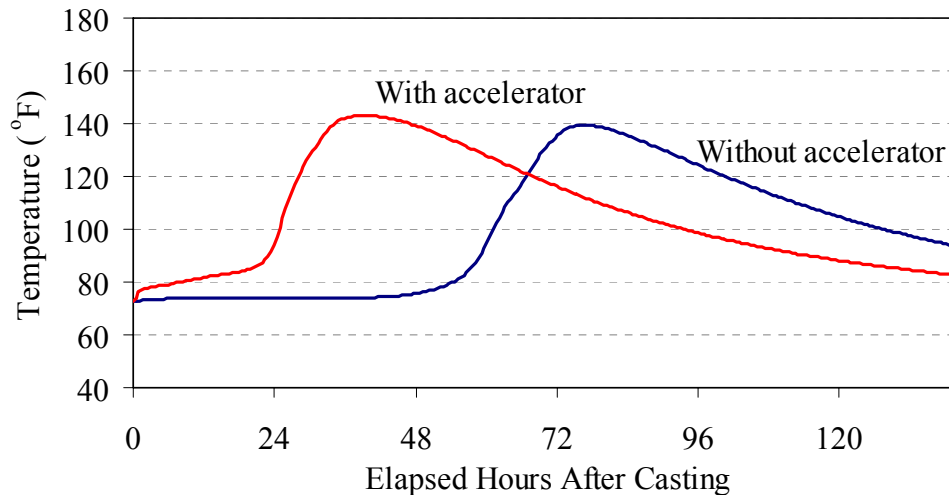


Figure 3.10-C: Heat signature for 6-in. diameter cylinders in a well insulated calorimeter

3.11 Air Void Analysis

An air void analysis was completed on the UHPC. The modified point-count method of ASTM C457 was used to determine the air void structure. The variables investigated in this testing included the effect of the analysis location within individual cast cylinders, the effect of the time a cylinder was held on a vibrating table after casting, the effect of mix stiffness, and the effect of using an accelerator in the mix design.

The casting procedure was as follows. The UHPC was mixed as usual, following the normal mix design and procedure, except that a non-accelerated mix (as described in Section 3.11) was included. The UHPC was then cast into 4-in. diameter plastic cylinder molds. The filling of the molds differed from the usual procedure in that some of the molds were filled without using the vibrating table while others were filled on the vibrating table and were then held in place on the table for a specific length of time. After

casting, the cylinders were screeded, covered in plastic, and left in a laboratory environment to set.

The preparation and testing of the cylinders for the air void structure analysis was as follows. After setting, the cylinders were cut in half lengthwise. One of the two halves was then polished using up to an 800-grit sandpaper. Each cylinder's half was then divided into a top and bottom section on its flat face. Modified point-count measurements were then completed on each of these sections. Because this UHPC did not contain any coarse aggregate, the fibers were counted as coarse aggregate within the data collection procedure. In total, each air void data collection set covered an area of 10.5 in.² and traversed a length of 50 in. while counting 1429 points.

The results from these tests are presented in Table 3.11-A. The results are grouped into sets for each of the three mixes tested. For reference, the stiff mix has a flow table reading of 6.5 in. after 20 impacts, and the normal flow mixes both have readings of 7.5 in. after 20 impacts. Each pair of rows shown with a common vibrating table time is the top and bottom results from the same cylinder half.

Although some slight differences were observed in various groupings of specimens, the limited sample set makes drawing specific conclusions difficult. In general, the air content across the range of mixes and specimen locations was approximately 6.5%. The bottom of the cylinders tended to have slightly more air, likely due to air in the top of the cylinders being removed by vibration. The cylinders that were held on the vibrating table

for 300 seconds after filling also tended to have a decrease in air content. The stiffer mix tended to have slightly less air than the more flowable mix, and the results of the accelerated and unaccelerated mixes had no clear differences.

Table 3.11-A: Air void analysis results

Vibration Table Time (seconds)	Location	Air (%)	Paste (%)	Fine Agg. (%)	Fiber (%)	Voids Counted	Mean Chord Length (in.)	Voids per in.	Specific Surface (in. ² /in. ³)	Spacing Factor (in.)
Stiff Mix w/ Accelerator (M1J)										
0	Top	5.7	47.2	43.3	3.8	249	0.0114	5.0	351	0.017
0	Bottom	6.2	51.2	38.8	3.8	267	0.0115	5.3	347	0.017
Fill + 20	Top	5.5	36.4	55.1	3.0	274	0.0101	5.5	397	0.013
Fill + 20	Bottom	6.9	30.7	59.5	3.0	257	0.0133	5.1	300	0.015
Fill + 60	Top	6.7	43.2	47.0	3.0	289	0.0116	5.8	344	0.015
Fill + 60	Bottom	7.4	42.4	47.2	3.0	287	0.0129	5.7	310	0.016
Fill + 300	Top	6.5	31.5	59.8	2.2	233	0.0140	4.7	286	0.016
Fill + 300	Bottom	4.7	25.1	66.3	3.9	221	0.0106	4.4	377	0.013
Normal Flow Mix w/ Accelerator (M1JxxA)										
0	Top	6.2	43.7	48.0	2.1	282	0.0110	5.6	362	0.015
0	Bottom	7.1	44.7	46.9	1.3	302	0.0118	6.0	338	0.015
Fill + 20	Top	6.4	45.8	46.5	1.4	291	0.0109	5.8	366	0.015
Fill + 20	Bottom	7.6	44.0	46.9	1.5	385	0.0099	7.7	404	0.012
Fill + 60	Top	7.8	29.9	60.8	2.0	349	0.0111	7.0	359	0.011
Fill + 60	Bottom	9.2	27.6	61.1	2.1	375	0.0122	7.5	327	0.009
Fill + 300	Top	6.9	42.2	49.3	1.5	234	0.0148	4.7	270	0.019
Fill + 300	Bottom	6.1	41.5	50.9	1.5	218	0.0140	4.4	286	0.019
Normal Flow Mix w/o Accelerator (M1K)										
0	Top	6.3	49.0	41.1	3.6	281	0.0112	5.6	357	0.016
0	Bottom	7.3	48.1	41.9	2.7	251	0.0145	5.0	276	0.019
Fill + 20	Top	6.7	43.0	47.9	2.4	244	0.0138	4.9	291	0.018
Fill + 20	Bottom	4.8	39.2	51.8	4.2	207	0.0117	4.1	343	0.017
Fill + 60	Top	7.5	49.5	39.7	3.3	233	0.0161	4.7	249	0.021
Fill + 60	Bottom	7.2	49.6	39.7	3.4	285	0.0126	5.7	316	0.017
Fill + 300	Top	3.2	44.0	50.5	2.2	107	0.0150	2.1	266	0.027
Fill + 300	Bottom	4.6	42.8	50.0	2.6	151	0.0153	3.0	262	0.022

3.12 Steel Fiber Dispersion Testing

Dispersion of fibers throughout UHPC is a necessary part of achieving many of its material properties. In this section, a simple set of tests is described wherein the dispersion of fiber throughout UHPC cylinders was measured. This batch of UHPC, L03, exhibited a relatively fluid rheology with a flow table result after 20 impacts of 9.25 in.

The 3-in. diameter cylinders for these tests were cast without the use of a vibrating table, and some of the cylinders were then impacted on an ASTM C230 flow table. After the cylinders had gained sufficient strength, they were cut in half along their length. Four 1 in.² areas were then marked on the flat face of the cylinders. The delineated areas were located in a line along the length of the cylinder at a 0.5 in. spacing. The fibers contained within each area were then counted.

Five cylinders were tested according to this procedure. Each of these cylinders underwent a different number of impacts on the flow table, ranging from 0 to 100. The fiber counting results are presented in Figure 3.12-A. The results seem to indicate that more fibers tend to be located toward the bottom of each cylinder. Whether this result is caused by the impacts administered on the flow table or if it is an artifact of the method used to pour the UHPC into the cylinder molds is not clear.

Of greater importance is the wide range of fiber concentrations evident throughout the five cylinders. Figure 3.12-B shows the four areas measured on the cylinder that underwent 25 impacts. One green dot has been placed on the head of each individual

fiber. Clearly, casting technique is very important if equal dispersion of fibers throughout the mix is desired.

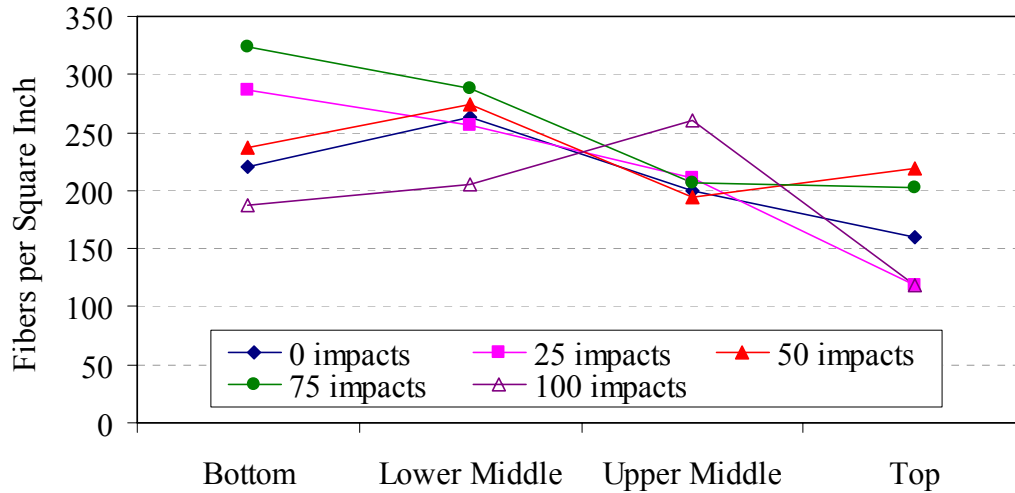


Figure 3.12-A: Fiber dispersion analysis results for cylinders impacted on an ASTM C230 flow table

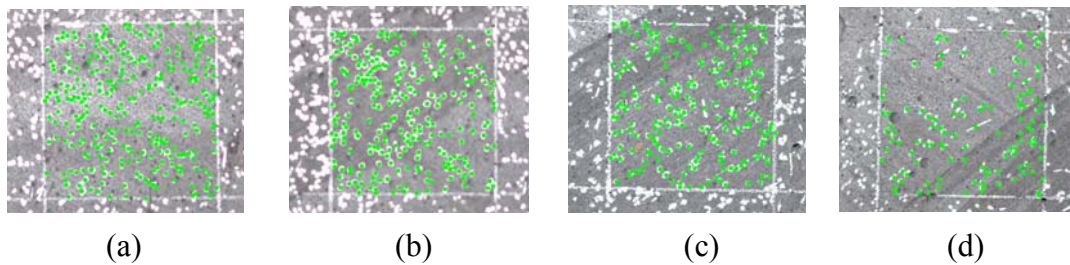


Figure 3.12-B: Fiber dispersion analysis photographs for a 1 in.² area in the (a) bottom, (b) lower middle, (c) upper middle, and (d) top of a cast cylinder

3.13 Durability Testing

A series of durability tests were conducted to determine the resistance of UHPC to various environmental aggressors. These tests included measurement of the chloride ion

penetrability, scaling and freeze-thaw resistance, abrasion resistance, and alkali-silica reaction susceptibility. The results are detailed throughout this section.

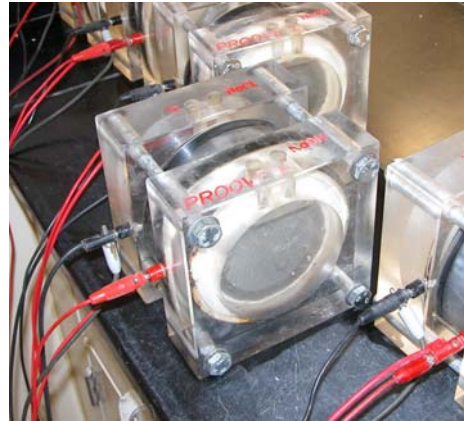
3.13.1 Rapid Chloride Ion Penetrability Testing

The ability of concrete to resist ingress of chloride ions can result in a significantly more durable concrete. The ASTM C1202 test for the Electrical Indication of Concrete's Ability to Resist Chloride Ion Penetration, frequently referred to as the rapid chloride ion penetrability test, was conducted on specimens from the four UHPC curing regimes. This test approximates the resistance that a concrete may exhibit to chloride ion penetration by measuring the amount of electrical current that passes through a 2-in. thick slice of concrete over 6 hours. A 60 Volt DC potential is applied across the slice of a 4-in. diameter cylinder, while a sodium chloride solution is applied to one side of the slice, and a sodium hydroxide solution is applied to the other side.

Figure 3.13.1-A shows a cylinder slice prior to being tested and while a test is in progress. The cylinders were cast and cured following normal procedures. For these tests, each cylinder was cast in a 4-in. diameter mold that was filled to 3 in. After both demolding and the application of any curing treatment, the cylinders were cut to length, and both ends of the cylinder were then ground to create a uniform finish. The outside circumference of each cylinder was sealed with epoxy. The standard amount of steel fiber reinforcement was included in all cylinders. The short, discontinuous nature of the steel fibers in the UHPC matrix allowed for this test to be completed without shortening the circuit or generating significant heat in the ponded fluids.



(a)



(b)

Figure 3.13.1-A: (a) Cylinder and (b) setup for rapid chloride ion penetrability test

Results from these tests are presented in Table 3.13.1-A. Three tests were performed for each curing regime at 28 days after casting. An additional three tests were performed on the Air and Tempered Steam treated regimes at 56 days, because these regimes had exhibited slightly higher results during the first tests.

Aside from the Air treated tests from 28 days, all of the results are in the negligible range as defined by ASTM C1202. Also, the Air and Tempered Steam treated regimes exhibited significant reductions in charge passed between 28 and 56 days. Figure 3.13.1-B shows averaged results for current versus time from three sets of cylinders. For reference, if 0.003 amps of current were passed through the concrete for the duration of the test then the total charge passed would be 65 Coulombs.

Table 3.13.1-A: Rapid chloride ion penetrability results

Curing Regime	Age (days)	No.	Coulombs Passed		Chloride Ion Penetrability
			Average	Standard Deviation	
Steam	28	3	18	1	Negligible
Air	28	2	360	2	Very Low
Air	56	3	76	18	Negligible
Tempered Steam	28	3	39	1	Negligible
Tempered Steam	56	3	26	4	Negligible
Delayed Steam	28	3	18	5	Negligible

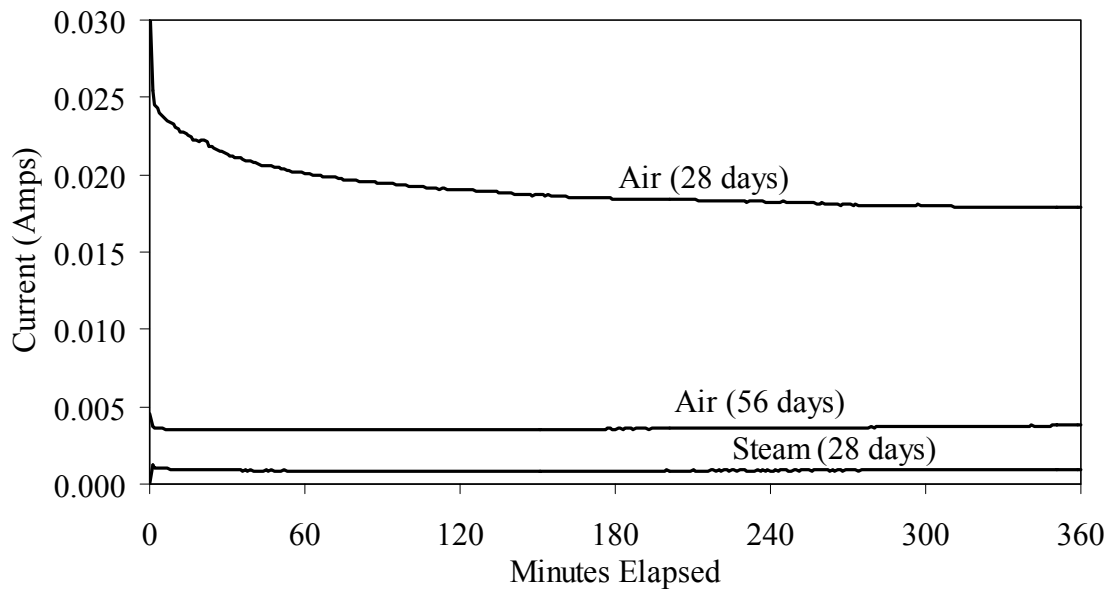


Figure 3.13.1-B: Average current passed versus time results for three sets of cylinders

3.13.2 Chloride Penetration

In conjunction with the chloride ion tests described in Section 3.13.1, standard chloride ion penetration testing was conducted according to the AASHTO T259 specification.

This test, often referred to as the chloride ponding test, entails ponding a 3-percent

sodium chloride solution on the surface of the concrete for 90 days. After 90 days, the level of migration of chloride ions into the concrete is determined.

This test was conducted on three specimens from each of the curing regimes. The specimens were cast in 4-in. diameter steel cylinder molds that were filled at least 3 in. full during casting. After both demolding and the application of any curing treatment, the circumferential surface of each cylinder was coated in epoxy. A section of rubber hose was then slid over the cast face end of the cylinder and affixed with a hose clamp. Finally, 28 days after casting, the sodium chloride solution ponded on the cylinder face. Note that the solution was ponded on the steel mold cast face of the cylinder to replicate the UHPC surface that would have been achieved in a precast concrete production facility.

The AASHTO T260 standard test method was used to sample and test the concrete following the ponding. Samples were taken from each cylinder at depths of 0.5, 1.0, 1.5, 2.0, 2.5, and 3.0 in. from the ponded surface. The samples were obtained by using a drill press with a ¼ in. masonry bit to drill into the side of the cylinder at the correct depth. Approximately 15 grams of the pulverized concrete was captured at each specified depth. The steel fiber shavings were then magnetically removed from each sample of the concrete powder. Thus, at least 10 grams of powder were available for the chloride ion testing.

The chloride ion testing was conducted according to Procedure A, Section 5.2: Procedure for Total Chloride Ion Content. The chlorides were unlikely to penetrate any significant distance into the concrete because of the penetrability of this concrete. This allowed a large collection of background chloride content samples to be obtained at 2.5 in. and 3.0 in. The average background chloride ion content in pounds per cubic yard of concrete was determined to be 0.086 with a standard deviation of 0.007.

Figure 3.13.2-A presents the corrected results for these tests. The removal of the background chloride content from each sample caused some of the samples to seem to exhibit negative chloride ion contents. The AASHTO specification indicates that these results should be rounded up to zero. Overall, the chloride ion content in the UHPC for all of the curing regimes is extremely low. There is some trend toward higher chloride ion contents near the ponded surface; however, the amount of chlorides that migrated into the concrete over 90 days is still extremely small.

An additional benefit of this set of tests is that the behavior of the surface of this steel fiber reinforced UHPC can be qualitatively observed. Figure 3.13.2-B shows a Tempered Steam treated cylinder just before the 90 days of ponding began and 1 day after it concluded. This specimen is representative of all twelve tests that were completed because minor corrosion of steel fibers on and very close to the surface occurred. This corrosion would probably more aptly be described as surface staining caused by exposed fibers. There was no indication that the corrosion of the fibers was progressing into the interior of the UHPC.

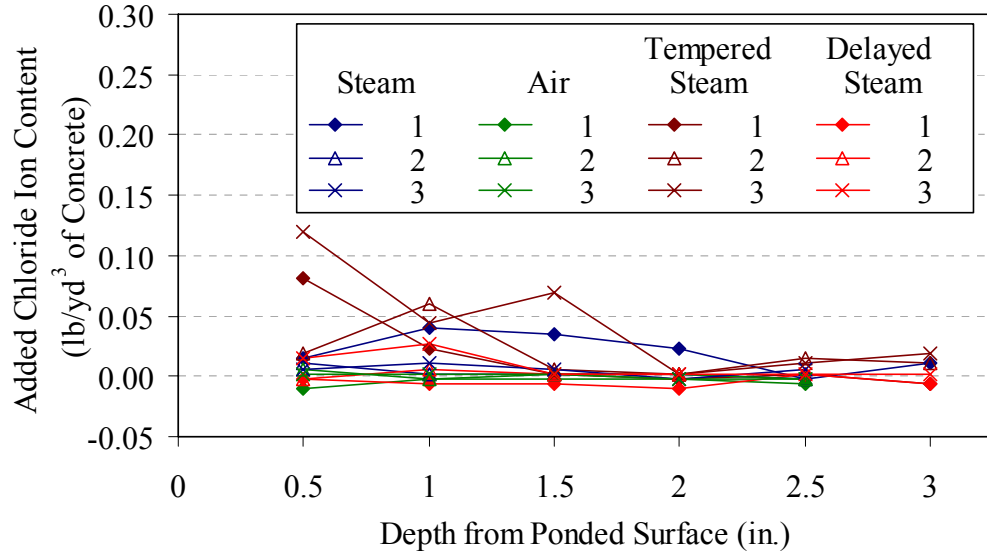


Figure 3.13.2-A: Chloride ion content results after 90 days of ponding



Figure 3.13.2-B: (a) Cylinder prior to and (b) after 90 days of chloride ponding

3.13.3 Scaling Resistance

The UHPC scaling resistance to deicing chemicals was evaluated through the use of the ASTM C672 standard test method. In this test method, a solution of calcium chloride is

ponded on the surface of the concrete. The concrete specimen is then placed in a 0°F freezing environment for 18 hours followed by a 73°F thawing environment for 6 hours. This cycle is repeated daily, while ensuring periodically that the surface of the specimen remains covered in the ponding solution.

The ASTM C672 testing included two slabs from each curing regime. Each slab was cast in a 14 in. by 14 in. square steel mold that was 3 in. deep. The cast surface on the bottom of the slab became the surface to be ponded after demolding. The curing treatments were applied to the slabs, and then the dams were epoxied to the ponding surface. The dams were composed of Steam treated UHPC. A rapid-setting, two-part epoxy was used as the bonding agent slab and the dam. Figure 3.13.3-A shows one of the slabs prior to the initiation of testing. The total exposed ponding area on the surface of each slab was approximately 100 in.².

The testing of these slabs commenced in two phases. In the first phase, a walk-in freezer was used to generate the freezing condition, while the standard laboratory environment generated the thawing environment. The capabilities of this freezer were such that a consistent temperature could not be maintained. Over the course of 4 months, 70 cycles were completed. Up through the fiftieth cycle, the temperature in the freezer was usually below 15°F. For the next twenty cycles, the temperature was usually in between 18°F and 26°F. Due to the inability of this freezer to maintain a sufficiently cold temperature, this phase of the testing was halted. At the cessation of these tests, no scaling was observed on the surface of any of the slabs.



Figure 3.13.3-A: Scaling slab prior to the initiation of ASTM C672 testing

The second phase of the ASTM C672 testing used an environmental chamber to carefully control the freezing and thawing portions of each cycle to within $\pm 2^{\circ}\text{F}$ of the prescribed values. A total of 145 additional cycles were completed on all eight slabs. Every few cycles, the slabs were checked for leaking of the dams and for the proper solution level on the ponded surface. The slabs were also drained, flushed, inspected, and refilled after cycles 20 and 50. No scaling was observed. After cycle 145, the slabs were drained through a #30 sieve to capture any small scaling particles that might have been present. Each slab produced less than 0.5 grams of material, which included small bits of concrete, pieces of epoxy, and other small detritus that had made its way onto the slabs over the course of 95 cycles.

A final inspection of the ponded surface indicated that no scaling had occurred, thus an ASTM C672 surface condition rating of 0 was warranted. No differences were observed between the slabs from any of the four curing regimes. The surfaces did tend to show a slightly rougher texture after testing, with many more of the small air bubbles visible just under the ponded surface. Figure 3.13.3-B shows the same slab that was pictured in Figure 3.13.3-A after having undergone the 70 plus 145 cycles of scaling as described above.



Figure 3.13.3-B: Scaling slab after ASTM C672 testing

Figure 3.13.3-C shows a byproduct of the ASTM C672 scaling tests. Some of the dams on top of the slabs did not properly seal with the slab surface. At the joint, the calcium chloride solution slowly leaked out and ran down the side of the slab. This leak allowed for an extremely aggressive environment on the vertical surfaces of these slabs. Even

after the 70 plus 145 cycles of freezing and thawing in this environment, these vertical surfaces only showed minor surface deterioration of the type shown in the figure. The corrosion of the fibers did not seem to penetrate into the slabs, and no scaling, spalling, or chipping of the concrete surface was apparent.

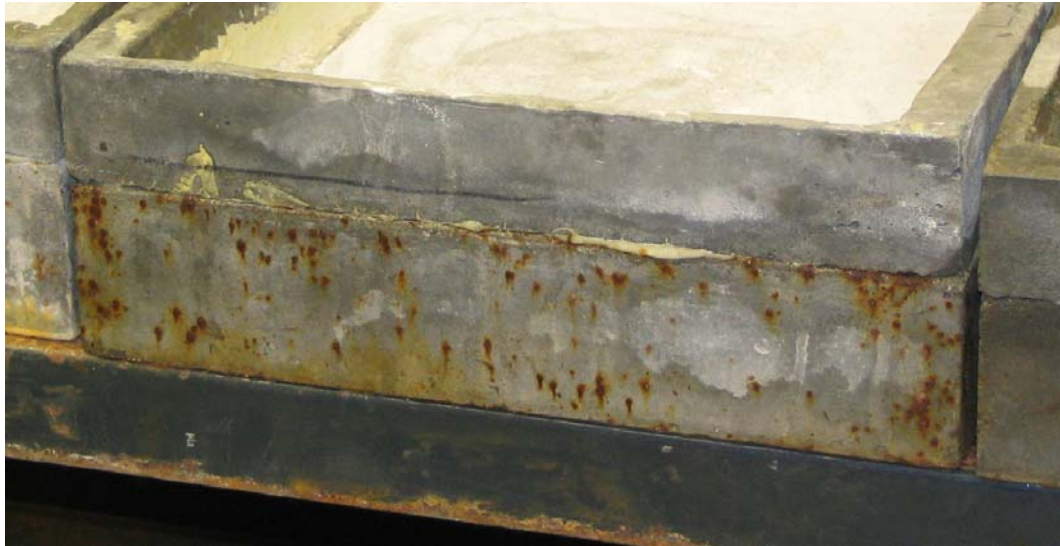


Figure 3.13.3-C: Surface deterioration of a vertical surface after 70 plus 145 cycles of wetting/drying with a chloride solution in a freezing/thawing environment

3.13.4 Abrasion Resistance

The abrasion resistance of UHPC was measured through the standard test method described in ASTM C944. This test determines abrasion resistance by measuring the amount of concrete abraded off of a surface by a rotating cutter in a given time period. The cutter consists of a series of dressing wheels mounted on a rod that is attached to a drill press. Figure 3.13.4-A shows a picture of the cutter head bearing on a specimen. The

drill press is used to apply a constant force through the cutter into the specimen and to rotate the cutter at 200 revolutions per minute.



Figure 3.13.4-A: ASTM C944 abrasion test setup

The test procedure specifies that the force exerted by the cutter on the specimen surface should be 22 lbs. unless the test is conducted on concrete that is particularly abrasion resistant. Preliminary testing on UHPC indicated that doubling the load to 44 lbs. as recommended by the standard would provide better results, thus this load level was used for the testing.

Cylinders with a 6-in. diameter were cast for these tests. The specimens were cast following normal procedures except that steel molds were used, and the molds were only filled approximately 3 in. full. Three cylinders were cast for each curing regime.

The abrasion resistance of a concrete surface will vary depending on the finish of its surface. For this reason, the ASTM C944 test was completed on the finishes of three different concrete surfaces for each of the four curing regimes. The surface finishes included a steel cast surface, a sandblasted surface, and a ground surface. In the test program, the 12 cylinders were all tested in the steel cast surface state. The cylinders were then sandblasted after which they were tested again. Finally, the cylinders were ground and tested a third time.

The ASTM test procedure indicates that the testing should include abrading the surface with the rotating cutter for 2 minutes. At the conclusion of the 2 minutes, the amount of concrete that has been abraded away is reported. In this test program, a modification was made to the test procedure in which the surface abrasion was repeated so that a total of between three and five abrasion sequences, with a duration of 2 minutes each, were applied to each specimen. The number of abrasion sequences varied depending on the abrasion depth capacity of the cutter and the resistance of the specimen.

Figure 3.13.4-B shows two of the steel cast surface specimens after abrasion testing. The Air treated cylinder on the left underwent four abrasion sequences that lasted 2 minutes each. The Steam treated cylinder on the right underwent five abrasion sequences that also lasted 2 minutes each. The photo clearly shows that the steel cast surface of Steam treated UHPC is much more abrasion resistant than the Air treated UHPC. The rotating cutter had difficulty breaking into the surface on the Steam treated cylinder and tended to skid, with only slight abrasion occurring near the center of rotation.



Figure 3.13.4-B: Steel cast surface Air and Steam Treated abrasion specimens after 8 and 10 minutes of abrading, respectively

The results for the ASTM C944 abrasion testing are presented in Figures 3.13.4-C through 3.13.4-E. Throughout these figures, the results for each curing regime and surface condition set are the averages of the results for the three cylinders tested. Figure 3.13.4-C presents the ASTM C944 abrasion weight loss as defined in the test specification. As detailed above, this result only includes the first 2 minutes of abrading for each specimen. The other two figures present the results from the entire sequence of tests completed on each specimen. Figure 3.13.4-D presents the average amount of concrete per abrading over the sequence of abradings. Figure 3.13.4-E presents the least-squares linear approximation of the weight loss per abrading.

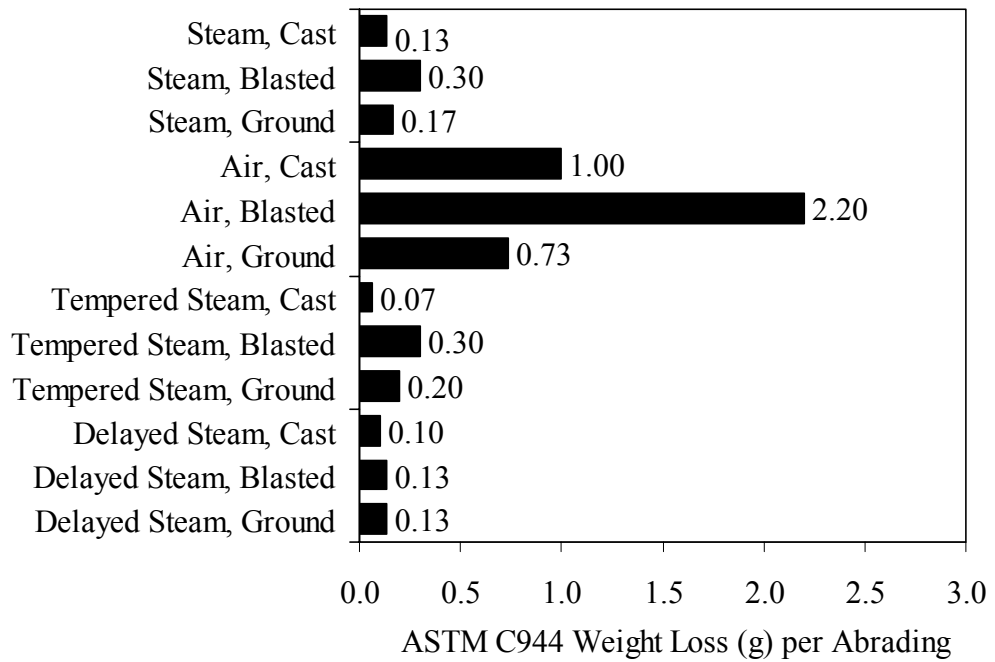


Figure 3.13.4-C: ASTM C944 weight loss (grams) per abrading

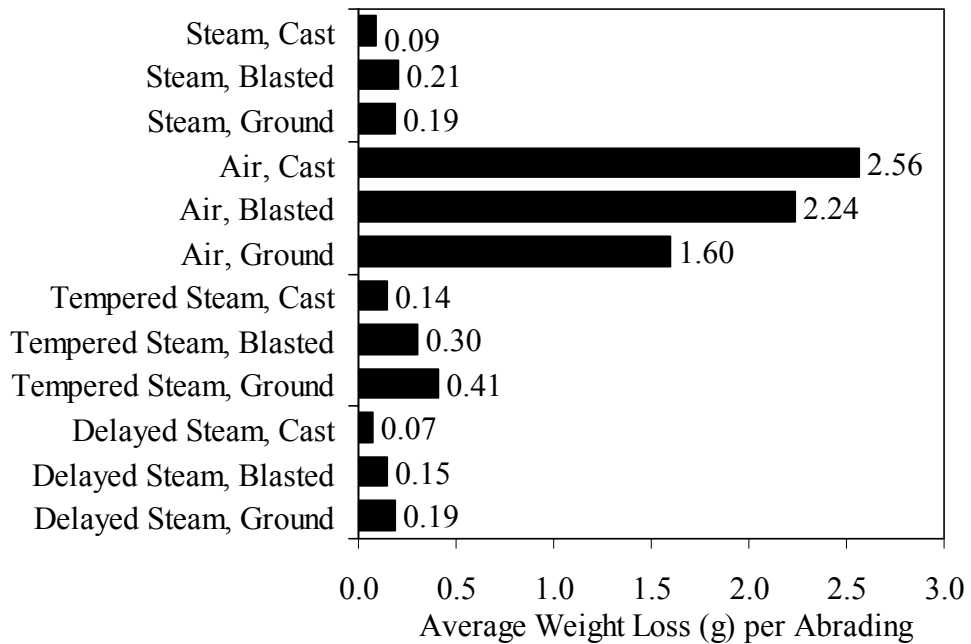


Figure 3.13.4-D: Average weight loss (grams) per abrading

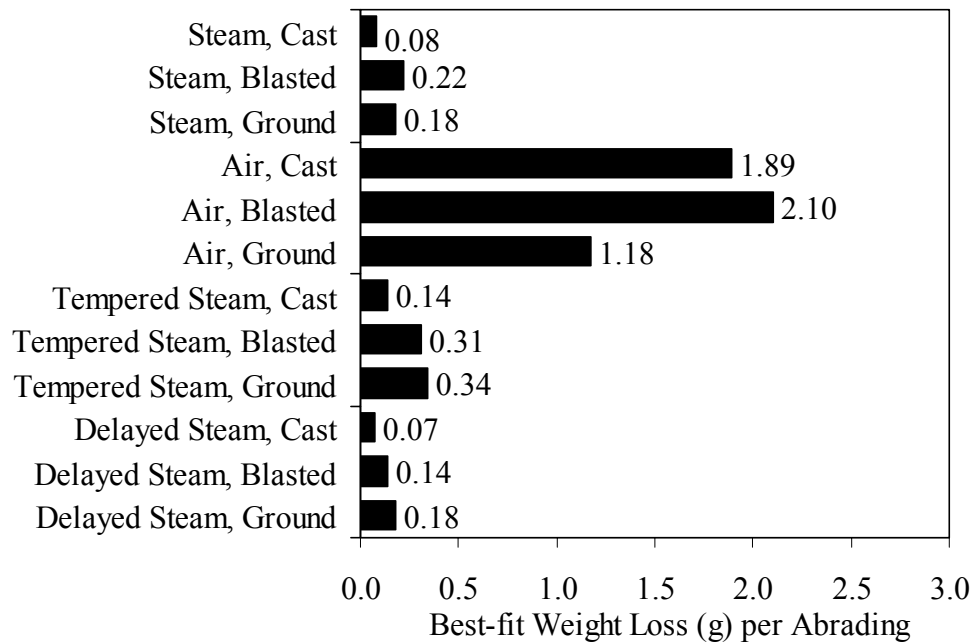


Figure 3.13.4-D: Linear best-fit weight loss (grams) per abrading

These results show that a steam-based curing treatment of any kind has a significant impact on the abrasion resistance of UHPC. In general, the Air treated cylinders lost approximately an order of magnitude more concrete per abrading than did any of the other cylinders. Quantitatively, the steam-based treated cylinders usually lost between 0.1 and 0.3 grams per abrading while the Air treated cylinders usually lost between 1 and 3 grams per abrading. Also, as would be expected given its smoother texture, the steel cast surface performed the best compared with the sandblasted and ground surfaces.

These results can be compared to the results from Horszczaruk (2004) presented in Section 2.4.5. The testing of 12 ksi to 14.5 ksi steel fiber reinforced concretes produced results ranging from 0.14 grams to 0.25 grams of mass loss per abrading for the more

abrasion resistant concretes. (These results are directly comparable to the UHPC results presented in 3.13.4-D.) However, these results are based on ASTM C944 with the standard 22 lb. load, as opposed to the double load used in the present research program. The UHPC mass loss would have been significantly lower with the decreased abrasive normal force on the cutter head. Also, note that Horszczaruk's research indicated that higher strength concretes exhibited constant abrasion resistance, from test initiation until conclusion. This seems not to be the case with UHPC, which displayed increased abrasion resistance prior to the breaching of the smooth cast surface.

3.13.5 Freeze-Thaw Resistance

The resistance of UHPC to freezing and thawing degradation was quantified through the use of the ASTM C666 (Procedure A) standard test method. In this test, concrete prisms are subjected to freezing and thawing while submerged in a water bath. The aggressive environment created in this accelerated durability test helps to determine if the concrete has a microstructure that can resist the thermal expansion and contraction effects of water. The concrete could achieve this resistance by either resisting the initial water penetration or by allowing the thermal expansion of any penetrated water to occur within a voided microstructure.

The specified lower and upper temperature value targets for the freezing and thawing environments are 0°F and 40°F, respectively. The automated equipment used in this test program allowed for five cycles of freezing and thawing to be completed per day. In this test method, each prism is housed in a water-filled container that is only slightly larger

than the prism itself. The containers are placed in an environmental chamber that freezes the prisms and their surrounding water layer using cold air and then thaws the prisms using water.

The 3 in. by 4 in. by 16 in. UHPC prisms produced for this test were cast following normal procedures. Three prisms were cast for each curing regime. After casting, any curing treatments were applied. The freeze/thaw testing began between 5 and 6 weeks after casting, following 2 days in which the prisms were submerged in 40°F water to prepare them for the initial test measurement. In total, 690 cycles of freezing and thawing were conducted over the course of 9 months. During stoppages in testing, the prisms were stored in a frozen state in a walk-in freezer. In a few instances, however, machine malfunctions did allow the prisms to soak in room temperature water for up to a few days until the malfunction was corrected.

Periodically, the freeze/thaw cycling was halted, and the prisms were measured. The data collection included mass determination and capture of the fundamental transverse frequency of each prism. Figure 3.13.5-A is a photograph showing the setup used to determine the fundamental or resonant frequency. In this test, a transducer records the vibrations induced in a prism supported on two wires by an instrumented hammer. The capture and determination of this frequency response was completed according to ASTM C215.

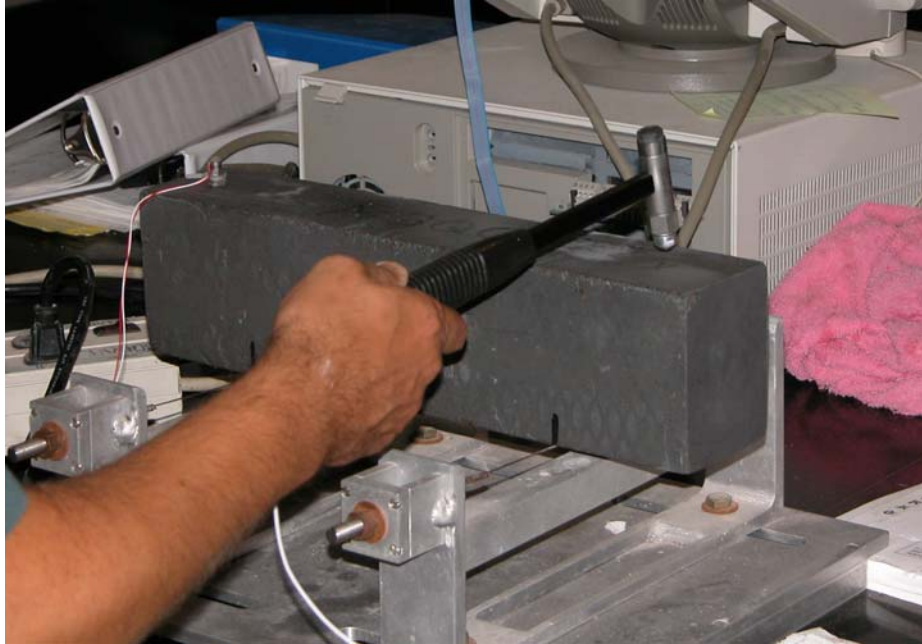


Figure 3.13.5-A: Resonant frequency testing of a freeze/thaw prism

Figure 3.13.5-B presents pictures of an Air treated prism both before and near the end of testing. The second photograph shows that the prism experienced some deterioration of fibers that were exposed on the surface. Also, the surface of the prism tended to become slightly pitted as the cycling progressed. Overall, this pitting was very minor and was much more prevalent on the Air treated prisms than on any of the steam treated regimes.

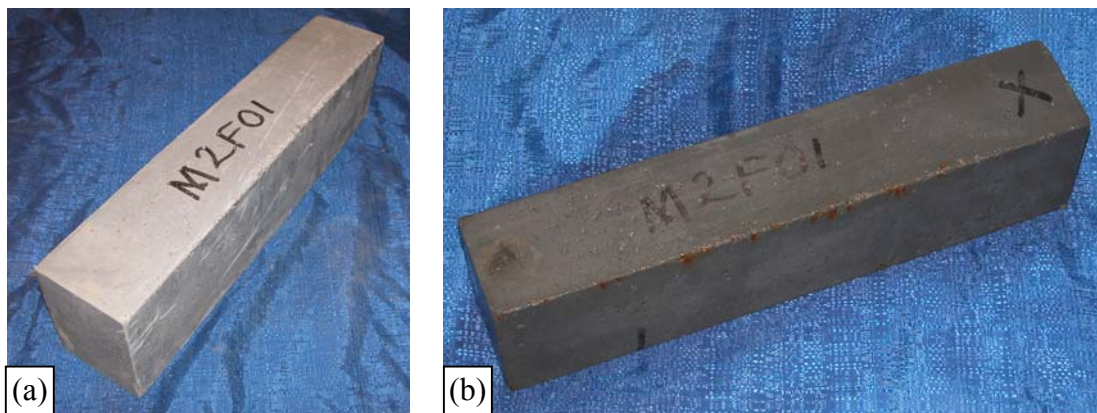


Figure 3.13.5-B: Freeze-thaw prism (a) before testing and (b) after 564 cycles

The resonant frequency results from this test program are presented in Figure 3.13.5-C. These results are the average values from the three prisms that were tested for each curing regime. Note the clear difference between the initial resonant frequency results from each curing regime. All prisms in each regime resonated within 16 Hz of one another, indicating a tight band of results.

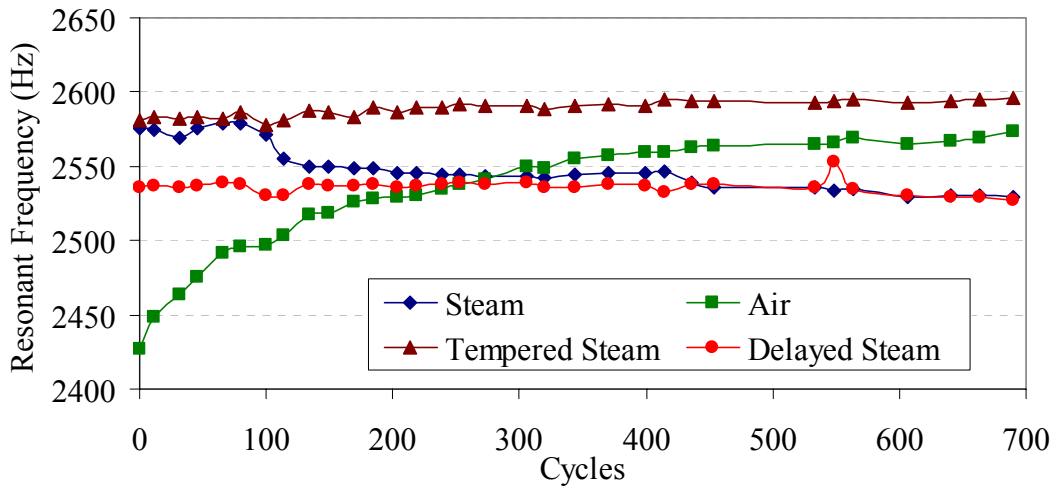


Figure 3.13.5-C: Resonant frequency of freeze/thaw prisms

The relative dynamic modulus (RDM) is a value defined in the ASTM C666 test method as the percent difference in the squares of the frequency at any cycle compared with the initial frequency before freeze/thaw cycling. This calculation normalizes the results for ease of comparison to other tests. Figure 3.13.5-D shows these results. In general, this test method assumes that freeze-thaw cycling will cause the RDM to decrease as the concrete deteriorates. This RDM decrease would occur due to the resonant frequency decreasing as the prism develops internal microcracking. The figure shows that the RDM changed very little in the Tempered Steam and Delayed Steam regimes, decreased

slightly in the Steam treated regime, and increased significantly in the Air treated regime. Overall, these results confirm that UHPC is very resistant to deterioration caused by freezing and thawing. However, it is premature to conclude that the Air treated UHPC exhibits the best freeze-thaw resistance because these RDM values are being influenced by other factors beyond those intended in the test.

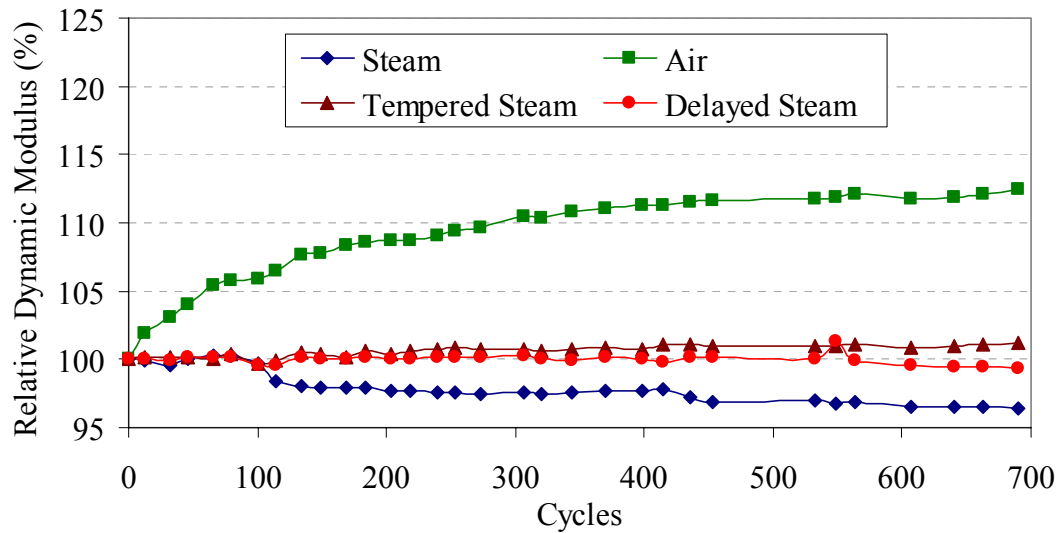


Figure 3.13.5-D: Relative dynamic modulus of elasticity of freeze/thaw prisms

One indicator that an additional unintended behavior was occurring during the freeze-thaw cycling was the mass change exhibited by the prisms. Figure 3.13.5-E presents the mass change results. All the regimes exhibited mass increase throughout the testing, with the Air treated prisms averaging a 0.2% increase by 125 cycles. In a normal freeze-thaw test, a prism will lose mass as it deteriorates. As mentioned previously, these prisms showed very little deterioration throughout the test. However, it seems that instead of

deteriorating during the cycling, these prisms were taking on water and possibly even hydrating.

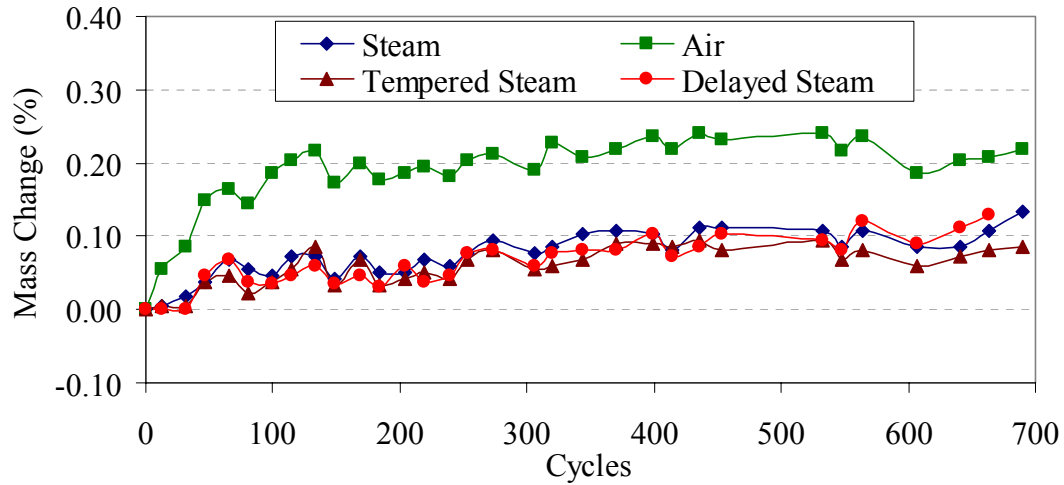


Figure 3.13.5-E: Mass change of prisms during freeze-thaw testing

Further experiments were conducted to investigate the increase in RDM in the Air treated prisms. To determine if the prisms were taking on water and possibly hydrating, an additional batch of eight prisms were cast. This batch included two prisms that were treated according to each curing regime. After 28 days, initial freeze-thaw measurements were completed on the prisms, and then one prism from each curing regime was placed in a water bath. The other prism from each curing regime was maintained in a laboratory environment. The prisms were kept under these conditions for 250 days, during which mass and dynamic modulus of elasticity testing was periodically completed.

The resonant frequency results from these eight prisms are presented in Figure 3.13.5-F. The RDM results are presented in Figure 3.13.5-G. The legend for each series indicates

the curing regime and whether the prism was placed in air or water after day 28. These figures show that for the three steam-based treatment regimes, a steady increase in frequency occurred throughout the testing in the prisms maintained in the laboratory environment. The submerged prisms from these same regimes show a more rapid increase initially followed by the same type of steady increase. The Air treated prisms show different behavior, with the submerged prisms exhibiting a rapid increase in frequency response during the first 10 days and both Air treated prisms showing large overall increases in frequency response. The mass change of these prisms is also instructive, with the results provided in Figure 3.13.5-H. The masses on all of the prisms increased throughout the testing, with the Air treated prisms tending to show a larger increase than their counterparts in the three steam-based treatment regimes.

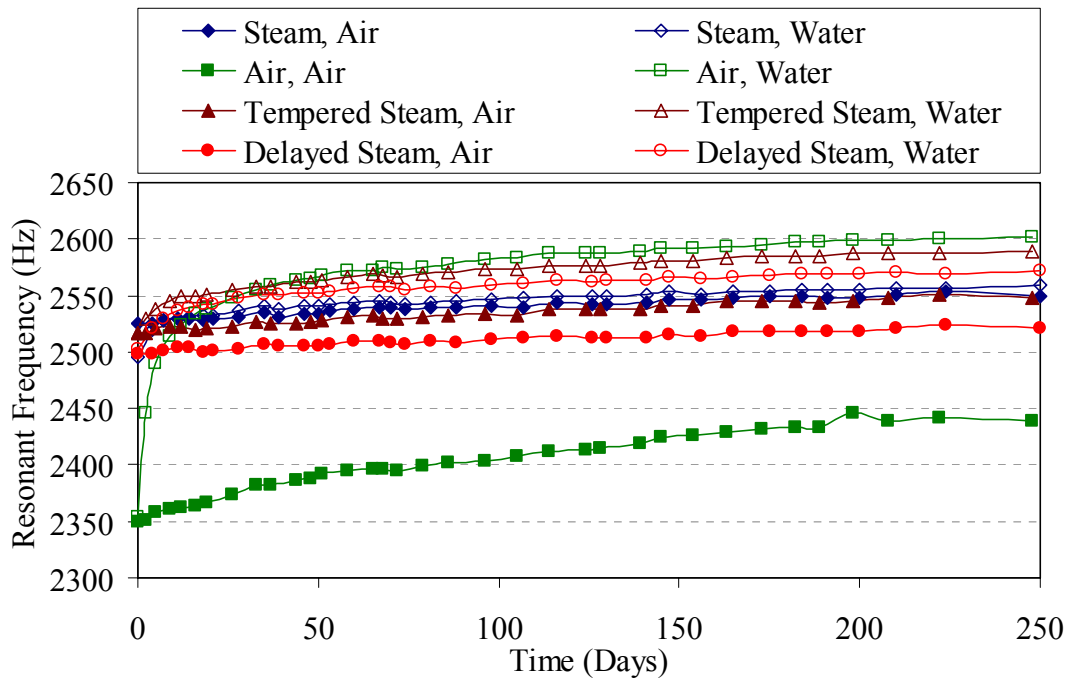


Figure 3.13.5-F: Resonant frequency of prisms maintained at room temperature in a laboratory environment or in a water bath

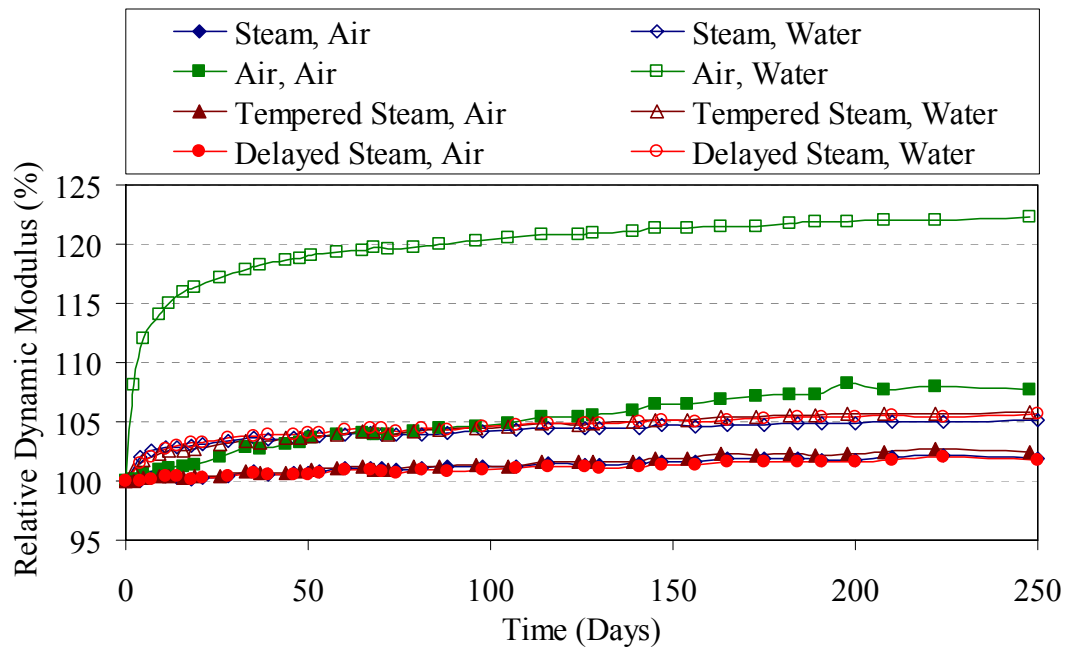


Figure 3.13.5-G: Relative dynamic modulus of elasticity of prisms maintained at room temperature in a laboratory environment or in a water bath

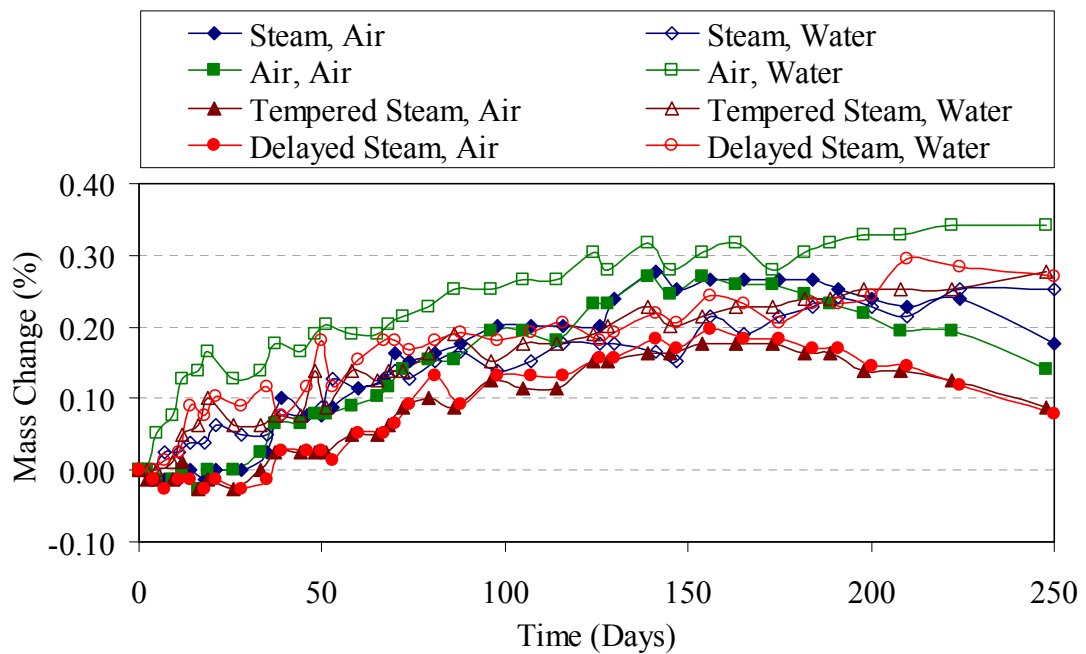


Figure 3.13.5-H: Mass change of prisms maintained at room temperature in a laboratory environment or in a water bath

One final experiment was conducted to determine if the prisms were hydrating as they were gaining water. A set of 3-in. diameter cylinders were cast along with the eight prisms previously discussed. These cylinders were divided into four groups, paralleling the conditions that the prisms in the Air and Steam treatment regimes underwent through the 56th day after casting. An additional two sets of control cylinders were cast for testing in compression at 28 days.

Table 3.13.5-A: Effect of a water bath on the compressive strength of Steam and Air treated UHPC

Curing Regime	Subsequent Environment	Age (days)	No.	Compression Strength	
				Average	Standard Deviation
Steam	N/A	28	4	20.77	0.72
Steam	Air	56	5	21.69	0.59
Steam	Water Bath	56	5	22.20	1.16
Air	N/A	28	4	15.25	0.20
Air	Air	56	5	15.64	0.74
Air	Water Bath	56	5	17.44	1.18

These compression results show that placing UHPC in a water bath can increase the compressive strength. As would be expected, the strength increase is greater in the Air treated UHPC than in the Steam treated UHPC. This greater increase is likely partially due to the greater permeability of the Air treated UHPC.

These additional tests, which were completed following the initial freeze-thaw testing, have shown that the procedure followed for the freeze-thaw testing could lead to unintended water permeation and to additional hydration of the UHPC. This effect has been shown to be limited in the steam-based treatment curing regimes; however, it can be

significant in the Air treated regime. The added hydration creates the possibility of a 15% increase in the RDM if a prism spends 250 days in a water bath and a 10% increase in compressive strength if a cylinder is placed in a water bath from day 28 to 56.

3.13.6 Alkali-Silica Reaction

Alkali-silica reaction (ASR) testing was performed in accordance with ASTM C1260. This accelerated test method allows for the possible detection of the deleterious effects of ASR far more rapidly that could be achieved using the standard test method, ASTM C1293. The ASTM C1260 test involves submerging mortar bars in an 80°C sodium hydroxide solution for 2 weeks, while periodically measuring the length of the bar. This series of tests were extended to 4 weeks.

Standard mortar bar molds were used to cast the specimens for this series of tests. Because this UHPC contains no coarse aggregate, no special preparation of the batch ingredients was necessary before casting of the bars. Six mortar bars were cast for each curing condition. The mortar bars had a 1 in. by 1 in. cross-section and were 11 in. long. The bars had gage studs cast into each end so that ASTM C490 length change measurements could be recorded throughout the testing. Figure 3.13.6-A shows one of the mortar bars in the length comparator for measurement.



Figure 3.13.6-A: Length comparator for ASR measurements

The standard test method includes specific instructions regarding timing throughout the test. These instructions include demolding the mortar bars at 24 hours, placing the bars in an 80°C water bath for the following 24 hours, then placing the bars in the 80°C sodium hydroxide solution bath until test completion. Due to the curing regimes being investigated in this research program, the timetable recommended in the standard test method could not be followed. Table 3.13.6-A provides the timetable for each of the five sets of specimens that were tested.

Submerging the UHPC in the 80°C bath is somewhat similar to the steam-based curing regimes wherein the UHPC is placed in a high-heat, high-humidity environment. For this reason, it is anticipated that the test method described in ASTM C1260 may inadvertently provide additional curing to the UHPC, especially UHPC that did not undergo a steam-based curing treatment. Thus, two sets of specimens were tested in the Air treated curing

regime. In what is deemed the Air (standard) set in Table 3.13.6-A, the ASR testing was not initiated until 28 days after casting. In the Air (modified) group, the ASR testing was initiated immediately after demolding.

Table 3.13.6-A: Timetable for ASTM C1260 specimens

Curing Regime	Demold	Curing Treatment	24 hr Water Bath	NaOH Bath Start
Steam	25 hrs	26 th – 74 th hr	98 th – 122 nd hr	122 nd hr
Air (standard) [†]	25 hrs	25 th hr – 28 th day	28 th – 29 th day	29 th day
Air (modified) [‡]	26 hrs	None	26 th – 51 st hr	51 st hr
Tempered Steam	26 hrs	26 th – 74 th hr	98 th – 122 nd hr	124 th hr
Delayed Steam	26 hrs	15 th – 17 th day	18 th – 19 th day	19 th day

[†] ASR testing initiated 28 days after casting

[‡] ASR testing initiated 26 hours after casting

Table 3.13.6-B presents the results from this series of tests. The standard test method indicates that expansion values less than 0.10% after 14 days of testing are indicative of innocuous behavior, whereas expansion values over 0.20% are potentially deleterious. The UHPC expansion results are an order of magnitude below this lower threshold after 14 days and even after 28 days of testing. Figure 3.13.6-B presents the entire set of test results, including approximately 10 length readings for each curing regime throughout the 28 days of testing.

These results indicate that there should be no concern of ASR problems with the concrete after a steam-based curing regime is applied. Given the procedures used in this test method to check for ASR susceptibility, an Air treated UHPC may not be as resistant to ASR as determined in these tests. However, for ASR to occur in any concrete, free water

must be present. Given the low permeability of UHPC, it seems unlikely that ASR would be an issue under any curing regime.

Table 3.13.6-B: ASTM C1260 alkali-silica reactivity expansion results

Curing Regime	Bars Tested	14-day Expansion (%)		28-day Expansion (%)	
		Average	Standard Deviation	Average	Standard Deviation
Steam	6	+0.013	0.008	+0.009	0.005
Ambient Air [†]	6	+0.011	0.002	+0.012	0.002
Ambient Air [‡]	6	-0.004	0.002	+0.012	0.001
Tempered Steam	6	+0.005	0.002	+0.004	0.003
Delayed Steam	6	+0.001	0.002	+0.002	0.002

[†] ASR test initiated 28 days after casting

[‡] ASR test initiated 1 day after casting

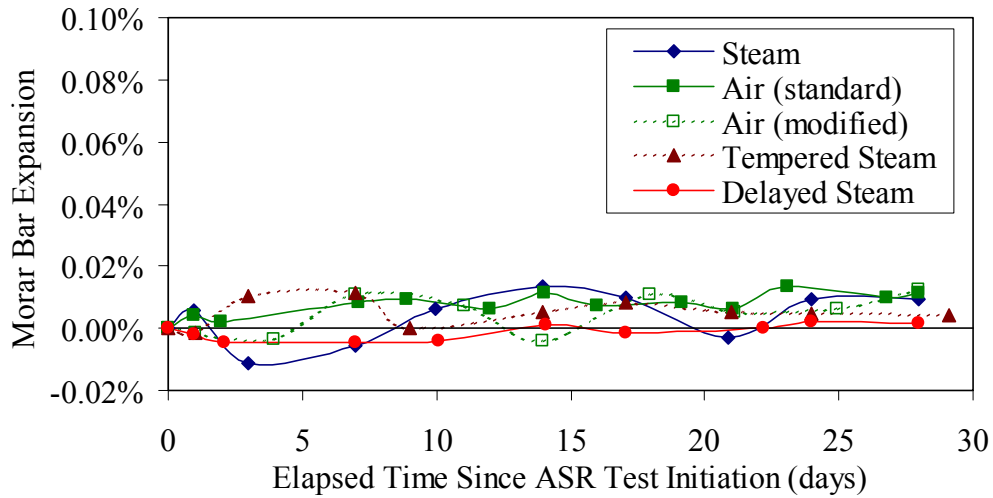


Figure 3.13.6-B: ASTM C1260 alkali-silica reactivity expansion results

3.14 Split Cylinder Tension Testing on Cracked Cylinders

Any material that is affected by external environmental aggressors will necessarily be more affected by those aggressors if pathways into the interior of the material are present.

The durability of uncracked UHPC has been well covered by the topics discussed in Section 3.13. However, in some applications cracked UHPC could be subjected to aggressive environments. The cracks could allow for ingress of contaminants and for a more rapid deterioration of the UHPC than would be expected based on uncracked durability results. Recall the research presented in Section 2.4.3 wherein Rapoport et al. (2002) indicated that the permeability of fiber reinforced normal concrete could be increased by cracking if the cracks were larger than 0.004 in.

To begin to assess the durability of cracked UHPC, a series of tests were conducted to determine if the ponding of a sodium chloride solution on cracked UHPC would negatively impact the post-cracking tensile strength. Although these tests are not standardized, they are a combination of the ASTM C496 split cylinder tensile tests discussed in Section 3.4.2 and the AASHTO T259 ponding tests discussed in Section 3.13.2. The split cylinder tensile test portion of this program was conducted identically to the tests discussed earlier in the chapter, including the measurement of lateral deformation using a pair of LVDTs. The only difference was in the staging of the test wherein specimens were not necessarily loaded directly to failure (as will be discussed below). The ponding portion of these tests was identical to the AASHTO T259 tests described previously.

This series of tests included thirty cylinders with a 4-in. diameter; half of the cylinders came from batch L1R and half came from L2R. Only the Steam and Air treated cases

were investigated. The casting and curing of the specimens followed standard procedures, and the testing discussed herein was initiated on the 28th day after casting.

The fifteen cylinders from each batch were divided into five groups of three. The first group of cylinders, the control group, was loaded to failure. The second group was loaded until cracking had occurred, then unloaded, then reloaded to failure. The third group was loaded identically to the second group, except that after unloading the cylinders were stored in a laboratory environment for 90 days. The fourth group was identical to the third group except that, during the 90 day storage, water was ponded on a cracked end of the cylinder. Finally, the fifth group was identical to the fourth group, except that a 3% sodium chloride solution was ponded on a cracked surface.

The cracking of each cylinder was determined by monitoring the lateral deformation behavior. The two means of determining if a crack had occurred included a clear jump in the lateral deformation or a definite reduction in stiffness of the load versus lateral deformation response. Most cylinders exhibited a clear jump in their response, but a few Air treated cylinders only exhibited the stiffness change. Cylinders from the second through the fifth groups were unloaded immediately after cracking was observed.

The cracks on these specimens were then identified and measured using an optical microscope. First, alcohol was used as a volatile penetrant to highlight each crack. A crack that was made visible using this technique can be seen in Figure 3.14-A. The cracks were then located using the microscope set at 350x magnification. In general, each end of

each cylinder only had one crack. Once located, each crack was traced to find its largest width. The cracks were then photographed for later analysis of the crack widths. A photograph of a crack from one of the Steam treated cylinders is shown in Figure 3.14-B. At this optical magnification and given the resolution of the digital photograph acquired, the crack shown in this figure is only 2 pixels wide, corresponding to a width of 0.00014 in.

The crack widths on the ponded faces of the twelve ponded cylinders ranged from 0.0007 in. to 0.00047 in. Ten of the twelve cylinders had crack widths between 0.00014 in. and 0.00027 in. Table 3.14-A provides the crack width and split cylinder peak strength results for the cylinders that were ponded.

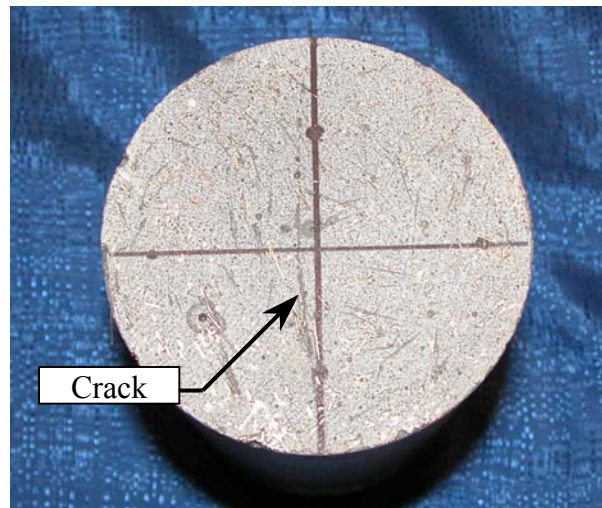


Figure 3.14-A: Crack in a split cylinder tensile specimen

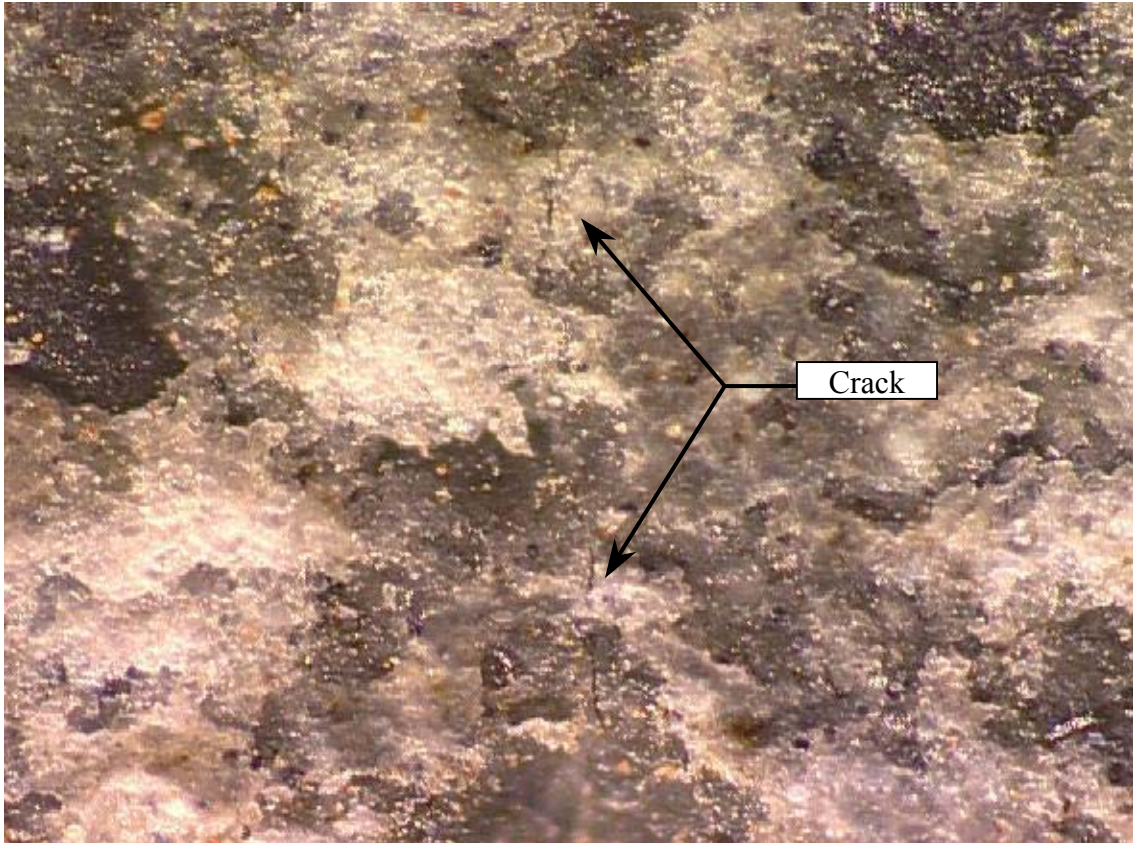


Figure 3.14-B: Crack in a split cylinder tensile specimen under 350x magnification

Table 3.14-A: Crack width and split cylinder peak strength results for ponded cylinders

Curing Regime	Ponding Solution	Cylinder Number	Crack Width (in)		Split Cylinder Peak Strength (ksi)
			Ponded End	Nonponded End	
Steam	Water	1	.00020	.00014	3.39
Steam	Water	2	.00027	.00014	3.74
Steam	Water	3	.00027	.00014	3.10
Steam	NaCl	1	.00014	.00020	3.21
Steam	NaCl	2	.00014	.00007	3.58
Steam	NaCl	3	.00014	.00007	3.89
Air	Water	1	.00047	.00020	2.84
Air	Water	2	.00027	No Crack	3.19
Air	Water	3	.00020	.00014	2.94
Air	NaCl	1	.00007	No Crack	3.21
Air	NaCl	2	.00020	.00020	3.12
Air	NaCl	3	.00020	.00014	3.17

The results of these tests indicate that the ponding of either the water or the sodium chloride solution had little effect on the peak tensile load carried by the cylinders. Figure 3.14-C provides the post-cracking strength results for all five groups of cylinders for both curing regimes. The peak load carried shows no clear change, and it is clear that the ponding of the water or the sodium chloride did not have a serious detrimental effect on the fibers crossing the crack in each cylinder. However, it must also be noted that the sodium chloride solution did cause corrosion of fibers exposed on the ground end of the cylinder, similar to what was observed in the AASHTO T259 and ASTM C672 tests. Further research into the permeability of cracked UHPC is necessary to determine what crack size results in a change in the permeability characteristics of the material.

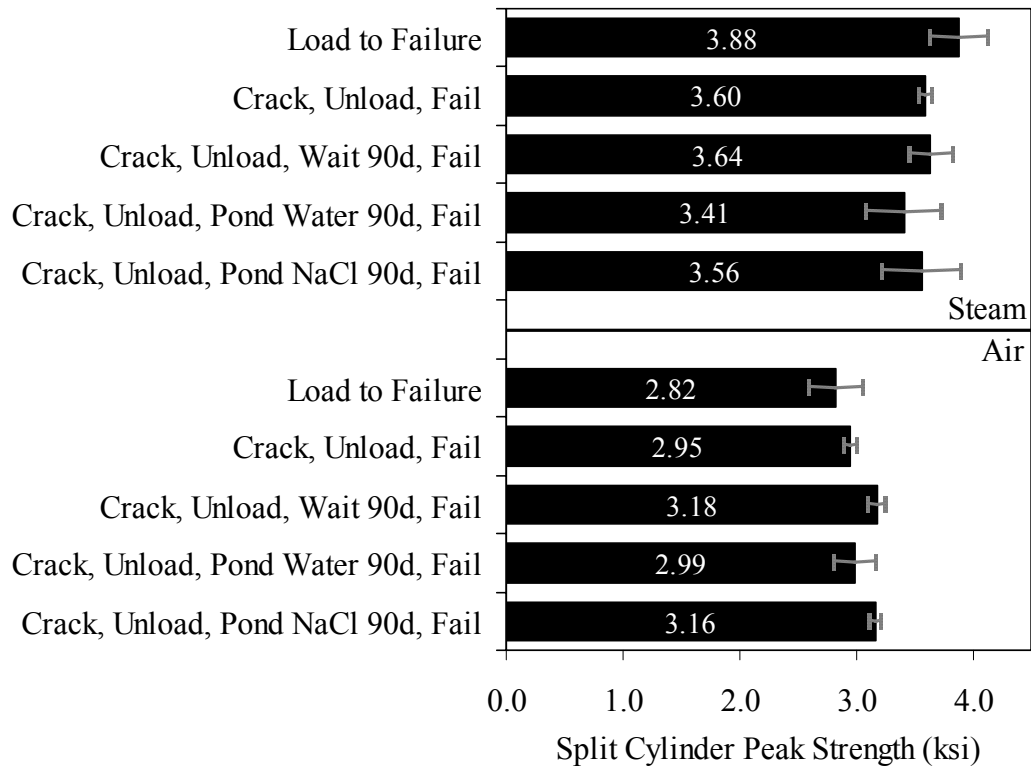


Figure 3.14-C: Split cylinder peak strength results

CHAPTER 4

GIRDER MATERIAL PROPERTIES

4.1 Test Specimen Casting, Harvesting, and Preparation

The initial UHPC AASHTO Type II girder test program included a limited amount of work on material characterization. During the casting of the two girders, which will be discussed in Chapter 5, a total of three cylinders and three prisms were cast for future testing. The cylinders had a 3-in. diameter, and the prisms were 2 in. by 2 in. by 11 in. The limited availability of test specimens increased the importance of each specimen. It also forced the use of specimens harvested from undamaged areas of the girders after the girder tests were completed. Both the cores and prisms were cut from the girders. The method used is described below.

The cast cylinders and prism molds were filled according to standard fiber reinforced concrete casting methods (these methods are described in Chapter 3). These specimens were treated to the same curing environment that was used for the girders throughout the fabrication process. The prisms required no special preparation, while the cylinders had their ends cut and ground to ensure parallel loading surfaces. This process resulted in 3-in. diameter cylinders with approximately 5-in. lengths.

After the girder tests were complete, cores and prisms were harvested from Girder 28S. The web and top flange at the east end of Girder 28S were not damaged during either the testing of this girder or of its parent girder, Girder 80F. Six cores with 4-in. diameters

were obtained by drilling vertically through the top flange of the girder between the strands. An additional sixteen prisms were cut from the web of the girder. These prisms had a nominal cross-section of 2 in. by 2 in., were approximately 16 in. long, and had a long axis that ran parallel to the length of the girder. Finally, five additional cores were drilled from the web of the girder. These cores had diameters of 2.75 in.

The preparation of the harvested cores included grinding the ends of the core, measuring the core to ensure parallel ends, and measuring the length and diameter. This method was similar to the method used within the larger material characterization program. The preparation of the harvested prisms was somewhat more extensive than would be expected for cast prisms. Because these prisms were cut from a large block of UHPC using a diamond saw, the cross-sectional dimensions of the prisms varied and had to be measured. The cut prisms were measured at eight locations along their lengths on all four faces of the prism. The average cross-sectional dimensions for each prism were then calculated.

4.2 UHPC Compression Testing

In total, 14 compression tests were completed on cylinders or cores composed of UHPC that was associated with the two AASHTO Type II girders. In general, these compression tests were performed in a 1000 kip capacity Forney test machine. The lone exception was cylinder “3,” which was tested in a 400 kip capacity Universal testing machine. The cylinders were all loaded at approximately 35 psi/sec as specified in ASTM C39. The

cylinders were all loaded directly to failure. The cores underwent two unloads between 40% and 10% of their projected strengths before being loaded to failure.

Most of the compression specimens were instrumented with resistance-based strain gages prior to testing. These gages were applied either axially or circumferentially on the outside of the cylinder. In general, four axial gages and two transverse gages were used on each specimen to capture the strain response while eliminating errors caused by uneven loading. Table 4.3 lists the strain gage configuration applied to each specimen. Gages with a 0.5-in. length were used in all instances except for cylinder “3,” which had axial gages with a 1-in. length.

Table 4.2-A provides the results from the cylinders and core tests. With the exception of core CW-5, the results show relatively little scatter. These results indicate that the compressive strength is 29 ksi, the modulus of elasticity is 7600 ksi, and the strain at peak strength is 0.0043. In terms of transverse behavior, the Poisson’s ratio is 0.18 with a transverse modulus of elasticity of 42600 ksi.

These UHPC compression tests also reiterated a number of the qualitative findings discussed in Chapter 3. Namely, the cores and cylinders tended to exhibit a dramatic decrease in load carrying capacity soon after the peak load was reached. However, the specimens remained largely intact throughout the failure. Again, this is due to the presence of the steel fiber reinforcement.

Table 4.2-A: Compression test results

Specimen	Strain Gages †	Diameter (in.)	Length (in.)	Strength (ksi)	Strain at Strength	Modulus of Elasticity (ksi)	Transverse Modulus of Elasticity (ksi)	Poisson's Ratio
Cylinder								
1	None	3.0	5.0	27.7	-	-	-	-
2	None	3.0	5.0	28.0	-	-	-	-
3	4A, 2T	3.0	5.1	28.4	0.0043	7340	44500	0.17
Core								
CW-1	4A, 2T	2.76	5.54	31.0	0.0044	7690	41340	0.19
CW-2	4A, 2T	2.76	5.58	28.9	0.0045	7490	43580	0.17
CW-3	4A, 2T	2.76	5.47	28.0	0.0040	7560	42590	0.18
CW-4	None	2.76	5.55	27.8	-	-	-	-
CW-5	4A, 2T	2.76	5.42	32.4	0.0059	6880	40630	0.17
CF-1	4A, 2T	3.98	7.98	28.8	0.0040	7830	41350	0.19
CF-2	4A	3.98	8.06	30.8	0.0045	7370	-	-
CF-3	4A	3.99	8.04	28.5	0.0042	7480	-	-
CF-4	4A, 2T	3.99	7.97	28.7	0.0041	7650	40930	0.19
CF-5	4A	3.98	7.91	28.5	0.0043	7620	-	-
CF-6	4A, 2T	3.98	7.97	30.7	0.0046	7730	43830	0.18

† “A” indicates axial strain gage. “T” indicates transverse gage.

4.3 UHPC Flexural Prism Testing

Monotonic flexural prism testing was successfully completed on two cast and six cut prisms associated with the AASHTO Type II girders. The prisms were all tested in four-point bending in MTS load frames. As previously mentioned, the prisms all had nominal cross-section dimensions of approximately 2 in. by 2 in. The span lengths ranged from 6 in. to 12 in. The cast prisms were oriented in the load frame such that the top and bottom of the prism as cast became the back and front of the prism as tested.

The load rate varied depending on the particular specimen being tested. Some prisms underwent essentially static loading wherein the load level was increased slowly enough so that it took minutes before the cracking load was reached. Other prisms were loaded much more rapidly, at up to 1500 lb/sec.

All prisms were instrumented with at least two resistance-based bonded strain gages on their top and bottom flanges. The gages had either a 0.5 in. or a 1.0 in. gage length and were centered on the midspan of the loading. The gages on the bottom flange served the dual purpose of both indicating the strain level prior to first cracking and recording the first cracking event.

The results from these tests are presented in Table 4.3-A. The cracking strain listed is the average strain recorded in the tension flange of the prism at first cracking. The two values of cracking stress shown are calculated via different, but equally viable, methods. In the left column, the cracking stress is calculated using the cracking strain and the

assumptions of pure bending and the applicability of Hooke's Law. The right column calculates the cracking stress based on the load at cracking, the cross-sectional dimensions, the loading configuration, and the assumption of pure bending. The value presented in the right column corresponds to the tensile stress that would be calculated based on the ASTM standard test methods for prism flexure testing. Because these prisms were all tested on relatively short spans, it is unlikely that either of these methods of calculating the cracking stress is truly accurate. The cracking strain results show that the strain at first cracking is approximately 0.0003. The cracking stress results indicate that an average cracking stress between 2.2 ksi and 2.4 ksi could be expected depending on the method used to calculate the result.

Because these prism flexure tests were not controlled based on the actual deflection of the prism, direct comparisons from post-cracking results obtained here cannot be compared with the results presented in Chapter 3. However, these results are still relevant because they provide information related to the qualitative post-cracking response of UHPC. The load versus MTS recorded cross-head deflection response of cast prism "1" is shown in Figure 4.3-A. The deflection is normalized based on the deflection at first cracking. Note the continued increase in load after first cracking occurs, until a peak load greater than twice the cracking load is reached. In general, the shape of this load-deflection response is very similar to the responses presented in the prism testing section of Chapter 3.

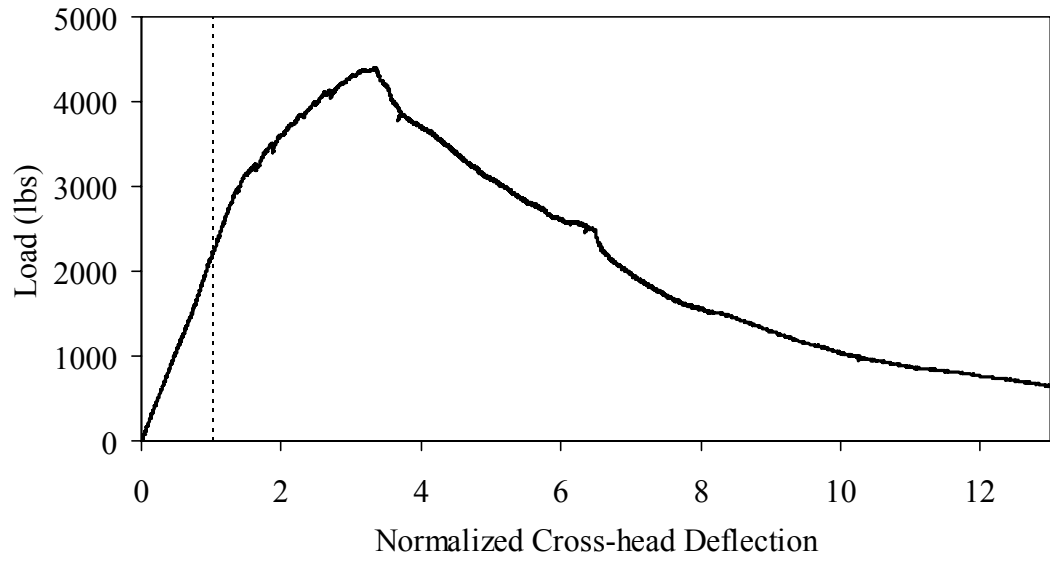


Figure 4.3-A: Third-point loading response of a 2 in. by 2 in. prism on a 9 in. span

Table 4.3-A: Prism flexure test results

Specimen	Width (in.)	Depth (in.)	Span (in.)	Shear Span (in.)	Initial Load Rate	Cracking Strain	Cracking Stress [†] (ksi)	Cracking Stress [‡] (ksi)
Cast								
1	2.0	2.0	9	3	Static	.000341	2.59	2.42
2	2.0	2.0	6	2	Static	.000300	2.28	2.08
Cut								
PW-10	1.95	2.06	12	4.5	Static	.000264	2.01	1.86
PW-12	2.08	2.07	12	4.5	Static	.000255	1.94	1.73
PW-13	1.85	1.90	12	4.5	350 lb/sec	.000310	2.36	2.20
PW-08	2.23	1.80	12	4.5	1500 lb/sec	.000383	2.91	2.60
PW-14	1.90	1.92	12	4.5	1500 lb/sec	.000351	2.67	2.32
PW-15	1.91	2.10	12	4.5	1500 lb/sec	.000315	2.39	2.23

[†] Based on pure bending, Hooke's Law, the cracking strain, and an assumed modulus of elasticity of 7600 ksi.

[‡] Based on loading configuration, cross-sectional dimensions, and load at first cracking assuming pure bending.

CHAPTER 5

GIRDER FABRICATION AND EXPERIMENTAL METHODS

The experimental program—from the girder fabrication through the methods used to test the full-scale UHPC girders—is described in this chapter. The girder fabrication process is described first, followed by a discussion of the test matrix and the test setup. The specific details of each girder specimen and the instrumentation plan for each girder are then presented. Finally, the loading procedure implemented in each test is described.

5.1 Girder Fabrication

Two AASHTO Type II girders were fabricated at Prestress Services of Kentucky, Inc., in Lexington, Kentucky. Normal AASHTO Type II formwork was used in the casting of the girders. The 80-ft and the 30-ft girders were cast end-to-end such that the same strands were stretched through both formworks. These girders did not contain any mild steel reinforcement.

The concrete premix was delivered to the fabricator in large bags that contained all of the non-liquid and non-steel concrete constituents. These constituents were then combined with the water and superplasticizer following the manufacturers recommendations. During the final stage of mixing, the steel fiber reinforcement was added. The overall mixing procedure was very similar to the procedures discussed within the presentation of the UHPC material characterization study results.

The fresh UHPC was transported to the formwork in standard ready-mix concrete trucks and was then poured into the formwork. The 80-ft girder required approximately 8 yd³ of concrete and was placed in three lifts. The 30-ft girder required approximately 3 yd³ of concrete and was cast in a similar fashion. The placement of the UHPC into the form for the shorter girder was completed in approximately 12 minutes. The girders were externally vibrated on an intermittent basis using a formwork vibrator during the casting. Immediately after casting, the exposed surface on top of the girder was covered with plastic.

The curing and steam treatment of the girders was completed during the week after casting. The girders remained covered and were allowed to cure in the ambient atmosphere until they had gained sufficient strength to resist the forces imparted by strand release. After the strands were released, the girders were steam treated for at least 48 hours. The steam treatment was completed through the use of the precast plant's steam generation system that is integral to each casting bed. After treatment, the girders were ready for shipment.

5.2 Test Matrix

As stated in Chapter 1, the objective of this research was to determine the applicability of UHPC to highway bridge superstructure applications. The test matrix, presented in Table 5.2-A, was developed to address this objective. As shown in the table, four girder specimens were tested, all with different overall spans and shear spans. The girder designations shown in the table will be used throughout this text. These designations

provide a general indication of the overall span length (in feet) and whether the test focused on shear or flexural behavior.

Table 5.2-A: Test matrix

Girder Designation	Behavioral Focus	Girder Section	Overall Span (ft)	Shear Span (ft)
80F	Flexure	AASHTO Type II	78.5	36.25
28S	Shear	AASHTO Type II	28	6.5
24S	Shear	AASHTO Type II	24	7.5
14S	Shear	AASHTO Type II	14	6

5.3 Test Setup and Specimen Details

The test specimens detailed in the test matrix above were not originally four separate specimens. As described in the girder fabrication account, two AASHTO Type II girders with lengths of 80 and 30 feet were originally cast. The four tests were completed in the same order that the specimens are listed in Table 5.2-A, thus allowing the broken pieces from the flexure test to be used in the subsequent two shear tests. The final shear test used a portion of the 30-ft girder. Figure 5.3-A provides a schematic indicating the origin of the four girder specimens from the original two girders.

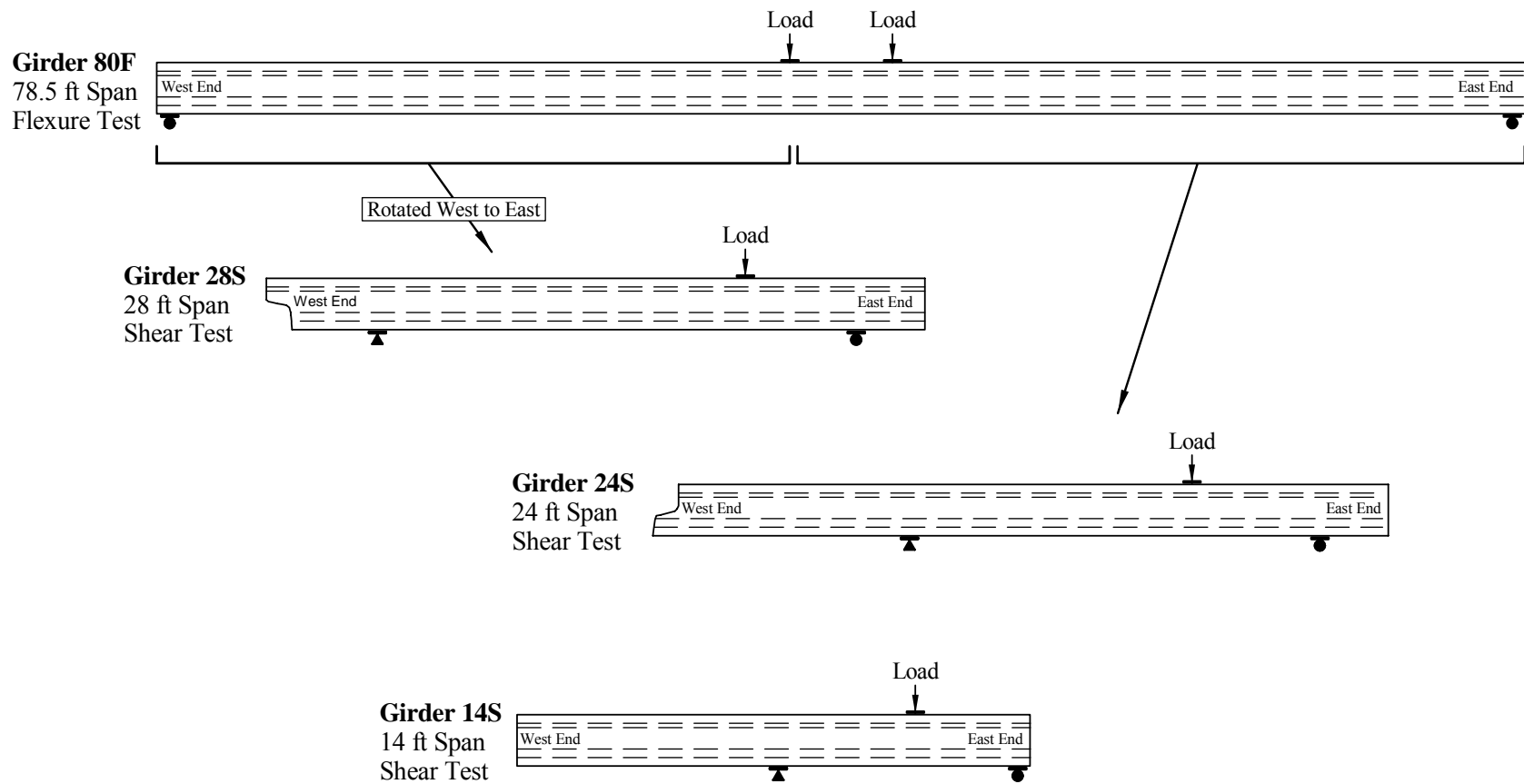


Figure 5.3-A: Origin of the four girder specimens, with the south elevation of the tested configuration shown

The cross-section of an AASHTO Type II girder is shown in Figure 5.3-B. This AASHTO shape is 36 in. deep and has a 12 in. wide top and an 18 in. bottom flange. The girder web is 15 in. deep and is 6 in. thick. These girders each contained twenty-six 0.5-in. diameter 270 ksi low relaxation prestressing strands. Twenty-four of these strands are located in the bottom flange, spaced in a grid pattern on 2 in. spacing. Alternating strands in the bottom flange are debonded for a length of 36 in. from each end of the original two girders.

Generally, AASHTO Type II girders contain significant amounts of mild steel reinforcement, primarily in the form of stirrups and possibly temperature and shrinkage steel. The girders tested in this study contained no mild steel reinforcement. These girders were designed to carry tensile flexural forces primarily via the prestressing strand and to carry tensile shear forces via the fiber reinforced concrete matrix.

Two basic loading configurations were used: one for the flexural test and one for the shear tests. In both configurations, the girder was simply-supported and the load was applied vertically downward through the top flange of the girder. Hydraulic jacks applied the loads.

Girder 80F was loaded symmetrically by two point loads each located 3 feet from midspan. The simple supports, each located 39.25 feet from midspan, were rollers that allowed for independent movement of the ends of the girder. The bearings were centered

9 in. from the ends of the girder. Prior to testing, this girder had a camber of approximately 2.5 in. at midspan.

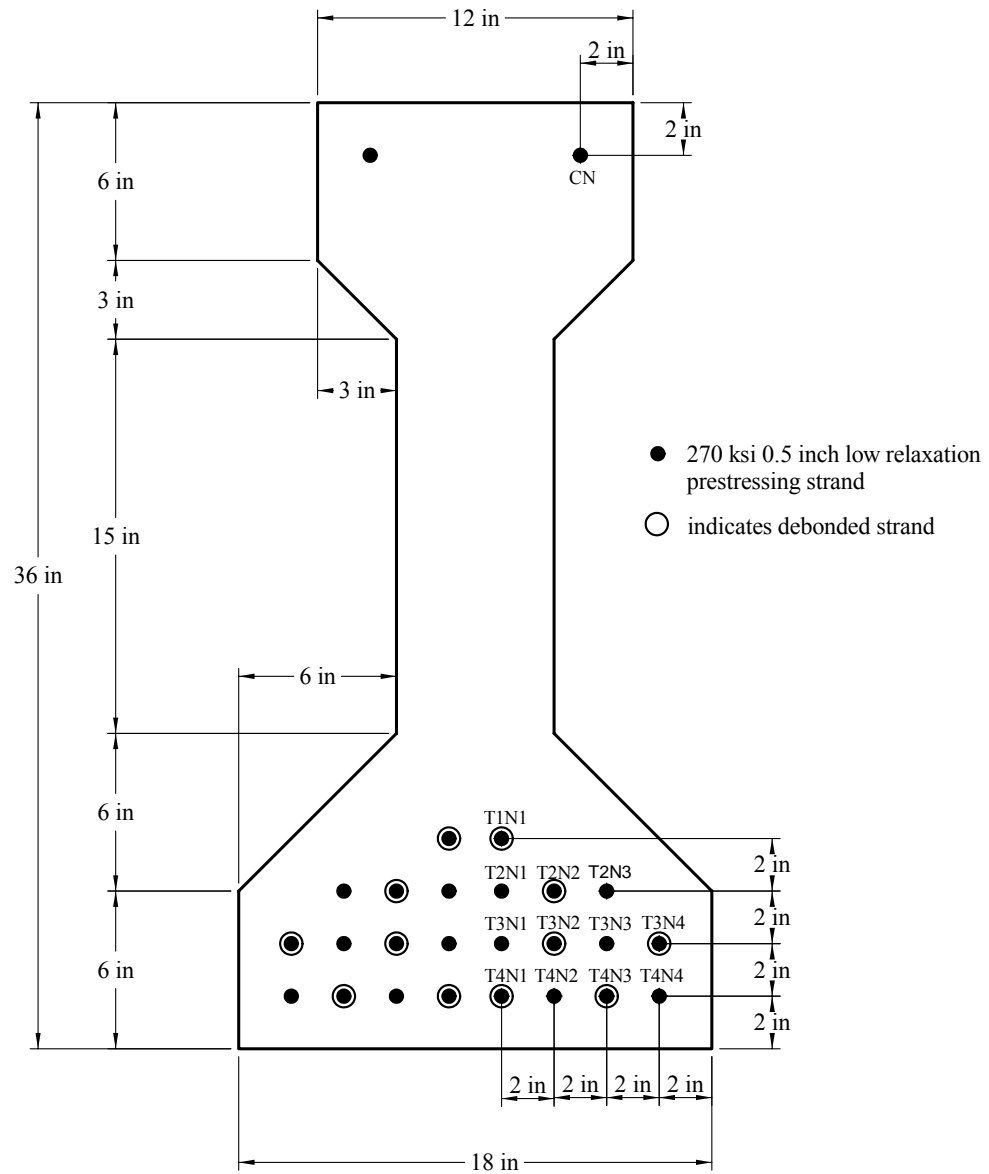


Figure 5.3-B: AASHTO Type II cross-section and strand pattern

The three shear tests were each loaded by a single point load located closer to the east end of the girder. The simple supports included a roller at the east end and a rocker bearing at the west end. The rocker was implemented to alleviate safety concerns emanating from the non-symmetric application of load. In girder tests 28S and 24S, the roller bearing was centered 4 feet from the east end of the girder. In girder test 14S, the roller bearing was centered 6 in. from the east end of the girder. This setup allowed for a determination of the effect of strand debonding on the shear strength of the girder.

5.4 Instrumentation

The instrumentation plan for the four girder tests included five basic types of instrumentation. Electrical resistance strain gages were used to capture the strain behavior on the surface of the concrete girder. One and two in. long gages were used, depending on application and availability. In general, the linear string potentiometers were used to measure girder deflection. Tilt meters were used to measure girder rotation. Linear variable differential transformer (LVDT) displacement transducers were used to measure prestressing strand slippage. Finally, load cells were used to measure the live load applied to the girder at the load point(s). The following discussion describes the instrumentation plan for each girder specimen in detail.

5.4.1 Girder 80F

Figure 5.4.1-A shows the test setup and instrumentation plan for Girder 80F. The majority of the instrumentation was placed on the girder in one of five vertical

instrumentation lines. The instrumentation lines (1 through 5) corresponded to the span quarter points (1 and 5), the load points (2 and 4), and the midspan (3).

Five potentiometers were attached to the bottom flange to measure vertical deflection of the girder at each instrumentation line. Tilt meters were located above the bearings at girder mid-depth to measure end rotation. Strain gages were attached to the top and bottom flange to measure compressive and tensile strains, respectively. The gages on the tensile flange were also used as indicators of tensile cracking behavior. Instrumentation Line 3, located at midspan, included six additional strain gages on both the north and south faces. The strain profile in the constant moment region between the load points was captured through these gages. The final strain gages were applied near the west bearing on the south face. A strain rosette was created from three strain gages to capture the shear strain behavior in a region experiencing very minimal flexural influence.

5.4.2 Girder 28S

Figure 5.4.2-A shows the test setup and instrumentation plan for Girder 28S. Again, most instrumentation was located along seven vertical instrumentation lines. The instrumentation included seven potentiometers to capture the vertical deflection of the girder. Additionally, two tilt meters were located above the bearings at girder mid-depth to measure rotation. LVDTs were attached to half of the strands extending from the east end of the girder. The strands to the north of the vertical centerline were monitored, and their designations are shown in Figure 5.3-B.

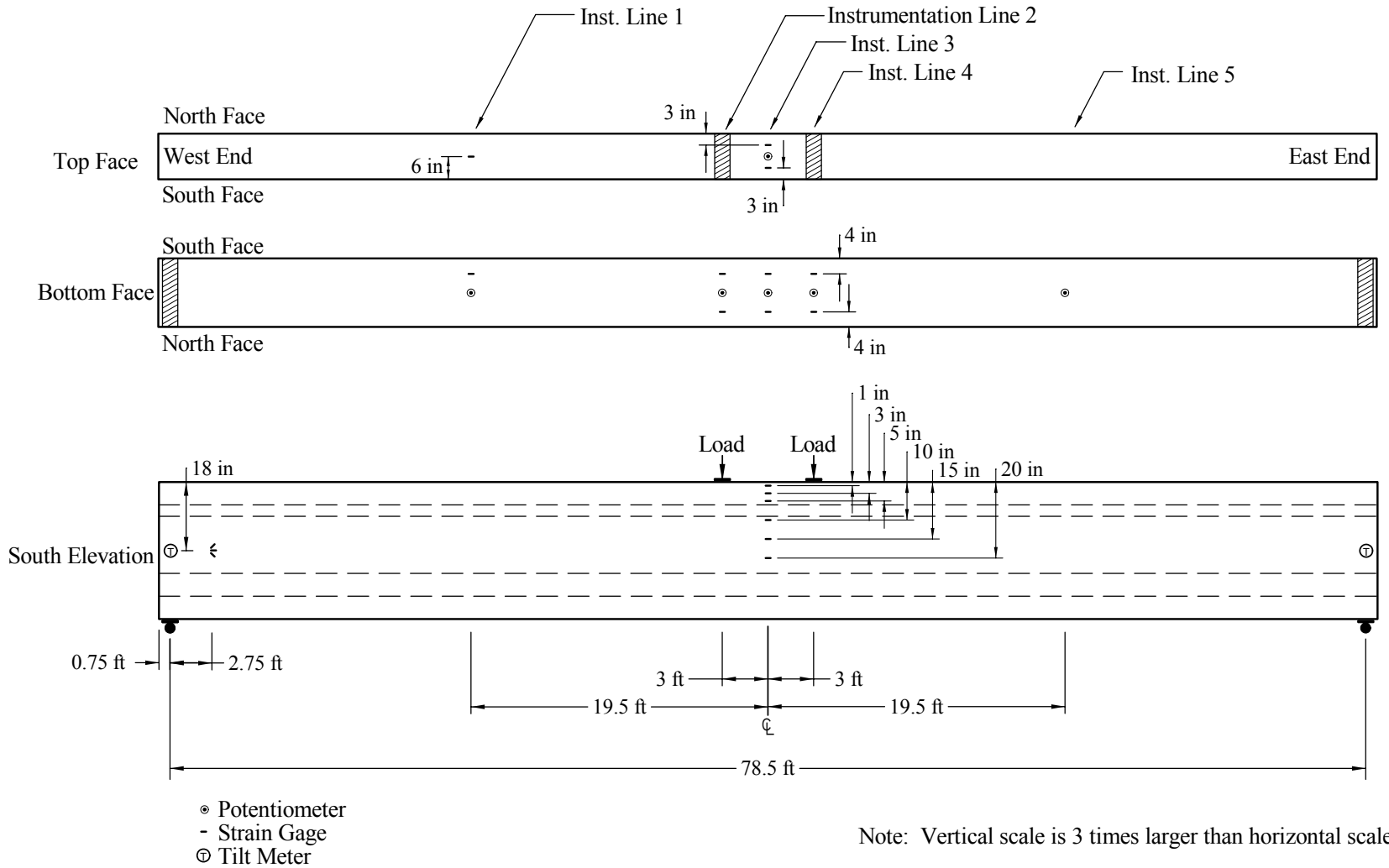


Figure 5.4.1-A: Instrumentation plan for Girder 80F

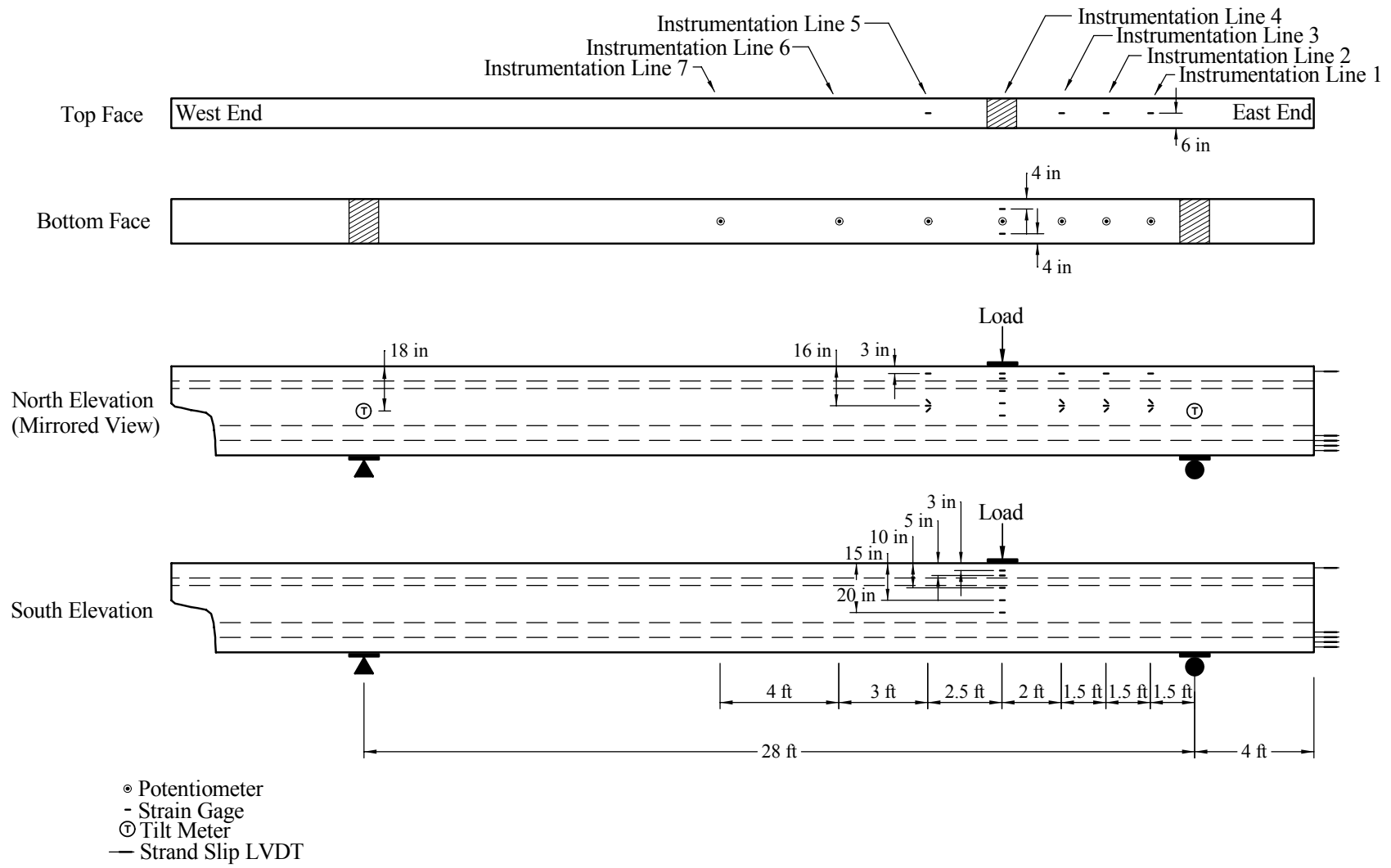


Figure 5.4.2-A: Instrumentation plan for Girder 28S

5.4.3 Girder 24S

Figure 5.4.3-A shows the test setup and instrumentation plan for Girder 24S. The instrumentation plan for this test was similar to—but more extensive than—that implemented for the testing of Girder 28S. This change resulted from the behaviors observed during the testing of Girder 28S. Most instrumentation was located along nine vertical instrumentation lines (Instrumentation Lines X, 0, 1, ..., 7). Note that Instrumentation Lines 1 through 7 were in similar locations in the previous test, while lines 0 and X are located above the east support and at midlength of the east end overhang.

Strain gages were used at various locations on the surface of the girder to monitor local tensile and compressive strains. Strain gages were applied to the top and bottom flanges to capture similar behaviors to those observed in the testing of Girder 80F. Gages were also applied along the depth of the cross-section under the load point to capture the strain profile on the cross-section. Four additional strain gages were applied to the north face of the top flange block to capture the compressive strains and to monitor the development of a compression strut as the test progressed. Finally, strain rosettes were created at three locations in the center of the web on the north face. These rosettes allowed for the monitoring of the principal compressive and tensile stresses in the web in both the shorter and longer shear spans.

Seven potentiometers were used to capture the vertical deflection behavior of the girder. Again, two potentiometers captured the rotation of the girder above the support points. In

an identical fashion to the setup for the previous test, LVDTs were used to measure the strand slip, as shown in Figure 5.3-B.

Strain gages were placed on the top and bottom of the girder and on the north face to capture the axial and shear strain behavior. A total of seven rosettes were applied to the web in this test, with the additional rosettes capturing the strain behavior in the east overhang, at the load point, and farther into the longer shear span. Strain gages were again placed on the north face of the compression flange. Additional gages were also placed along the transition at the bottom of the web. Cracking along this transition had influenced the girder behavior on the previous test, so these gages were intended to capture localized strain aberrations occurring across this plane at the base of the web.

5.4.4 Girder 14S

Figure 5.4.4-A shows the test setup and instrumentation plan for Girder 14S. This instrumentation plan was very similar to that implemented for Girder 24S. The primary difference is that the 4-ft overhang on the east end was eliminated, thus so was Instrumentation Line X. In addition, Instrumentation Line 7 was eliminated due to the shorter overall span.

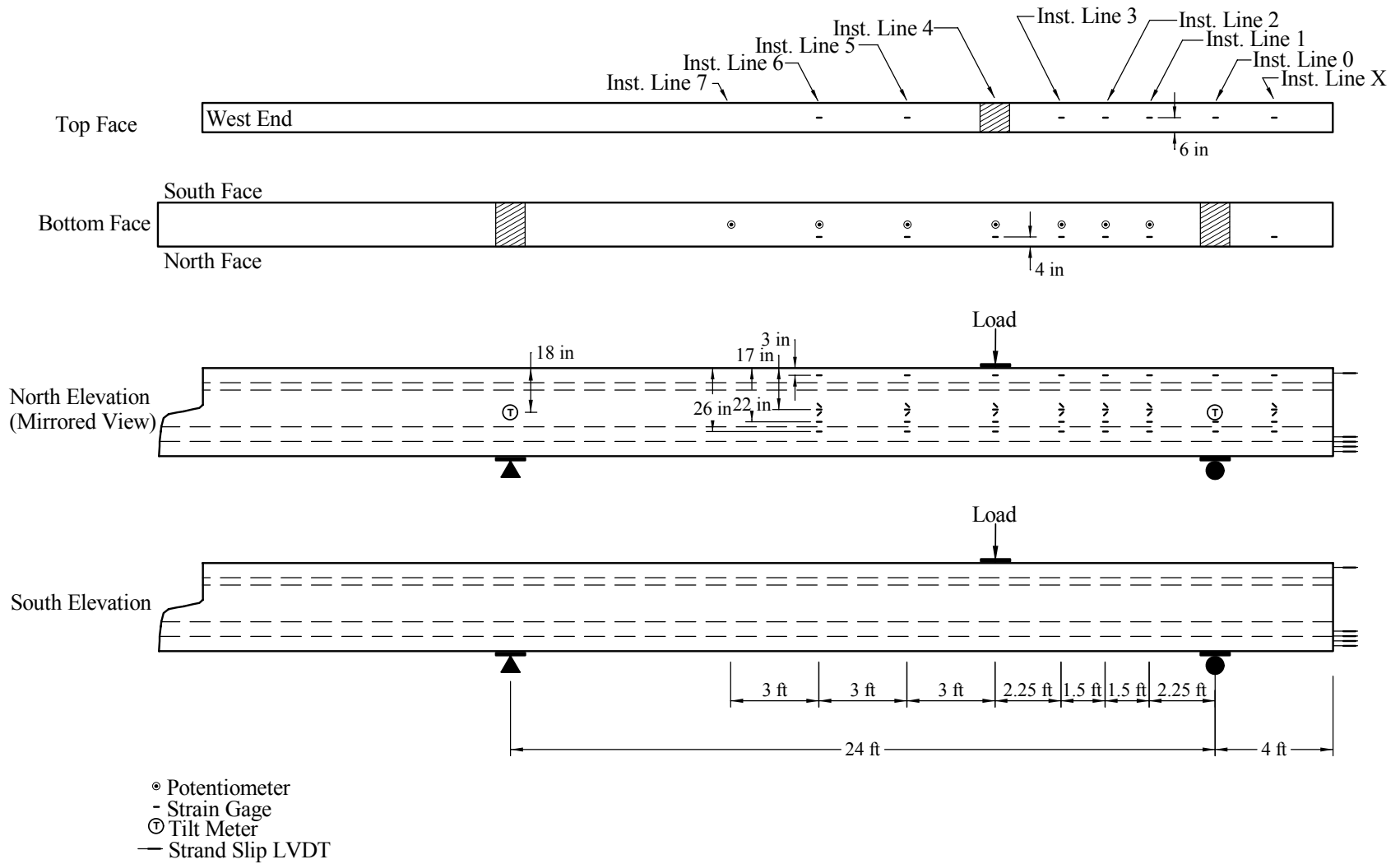


Figure 5.4.3-A: Instrumentation plan for Girder 24S

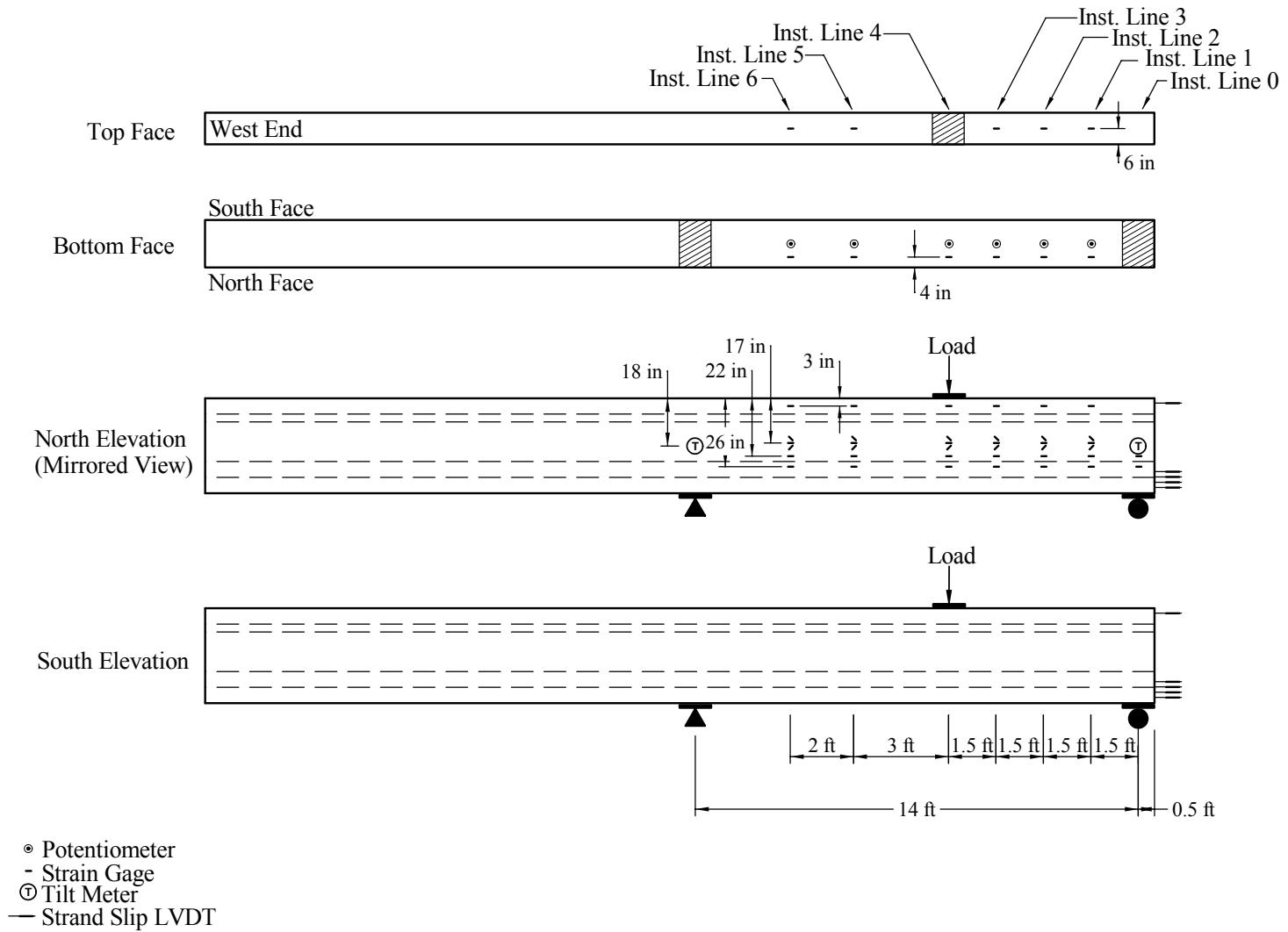


Figure 5.4.4-A: Instrumentation plan for Girder 14S

5.5 Loading Procedure

Loads were applied to the girders through their top flange using hydraulically actuated jacks. The loads were applied vertically in the plane of the strong axis of each girder. In the Girder 80F test, the load was applied through two load points, each 3 feet from midspan. The load point bearing was a pair of back-to-back channels grouted to the surface. The shear tests were all loaded through a single load point. The load point bearing assembly was a steel plate grouted to the surface with a half-round bearing welded to the jack side of the plate. The jack applied a vertical force to this half-round bearing, thus limiting the horizontal forces imparted to the girder.

All the data collection instruments described within the instrumentation plan were monitored throughout the test. The test plan was conducted and modified throughout the test based on these values. Initially, each test was conducted under load control. Load was increased in predefined increments, then the loading was stopped, and the data were collected. This procedure continued until the girder was observed to be softening. The test control was then shifted to deflection control, wherein the vertical deflection of the girder under the load point was incremented. The hydraulic jacks were instructed to extend until a certain girder deflection was reached, then the loading was stopped, and the data were collected. The deflection increments varied from smaller values when the specimen was initially beginning to soften to larger values when the specimen was exhibiting little residual stiffness.

At predefined intervals throughout each test, the loading was stopped and unload/reload data were captured. This testing protocol allowed for the capture of the residual elastic response of the girder, regardless of the level of inelastic damage that had already occurred. In general, six to eight unloads were completed and were evenly spaced throughout each test. The unloads usually decreased the load on the specimen to approximately $0.75P_{\max}$, or 75 percent of the current maximum load. The load was then increased and the data were collected at $0.80P_{\max}$, $0.85P_{\max}$, $0.90P_{\max}$, and $0.95P_{\max}$. The load was then increased to P_{\max} , and the test continued in the same manner as it had before the initiation of the unload/reload protocol.

All girders were loaded until they were determined to have failed. Failure was defined as either crushing of the concrete or gross cracking of the concrete accompanied by rupture or significant slippage of prestressing strands.

CHAPTER 6

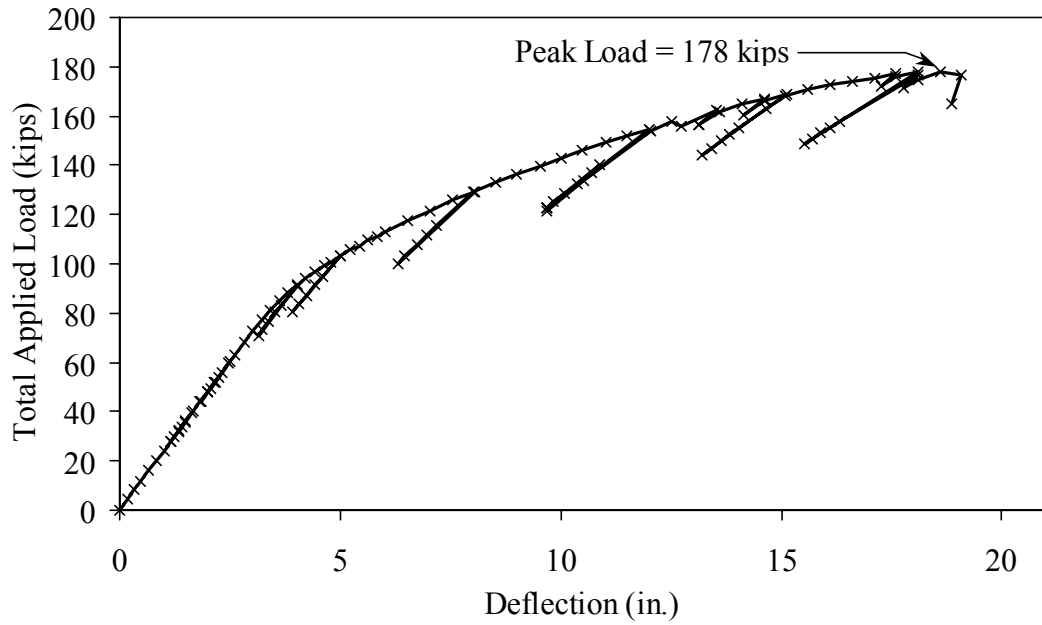
UHPC GIRDER TEST RESULTS

This chapter presents detailed results from the four UHPC girder tests. The results from the flexure test on the 80-ft long AASHTO Type II girder are presented first, followed by the results from the three full-scale shear tests.

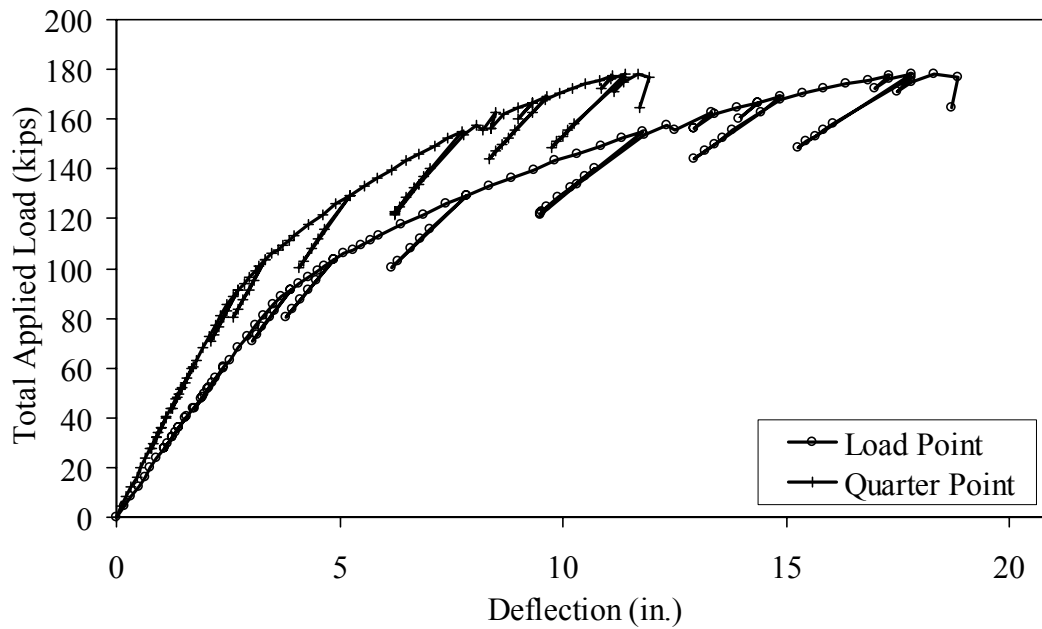
6.1 Static Flexural Testing

As discussed in Chapter 5, Girder 80F was an 80-ft long AASHTO Type II prestressed girder. The girder was loaded in four-point bending by point loads located 3 feet from the centerline and by roller supports located 39.25 feet from the centerline. The girder contained twenty-six 270 ksi low relaxation strands and no mild steel.

Figure 6.1-A shows the applied load versus the vertical deflection response for this girder. The response as measured from the girder's bottom flange at the centerline is shown in Figure 6.1-A(a), and the average deflection at the load points and quarter points is shown in Figure 6.1-A(b). The load-deflection response shows that the girder behavior began to soften between 70 and 80 kips at a deflection of approximately 3.0 in. The girder exhibited significant additional capacity reaching a peak load of 178 kips at a deflection of 18.5 in. A similar response can be observed in Figure 6.1-B, which shows the applied load versus rotation at the girder support. Figure 6.1-C provides a plot of the deflected shape of the girder at seven load steps throughout the test. Note that the data points closest to the supports were derived from the support rotation values.



(a) Deflection measured at midspan



(b) Average deflections measured at load and quarter points

Figure 6.1-A: Load-deflection response of Girder 80F

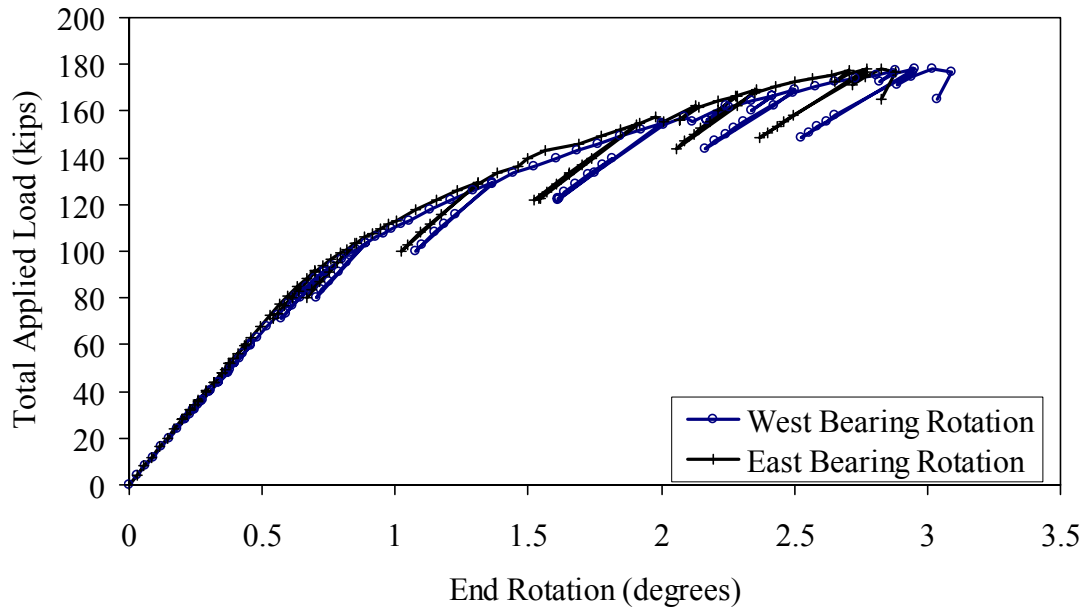


Figure 6.1-B: Load-rotation response of Girder 80F

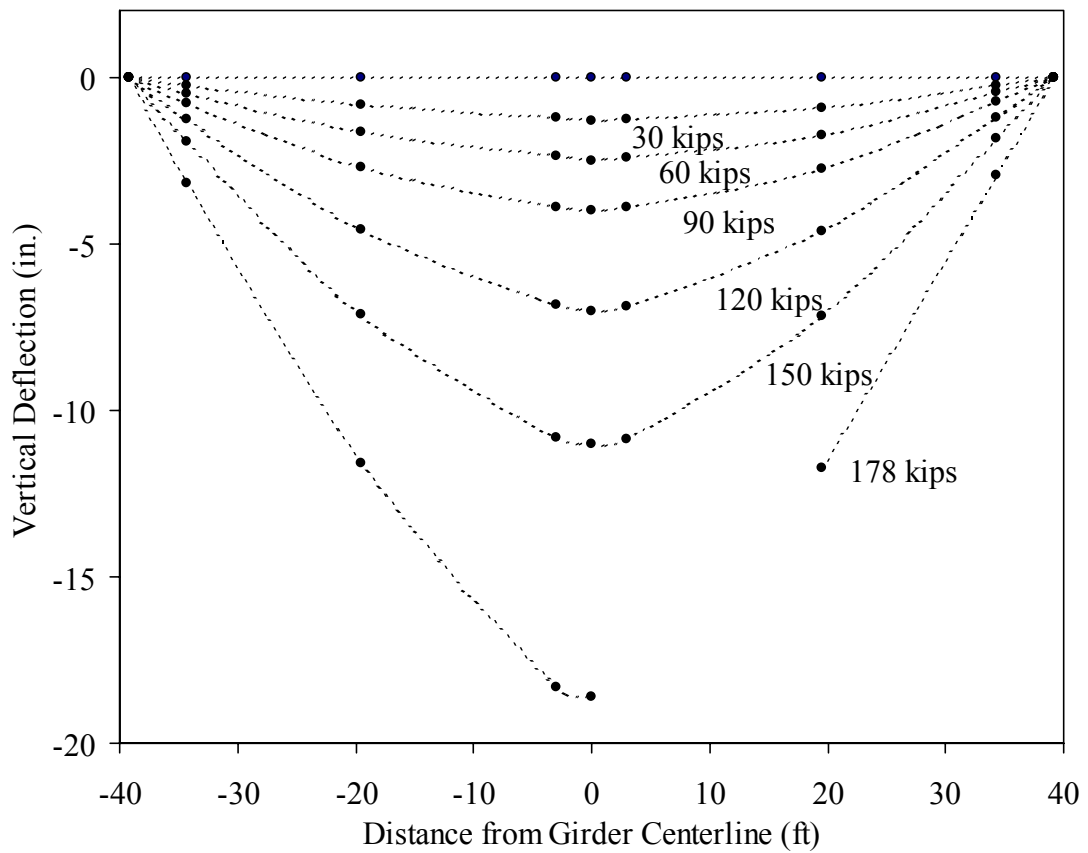


Figure 6.1-C: Deflected shape of Girder 80F at selected load levels

The sixteen strain gages located at the girder's centerline were used to create a strain profile over the depth of the girder throughout the test. Individual gages were used until their readings became unreliable due to cracking of the underlying concrete. The data from both sides of the girder correlated well. The neutral axis location and the curvature of the cross-section could be computed from these results. Figure 6.1-D shows the applied moment versus midspan curvature response. Similarly, Figure 6.1-E shows the neutral axis depth from the top of the girder versus the applied moment. Note that the basic elastic section analysis indicates that the neutral axis at test initiation should have been located approximately 20.5 in. down from the top of the girder. This plot shows that the neutral axis began to rise at an applied moment of approximately 17000 k-in., which corresponds to a load of approximately 78 kips. Also, note the stability of the neutral axis depth during the unloads/reloads.

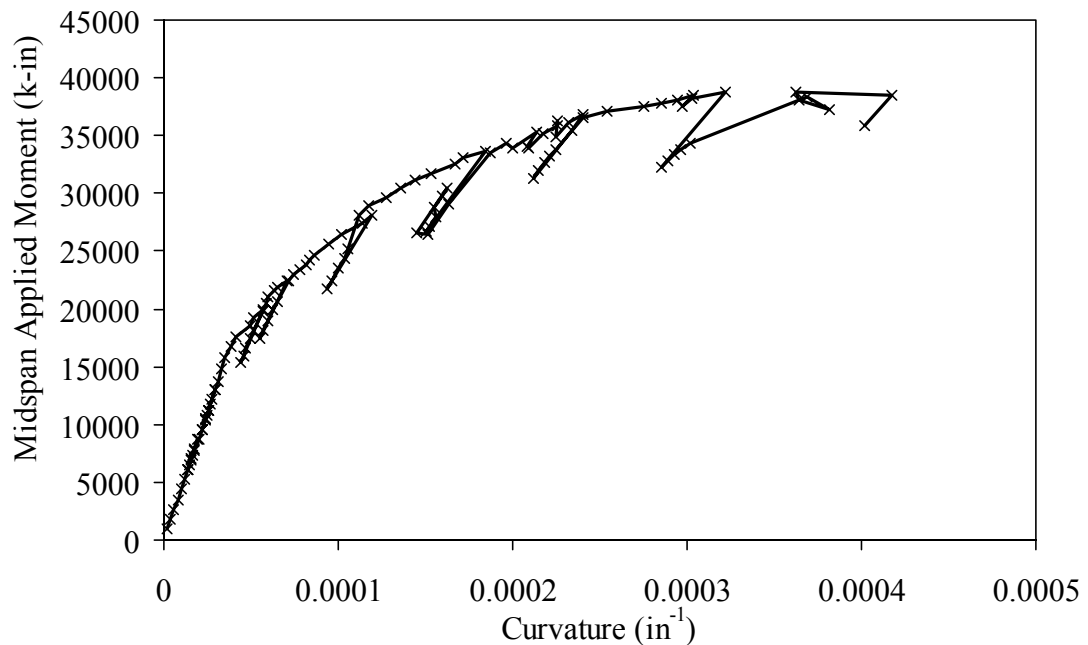


Figure 6.1-D: Moment-curvature response of Girder 80F

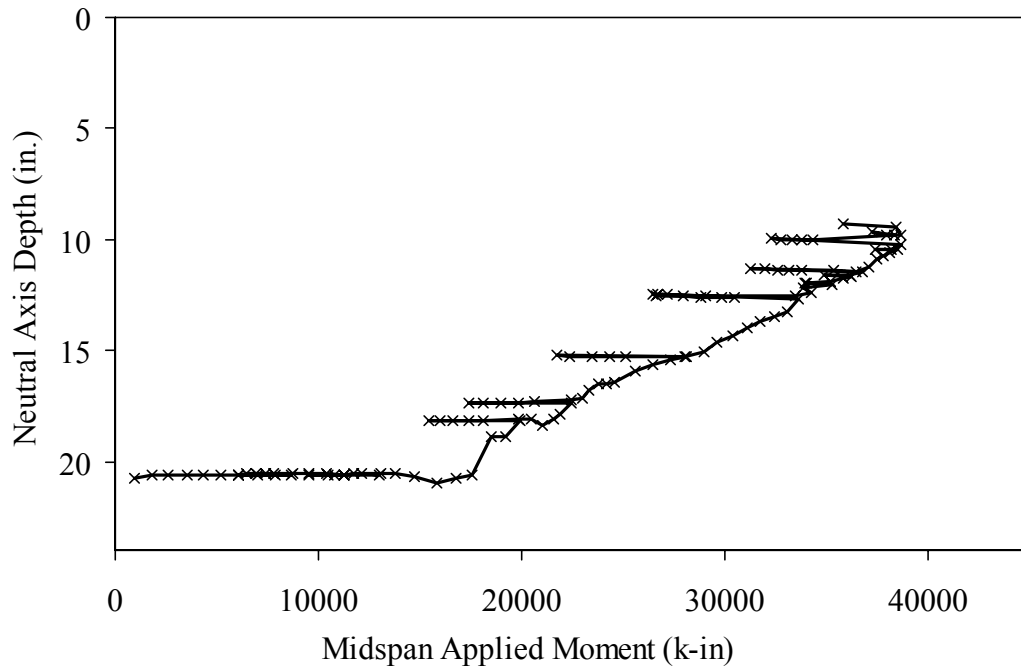


Figure 6.1-E: Midspan neutral axis depth from the top of Girder 80F

The strain rosette on the south face of the girder near the west bearing was used to capture the data presented in Figures 6.1-F and 6.1-G. The data shown in these plots are not continuous because difficulties with the data acquisition system resulted in the loss of ten data points in the middle of the test. Figure 6.1-F provides the principal tensile and compressive strains at the rosette. Figure 6.1-G shows the angle of the principal strains in clockwise degrees from horizontal on the south face. In both figures, note the linearity of the results. The tensile principal strain angle was approximately 40 degrees from vertical, and the strain increased elastically up to over 75 microstrain. No shear cracking was observed in the girder.

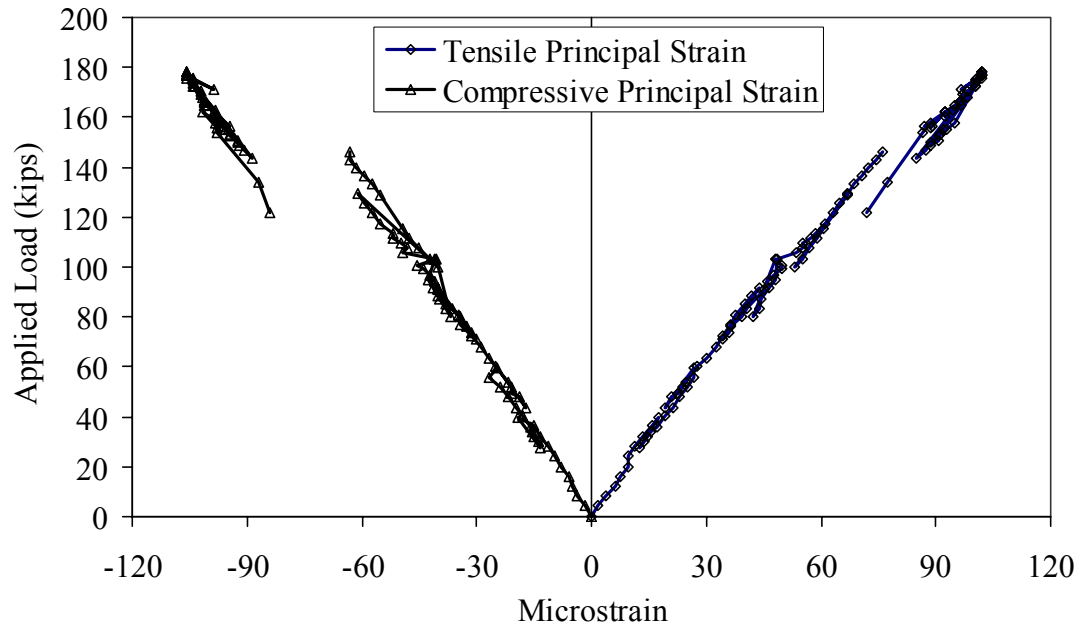


Figure 6.1-F: Principal strains in the web near the west support of Girder 80F

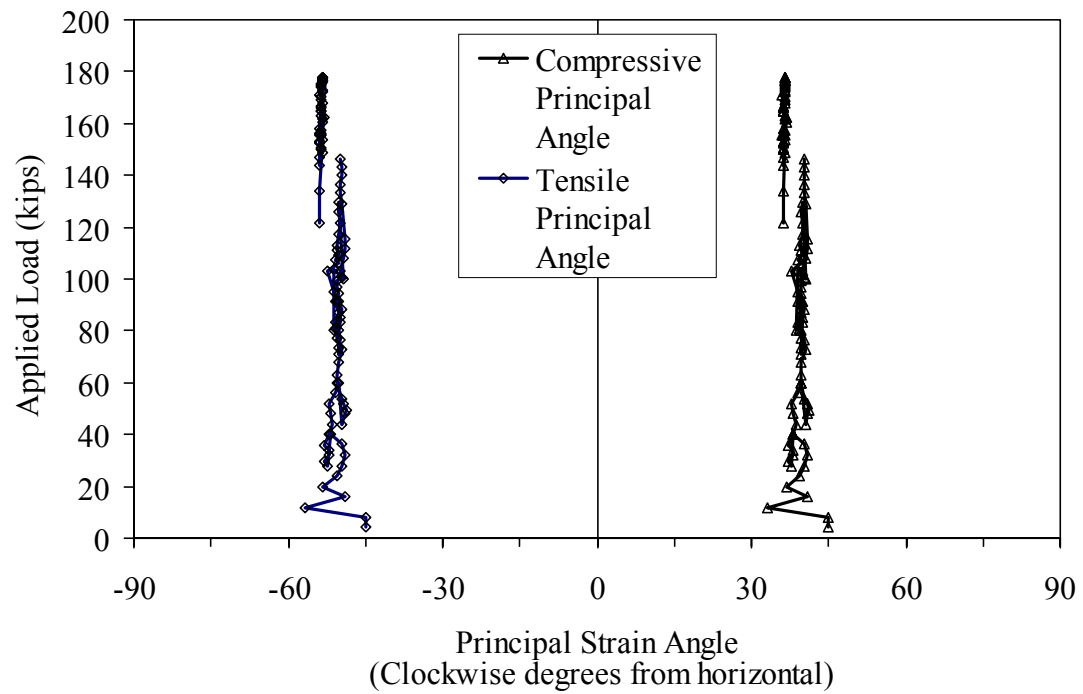


Figure 6.1-G: Principal strain angles in the web near the west support of Girder 80F

Significant audible cracking—which started when the load reached 73 kips and continued throughout the remainder of the test—emanated from the girder. However, in general, these cracking sounds could not individually be correlated to cracks on the surface of the girder. In fact, the cracks were not visible without the aid of a highly volatile crack revealing spray until the load had reached approximately 160 kips. After this load was reached, many tightly spaced hairline flexure cracks were visible in the bottom flange and web near midspan.

The test was halted overnight just after a peak load of 140 kips was reached. The girder was locked in place with a deflection of 12 in. Prior to resuming the test, the cracks on the bottom flange were mapped using the volatile spray. Figure 6.1-H shows photographic results of this mapping from six points along the length of the girder. The crack spacing near midspan was approximately 0.2 in. This spacing had increased to 0.4 in. at 10 feet from midspan, 1.0 in. at 16 feet, and 5 in. at 22 feet. No cracks were visible either to the unaided eye or through simple magnification devices.

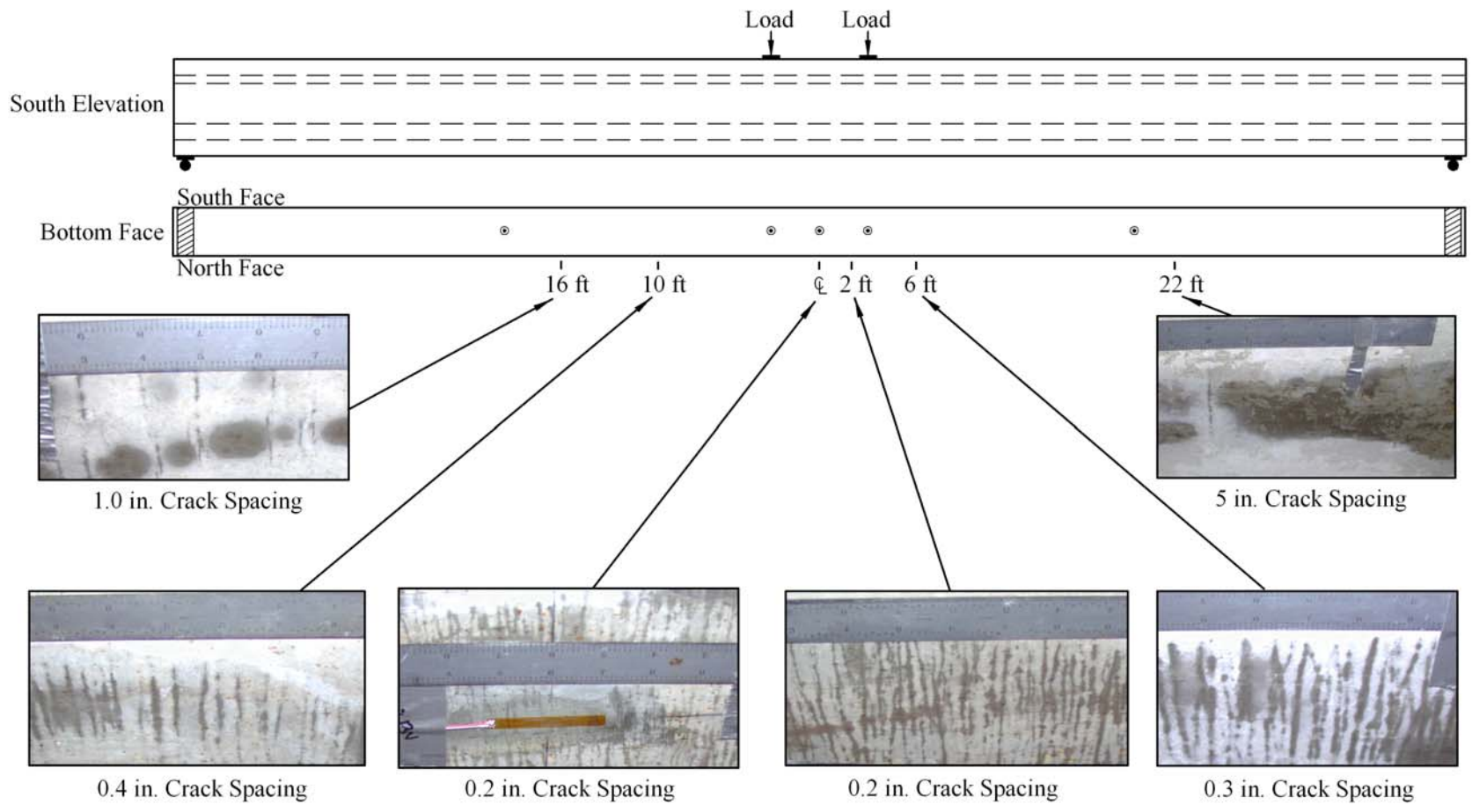


Figure 6.1-H: Crack spacing on the bottom flange of Girder 80F at 12 in. midspan overall girder deflection

As previously mentioned, Girder 80F exhibited a significant deflection capacity prior to failure. Figure 6.1-I shows the girder carrying a load of 175 kips with a resulting deflection of 17 in. Soon after this photograph was captured, the girder reached its maximum applied load of 178 kips, which corresponds to an applied moment of 38700 k-in. The maximum combined dead and live load moment was 42500 k-in. For comparison, recall from Section 2.5.3 that a similar ultimate flexural capacity was attained experimentally by Russell and Burns (1993) during the testing of a 46 in. deep decked I-girder. This girder had a 6 ksi, 72-in. wide top flange, and was prestressed with 28 0.5-in. strands.

After the maximum load was reached, the girder began to exhibit drastically decreased stiffness. The loading was stopped at this point. As the girder softened the load decreased, because the loading apparatus was hydraulically actuated. Approximately one minute prior to failure, a single gross crack was observed growing up from the bottom flange at the west load point. Unlike any other cracks in the girder, this crack was clearly visible to observers from a distance of 15 feet. Failure of the girder was dramatic, with the girder fracturing into two separate, unconnected pieces. Failure occurred due to a combined tensile failure of the concrete matrix and the prestressing strands. At the failure location, the fibers pulled out and all the strands necked and ruptured. Figure 6.1-K shows the west failure surface.



Figure 6.1-I: Girder 80F after approximately 17 in. of deflection



Figure 6.1-J: Girder 80F immediately after failure



(a)



(b)

Figure 6.1-K: Failure surface of Girder 80F including (a) overall west failure surface and (b) close-up of west failure surface showing pulled-out fibers and necked strands

6.2 Static Shear Testing

The results from three shear tests of full-scale AASHTO Type II prestressed UHPC girders are presented in this section. Results for Girder 28S are presented first, followed by results for Girder 24S and Girder 14S.

6.2.1 Girder 28S

The first shear test was completed on Girder 28S. The test specimen had an overall span of 28 feet and a shear span of 6.5 feet resulting in a shear span-to-depth ratio of 2.17. The east bearing on this girder was placed 4 feet from the end of the girder to minimize the effect that the debonding of the strands would have on the test results.

As shown in Figure 5.3-A, Girder 28S was originally the west end of Girder 80F. Prior to the Girder 28S test, the girder was examined for damage that may have resulted from the Girder 80F test. Significant flexural cracking was observed toward the midspan of Girder 80F (i.e., the west end of Girder 28S). Additionally, a longitudinal hairline crack was observed along the base of the web, which went from 1 ft east of the east bearing to just west of the load point. This crack may have either occurred due to the failure of Girder 80F or during fabrication or shipping of the girder.

The response of Girder 28S to the applied loading is shown in Figure 6.2.1-A through 6.2.1-C. Figure 6.2.1-A shows the applied load versus the vertical deflection response at the seven instrumentation lines. Figure 6.2.1-B focuses on the data from the tilt meters at the east and west bearings. Figure 6.2.1-C shows a plot of the deflected shape of the

girder at six load levels. Recall that the single point load was applied 21.5 feet from the west support. Note how the location of maximum deflection shifts east as the test progresses. This shift, a direct function of the softening of the east end of the girder, will be discussed later in this chapter.

The potentiometer readings nearest to the load point clearly indicate that the girder began to show softening behavior at a load of 250 kips. The girder still had a significant reserve load capacity and reached a peak load of 500 kips. At this peak load, the shear load carried by the east shear span was 384 kips. For comparison, Tawfig (1995, 1996) found that decked AASHTO Type II girders composed of 8 to 12 ksi HPC and containing shear reinforcement carried approximately 270 kips of shear before failure.

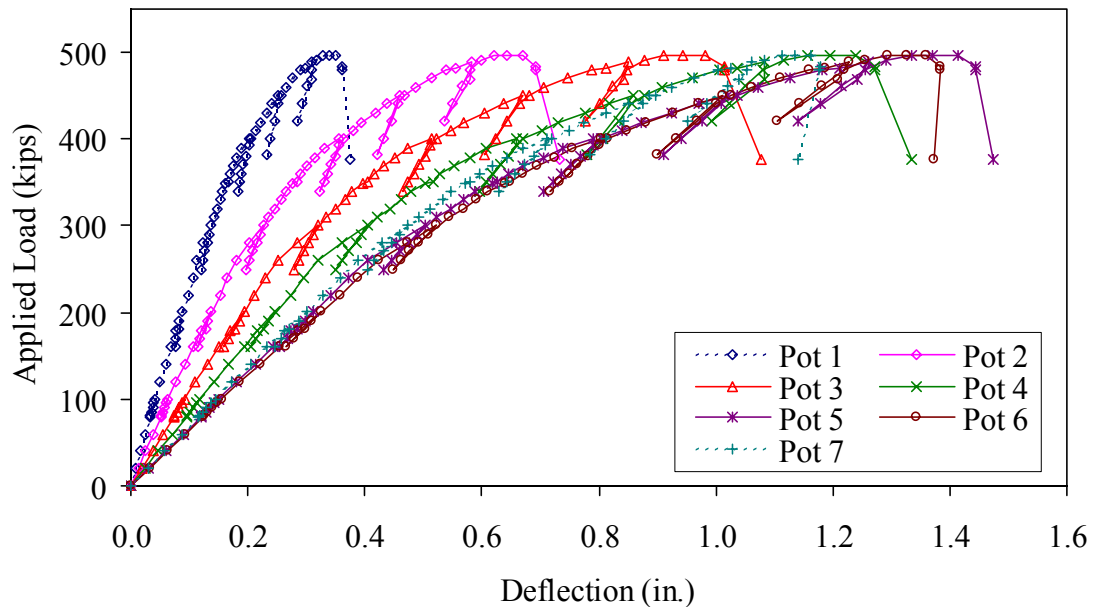


Figure 6.2.1-A: Load-deflection response of Girder 28S

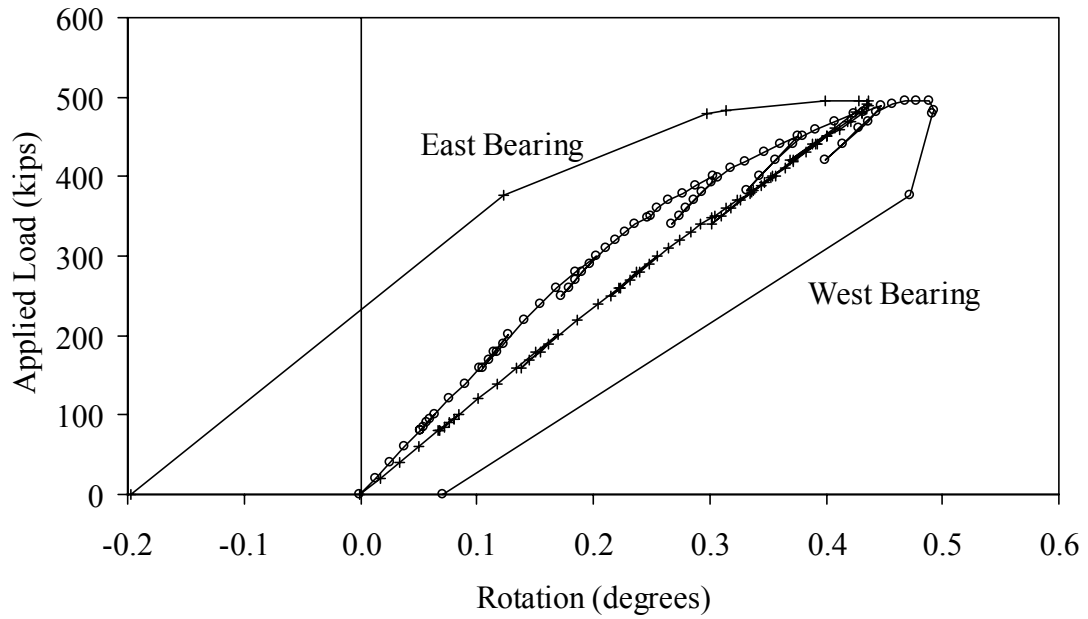


Figure 6.2.1-B: Bearing rotation response of Girder 28S

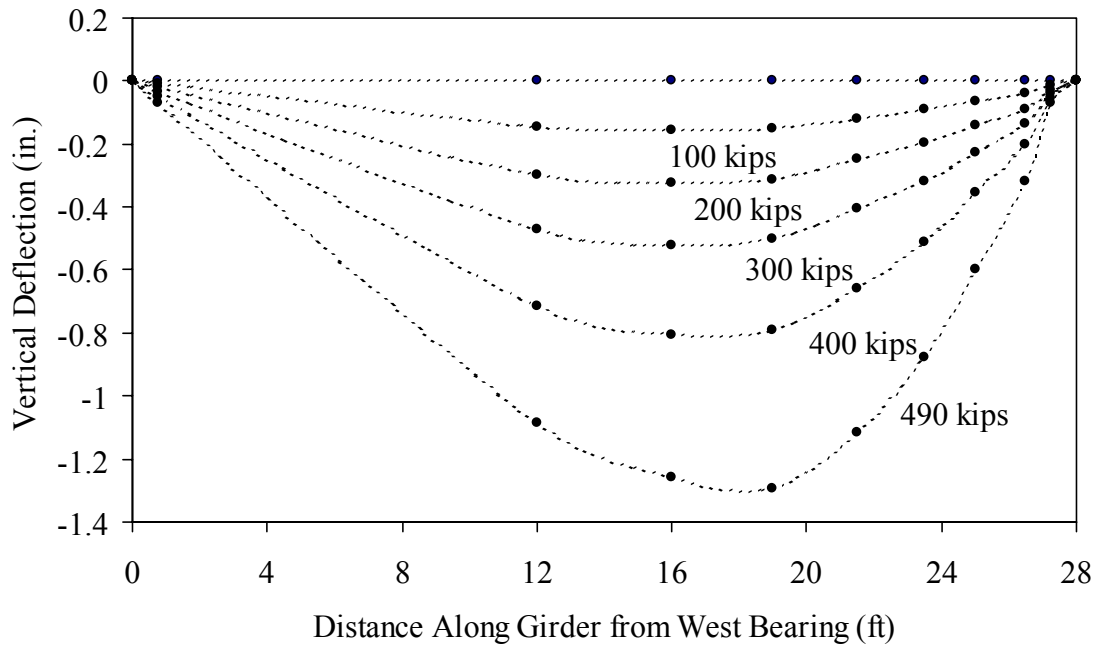


Figure 6.2.1-C: Deflected shape of Girder 28S

Half of the prestressing strands extending from the east end of the girder were instrumented to measure strand slip. Figure 6.2.1-D shows the strand slip behavior throughout the test. Only the instrumented debonded strands are shown because all of the fully bonded instrumented strands showed less than 0.002 in. of slip throughout the test.

Results from the four strain rosettes are presented in Figures 6.2.1-E through 6.2.1-H.

The tensile principal strain and strain angle values are presented in the first two figures.

The compressive principal strain and strain angle are presented in the second two figures.

Note that the strain angles are measured in clockwise degrees from horizontal as viewed from the south face of the girder.

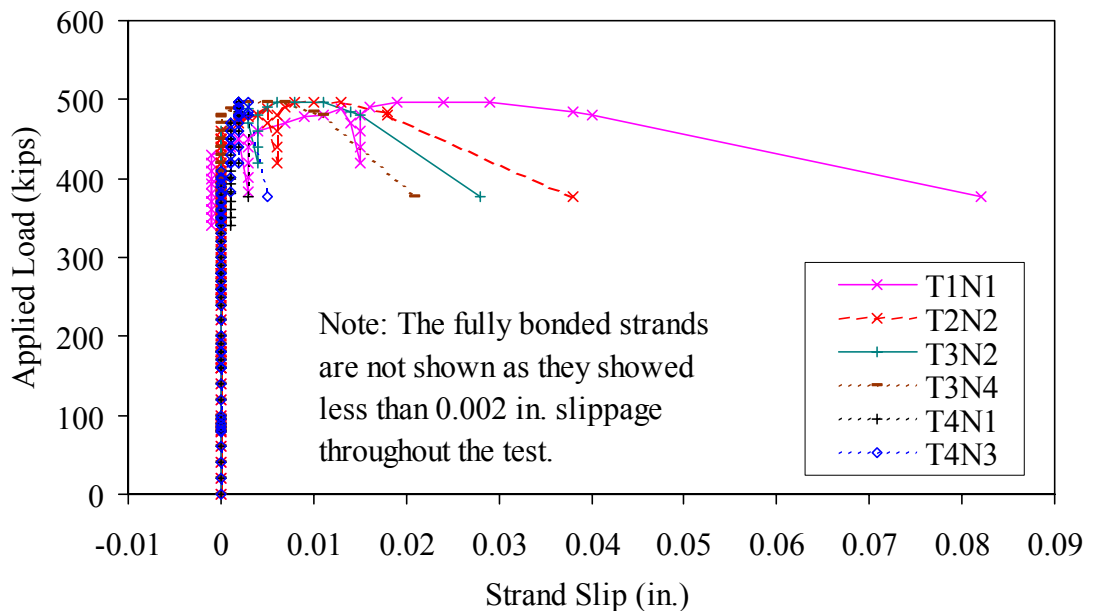


Figure 6.2.1-D: Strand slip in Girder 28S

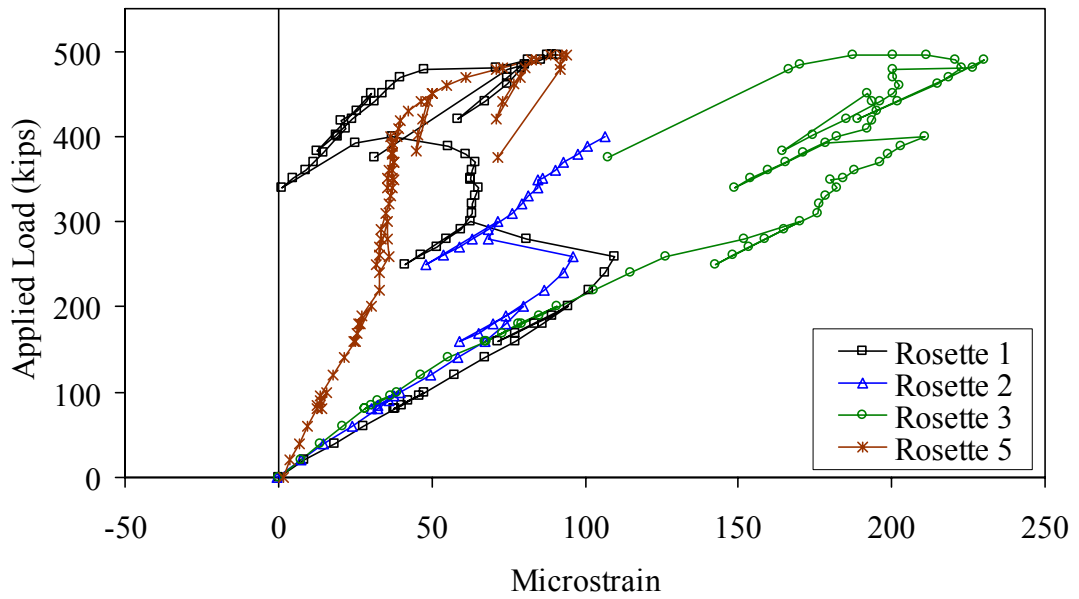


Figure 6.2.1-E: Principal tensile strain in the web of Girder 28S

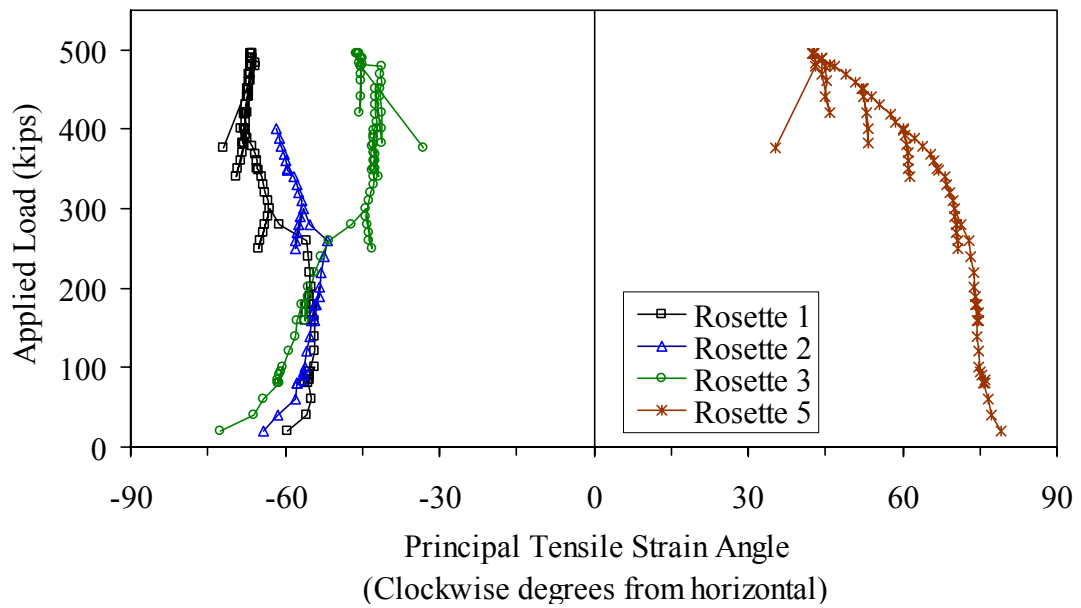


Figure 6.2.1-F: Principal tensile strain angle in the web of Girder 28S

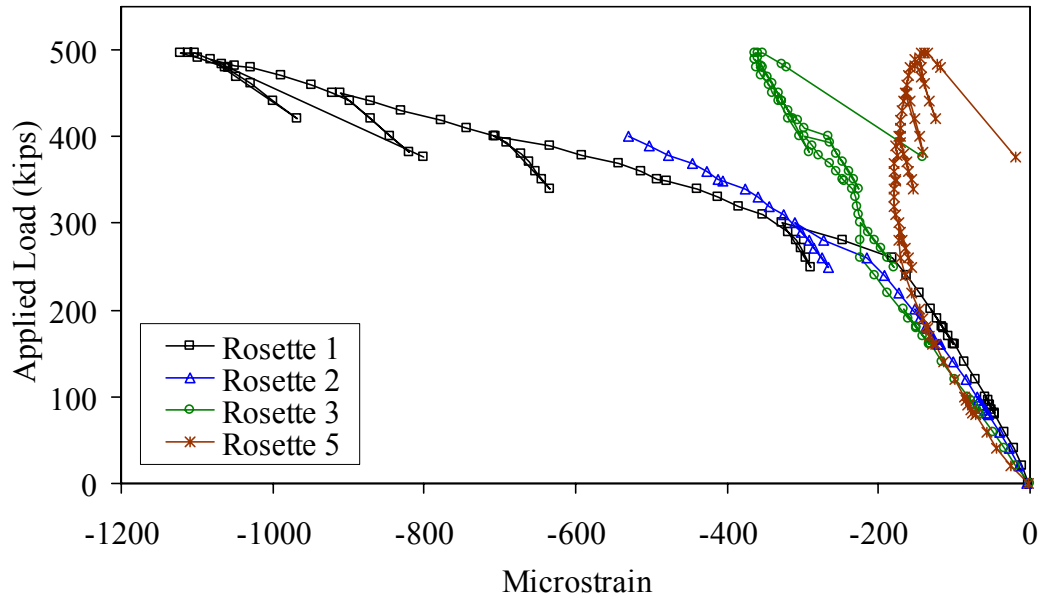


Figure 6.2.1-G: Principal compressive strain in the web of Girder 28S

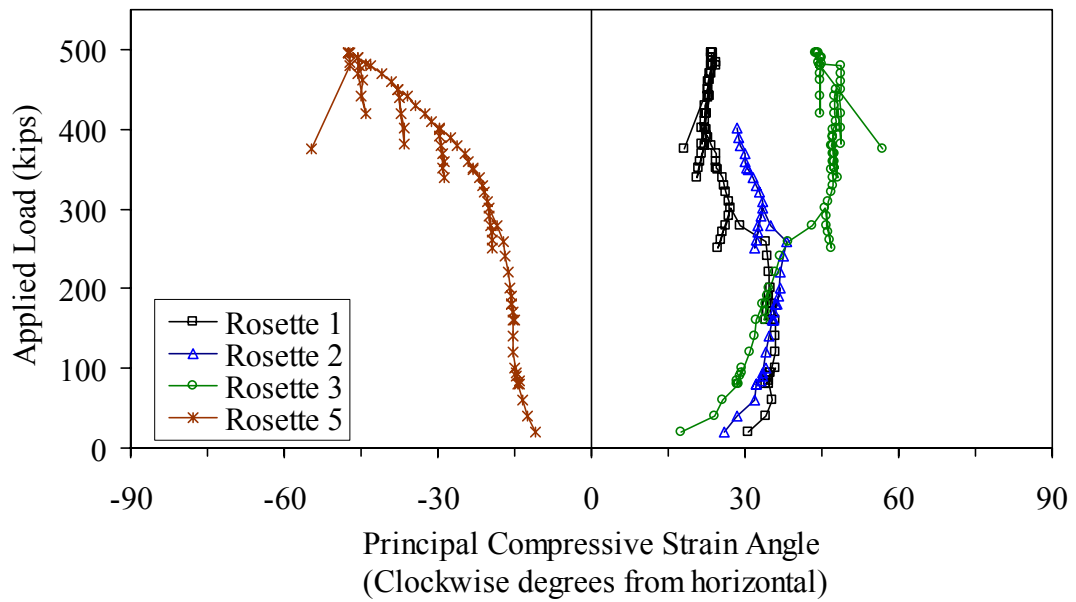


Figure 6.2.1-H: Principal compressive strain angle in the web of Girder 28S

Cracking and other damage to the girder were observed both audibly and visually throughout the test. The first cracking was heard at a load of 280 kips. The cracking continued throughout the remainder of the test and seemed to primarily emanate from the eastern half of the girder. Throughout the test, the preexisting hairline crack at the base of the web continued to grow larger and longer. At a load of 350 kips, this crack was clearly visible from 15 feet. Figure 6.2.1-I shows the size of this crack at a load of 450 kips. This crack, along with its branch that rose toward the load point beginning around 450 kips, was the only gross cracking observed prior to girder failure. However, many other smaller cracks were present. These cracks were initially only visible through the use of an indicating spray, and were later visible by short-range unaided viewing.

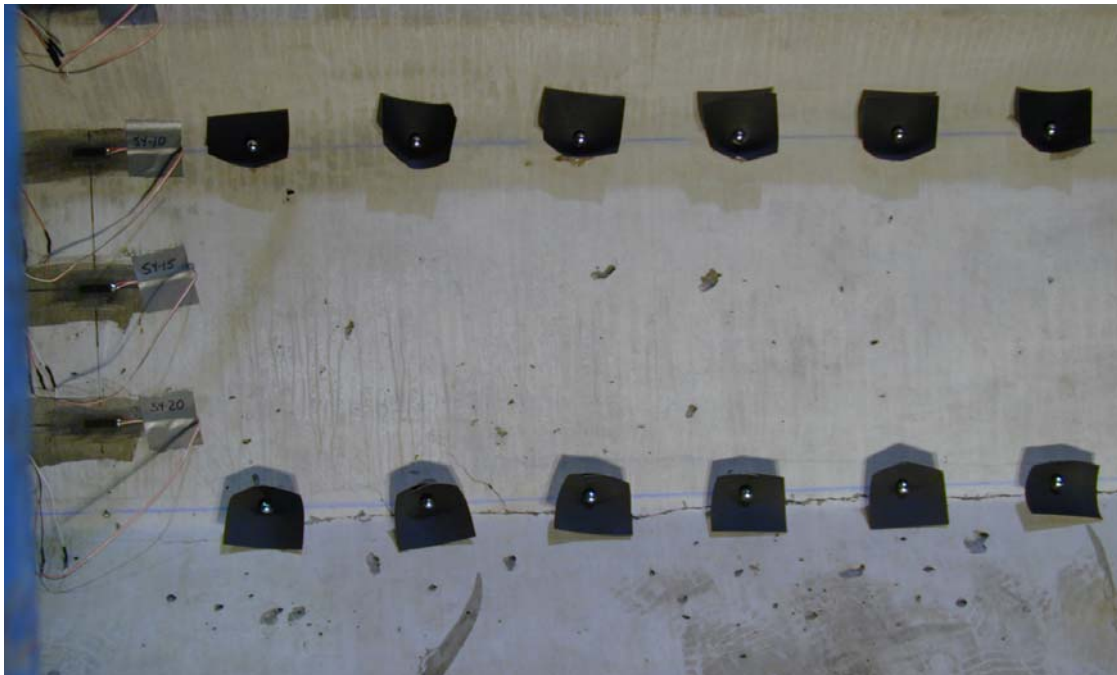


Figure 6.2.1-I: Crack at south base of Girder 28S web at a load of 450 kips

Figure 6.2.1-J shows the south face of the east shear span near the east bearing just after girder failure. Note the longitudinal crack at the base of the web, the vertical crack descending from the top of the top flange, and the crushed area in the web above the bearing. Figure 6.2.1-K shows the damage recorded after girder failure.

The failure of the girder was precipitated by a number of events. First, the longitudinal shear crack at the base of the web continued to grow longer and wider throughout the test. Near the completion of the test, the width of the crack was sufficient that only minimal tensile load transfer via fiber reinforcement across the crack would have been possible. Just after the peak load was reached, the base of the girder web just above the bearing began to crush. This slow process (lasting approximately 90 seconds) was finally halted by the rupturing of the two strands in the top flange. Note that the instrumented top flange strand did not show any slip throughout the test and that the rupture was 48 in. from the end of the girder. The failure mode of this girder will be discussed in more depth in Chapter 7.

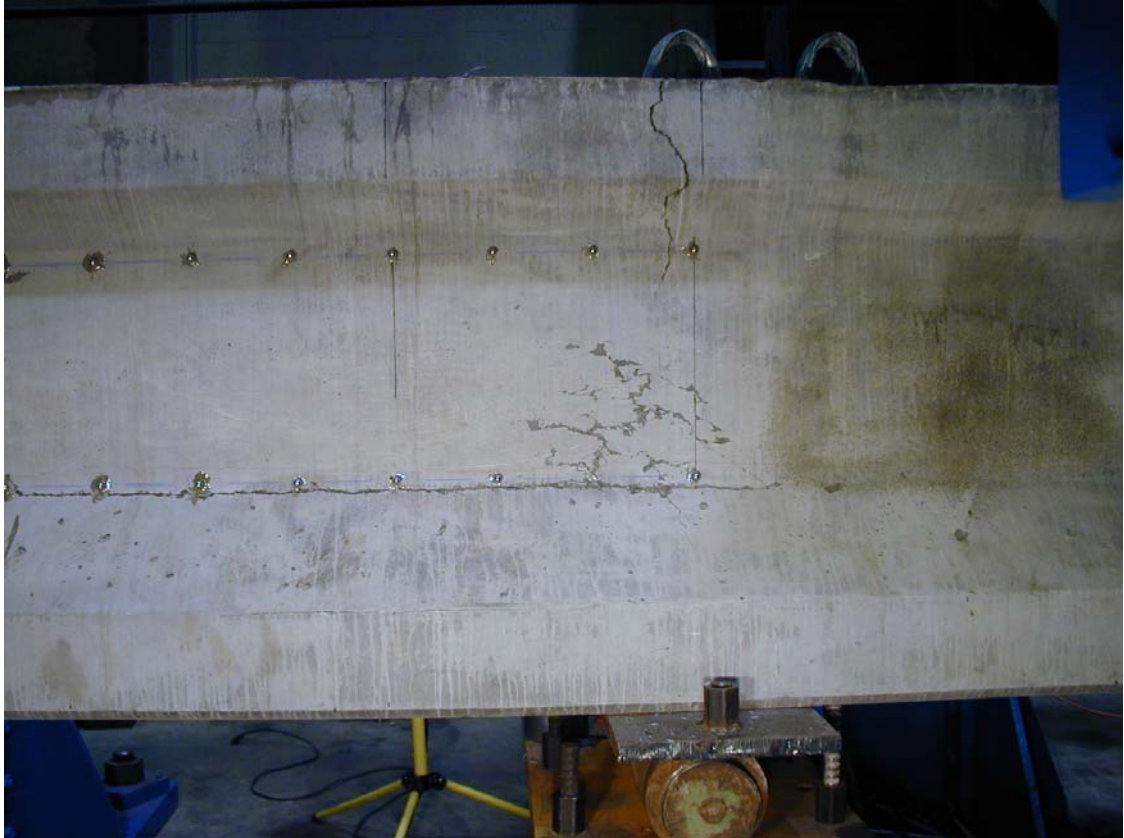
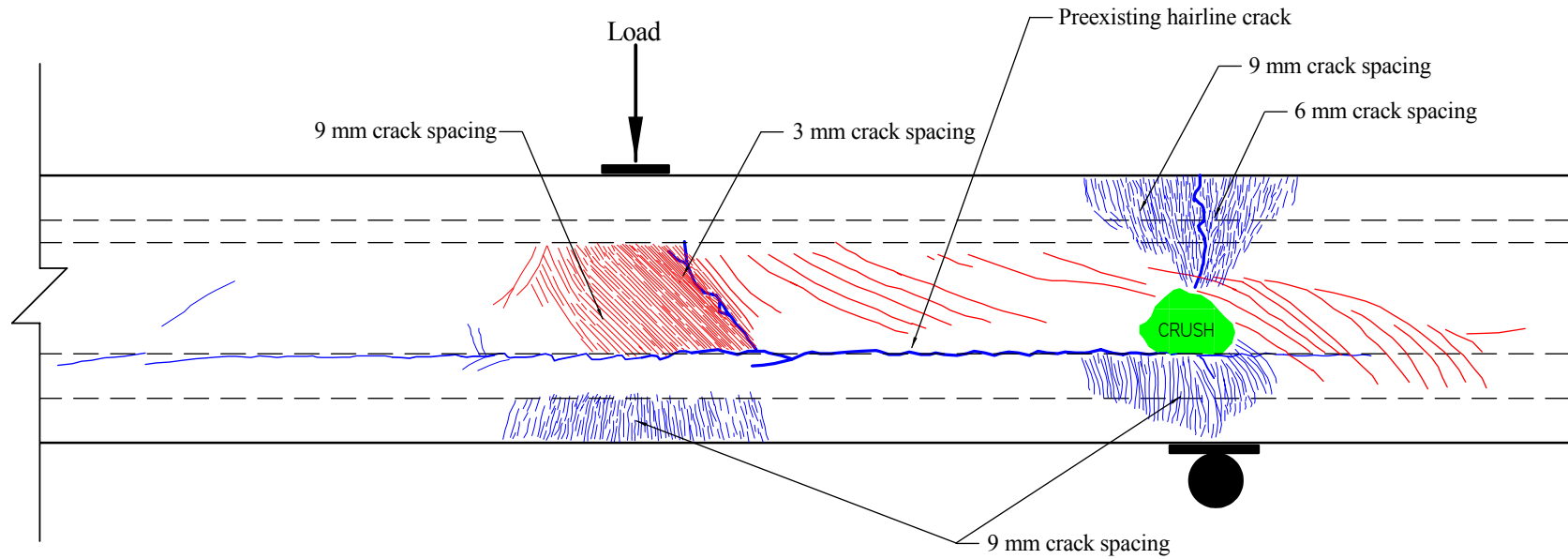


Figure 6.2.1-J: Tension failure of top flange and crushing of web at conclusion of test



Note: 1. Crack widths are not drawn to scale.
2. Tightly spaced crack areas are not drawn to scale.

Figure 6.2.1-K: Crack pattern at failure in Girder 28S

6.2.2 Girder 24S

The second shear test was completed on Girder 24S. This girder had an overall span of 24 feet and a shear span of 7.5 feet, resulting in a shear span-to-depth ratio of 2.5. The east bearing on this girder was centered 4 feet from the end of the girder to minimize the effect that the debonding of the strands would have on the test results.

As shown in Figure 5.3-A, Girder 24S was originally the east end of Girder 80F. Similar to Girder 28S, this girder was examined for damage that may have resulted from the Girder 80F test. Significant flexural cracking was observed toward the west end of the girder; however, the majority of this cracking was outside of the test span. Additionally, a single crack was observed that started in the east overhang region at the bottom flange and ended in the web just west of the east bearing. This crack probably resulted from the motion of this end of the girder immediately following the failure of Girder 80F.

Figure 6.2.2-A shows the applied load versus the vertical deflection response of the girder. Individual curves are shown for each potentiometer, including Pot 4, located under the load point. Figure 6.2.2-B shows the applied load versus the girder rotation at the east and west supports. Figure 6.2.2-C shows the deflected shape of the girder at nine points throughout the test. Recall that the load was applied 16.5 feet from the west bearing.

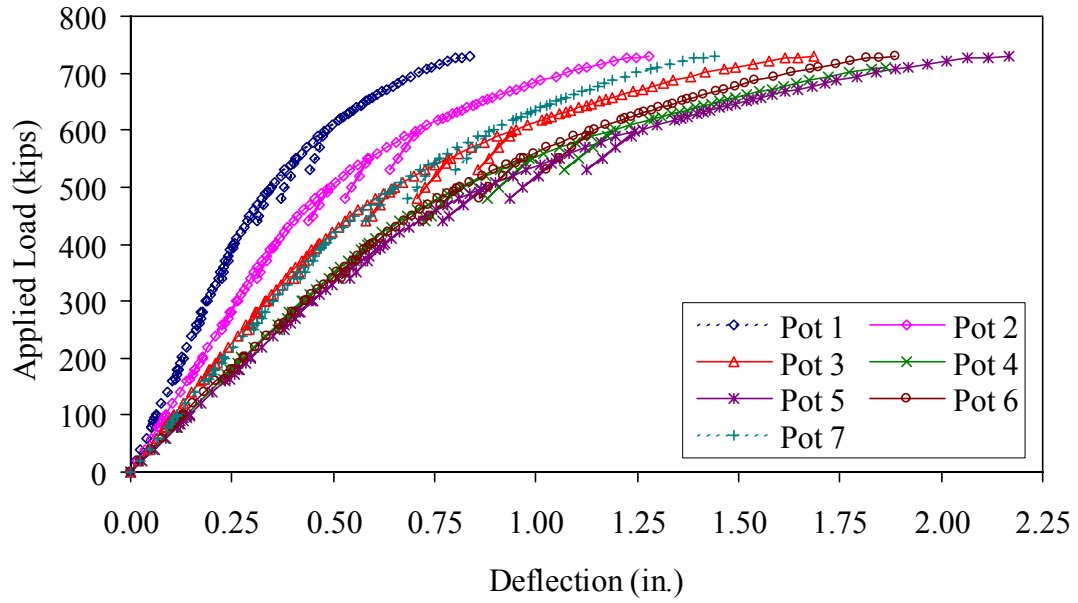


Figure 6.2.2-A: Load-deflection response of Girder 24S

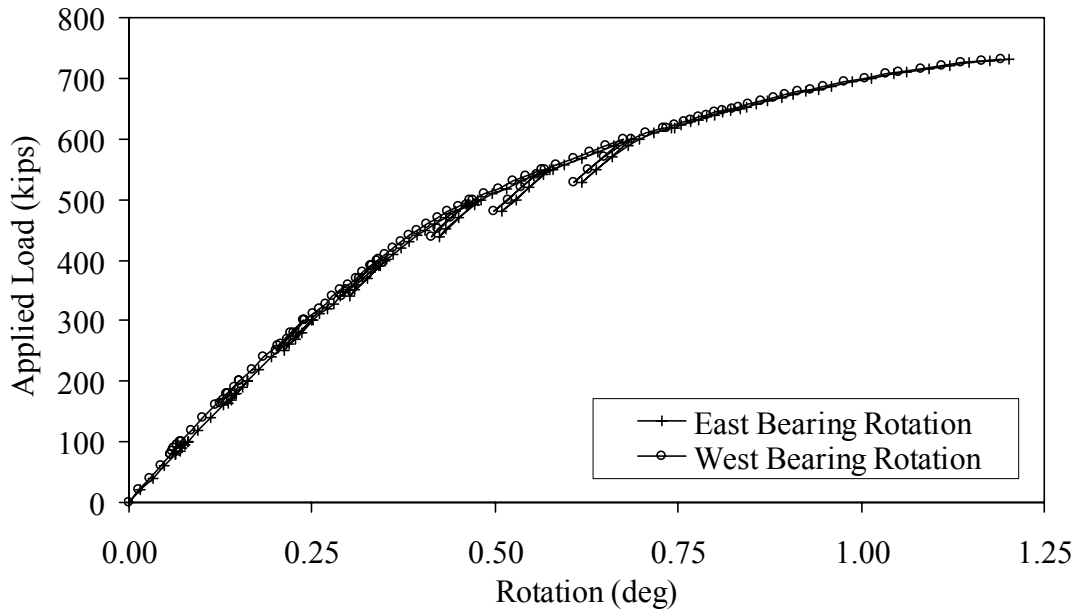


Figure 6.2.2-B: Bearing rotation of Girder 24S

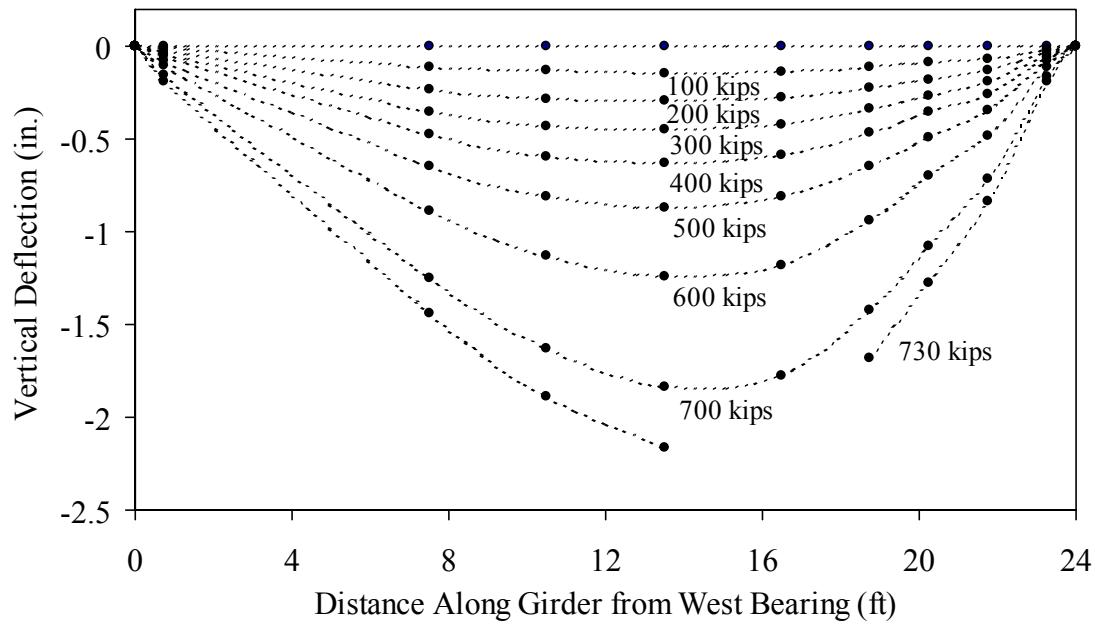


Figure 6.2.2-C: Deflected shape of Girder 24S

The deflection measurements nearest to the load point indicate that the girder began to show softening behavior at a load between 300 and 400 kips. The girder still had a significant reserve load capacity and reached a peak load of 731 kips. At this peak load, the shear load carried by the east shear span was 502 kips. Again, this capacity is significantly above the decked AASHTO Type II shear capacity determined by Tawfig (1995, 1996) for HPC.

Half of the prestressing strands extending from the east end of the girder were instrumented to measure strand slip. None of the strands showed any slippage until after the girder failed. For this reason, the strand slip results are not plotted here.

Results from the seven strain rosettes are presented in Figures 6.2.2-D through 6.2.2-G. The tensile principal strain and strain angle are presented in the first two figures. The compressive principal strain and strain angle values are presented in the second two figures. Note that the strain angle values are measured in clockwise degrees from horizontal as viewed from the south face of the girder. Also, in these figures, tension and compression are not always strictly correct. For instance, at certain load levels, Rosette 4 in Figure 6.2.2-D exhibits a principal tensile strain that is actually compressive. A subsequent comparison with Figure 6.2.2-G shows that the compressive principal strain for Rosette 4 is compressive and is far larger. In this case, both principal strains were compressive; therefore, the less compressive strain is presented as tensile.

Cracking and other damage to the girder throughout the test were observed both audibly and visually. The first cracking was heard at a load of 370 kips. The cracking continued throughout the remainder of the test and seemed to primarily emanate from the eastern half of the girder. Up until just before failure, no gross cracking was observed in the girder. However, many small cracks were present. These cracks were only visible through the use of an indicating spray and were primarily shear cracks in the girder web.

The failure of this girder was sudden and dramatic. Toward the conclusion of the test, two parallel shear cracks appeared in the girder web that were clearly visible from 15 feet. These cracks were approximately on the direct line from the bottom flange bearing plate to the top flange load plate. One of the cracks ran from the bottom to the top of the web while the other ran from the bottom to halfway up the web.

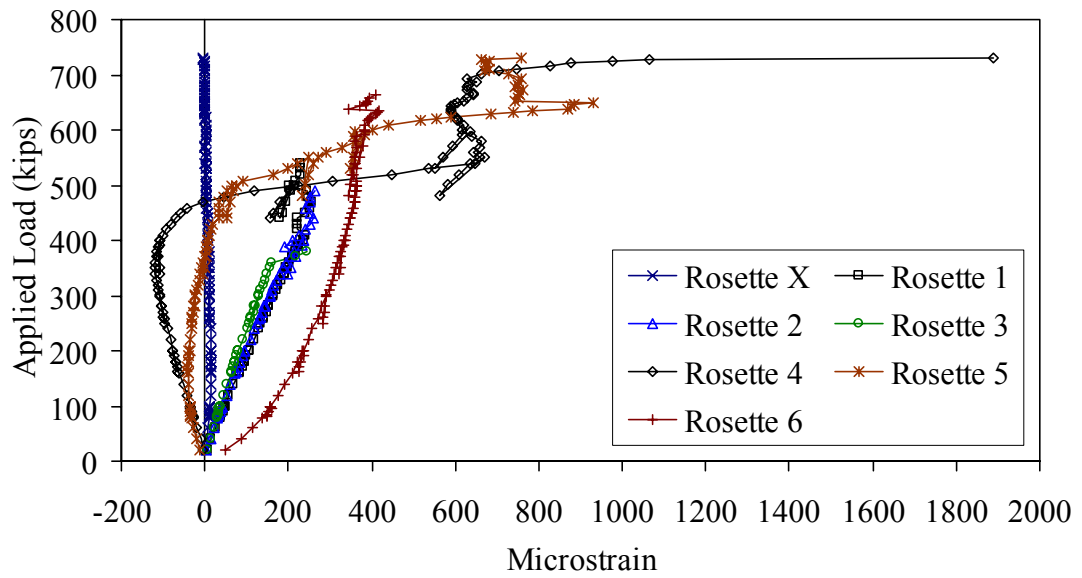


Figure 6.2.2-D: Principal tensile strain in the web of Girder 24S

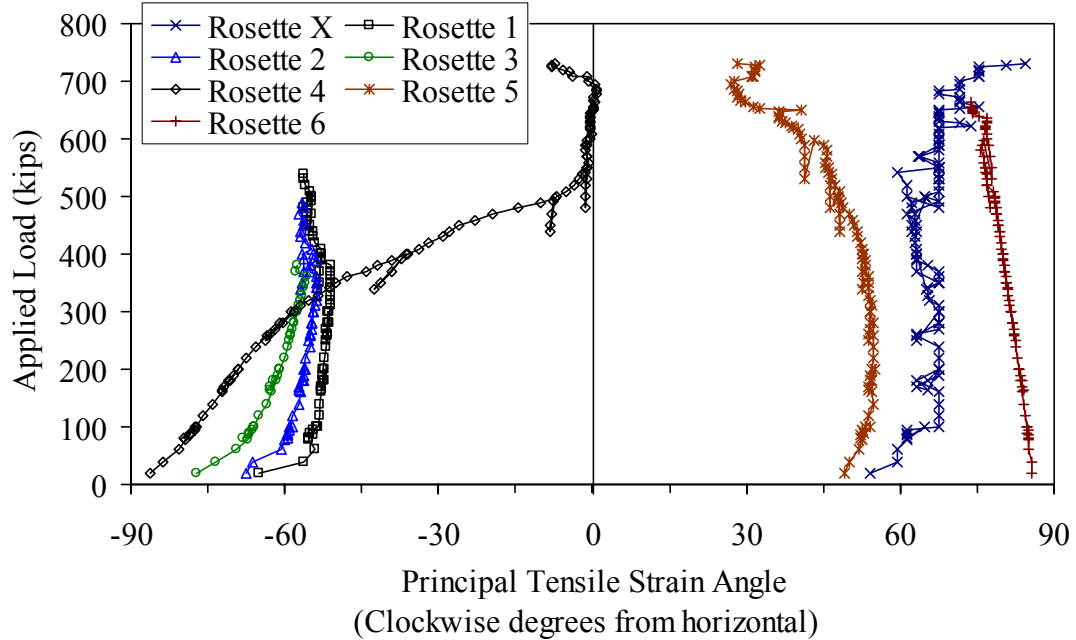


Figure 6.2.2-E: Principal tensile strain angle in the web of Girder 24S

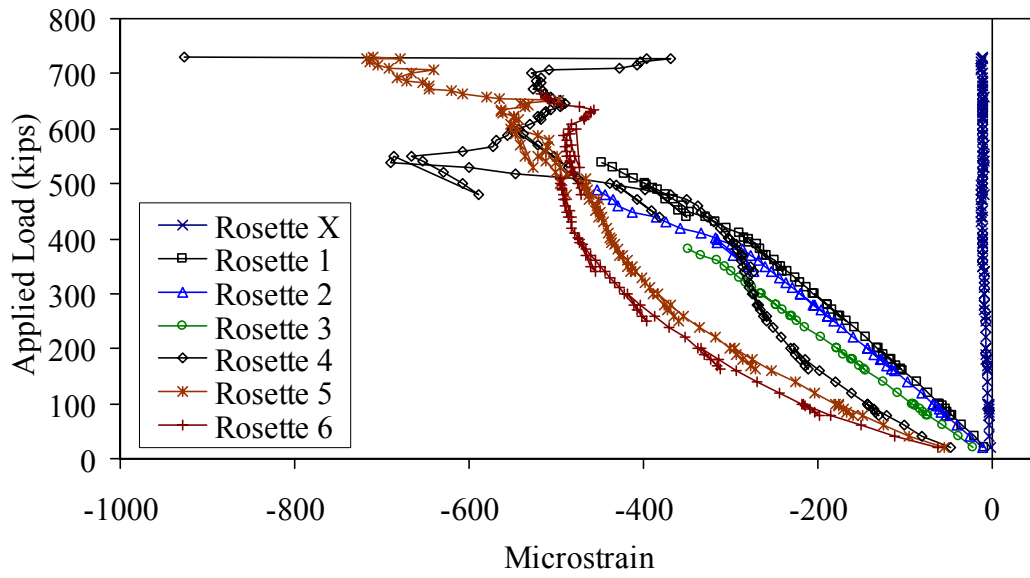


Figure 6.2.2-F: Principal compressive strain in the web of Girder 24S

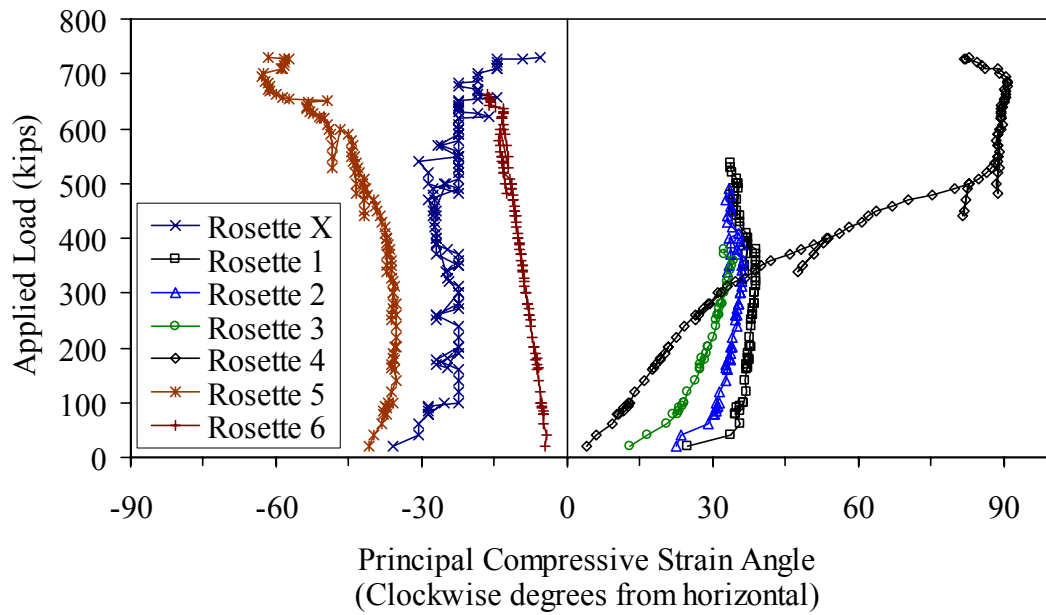


Figure 6.2.2-G: Principal compressive strain angle in the web of Girder 24S

Figure 6.2.2-H shows photographs taken from a digital video of the failure. These two parallel shear cracks released in a brittle fashion, and the girder failed. As previously mentioned, none of the strands slipped until after the failure. The two top flange strands did break in three locations during the failure; however, this secondary failure was related to the large release of energy coming from the concrete tensile (shear) failure. Figure 6.2.2-I shows the girder after failure. Figure 6.2.2-J shows the crack and failure patterns recorded after the girder had failed.

6.2.3 Girder 14S

The third shear test was completed on Girder 14S. As shown in Figure 5.3-A, this girder was one end of an untested 30-ft girder. This specimen had an overall span of 14 feet and a shear span of 6 feet, resulting in a shear span-to-depth ratio of 2.0. The east bearing on this girder was placed 6 in. from the end of the girder, similar to where it would be placed in practice. Note that half of the bottom flange strands are debonded to 36 in. from the end of the girder.

Figure 6.2.3-A shows the applied load versus the vertical deflection response of the girder. Similarly, Figure 6.2.3-B shows the applied load versus the girder rotation at the east and west supports. Figure 6.2.3-C shows the deflected shape of the girder at nine points throughout the test. Recall that the load was applied 8 feet from the west support.

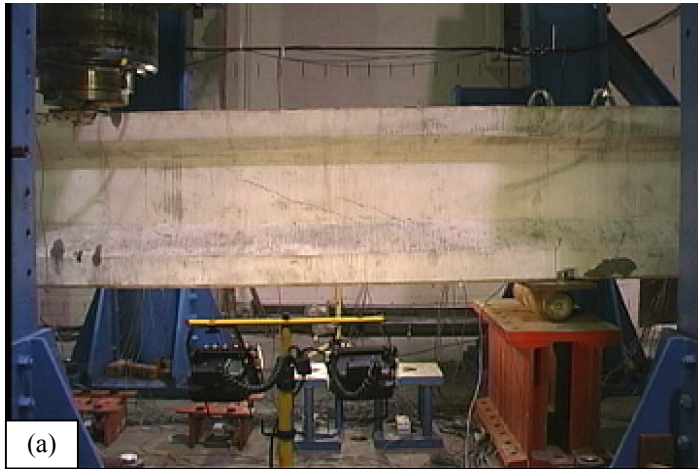
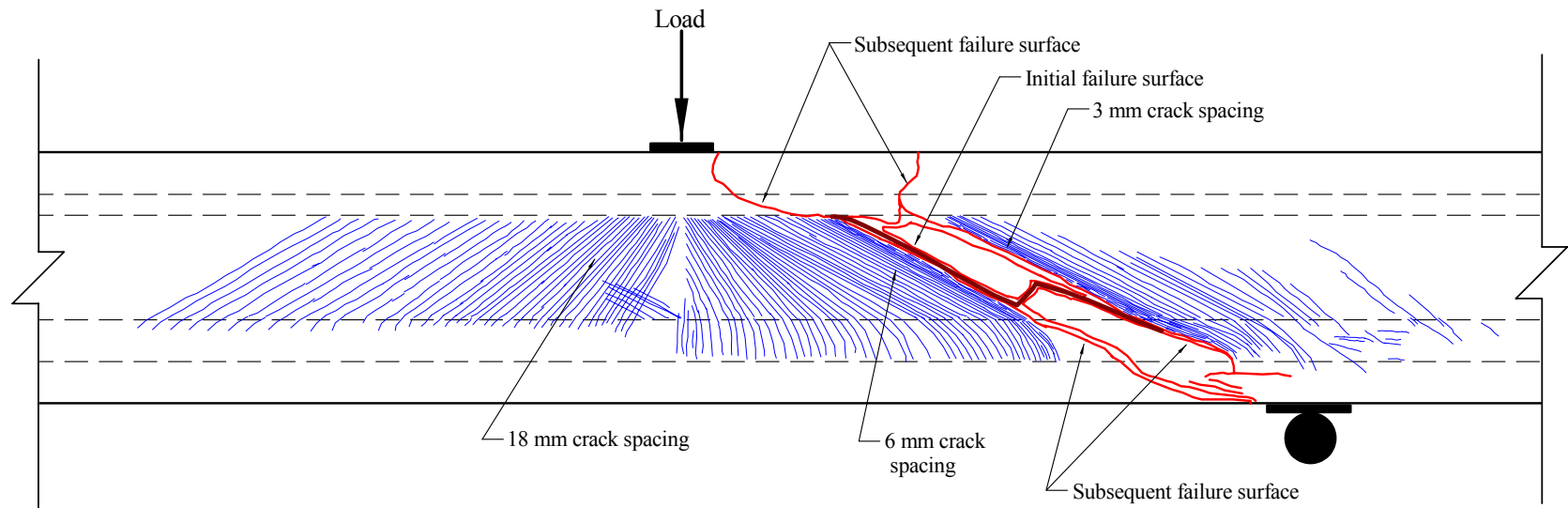


Figure 6.2.2-H: Failure of Girder 24S. (a) $1/15^{\text{th}}$ second before failure. (b) $1/30^{\text{th}}$ second before failure. (c) At failure. (d) $1/30^{\text{th}}$ second after failure.



Figure 6.2.2-I: Failed Girder 24S (a) south elevation and (b) bottom flange near bearing



- Note: 1. Crack widths are not drawn to scale.
2. Tightly spaced crack areas are not drawn to scale.

Figure 6.2.2-J: Crack pattern at failure in Girder 24S

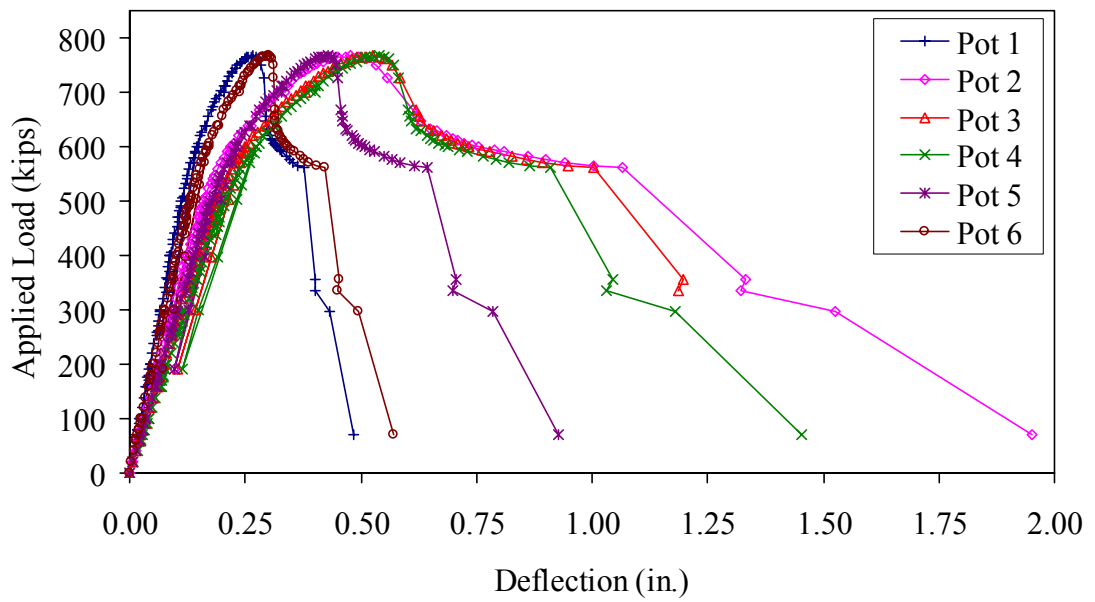


Figure 6.2.3-A: Load-deflection response for Girder 14S

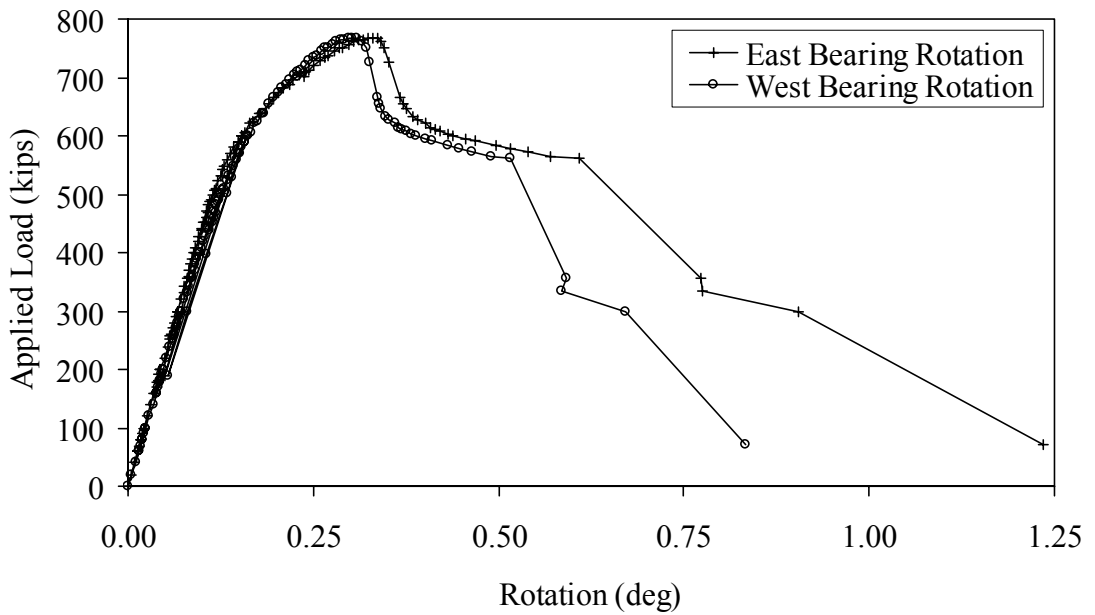


Figure 6.2.3-B: Bearing rotation for Girder 14S

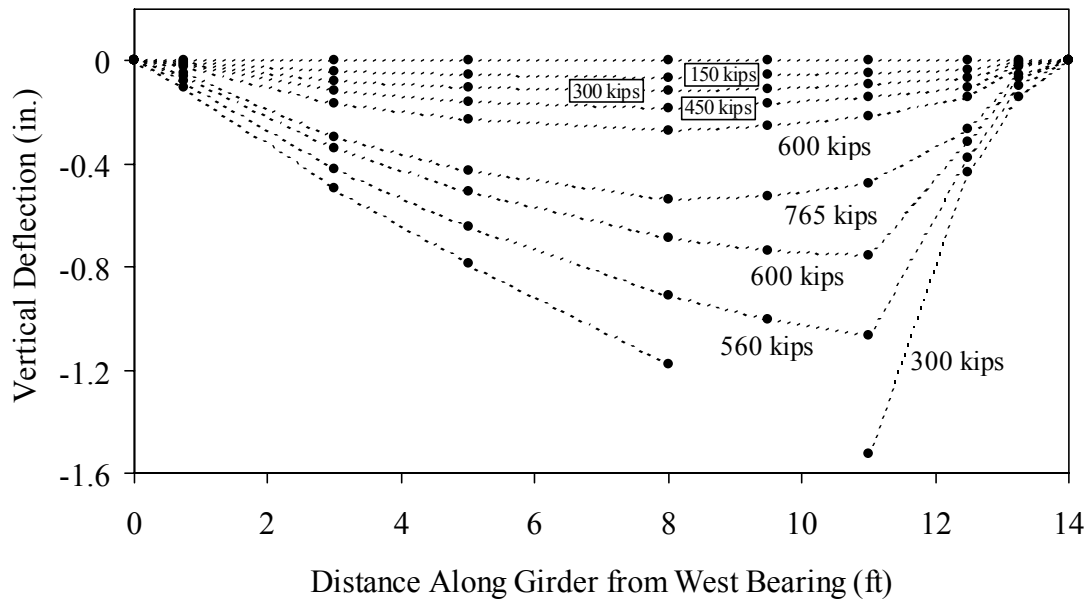


Figure 6.2.3-C: Deflected shape for Girder 14S

The deflection measurements nearest to the load point indicate that the girder began to show softening behavior at a load of between 450 and 500 kips. The girder still had a significant reserve load capacity and reached a peak load of 766 kips. At this peak load, the shear load carried by the east shear span was 438 kips.

Half of the prestressing strands extending from the east end of the girder were instrumented to measure strand slip. Figure 6.2.3-D shows the strand slip results throughout the test. The results for 11 of the 13 instrumented strands are shown. The LVDTs attached to the remaining two strands were not providing reliable results at the conclusion of the test; therefore, the results from these instruments were disregarded.

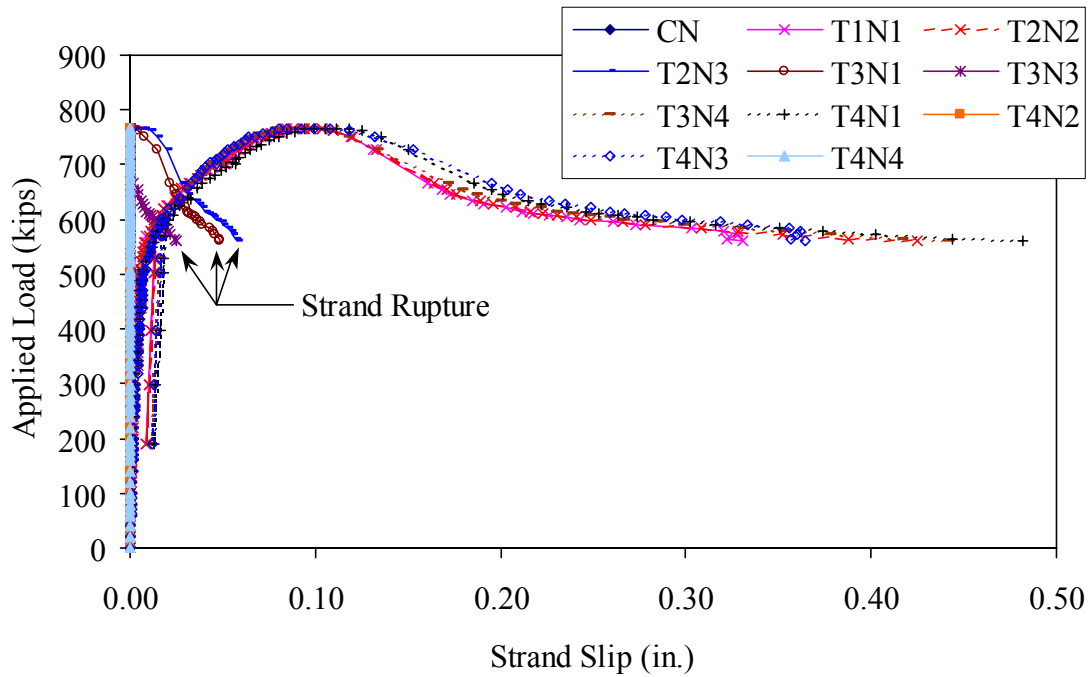


Figure 6.2.3-D: Strand slip in Girder 14S

Results from the six strain rosettes are presented in Figures 6.2.3-E through 6.2.3-H. The tensile principal strain and strain angle values are presented in the first two figures. The compressive principal strain and strain angle values are presented in the second two figures. Note that the strain angle values are measured in clockwise degrees from horizontal on the south face of the girder. Also, similar to the Girder 24S results, tension and compression are not always strictly correct with regard to the sign of the principal strains.

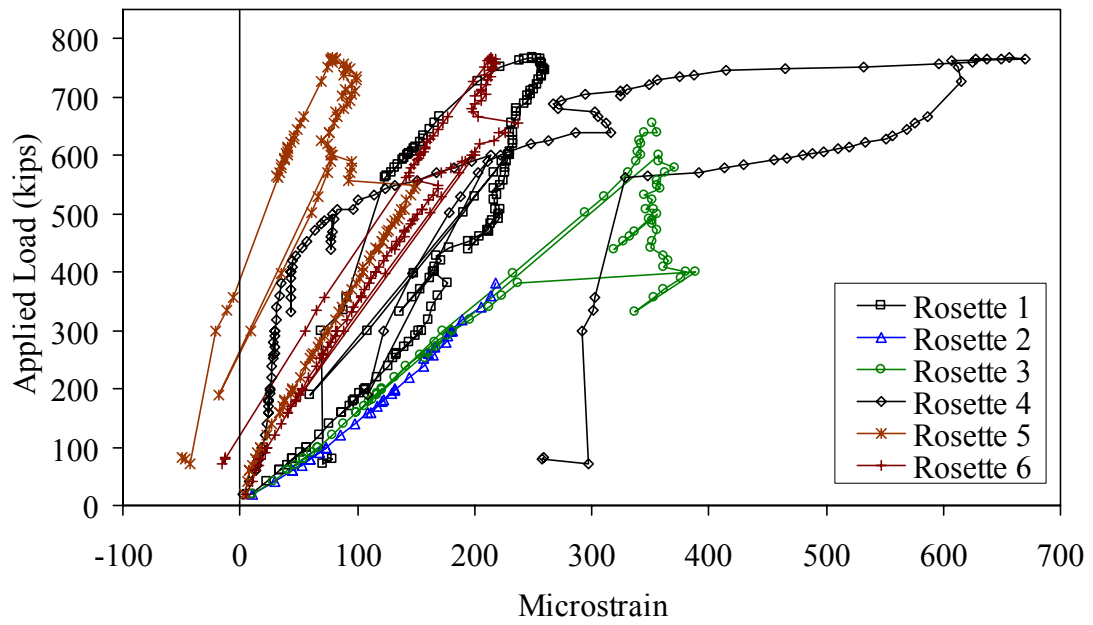


Figure 6.2.3-E: Principal tensile strain in the web of Girder 14S

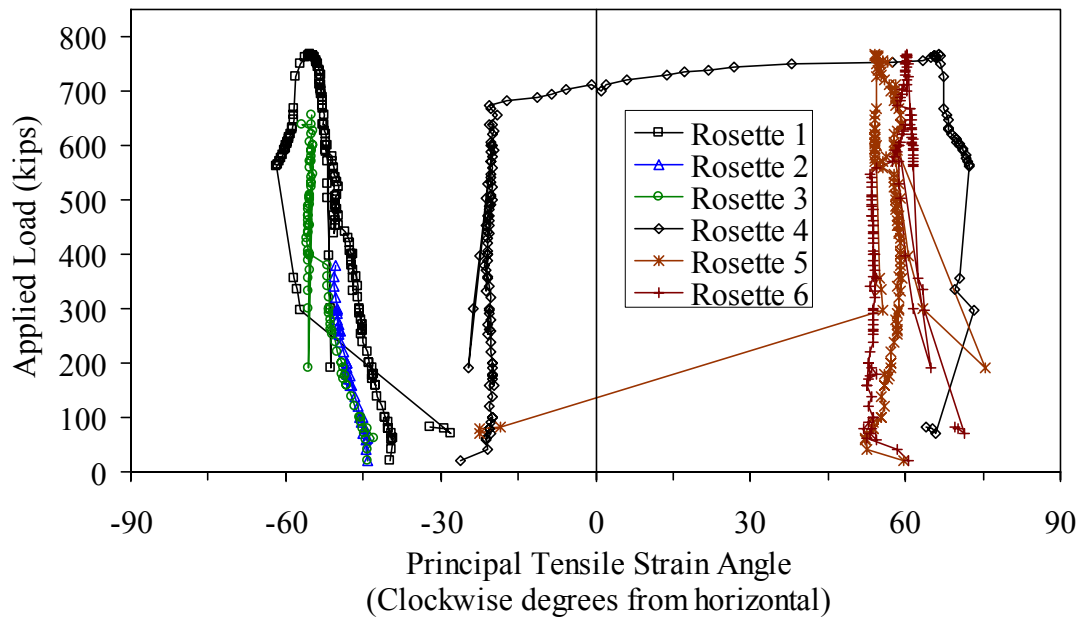


Figure 6.2.3-F: Principal tensile strain angle in the web of Girder 14S

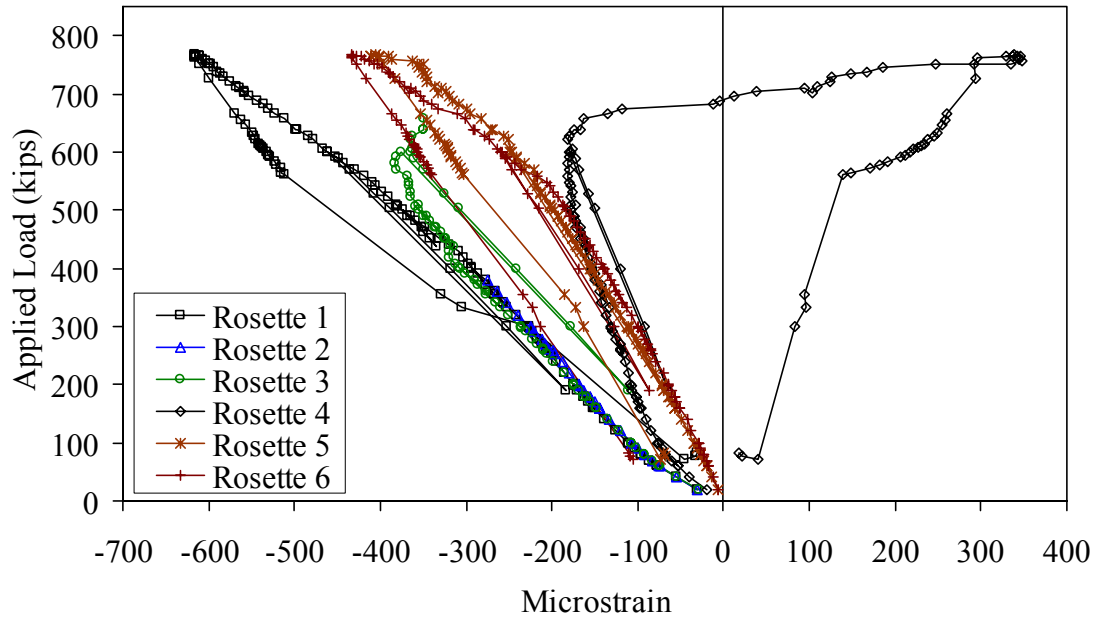


Figure 6.2.3-G: Principal compressive strain in the web of Girder 14S

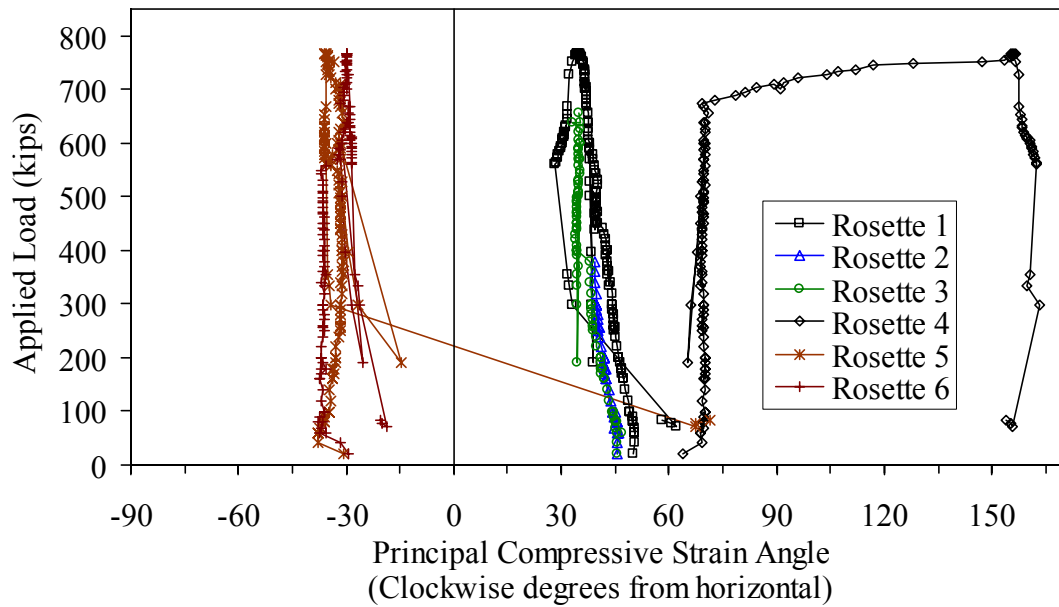


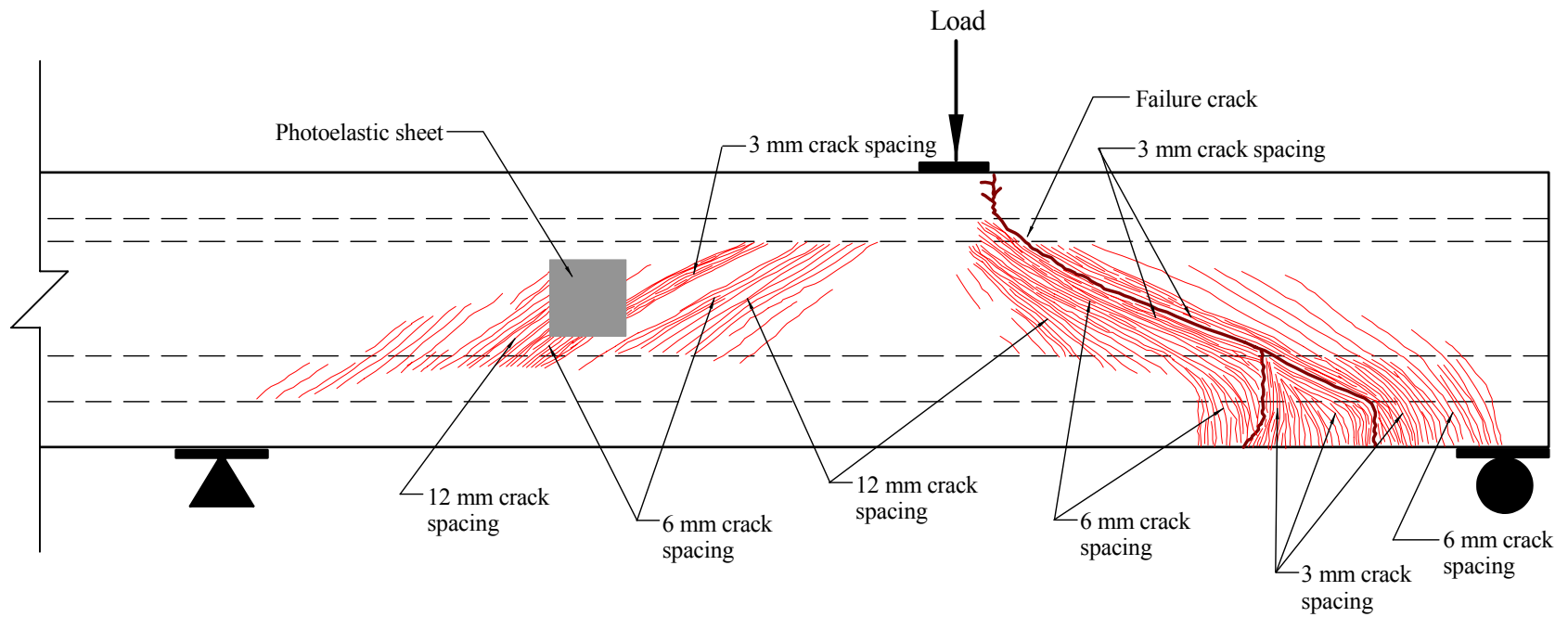
Figure 6.2.3-H: Principal compressive strain angle in the web of Girder 14S

Cracking and other damage to the girder throughout the test were observed both audibly and visually. The first cracking was heard at a load of 360 kips. The cracking continued throughout the remainder of the test and seemed to primarily emanate from the eastern half of the girder. At a load of approximately 700 kips, a larger crack became visible that could clearly be seen from 15 feet away. This crack continued to grow longer and wider as the applied load was increased. Figure 6.2.3-I(a) shows the crack at the peak load carried by the girder. Subsequent to this point in the test, the girder continued to soften while the displacement increased and the load decreased. The crack continued to grow toward the bearing and load point until it a secondary crack formed. Figure 6.2.3-I(b) shows the girder after the formation of the secondary crack in the bottom flange 36 in. from the end of the girder. This is precisely the location to which half of the bottom flange strands were debonded.

Failure of the girder occurred when prestressing strands in the bottom flange began to rupture. The vertical crack in the bottom flange at the end of the debonding length continued to widen as, sequentially, the fully bonded strands broke. As more displacement was imparted into the girder, more strands ruptured until all 12 fully bonded bottom flange strands had ruptured. Figure 6.2.3-J shows the crack and failure patterns that were recorded after girder failure.



Figure 6.2.3-I: Girder 14S at (a) peak load and (b) post-peak load of 595 kips



- Note: 1. Crack widths are not drawn to scale.
2. Tightly spaced crack areas are not drawn to scale.

Figure 6.2.3-J: Crack pattern at failure in Girder 14S

CHAPTER 7

DISCUSSION OF RESULTS

7.1 Tensile Behavior of UHPC

Four small-scale experimental test methods were used to study the tensile behavior of UHPC. These test methods included the ASTM C1018 prism flexure test, the ASTM C496 split cylinder test, the AASHTO T132 mortar briquette test, and the cylinder direct tension test. Individual test results were presented in Section 3.4. In this chapter, the results will be combined and compared and the test methods and their applicability and practicality for UHPC will be discussed.

7.1.1 Summary of Experimental Results

The four small-scale concrete tension testing methods used in this research provided varied bodies of results. Table 7.1.1-A presents the primary quantifiable results from the four test methods. Each test provided an indication of the tensile cracking strength of UHPC. The direct tension and prism flexure tests also provided an indication of the modulus of elasticity of UHPC. Finally, the prism flexure tests provided an indication of the post-cracking toughness of UHPC. For reasons discussed in Section 3.4.1, the third-point loaded UHPC prism with the 12-in. span is taken as the standard prism flexure loading configuration, and its results are presented in this section.

Table 7.1.1-A: UHPC material characterization results for average tensile properties of UHPC

Material Characteristic	Steam	Air	Tempered Steam	Delayed Steam	Supplemental Description
First Cracking Strength (ksi)					
Split Cylinder	1.7	1.3	1.7	1.7	ASTM C496
Prism Flexure	1.3	1.3	1.5	1.4	ASTM C1018; 12 in. span; corrected result
Mortar Briquette	1.2	0.9	1.4	1.0	AASHTO T132
Direct Tension	1.4 – 1.6	0.8 – 1.0	1.1 – 1.3	1.3 – 1.6	Axial tensile load
Combined Result, f_{ct}	1.3	0.9	1.3	1.3	Best estimate of tensile cracking strength
Modulus of Elasticity (ksi)					
Direct Tension	7500	6900	7550	7550	Axial tensile stress and strain based
Prism Flexure	8540	7150	8160	8100	Flexural and shear deflection based; 12-in. span
Post-Cracking Strength (ksi)					
Mortar Briquette	1.3	0.9	1.3	0.9	AASHTO T132; influenced by fiber dispersion and orientation
Flexural Toughness					
Prism Flexure: I_{10}	14.4	12.8	13.0	13.8	ASTM C1018; 12-in. span
Prism Flexure: I_{30}	53	48	43	48	ASTM C1018; 12-in. span
Compression Testing Results					
Compressive Strength, f_c' (ksi)	28.0	18.3	24.8	24.8	ASTM C39; 28-day strength
Modulus of Elasticity (ksi)	7600	6200	7400	7300	ASTM C469; 28-day modulus
Tension, Compression					
$f_{ct} = x (f_c')^{0.5}$	7.8	6.7	8.3	8.3	
$f_{ct} = x f_c'$	0.046	0.049	0.052	0.052	

The tensile cracking strength of UHPC is critical to the design of UHPC structures; however, it is difficult to experimentally determine. All of the four test methods provide realistic tensile cracking strengths that could be assumed to be accurate representations of actual tensile behavior. However, Table 7.1.1-A also shows that, for each curing regime, the tensile cracking strength can vary by approximately 0.5 ksi depending on the test method used. For this reason, engineering judgment must be used to predict the true tensile cracking behavior.

Table 7.1.1-A shows that the results for the cylinder direct tension and mortar briquette test cracking tensile strength were generally similar for each curing regime. This similarity is not surprising because both test methods are based on the uniaxial application of tensile stresses. The prism flexure results, after the application of the correction factor discussed in Section 3.4.1.1, are generally slightly higher than the direct tension results. Note that without the correction factor, the prism flexure results would be approximately two times the direct tension results. Finally, the split tensile results are approximately one-third larger for all curing regimes, a result that is not unexpected when comparing split cylinder test results with direct tension results (Petroski 1987). Direct tension results are normally more highly regarded than split cylinder results. However, direct tension tests may possibly be disproportionately impacted by local heterogeneities as compared to the larger structures that they are supposed to mimic. Therefore, lower tensile cracking strengths may be reported than what would actually be observed in practice.

The results from these four test methods were combined together to determine the tensile cracking strength. The combining of these results takes into account the overall body of results, the number of tests, and the deviation of results from the average value. When these factors are combined, the tensile cracking strength of Steam treated UHPC is 1.3 ksi. The tensile cracking strength of Air treated UHPC is 0.9 ksi. The tensile cracking strength of Tempered Steam and Delayed Steam treated UHPC are both 1.3 ksi.

These tensile cracking strength results can be compared with the compressive strength results discussed previously in this report. The bottom of Table 7.1.1-A shows that the tensile cracking strength, f_{ct} , is approximately 5% of the compressive strength, f_c' , in all four curing regimes. Alternatively, Equation 7.1.1-A is frequently used to approximate a tensile strength from a given compressive strength. In this equation, the square root of the compressive strength is related to the tensile strength by a linear multiplier, x . In this case, the UHPC that underwent the Steam treatment has a multiplier of 7.8, the Air treated UHPC has a multiplier of 6.7, and the Tempered and Delayed Steam treated regimes have a multiplier of 8.3.

$$f_{ct} = x\sqrt{f_c'} \quad (7.1.1-A)$$

The modulus of elasticity results obtained from the tension tests are also presented in the table. Given the limited number of direct tension tests completed, these results can be considered to be similar to the compression test modulus of elasticity results discussed in Chapter 3. Although the Air treated result is 11% higher, the remainder of the results are

within 3.5%. However, the prism flexure modulus of elasticity results are generally between 10% and 15% higher than the comparable compression test results. This result indicates that the UHPC prism flexure tests tend to overestimate the modulus of elasticity as compared to the standard compression testing methods because nearly all of the prism groups exhibit this behavior, regardless of cross-section and loading configuration.

The post-cracking tensile behavior is much more difficult to quantify, but this research program has resulted in a number of both general and specific findings. The mortar briquette tests provide the most direct indication of the post-cracking behavior. Figure 3.4.3-B through 3.4.3-E show the full load-displacement curves for all of the mortar briquette tests. First and foremost, these figures indicate that UHPC tends to display post-cracking strength levels similar to its precracking strength levels. The table lists the average post-cracking strength values, which are all within 0.1 ksi of the mortar briquette first tensile cracking strength levels. Note, however, that post-cracking behavior is very dependent on fiber dispersion and orientation. The small-scale mortar briquettes most likely did not accurately represent the large-scale tensile members for these two factors.

Limited post-cracking strength results are also available from the split cylinder tests. These tests indicate that, under the biaxial state of stress present in this test configuration, UHPC exhibits significant post-cracking load carrying capacity. For each curing regime, the peak load carried after cracking is approximately twice the cracking load. However, the compressive forces paralleling the tensile crack in this loading configuration increase the fiber/matrix bond and thus contribute to the post-cracking load carrying capacity.

Finally, comparative results were also obtained from the prism flexure tests. The results from this standardized test can easily be compared both within this study and with normal and fiber reinforced concretes tested by other researchers. Comparisons with the standard toughness levels set in ASTM C1018 and with the results from other researchers indicate that UHPC exhibits very high post-cracking toughness values. Specifically, all the UHPC curing regimes were at or above the stated fiber reinforced concrete toughness upper limit for the values of I_5 , I_{10} , and I_{20} . Also, these tests indicate that a relatively uniform level of toughness will be achieved throughout the curing regimes. However, these results do not mean that all UHPC display identical post-cracking load carrying behavior, because the ASTM C1018 toughness measure relates post-cracking to pre-cracking behaviors and thus is biased by the pre-cracking strength.

7.1.2 Summary of Experimental Test Methods

Sections 7.1.1 and 3.4 describe the small-scale tension tests employed in this research program and the relevant results from each test. This section builds on those presentations to present and to compare the test methods. Test capabilities and the difficulties associated with completing each test will be discussed.

The split cylinder test is the simplest UHPC tension test to successfully complete. This test program has shown that consistent UHPC tensile cracking strength results can be obtained by following the ASTM C496 test procedure. The only addition to the test is the inclusion of a cylinder lateral expansion measurement and recording device. Thus, a

measure of the tensile cracking strength of UHPC can be obtained using a standard hydraulic compression testing machine, a simple data acquisition system, and a pair of displacement transducers. Alternatively, an evaluation technique capable of detecting a crack in UHPC, such as ultrasonic inspection, could be used to note cracking in steam-based treated UHPC, thus eliminating the need for data acquisition and full range transducers. Test results presented in Section 7.1.1 indicated that conversion of the split tensile cracking strength result to the overall tensile cracking strength result could be obtained by multiplying the split cylinder result by a factor of 0.75. Unfortunately, the unknown post-cracking stress distribution in the cylinder does not allow for the quantitative determination of any post-cracking tensile behaviors.

A slightly more advanced loading setup is required for completing the AASHTO T132 mortar briquette test. The test performed in this research program required a test machine capable of loading under crosshead displacement control and a data acquisition system capable of recording load and displacement readings throughout the test. The primary benefit of this test over the split cylinder test is that it directly measures uniaxial tensile properties of UHPC. This benefit allows for a more accurate rendering of the UHPC tensile cracking strength. Also, this test method can provide some indication of the post-cracking tensile strength of UHPC; however, the difficulties inherent in the casting of these small briquette specimens decrease the confidence in any post-cracking strength results. As such, the benefits of this test over the split cylinder test are marginal unless a qualitative verification of post-cracking load-carrying capacity is desired.

The ASTM C1018 prism flexure test is significantly more intensive with regard to testing equipment than either of the previous two test methods. To successfully complete this test, a test machine capable of loading under an external displacement transducer control is necessary, along with a data acquisition system to record load and displacement. Additionally, an electronic averaging circuit to combine the deflection results from the specimen can provide for more consistent, uniform loading. The benefit of the prism flexure test is that it provides an indication of the tensile cracking strength, the modulus of elasticity, and an arbitrarily defined but widely used measure of the post-cracking tensile toughness. Because a cross-comparison between different fiber reinforced concretes or concretes cast in different laboratories is important, this test can provide needed results that are unavailable through simpler test setups. However, as discussed in Section 3.4.1.1, tensile cracking strength results from this test method must be corrected using an empirical relationship. The acquisition of pure tensile cracking behaviors from this test method is not possible.

The final test method, the direct tension test, is the most difficult test to implement and also provides the most complete body of results. This method requires a test machine capable of loading under external displacement control, an electronic averaging circuit for at least three displacement transducers, and a data acquisition system to record the load and displacements. Additionally, a means of gripping the tensile specimen, such as the high-strength, high-modulus epoxy used in the research, is necessary. Finally, great care must be taken in the fabrication of the small-scale specimens to ensure that they replicate the regions in large-scale structures that are subjected to tensile stresses. If all

these requirements are met, this test has the possibility of capturing the full tensile stress-strain or stress-crack opening behavior. These results would include the tensile cracking strength, the modulus of elasticity, the post-cracking tensile strength, and the load-carrying capacity from tensile cracking through fiber pullout. The test program discussed in this report did not achieve the goal of successfully completing direct tension tests, and thus was not able to determine the full tensile stress-strain response of UHPC from small-scale tension tests.

The selection of a particular tension test for UHPC must be predicated on the results desired. The tests discussed in this section could be used to meet certain needs, but other tests or modifications of these tests could also be used. For example, it is likely that UHPC used in structures will require a minimum level of tensile strength. As a quality control issue, a hydraulically operated test machine under load control could be used to ensure that the minimum level of tensile strength is achieved. This could be accomplished by an experienced quality control professional performing a mortar briquette or split cylinder test wherein the UHPC was required to hold a sustained stress level prior to the audible indication of tensile cracking.

7.2 Local and Global Mechanical Failure Modes of UHPC

UHPC exhibits a number of macrostructural mechanical failure modes. These failure modes can be categorized into three specific types: compressive, tensile cracking, and tensile fiber pullout. A fourth failure mode, the high-cycle fatigue failure of crack-

bridging steel fibers, has been observed under special loading conditions but will not be discussed in this report.

The compressive failure of UHPC can be considered to be similar to the compressive failure of any fiber reinforced concrete. In general terms, UHPC fails under axial compressive load through lateral tensile expansion. This lateral expansion is partially restrained by the internal steel fiber reinforcement, thus allowing for a more ductile failure than may be expected. As with any concrete, higher strength UHPC tends to fail in a more brittle manner than lower strength UHPC.

On a large scale, the compressive failure of a girder web being subjected to shear loading was observed during the Girder 28S test. This compression failure can be described as a slow crushing and surface cracking of the UHPC girder web as loads were being redistributed around the failing area. No significant spalling of the concrete was observed during this compression failure. This slow crushing continued for over 1 minute before the newly redistributed loads caused a tensile fiber pullout failure to occur in another location.

On a smaller scale, compression failures in hundreds of UHPC cylinders were observed while performing the ASTM C39 compression test. The failure of any cylinder that underwent steam-based treatment was brittle, with a rapid load decrease occurring immediately after the peak load was achieved. Even as such, these cylinders remained largely intact with relatively few small fragments leaving the cylinder. The failure of the

cylinders that underwent the Air treatment behaved in a much more ductile manner. Some of these cylinders, particularly the ones with strengths above the average of 18.3 ksi, did exhibit brittle behavior. However, most of these cylinders failed through a continuous, non-abrupt decrease in load after reaching the peak. The failures of these lower strength (and less cured) cylinders were significantly more ductile and exhibited quantifiable post-peak behavior that was not achievable on a hydraulically-actuated load testing machine with the higher strength cylinders. Finally, the compression testing of a 3-in. diameter Steam treated UHPC cylinder that did not contain any fiber reinforcement resulted in an extremely brittle failure with significant fragmentation of the UHPC.

The tensile behavior of UHPC allows for continuing tensile load carrying capacity across a cracked plane. The design of the structure will determine whether the tensile cracking of UHPC is a failure mode. Regardless, for the purposes of this discussion the UHPC behavior at this critical junction will be described.

Similar to the compression failures described above, the tensile cracking of UHPC can be either brittle or ductile. Although these differences in behaviors were observed in all small-scale tensile tests, the differences were most clearly observed in the split cylinder tensile tests. In these tests, the cylinders that had been subjected to steam-based treatments tended to exhibit a clear aural indication of first cracking and displayed discontinuous load-displacement behavior as the crack abruptly formed then was arrested by the bridging fibers. Conversely, the Air treated cylinders did not exhibit an aural indication of first cracking and sometimes displayed continuous load-displacement

behavior at cracking. Also, the crack width at crack arrest tended to be larger in the cylinders that underwent the steam-based treatment, which was likely due to the higher tensile strengths at which cracking occurred.

The full-scale flexure and shear girder tests provide a significant amount of additional information regarding the cracking behavior of Steam treated UHPC. Observations during these tests indicate that tensile cracks form perpendicular to highly stressed tensile regions, and their formation is clearly indicated by an audible signal. These cracks were highly linear because the girders contained no passive reinforcement and the UHPC contained no coarse aggregate. The initial cracks that formed in these tests were extremely tight. The only method that could determine the location of these surface cracks was the use of a volatile indicating spray. As the tests progressed, the cracks began to widen slightly, and additional cracks filled in nearby. Observations from the full-scale flexure test indicate that the crack spacing of 1/8 in. or less is possible in highly stressed regions. These results clearly indicate UHPC's ability to redistribute stresses and to undergo multiple cracking prior to fiber pullout.

Final tensile failure of UHPC generally occurs when the steel fiber reinforcement begins to debond from and to pull out of the UHPC matrix. Because fibers are randomly distributed and oriented in the UHPC, individual fiber loads vary at any particular global load level. Mechanically, pullout occurs when the load carried by an individual fiber overcomes the ability of the UHPC to grip the fiber. Pullout by any fibers increases the load that other nearby fibers have to carry. Multiple pullouts in a specific location that

require gross load redistribution through alternate load paths can be defined as fiber pullout failure.

The full-scale flexure test on Girder 80F and the shear test on Girder 24S provide clear indications of the effect of fiber pullout on global girder behavior. In Girder 80F, hundreds of tightly spaced cracks carried significant flexural tensile forces in the bottom bulb of the girder. At the peak load carried by the girder, the fibers at one specific cross-section began to pull out. This crack quickly became significantly wider than any other crack in the girder and placed large additional strains on the prestressing strands at this location. Because the strands could not sustain this large strain, the strands ruptured and the girder failed.

In Girder 24S, many tightly spaced cracks formed perpendicular to the diagonal tensile forces being carried by the web of the girder. As the loads on the girder increased, more cracks formed and the fibers bridging the existing cracks became more highly stressed. Eventually, the fibers bridging a very highly stressed crack began to pull out. Because this girder contained no mild steel reinforcement to aid in load redistribution, the girder abruptly failed.

In both girder tests discussed above, the failure of the girder as a whole was precipitated by the local bond failure between the fibers and the UHPC matrix. These results clearly indicate that unless significant mild or prestressing steel redundancy exists in the UHPC member, fiber pullout will result in member failure.

7.3 Effect of Curing Procedure on UHPC Properties

One of the primary focuses of this research program was to determine the effect that the application of a curing treatment had on the behaviors exhibited by UHPC. To quantify this effect, the majority of the research completed within the material characterization portion of this study included four different curing regimes. The curing regimes included the manufacturer recommended Steam treatment, a delayed version of the same treatment, a reduced temperature version of the same treatment, and an untreated case in which the UHPC remained in a laboratory air environment until testing.

Table 7.3-A presents a compilation of results from the material characterization study. The results provided in the table are average values that were summarized for ease of discussion. A full discussion of each portion of this test program is provided in Chapter 3.

The application of a curing treatment clearly impacts UHPC behavior. A comparison of the Steam and Air treated regime results indicates that the application of the recommended Steam treatment has a significant effect on some properties. In terms of mechanical properties, Steam treatment will increase the compressive strength, tensile cracking strength, and elastic modulus. In terms of long-term stability, Steam treatment will decrease creep and speed the realization of the asymptotic shrinkage virtually eliminating any shrinkage after the treatment is complete. In terms of durability, Steam treatment seems to decrease the permeability of UHPC thus increasing its resistance to chloride penetration. A more durable mechanical matrix that is better able to resist abrasive forces is also created.

The application of intermediate curing treatments, such as in the Tempered Steam and Delayed Steam regimes, also has a significant—although generally slightly reduced—impact on the UHPC behavior. While the compressive strength and elastic modulus are increased by these treatments, they both fall short of the level achieved with the full Steam treatment. Interestingly, tensile cracking behavior enhancements seem to be similar regardless of the type of steam treatment applied. Note that the creep behavior is significantly enhanced by the Delayed Steam treatment while it is only slightly enhanced by the Tempered Steam treatment. In terms of durability, the chloride ion penetrability is extremely low regardless of the steam treatment applied.

Another curing treatment procedure, illuminated during this test program, is slightly outside of the clearly defined boundaries of the curing regimes. In Section 3.3.5, the effect of demolding cylinders in terms of their early age setting and strength gain was discussed in terms of compressive strength. These tests showed that demolding UHPC, and thus exposing it to a low humidity environment, prior to sufficient setting and strength gain could have a significant impact on the 28-day compressive strength. It is extremely important to wait until a sufficient strength level has been achieved before demolding UHPC and to keep UHPC in a moist environment during the continued strength gain. This procedure was not always followed within this material characterization study and, as discussed in Chapter 3, some of the observed behaviors were reduced as a result.

The overriding result of the entire UHPC curing treatment comparison is that, regardless of the curing treatment applied, UHPC exhibits significantly enhanced properties compared with standard normal strength and high performance concretes. The application of the Steam treatment is clearly beneficial; however, this procedure is also not always necessary as long as the user is willing to accept decreases in strength, long-term stability, and durability.

7.4 Early Age Strength Gain of UHPC

The compressive strength gain behavior of UHPC is an important characteristic of the concrete. Results detailed in Chapter 3 indicated that UHPC does not have any compressive strength for nearly 1 day after casting. Then, once initial set occurs, UHPC rapidly gains strength over the course of the next few days until over 10 ksi of strength is achieved. At that point, the rate of strength gain decreases, but the strength gain continues until over 18 ksi of compressive strength is achieved by 28 days.

Figure 7.4-A presents a compilation of the compressive strength data for the Air treated cylinders tested between 1 and 56 days (the results are discussed in Section 3.3.2). These results include both cylinders in the Air treatment group and cylinders in the other treatment groups that had not yet undergone their own steam treatment. Also, recall from Section 3.6 that initial set tended to occur at approximately 15 hours, and final set occurred 2 hours later.

Table 7.3-A: Average UHPC material properties presented according to curing treatment

Material Characteristic			Tempered	Delayed	Supplemental Description
	Steam	Air	Steam	Steam	
Compressive Strength (ksi)	28.0	18.3	24.8	24.8	ASTM C39; 28-day strength
Modulus of Elasticity (ksi)	7600	6200	7400	7300	ASTM C469; 28-day modulus
Split Cylinder Cracking Strength (ksi)	1.7	1.3	1.7	1.7	ASTM C496
Prism Flexure Cracking Strength (ksi)	1.3	1.3	1.5	1.4	ASTM C1018; 12-in. span; corrected
Mortar Briquette Cracking Strength (ksi)	1.2	0.9	1.4	1.0	AASHTO T132
Direct Tension Cracking Strength (ksi)	1.4 – 1.6	0.8 – 1.0	1.1 – 1.3	1.3 – 1.6	Axial tensile load
Prism Flexural Tensile Toughness (I ₃₀)	53	48	43	48	ASTM C1018; 12-in. span
Long-Term Creep (C _{cu})	0.29	0.78	0.66	0.31	ASTM C512; 11.2 ksi sustained load
Long-Term Shrinkage (microstrain)	766	555	620	657	ASTM C157; initial reading after set
Total Shrinkage (microstrain)	850	790	–	–	Embedded vibrating wire gage
Coeff. of Thermal Exp. (x10 ⁻⁶ in/in/°C)	15.6	14.7	15.4	15.2	AASHTO TP60-00
Chloride Ion Penetrability (Coulombs)	18	360	39	18	ASTM C1202; 28-day test
Chloride Ion Permeability (lb/yd ³)	< 0.1	< 0.1	< 0.1	< 0.1	AASHTO T259; ½-in. depth
Scaling Resistance	No Scaling	No Scaling	No Scaling	No Scaling	ASTM C672
Abrasion Resistance (grams lost)	0.17	0.73	0.20	0.13	ASTM C944 2x weight; ground surface
Freeze-Thaw Resistance (RDM)	96%	112%	100%	99%	ASTM C666A; 600 cycles
Alkali-Silica Reaction	Innocuous	Innocuous	Innocuous	Innocuous	ASTM C1260; tested for 28 days

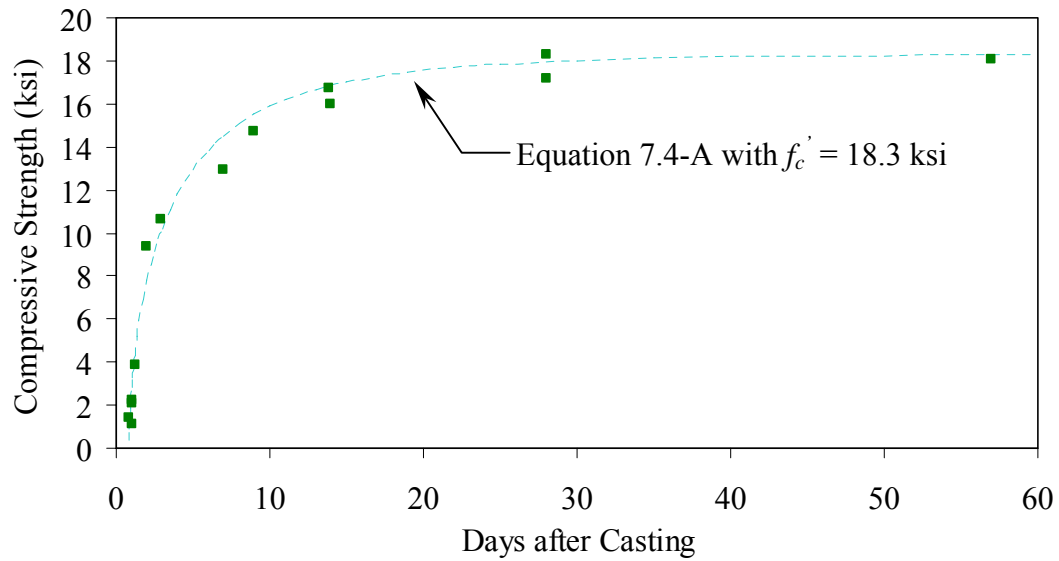


Figure 7.4-A: Compressive strength gain as a function of time after casting

A regression analysis was completed to fit a transition function to the data presented in Figure 7.4-A. The delayed then rapid early age strength gain behavior of UHPC results in a somewhat complex approximating function. The Weibull Cumulative function, provided as Equation 7.4-A below and plotted in Figure 7.4-A, accurately describes the strength gain behavior for any time after 0.9 days following casting. This equation includes the time in days after casting, t , the 28-day compressive strength in ksi, f_c' , and the compressive strength at time t in ksi, $f_{c,t}'$. The initial and final set times of UHPC can vary depending on the age of the premix and the environmental conditions, thus this equation may not be applicable to UHPC exhibiting different setting behaviors.

$$f_{c,t}' = f_c' \left[1 - \exp \left(- \left(\frac{t + 3(\ln 2)^{1/0.63} - 2.5}{3} \right)^{0.63} \right) \right] \quad (7.4-A)$$

7.5 Comparison of Cylinder and Cube Compression Strength Results

The cylinder is the standard concrete compression test specimen geometry used in the United States. This is understandable because cylinder molds are inexpensive and the casting of concrete cylinders is relatively easy. However, as opposed to traditional concrete, UHPC cylinders cannot be easily prepared for testing. In any concrete compression test, the even and parallel loading of the ends of the cylinder is critical to achieving accurate test results. The high compressive strength of UHPC eliminates the possible use of end capping materials and predicated grinding or milling to ensure plane, parallel loading surfaces. Unfortunately, the equipment necessary to perform this end preparation on UHPC cylinders is not yet locally available to all quality control and testing departments.

One method of eliminating the need for cylinder end preparation is to use cubes as the standard means to measure the compressive strength of UHPC. Cubes are cast with two pairs of plane, parallel faces thus greatly simplifying the specimen preparation process. The primary drawbacks to the use of cubes are the expense of the molds, the unfamiliarity with the test methods, and the indirect nature of the results obtained from the test. In general, cube compression test results are higher than cylinder compression test results on the same concrete due to the aspect ratio of the specimens and the confining effect of the machine platens. To account for these differences, a strength reduction factor normally needs to be applied to a cube compression test result. This factor can vary significantly depending on many concrete properties, but has been

reported to be in the vicinity of 0.82 for ordinary concrete and increases toward 1.0 as the concrete strength increases (de Larrard et al. 1994).

Section 3.3.4 presented the results from a series of cube and cylinder compression tests. Recall that the 2-in., 3-in., and 4-in. diameter cylinders, as well as the 2 in. and 100 mm cubes were tested and that the series of tests were repeated three times on different batches of UHPC. If the 3-in. diameter cylinder is considered to be the control specimen, the results showed that the compressive strength exhibited by the 100 mm cube specimens ranged from 1.2% below to 8.0% above the control specimen strength. The strength of the 2 in. cube ranged from 4.6% to 6.1% above. These increases of less than 10% are sufficiently small; therefore, cube tests should be able to be used as a direct substitute for cylinder compression tests in some applications. Although most owners will probably require cylinder compression tests as the standard strength test result reported for the foreseeable future, the UHPC component fabricator internal quality control testing using the cube specimens would not be precluded.

One additional finding from the results presented in Section 3.3.4 relates to the size of the compression specimen (for either the cylinder or the cube). The results indicate that smaller specimens, particularly the 2-in. diameter cylinders and the 2 in. cubes, tended to exhibit larger standard deviations. The casting-based heterogeneities (i.e., entrapped air voids) in the UHPC that are proportionally larger in smaller specimens are likely behind these results. For this reason, the use of compression specimens that have a minimum dimension smaller than 3 in. is not recommended.

7.7 Shrinkage Behavior of UHPC

A significant portion of this research program has focused on the tensile behaviors of UHPC and the applicability of those tensile behaviors to structural engineering.

Assurance of those tensile properties in a completed structural member is a factor of many things, including both casting/placing techniques and curing treatments. Another important factor is the formwork and its ability to restrain shrinkage forces.

The test results presented in Section 3.7 indicate that UHPC exhibits shrinkage behaviors that are somewhat different than those exhibited by normal concrete. Overall long-term shrinkage of UHPC is somewhat large, with an asymptotic value nearing 850 microstrain. More importantly, the results indicate that UHPC shrinks very rapidly in the 24 hours after the initiation of setting behaviors. This rapid shrinkage can include up to 400 microstrain of shrinkage during this time frame with a shrinkage rate of up to 60 microstrain per hour. The shrinkage continues at an increased rate as compared to normal concrete with 95% of its ultimate shrinkage occurring by 2 months after casting.

These early age shrinkage behaviors are important to the successful casting of UHPC structural members, because UHPC will crack at tensile strains significantly below these shrinkage strains. Thus, the casting of UHPC must mitigate or eliminate shrinkage restraints on the cast member. For highway bridges, standard I-shaped girders are not particularly susceptible to restrained shrinkage cracking. However, in the casting of a member with restrained areas, such as a double-tee section or a box section, special care must be taken to allow for monitoring and the release of shrinkage strains.

7.8 Long-Term Stability of UHPC

The basic premise behind the application of prestressing forces into concrete girders is that the application of an eccentric compressive axial force onto a beam will delay inelastic behaviors and increase the ultimate capacity. To achieve these goals, the prestressing forces must be maintained indefinitely. Time-dependent concrete behaviors such as creep and shrinkage can both negatively impact the maintenance of the prestressing force, thus reducing the enhancement provided by the prestress.

Section 7.12 addresses the long-term stability of UHPC specifically as it relates to the material characterization results and the AASHTO Type II prestressed girders discussed in this study. This section addresses the general long-term stability of UHPC, including the creep and shrinkage behaviors that can be expected and the possible methods to alleviate those behaviors.

In large scale prestressed concrete girder fabrication facilities, the time required to fabricate a girder from initial form setup to cutting of strands and removing the girder from the form is critical. This amount of time determines the turnover for the casting bed and directly influences the cost of each girder. In general, precasters want to create a rapid turnover, thus they are interested in stressing the girder as soon as possible after casting. The results of this method, for any concrete, are that the expected creep and shrinkage values will be larger and the prestress losses will be greater.

The shrinkage behavior of UHPC has been discussed in Sections 3.7 and 7.7. UHPC can be expected to undergo nearly half (400 microstrain) of its long-term shrinkage (850 microstrain) during the first 24 hours after setting. Also, Steam treatment will hasten the achievement of the ultimate shrinkage value and will effectively stabilize the UHPC against further shrinkage indefinitely. For these reasons, delaying the stressing of the girder is clearly beneficial.

The creep behavior is also influenced by the concrete strength at girder stressing. The long-term creep results from Section 3.8 indicate that creep coefficients between 0.3 and 0.8 can be expected for UHPC that is treated according to one of the curing regimes. However, the prestress would likely be applied before any of these treatments are completed in a production environment. For this reason, the creep behavior at earlier ages, and thus at lower compressive strengths, is important. The early age creep testing presented in Section 3.8.2 focuses on this behavior for UHPC that is still of relatively low strength. Creep at two compressive strength levels was investigated, namely 9 ksi and 12.5 ksi. These results indicate that significantly less creep will occur after moderate increases in strength; however, the creep strains observed only 30 minutes after loading a 12.25 ksi cylinder to 10.15 ksi were still over 50% of the elastic strains from the initial loading. This 30 minute effective creep coefficient of 0.52 is quite high considering that the long-term final creep coefficient for a 16.5 ksi UHPC loaded after 28 days of curing is only 0.78.

Similar to the shrinkage results discussed above, the creep results indicate that delaying the stressing of the girder until higher strengths are achieved can be beneficial in terms of long-term prestressed girder behavior. These higher strengths and the better resistance to creep can come either from purely delaying the stressing as in the Air treatment regime or from Steam treating the UHPC prior to application of the prestress.

7.9 Modulus of Elasticity of UHPC

Because compression testing of cylinders is a frequently used quality control method for structural concrete, engineers often attempt to relate other characteristics of concrete's behavior to the compression test results. Many researchers have performed work that focuses on the relationship between the compressive strength of concrete and its elastic modulus. This section compares the strength and modulus results of this test program with the results from predictor equations developed elsewhere.

Recall that the modulus of elasticity testing was completed on compression cylinders according to the ASTM C469 test method. The results from these tests were presented in Section 3.3. Table 7.9-A summarizes the overall 28-day results from these tests for each curing regime along with the compressive strength values.

Table 7.9-A: Compressive strength and modulus of elasticity results

Curing	28-day Compressive Strength	Modulus of Elasticity
Steam	28.0 ksi	7650 ksi
Air	18.3	6200
Tempered Steam	24.8	7400
Delayed Steam	24.8	7300

The American Concrete Institute's Building Code and Commentary (ACI 318) provides two relationships for the modulus of elasticity. Equation 7.9-A shows the first relationship wherein the square root of the compressive strength of concrete is related to the modulus of elasticity through a scalar factor. In this equation, both the compressive strength, f_c' , and the modulus of elasticity, E , are in psi. This equation was derived from, and is most relevant to, normal strength and normal weight concrete.

$$E = 57000\sqrt{f_c'} \quad (7.9-A)$$

ACI 318 provides a second relationship for the modulus of elasticity wherein the unit weight of the concrete is included. This modification allows for estimation of the modulus of elasticity for concrete with a unit weight between 90 and 155 lb/ft³. This modification of the estimation equation is important, because both the weight of the concrete and the modulus of elasticity are normally heavily dependent on the type of aggregate used. Equation 7.9-B presents this relationship, with ρ as the unit weight of concrete in lb/ft³. Recall that the unit weight of UHPC is approximately 155 lb/ft³. Using this unit weight in Equation 7.9-B would result in an equation similar to 7.9-A with a scalar of 63700. Note that Equation 7.9-B is also the relationship provided in the AASHTO LRFD Bridge Design Specification.

$$E = 33\rho^{1.5}\sqrt{f_c'} \quad (7.9-B)$$

The Comité Européen du Béton (Popovics 1998) has presented a different relationship between the compressive strength and the modulus of elasticity. This relationship is shown in Equation 7.9-C for metric units and in Equation 7.9-D after being converted into English units (psi).

$$E = 9.5(f'_c + 8)^{0.33} \quad (7.9-C)$$

$$E = 266600(f'_c + 1160)^{0.33} \quad (7.9-D)$$

A final relationship between the compressive strength and the modulus of elasticity was developed by Kakizaki et al. (1992). This research focused on high strength concretes (12 to 20 ksi). After an algebraic manipulation into English units (psi), the equation can be expressed as shown in Equation 7.9-E.

$$E = 43960\sqrt{f'_c} \quad (7.9-E)$$

A comparison of these published relationships to the data obtained in this study indicates that some relationships are more applicable than others. Figure 7.9-A plots the four relationships and the data presented in Table 7.9-A. It is clear that the ACI 318 equations significantly overestimate the modulus of elasticity in this strength range; however, it must be stated that this strength range is well outside the typical applicability of these equations. The Comité Européen du Béton equation is closer but also overestimates the

results. The Kakizaki equation slightly underestimates the results with a reasonable level of accuracy.

All of these equations have a similar form, and three of the four differ only by the scalar factor. The UHPC modulus of elasticity results were reevaluated to determine what value of the scalar factor would provide the best fit to the observed results. The result of this analysis is Equation 7.9-F. This relationship is also shown in Figure 7.9-A and is recommended as a strength to modulus of elasticity relationship for UHPC regardless of the curing condition applied.

$$E = 46200\sqrt{f'_c} \quad (7.9-F)$$

The test results presented in Section 3.3 also provide information regarding the modulus of elasticity increase as the UHPC sets and gains strength. Inclusion of these data points, collected from the Air treated cylinders between 1 and 21 days removed from casting, into the compressive strength versus modulus of elasticity relationship provides a fuller view of the overall behavior of UHPC. Figure 7.9-B shows the data that are included in Table 7.9-A and the additional modulus of elasticity results. Figure 7.9-B also includes Equation 7.9-F. The figure clearly shows that this equation is applicable to UHPC over a wide range of strengths, not just to the final strength values between 18 and 28 ksi. Therefore, Equation 7.9-F is considered applicable over the compressive strength range of 4 to 28 ksi.

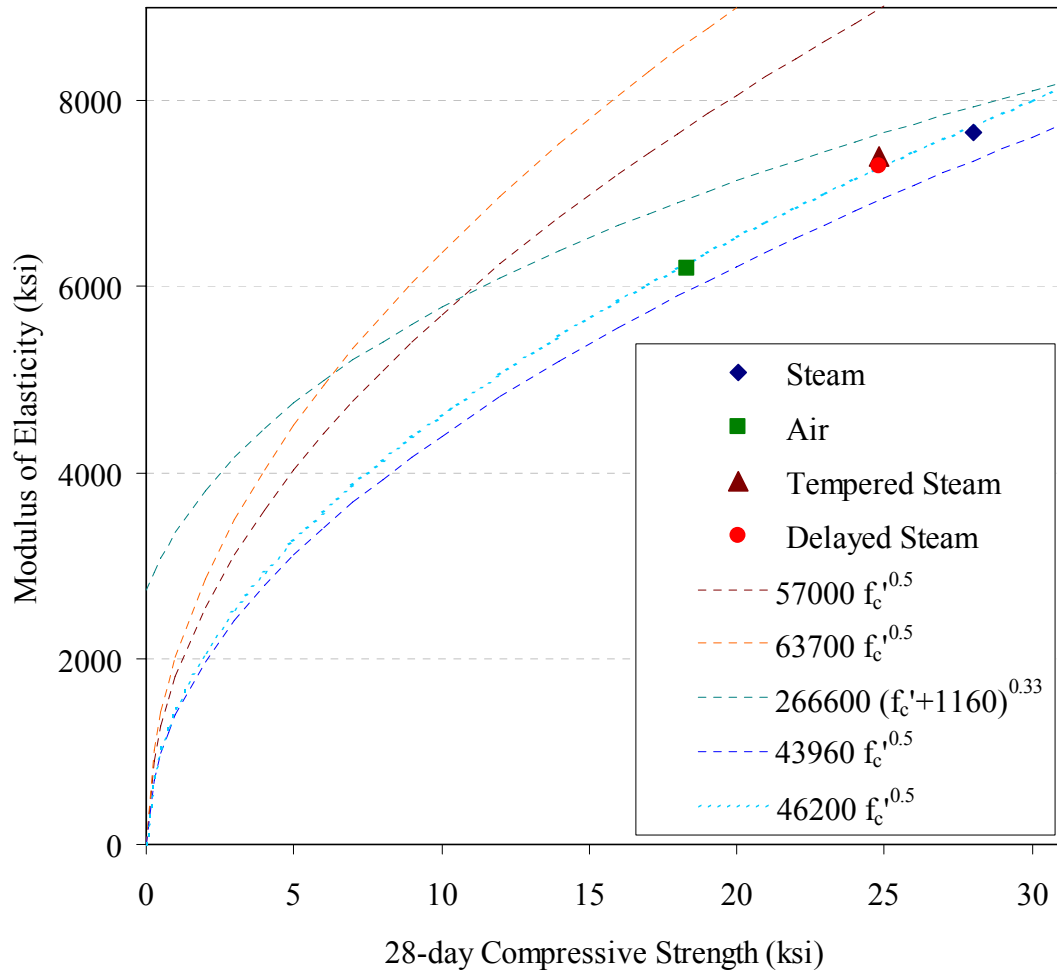


Figure 7.9-A: Modulus of elasticity as a function of 28-day compressive strength

Equation 7.9-F does not accurately estimate the modulus of elasticity for UHPC with a compressive strength in the 1 to 3 ksi range. The equation can overestimate the modulus of elasticity by as much as 50%. To rectify this lapse in the applicability of the equation, a more sophisticated equation was used to approximate the Air treated data shown in Figure 7.9-B. A best-fit regression analysis was applied to these data to determine a function that accurately represented the behavior. The simplest function to meet the

requirements was the Log Normal function as shown in Equation 7.9-G. In this equation, f'_c is the compressive strength of the concrete at a particular age and E is the corresponding modulus of elasticity, both in psi. This equation can be used to approximate the modulus of elasticity for compressive strengths as high as 19 ksi.

$$E = 7100000 \exp \left[-\frac{1}{2} \left(\frac{\ln \left(\frac{f'_c}{44000} \right)}{1.7} \right)^2 \right] \quad (7.9-G)$$

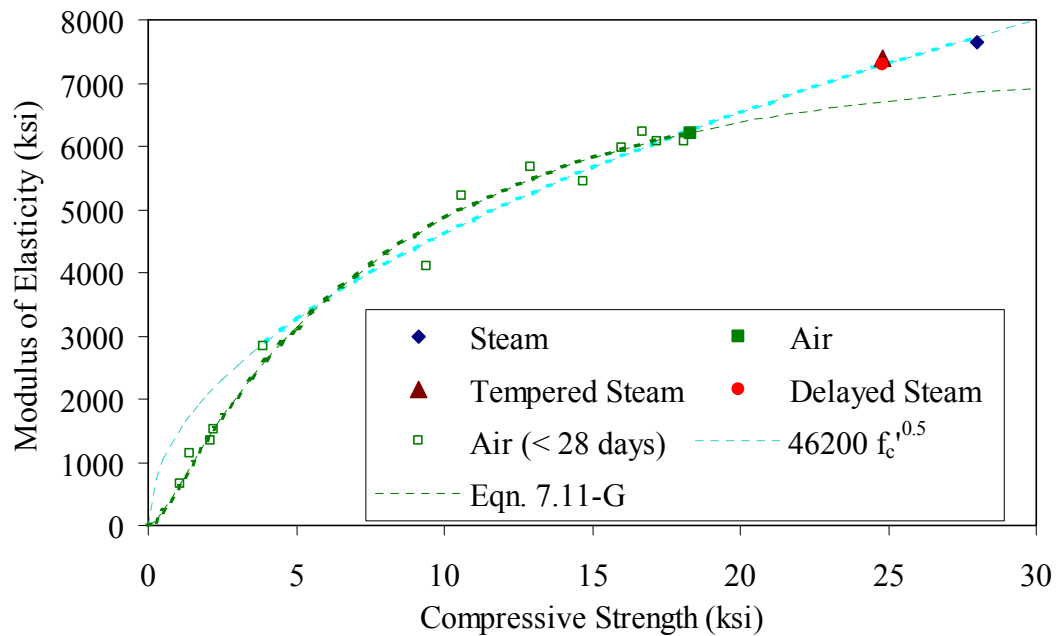


Figure 7.9-B: Modulus of elasticity as a function of compressive strength

7.10 Compressive Stress-Strain Behavior of UHPC

The compressive stress-strain behavior of UHPC has been discussed extensively in this report, including the material property characterization results presented in Section 3.3

and a further analysis of those results presented in Section 7.9. The current section presents an analysis wherein an equation is determined that represents the ascending branch of the compressive stress-strain response for each of the four curing regimes. This analysis is based on the experimental results presented in Section 3.3.3.

The compressive stress-strain responses of different concretes vary because concrete is a heterogeneous material without standardized mix designs. Many researchers have presented analytical approximations for the ascending branch of the compressive stress-strain behavior, all of which have been based on specific sets of experimental data. However, this body of research has resulted in minimal consensus on the equation's formulation or results (Popovics 1998).

From an experimental standpoint, gathering consistent, accurate data from the full range of compressive behavior response is very difficult. This fact is primarily due to the increasingly nonlinear behaviors that concrete tends to exhibit as the strain at the compressive strength is reached and surpassed. Even if the descending branch of the behavior is ignored as the compressive strength is approached, the observed straining behavior of the concrete becomes very dependent on the experimental loading and strain measurement techniques that have been used.

The preceding discussion leads to the conclusion that any strength values and strain values from earlier in the concrete response are likely more accurate than strain values from later in the concrete response. The concrete compressive strength, f_c' , and the

concrete modulus of elasticity, E , can both be considered to be relatively accurate based on experimental results. However, the concrete strain at the compressive strength and the associated secant modulus are both based on strain measurements that are more difficult to accurately capture and are thus less accurately known. This fact points to a weakness of many other models of concrete compressive stress-strain behavior, because they are based on an accurate knowledge of the compressive strain at the peak strength.

Recall from Section 3.3 that a number of specific parameters were quantified within the compressive stress-strain responses of the UHPC. Intermediate stress and strain level benchmarks were identified in addition to the standard strength and stiffness measures. These benchmarks were defined by the decrease in observed stress compared with a theoretical linear elastic response at a particular strain. Average results for the one, three, and 5% decrease levels were presented in Table 3.3.3-A. For this analysis, additional benchmarks were defined at the 10% decrease level and at the cessation of the continuous, steady increase in stress-strain response. Figure 7.10-A illustrates the stress decrease factor compared with the linear elastic behavior, α , on a sample Air treated UHPC compressive stress-strain curve. Sample actual stress, f_c , and strain, ϵ_c , values are shown along with the stress and strain differences from the linear elastic response.

These benchmarks were used to define the behavior of each compressive specimen. The results were then normalized based on the compressive strength and modulus of each specimen. Note that although the compressive stress normalization is based on the experimentally obtained compressive strength, the strain normalization is based on the

theoretical linear elastic strain at the compressive strength. This normalization technique minimizes the inaccuracies discussed above by avoiding the use of the actual strain at the compressive strength. Finally, the results from each curing regime were compiled into individual data sets.

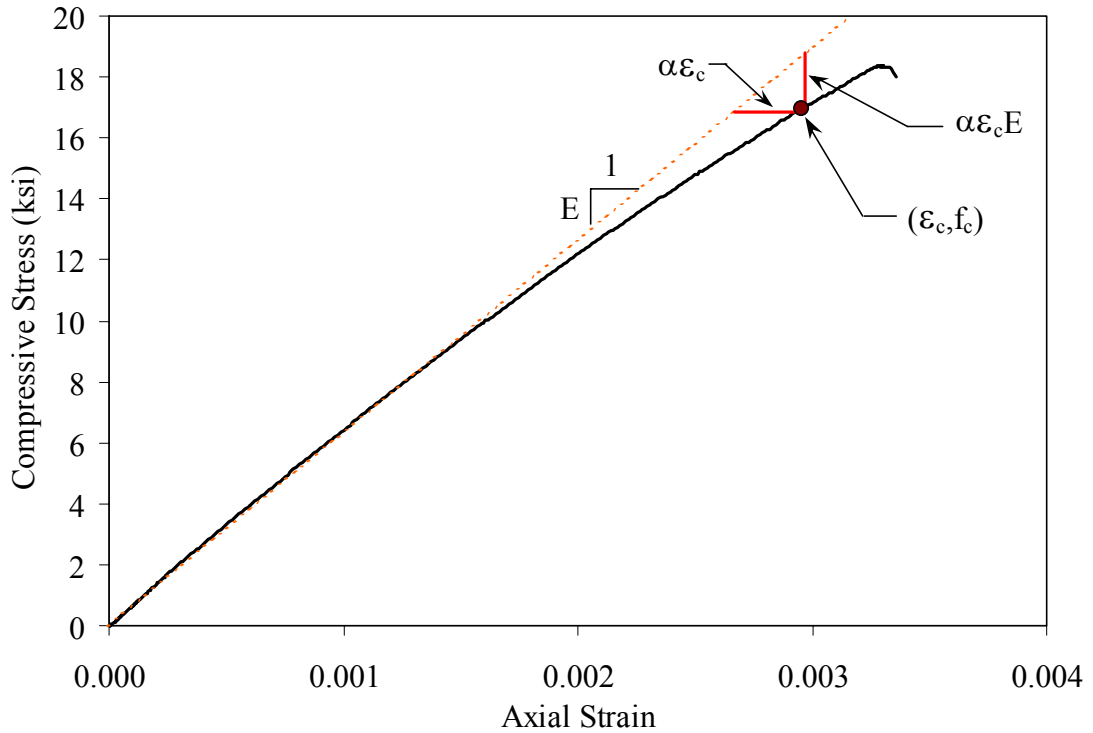


Figure 7.10-A: Compressive stress-strain behavior compared with linear elastic response

Figure 7.10-B presents the normalized stress-strain response benchmark data points for the Steam treated UHPC cylinders discussed in Section 3.3. This figure shows the general shape that the approximation must match to accurately represent the UHPC behavior. However, it does not allow for easy differentiation between potential curves that fit the data. A more accurate representation of the overall behavior can be obtained by focusing on the deviation of the actual behavior of the concrete compared with the theoretical

linear elastic response. Figure 7.10-C presents the same benchmarks in terms of the decrease from the linear elastic response compared with the normalized strain. This presentation highlights the behaviors that must be captured in the model.

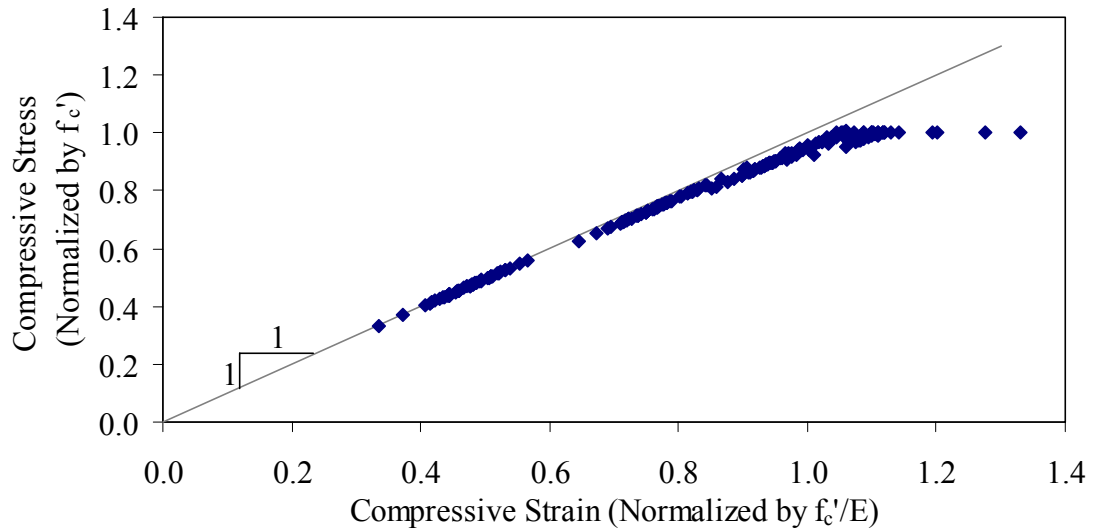


Figure 7.10-B: Normalized compressive stress-strain results for Steam treated UHPC

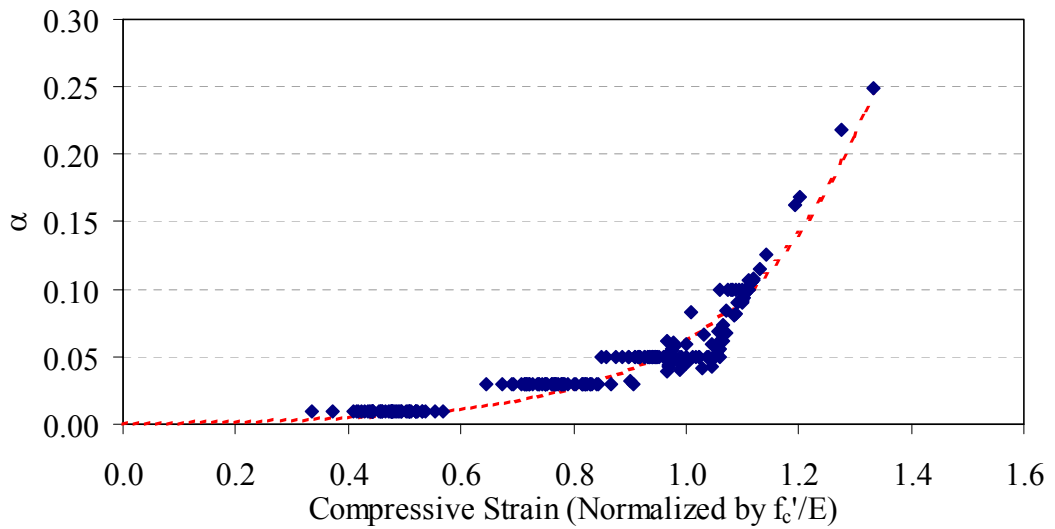


Figure 7.10-C: Deviation from linear elastic compressive behavior for Steam treated UHPC

Figures similar to 7.10-C were created for the other three curing regimes as well. In all cases, the figures indicate that the UHPC remains close to the theoretical linear elastic response through much of its behavior. Approximation curves were fit to each of these data sets. The simplest equation that fits the data moderately well was an exponential function with two constants as shown in Equation 7.10-A. These constants, a and b , help fit the equation to the data, and their values for each curing regime are provided in Table 7.10-A. The approximation curve for the Steam treated UHPC is shown in Figure 7.10-C.

$$\alpha = ae^{\frac{\epsilon_c E}{bf_c}} - a \quad (7.10-A)$$

Table 7.10-A: Constants for Equation 7.10-A

Curing Regime	a	b
Steam	0.0010	0.243
Air	0.0114	0.440
Tempered Steam	0.0041	0.341
Delayed Steam	0.0044	0.358

The analysis discussed above leads to a simple means of defining the ascending branch of the compressive stress-strain response of UHPC. Equation 7.10-B presents the standard linear elastic relationship between stress and strain with the inclusion of a modifying factor. This factor, specifically $(1-\alpha)$, determines the extent to which the actual curve deviates from the linear elastic response. Recall that α is defined by Equation 7.10-A. Dividing Equation 7.10-B by the compressive strength normalizes the equation and allows for the direct inclusion of Equation 7.10-A and therefore a single equation

defining the normalized compressive stress in terms of the normalized compressive strain. Recall that this equation was derived to be applicable only for the ascending branch of the curve.

$$f_c = \varepsilon_c E(1 - \alpha) \quad (7.10-B)$$

These relationships were used to create general stress-strain responses for the four curing regimes. These responses were based on the compressive strength and modulus of elasticity results presented in Chapter 3. The curves are shown in Figure 7.10-D.

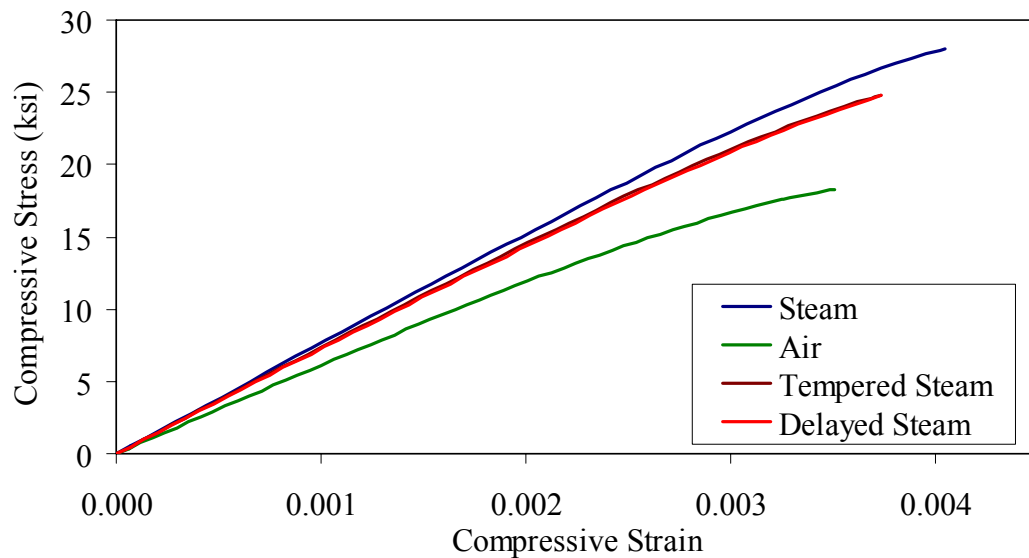


Figure 7.10-D: Compressive stress-strain response approximations

7.11 Development Length of Prestressing Strand in UHPC

Results from two of the UHPC girder shear tests provide an indication of the development length of 270 ksi low relaxation prestressing strand in this type of concrete.

In both tests, sufficient stresses were placed onto prestressing strands with 4 feet or less of embedment length to cause the strands to rupture.

Section 6.2.1 presents the results from the testing of Girder 28S. Recall that this three-point loading test setup included a 28 ft total span, a 6.5 ft shear span, and a 4 ft overhang beyond the shear span. This overhanging portion of the girder allowed for the partial to full development of the prestressing strands outside of the region of the girder that traditionally encounters high stresses from flexure or shear. Figure 6.2.1-K shows the distress that was apparent in this girder at failure. As mentioned in Chapter 6, the failure of this girder included the simultaneous rupturing of the two strands in the top flange of the girder directly over the bearing. Because no slip was observed in the instrumented top strand prior to rupture, it is clear that the full development length of these strands was less than the 48 in. of embedment between the rupture location and the end of the girder.

The failure of Girder 14S provides further information regarding the development length of this prestressing strand in UHPC. Recall that this three-point loading test setup included a 14 ft total span, a 6 ft shear span, and no overhang (i.e., the bearing was centered 6 in. from the end of the girder). As with all of the girders, half of the strands in the bottom flange were debonded for 3 feet from the end of the girder. The sequential rupture of the 12 fully bonded strands in the bottom flange defined the failure of this girder. Figure 6.2.3-J illustrates the distress apparent in the girder at failure, with the strand ruptures occurring at the second large bottom flange crack from the right end of

the girder. Note that this crack was 37 in. from the right end of the girder, at the precise location where the full complement of strands became bonded.

Figure 6.2.3-D shows the strand slip behavior for five of the fully bonded strands in the bottom flange and for five of the debonded strands in the bottom flange, along with one of the top flange strands. The debonded strands all behaved very similarly, showing initial slip at an applied girder load of 500 kips, 0.1 in. of slip at the peak girder load of 766 kips, and between 0.35 and 0.5 in. of slip when the fully bonded strands began to rupture. Of the five fully bonded strands that were monitored, the two in the bottom row of strands showed no slippage prior to rupture. The three in the second and third rows from the bottom of the girder showed less than 0.06 in. of slippage, with the slippage beginning at the girder's peak load capacity and ceasing when these strands ruptured. The results from these five instrumented strands indicate that the development length of UHPC under realistic shear loading conditions is less than 37 in.

The girder test results discussed above indicate that the development length of 0.5 in. 270 ksi low-relaxation prestressing strand in UHPC under realistic full-scale loading conditions is less than 37 in. In total, one monitored strand ruptured prior to slipping while being subjected to a flexural tensile loading with 48 in. of embedment, two monitored strands ruptured prior to slipping while spanning 37 in. through a heavily distressed shear region, and three strands ruptured after a slight slippage while spanning 37 in. through a heavily distressed shear region. This result is consistent with the findings of Steinberg and Lubbers (2003) as discussed in Section 2.4.2.

7.12 Estimation of Prestress Losses in UHPC Girders

The loss of prestressing force due to instantaneous and long-term effects is an inherent part of pretensioning concrete. In prestressed concrete, the primary instantaneous effect is elastic shortening of the concrete member. The long-term effects are comprised of concrete shrinkage, concrete creep, and relaxation of the prestressing strand.

This section focuses on determining the prestress losses that occurred in the AASHTO Type II girders. The experimental results for these girders were presented in Chapter 6. The AASHTO LRFD Bridge Design Specification defines the total loss of prestress as being comprised of the four effects mentioned above. The specification provides empirical relationships that can be used to estimate these losses. However, these estimations are based on conventional concrete technology, thus more accurate estimations of UHPC girder behavior can be achieved through the use of the experimental results presented in this report.

The AASHTO Type II girders discussed in Chapters 5 and 6 were each prestressed with 24 strands in the bottom bulb and 2 strands in the top bulb. The fabricator stressed these 270-ksi low-relaxation strands to 55% of their ultimate strength or 149 ksi. The strand stressing was completed within 1 day prior to the casting of the UHPC. After casting, approximately 3 days passed before each girder was stressed. The girders were then steam treated.

The time-dependent prestress loss due to shrinkage of the UHPC can be approximated based on the experimental results presented in Section 3.7. The early age unrestrained shrinkage of UHPC was determined to be approximately 500 microstrain at 3 days after casting. The final stabilized asymptotic shrinkage value after steam treatment was determined to be approximately 850 microstrain. Thus, 350 microstrain of shrinkage can be expected to occur after the stressing of the girder. The strands can be assumed to have a stiffness of 28500 ksi; therefore, this shrinkage will reduce the stress in the strand by 10.0 ksi.

The time-dependent prestress loss due to creep of the UHPC can be approximated based on the experimental results presented in Section 3.8. An elastic analysis of the UHPC girders at transfer indicates that the stress in the concrete at the centroid of the prestress is approximately 3.0 ksi. The strength of the concrete at transfer would have been at least 10 ksi and would have continued to increase both before and during steaming until the final compressive strength of 28 ksi was achieved. Based on this information, the level of stress on the concrete was clearly at or below 30% of the compressive strength.

The creep coefficient for UHPC can vary depending on the age of the concrete and the curing treatment that has been applied. The results presented in Chapter 3 indicate that a creep coefficient of 0.3 can be expected after the Steam treatment, but that the creep coefficient could be as high as 0.78 if Air treated UHPC is subjected to a compressive stress equal to 67% of its compressive strength. Based on these results, a reasonably

conservative aggregate value for the long-term creep coefficient of UHPC stressed as described above is estimated to be 0.5.

Additionally, this analysis requires an estimation of the modulus of elasticity of the UHPC throughout the time frame during which creep is occurring. Experimental results have indicated that the modulus of elasticity can range from 6200 ksi to 7650 ksi for the 28-day Air treated to Steam treated UHPC, respectively. Also, early age modulus of elasticity testing has indicated that the modulus of elasticity for 10 ksi UHPC will be approximately 5000 ksi. Conservatively, the modulus of elasticity for this analysis is assumed to be 6000 ksi because a smaller modulus will result in larger overall creep losses.

The goal of this creep analysis is to determine the stress loss in the strands resulting from the creep strain imparted into the concrete. The creep strain in the concrete is calculated by multiplying the creep coefficient by the initial concrete strain at prestress transfer. This concrete strain can be approximated to equal the 3.0 ksi initial prestress divided by the modulus of elasticity of 6000 ksi. Thus, the creep strain in the concrete is 240 microstrain, and the resulting loss of prestress in the strands is 6.9 ksi.

The elastic shortening loss in the UHPC girder was calculated based on a strain compatibility analysis of the girder cross-section. All prestressing strands were considered separately, thus strands at different distances from the neutral axis exhibited different levels of stress. The modulus of elasticity of the UHPC was assumed to equal

5000 ksi at transfer. The elastic shortening of the UHPC girder at the center of gravity of the prestressing strands is 540 microstrain. Multiplying this value by the modulus of elasticity of the strands results in an average elastic shortening loss in the strands of 15.4 ksi.

Finally, the time-dependent losses due to strand relaxation after transfer were calculated based on the relationship provided in the AASHTO LRFD Bridge Design Specification. The calculation estimates the relaxation loss by relating it to the other three losses detailed above. Specifically, this loss equals 6 ksi minus 12% of the elastic shortening loss minus 6% of the creep and shrinkage losses. In total, the strand relaxation loss for the UHPC girder described above is 3.1 ksi.

The total prestress losses for this prestressed girder equal 35.6 ksi. This value includes the time-dependent 10.0 ksi shrinkage loss, the 6.9 ksi creep loss, and the 3.1 ksi strand relaxation loss. It also includes the 15.4 ksi elastic shortening loss that occurs at the stressing of the girder. Because the girders were only stressed to 55% of the ultimate strand strength, the time-dependent losses total 14% of the strand jacking stress, and the instantaneous elastic losses total 10% of the strand jacking stress.

These losses are of similar magnitude to the losses that normally occur in prestressed concrete girders, which seems to indicate that UHPC provides minimal benefit in terms of prestress loss behaviors. However, it must be noted that the low level of initial jacking stress results in a significantly larger percentage of stress loss than would occur with a

higher initial jacking stress. Also, the stressing of the girder when the UHPC compressive strength is 10 ksi results in much higher losses than would occur if the UHPC had reached 15 ksi or more without the Steam treatment or had reached 28 ksi with the Steam treatment. These higher compressive strengths would result in decreased shrinkage strains, decreased creep strains, and a higher modulus of elasticity that would reduce elastic shortening.

7.13 Flexural Behavior of Prestressed UHPC Girders

The static loading of Girder 80F provided significant information regarding the full-scale flexural behavior of UHPC girders. The results of this test are presented in Section 6.1. The following sections provide an in-depth analysis of these test results with a focus on modeling the global girder behaviors.

7.13.1 Analytical Predictions of Global Behavior

Simple, accepted analytical methods exist for the prediction of the flexural behavior of prestressed concrete girders. These methods are based both on structural mechanics and on empirical relationships. In general, these empirical relationships approximate the non-linear stress-strain behaviors of normal reinforced concrete. Although these analytical methods cannot accurately model the entire mechanical behavior of UHPC, the flexural capacity and centerline load-deflection behaviors were analyzed using these techniques for comparative purposes.

Recall from previous discussions that Girder 80F is an AASHTO Type II girder spanning 78.5 feet and composed of 28 ksi UHPC. The girder is prestressed with 24 270-ksi low-relaxation strands in the bottom flange and 2 strands in the top flange. It contains no mild steel reinforcement. The strands were all initially stressed to 55% of their ultimate strength. As discussed in Section 7.12, the time-dependent stress losses in the strands total 14%.

The initial, elastic behavior of the girder was analyzed through a strain compatibility analysis. In this analysis the prestress forces are applied to the girder cross-section at discrete locations, thus allowing strands at different depths from the neutral axis to apply different force levels onto the girder. The stiffness of the concrete at girder stressing, $E_{c,stressing}$, was approximated to be 5000 ksi for this portion of the analysis, which determines the elastic shortening losses in the strands. The girder's self-weight flexural stresses were also calculated using this concrete stiffness. The time-dependent losses were then applied to the girder through the use of a second concrete stiffness, $E_{c,losses}$. This value was assumed to be 6000 ksi for Girder 80F.

The preceding analyses determine the state of stress in the girder at the initiation of live load application. Based on these results, the flexural capacity of the girder can be approximated. For normal concrete, this analysis requires only an empirical approximation of the compressive stress-strain behavior. The modeling presented here is based on the assumptions that the Whitney stress block is applicable to UHPC and that

UHPC carries no tensile forces after cracking. This second assumption is significantly in error, as will be discussed in Section 7.13.5.

The peak load applied to Girder 80F was 178 kips, corresponding to an applied moment of 38700 k-in. with the neutral axis located 10 in. down from the top of the girder. A flexural analysis of the girder that was based on the analytical techniques discussed above indicates that the moment capacity should be 27840 k-in. with the neutral axis located 5 in. down from the top of the girder at failure. An additional flexural analysis was completed to compare the capacity of this girder to an HPC girder of identical configuration with a compressive strength of 8 ksi. The modulus of elasticity of this girder was assumed to be 5150 ksi based on AASHTO LRFD equation 5.4.2.4-1. The analysis indicates that the flexural capacity of this girder is 20400 k-in. with the neutral axis located 16.5 in. down from the top of the girder at failure.

Modeling the load-deflection behavior requires further approximations of elastic behavior limits and inelastic behaviors. Specifically, approximations of the tensile cracking stress and the effective flexural stiffness of the cross-section are required. AASHTO LRFD equation 5.7.3.6.2-1 was used to model the post-cracking flexural stiffness of the girder. The tensile cracking strength, f_{ct} , of the UHPC was approximated by the equation for normal weight concrete presented in AASHTO LRFD Section 5.4.2.6.

Figure 7.13.1-A presents the load-deflection response for Girder 80F and for three other cases analyzed through the methods discussed above. One of the alternate cases

corresponds to the flexural capacity of the 8 ksi HPC girder, and the other two alternate cases both correspond to the 28 ksi UHPC flexural capacity analysis. The tensile cracking strength of the 8 ksi concrete is assumed to be 0.67 ksi. The tensile cracking strength of the 28 ksi concrete is assumed to be 1.25 ksi in one case and 2.9 ksi in the other. These tensile strengths represent the AASHTO LRFD approximation and the observed tensile cracking strength, respectively.

A comparison of the observed girder flexural behavior with the three other curves shown in Figure 7.13.1-A indicates three primary findings. First, it is clear that Girder 80F carried a significant additional load and displayed significant additional ductility as compared with the predicted behavior of an 8 ksi HPC girder. Second, the significantly decreased flexural capacity and residual stiffness of the two theoretical 28 ksi girders indicate that the elimination of the fiber reinforcement's contribution to the strength and stiffness approximations results in a very conservative answer. Finally, the difference between the two 28 ksi girder theoretical approximations indicates that the tensile cracking strength of UHPC has a significant impact on the deflection response of a girder at a particular load level.

7.13.2 Cracking Behavior

The tensile cracking behavior of prestressed UHPC girders has been observed to be significantly different than would be expected in normal concrete girders. As discussed in Section 6.1 and as presented in Figure 6.1-H, the tensile flange of this prestressed girder displayed a very high crack spacing density. Also, the crack spacing throughout the span

seemed proportional to the flexural forces applied. The focus of this section is to derive a general relationship between the cracking behavior of UHPC in the tension flange of a prestressed concrete girder and the strain observed in the girder.

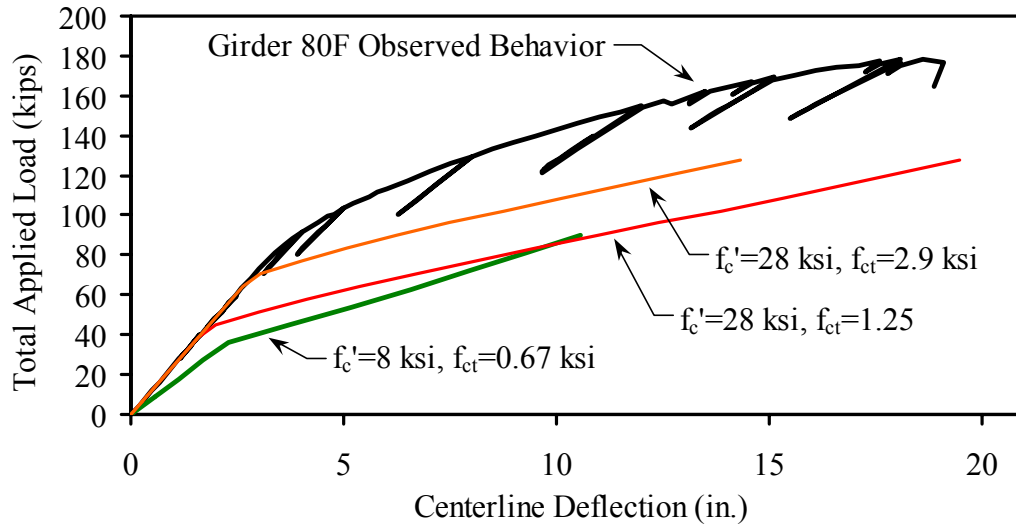


Figure 7.13.1-A: Predicted behavior of girders tested in the configuration of Girder 80F

The load and strain data collected during the testing of Girder 80F, along with the crack spacing density observations, allows for the derivation of a relationship between the apparent UHPC strain and the cracking of UHPC. The basic assumption required to initiate this derivation is that the girder is undergoing pure flexural behavior with plane sections remaining plane. Under pure flexural behavior, the neutral axis location and curvature of the midspan cross-section recorded during the testing of Girder 80F can be used to derive the effective strain in the bottom flange of the girder at any applied live load moment. This calculation was performed, and the results for each data point recorded throughout the test are presented in Figure 7.13.2-A. A curve, also shown in the

figure, was then fit through the data to define a continuous relationship between these two variables.

The preceding analysis has allowed for a general relationship between the applied moment and the bottom flange strain. The next step is to determine the actual bottom flange strain in the girder at the load step where the crack spacing observations were recorded. As previously mentioned, the crack spacing observations were recorded when the total applied load on the girder was 155 kips, thus defining the applied moment throughout the span and, with Figure 7.13.2-A, the bottom flange strain. The preexisting bottom flange strain due to prestress forces and dead load were calculated based on the known prestress forces, the assumed prestress losses, and the dead weight of the girder. Recall that the 14% prestress losses resulted in an overall prestressing force of 455 kips at an eccentricity of 9.15 in. below the elastic neutral axis. The addition of the live load strains to the preexisting strains results in the total tensile strain that existed in the bottom flange of the girder at the time of the crack density observations.

The specific crack spacing observations from Girder 80F are presented in Figure 7.13.2-B. This figure shows the crack spacing in terms of the distance from midspan. The calculations discussed above allow for the transformation of this distance value into the strain in the UHPC caused by the prestressing forces, dead load, and live load. The results of this transformation are presented in Figure 7.13.2-C. This figure, presented in semilog format, displays the observed crack spacing as related to the strain in the UHPC.

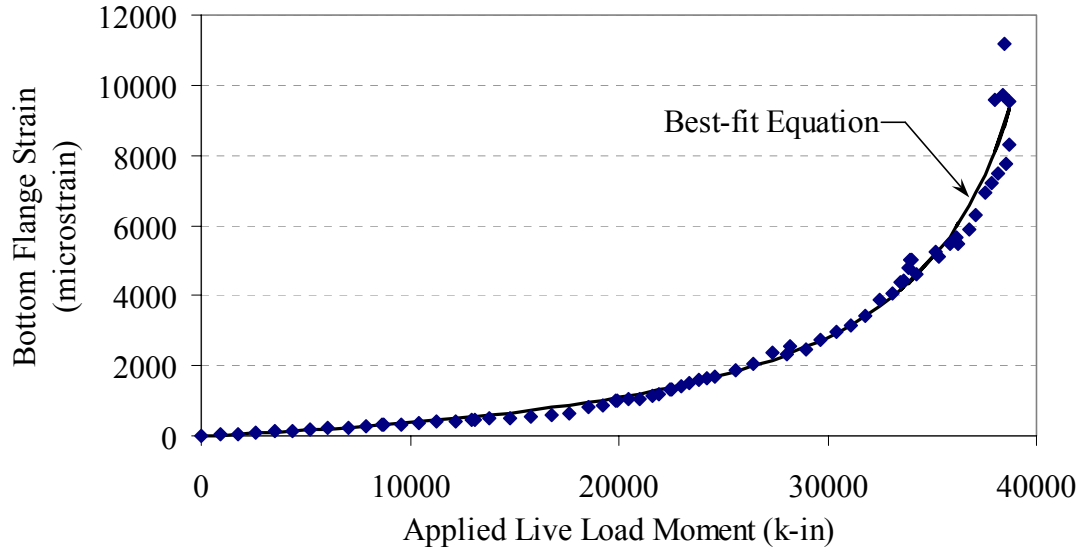


Figure 7.13.2-A: Girder 80F midspan bottom flange strain throughout testing

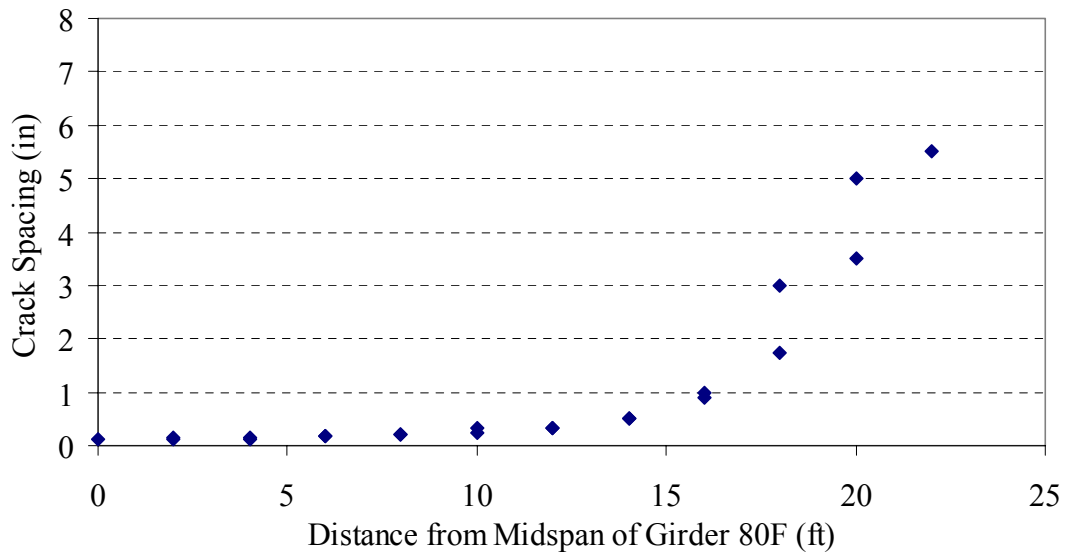


Figure 7.13.2-B: Flexural crack spacing observed on the bottom flange of Girder 80F at a total applied load of 155 kips

Figure 7.13.2-C also presents a curve representing the best-fit equation that was fit to the strain versus crack spacing results. The equation for this curve is presented in Equation 7.13.2-A. The crack spacing, w , in inches can be determined from the strain, ϵ , in

microstrain and the constants a through d that equal 0.113, 71700, $-2.25E+06$, and $1.44E+07$, respectively.

$$w = a + \frac{b}{\varepsilon^{1.5}} + \frac{c \ln \varepsilon + d}{\varepsilon^2} \quad (7.13.2-A)$$

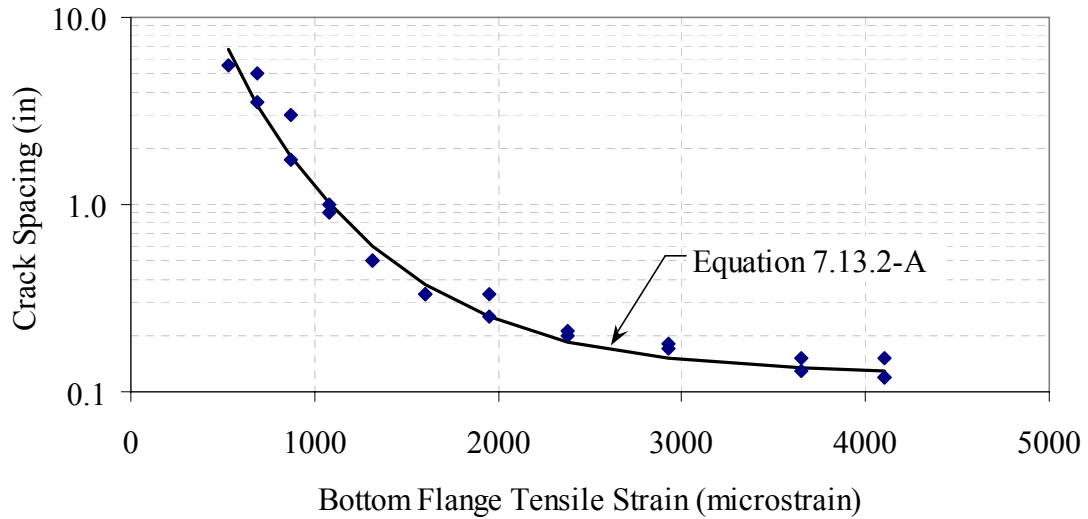


Figure 7.13.2-C: Flexural crack spacing related to tensile strain

Alternatively, the crack spacing could be viewed as the independent variable. This revision allows for the estimation of strain based on crack spacing. Figure 7.13.2-D revises the previous figure into this more convenient format. This figure also graphically presents Equation 7.13.2-B. This equation provides a more convenient format for determining the strain in microstrain based on the crack spacing in inches. Here, the variables a through c are 450, 500, and 40, respectively.

$$\varepsilon = a + \frac{b}{\sqrt{w}} + \frac{c}{w^2} \quad (7.13.2-B)$$

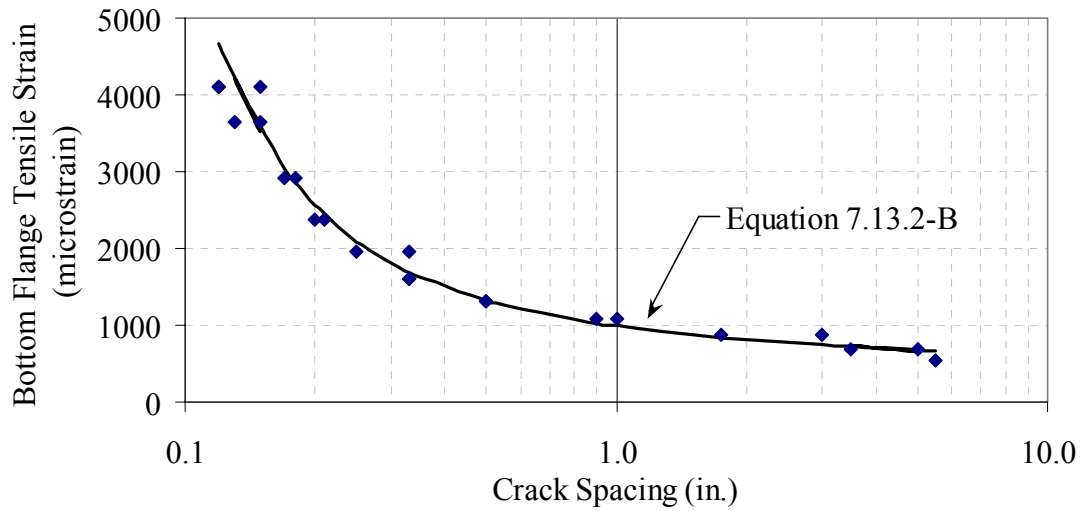


Figure 7.13.2-D: Tensile strain related to flexural crack spacing

7.13.3 Effective Moment of Inertia

Elastic flexural analysis was used to determine the stiffness of Girder 80F, including both before and after flexural cracking of the girder. The testing of Girder 80F included periodic partial unloading cycles. During these cycles, approximately 30% of the load was removed from the girder before being reapplied incrementally. The data collected during the reloading cycles allow for the analysis of the residual elastic behavior of the girder. This analysis focuses on the load-deflection behavior of the girder.

The load and deflection behaviors recorded during the initial loading of the girder and during eight unloadings were analyzed. This analysis assumed pure flexural behavior and a constant UHPC modulus of elasticity, E , of 8100 ksi. Recall that vertical deflections of the girder were recorded at six locations: midspan (bottom and top flange), both load points, and both quarter points. The slope of the load-deflection behavior at each

potentiometer was determined for each loading or reloading cycle using a best-fit linear approximation.

These slopes were then used to determine the effective moment of inertia, I_{eff} , of the girder as a whole. A revision of standard flexural deflection relationships allows for the calculation of I_{eff} through the use of the known geometry of the loading. Equation 7.13.3-A provides the relationship between the slope of the load deflection response, $m_{P/\Delta}$, and the load, P , and I_{eff} for deflections measured at the centerline of the girder. This equation includes variables for the girder span, L , the distance from the bearing to the load point, a , the dead load of the girder, ω , and the initial uncracked moment of inertia of the cross-section, $I_{uncracked}$. Note that this analysis accounts for the effects of the dead load on the residual stiffness of the girder.

$$I_{eff} = \frac{8Pa(3L^2 - 4a^2) + 5\omega L^4}{384E \left(\frac{P}{m_{P/\Delta}} \right) + \frac{5\omega L^4}{I_{uncracked}}} \quad (7.13.3-A)$$

Equation 7.13.3-B is very similar to the previous equation, except that it is a generalized relationship that is applicable for deflections recorded at any point on the girder between a bearing and its closest load point. In this equation, x is the distance from the bearing to the location of the deflection measurement.

$$I_{eff} = \frac{2Px(3La - 3a^2 - x^2) + \omega x(L^3 - 2Lx^2 + x^3)}{24E\left(\frac{P}{m_{P/\Delta}}\right) + \frac{\omega x(L^3 - 2Lx^2 + x^3)}{I_{uncracked}}} \quad \text{for } x \leq a \quad (7.13.3-B)$$

The analysis described above allows for the determination of I_{eff} values for the girder at various load levels and at various locations across the span. The results, presented in Figure 7.13.3-A, from the six deflection measuring locations were averaged for each load level. The I_{eff} values are displayed on the midspan load-deflection response of the girder, with I_{eff} being indicated at the location on the curve for which each analysis was conducted. Note that the value calculated based on the initial loading of the girder is shown in the lower right corner of the figure.

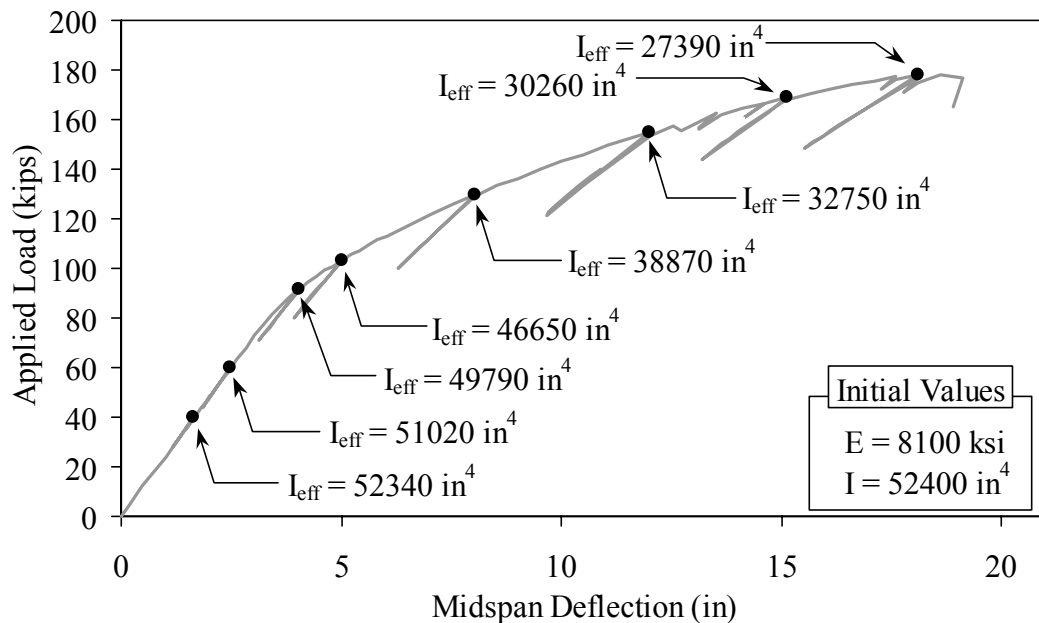


Figure 7.13.3-A: Effective moment of inertia of Girder 80F

7.13.4 Flexural Stiffness Under Flexural Loading

Observations gathered during the testing of Girder 80F and calculations completed after the test indicate that the overall flexural behavior of this girder is more likely to be accurately modeled by standard structural mechanics than would normally be expected for concrete girders. The cracking behavior of UHPC wherein the material continues to possess tensile strength and stiffness after cracking is the driving factor behind this conclusion. Based on the fact that the deflection and rotation of the girder are known at all load levels up to failure, it is reasonable to perform a section-based analysis of the girder wherein the flexural stiffness of the girder at each cross-section will be determined based on the overall girder behavior.

A flexural analysis of Girder 80F was performed to determine the flexural stiffness of any cross-section along the length of the girder as a function of the live and dead load moment, M , applied to the girder at that location. The virtual work analysis technique was used. Equation 7.13.4-A provides the basic analytical relationship wherein the moment on the girder, M , is multiplied by the moment, m , generated in the equilibrium system by a “dummy” load at the location where the deflection, Δ , is desired. The flexural stiffness of the girder, EI , which also varies along the length of the girder, is included as well. The integration, or in this case the summation, of nearly 1000 discrete cross-sectional slices along the length of the girder provides the solution. Note that shear deformations were excluded from the analysis because they were assumed to be minimal given the loading and girder configurations.

$$\Delta = \int_0^L m(x) \frac{M(x)}{EI(x)} dx \quad (7.13.4-A)$$

In this analysis, the UHPC modulus of elasticity was held constant and the moment of inertia was allowed to vary to achieve the correct overall flexural stiffness, K . The initial value for the modulus of elasticity was determined through the method described above with the uncracked moment of inertia of the girder, I_{uncr} , equal to 52400 in.⁴ Recall that this value is the moment of the inertia as calculated for the transformed section at the time the girder was tested. The initial elastic behavior of the girder as recorded through the deflection and rotation gages indicates that the overall modulus of elasticity of the girder is 8100 ksi. Additionally, recall that the experimentally observed dead plus live load cracking moment of the girder is 17800 k-in., and the corresponding moment capacity was 42300 k-in.

The analysis described above was completed on a trial-and-error basis. First, a potential relationship was proposed between the flexural stiffness and the total moment. The analysis was performed to determine the resulting deflections and rotations at each of the potentiometers and tilt meters. This analysis was repeated for each observational step (or load level) throughout the experimental testing of the girder. The analytical results were then compared with the experimental observations, and the K versus M relationship was revised accordingly. The analyses were then repeated until a sufficiently accurate flexural stiffness was determined.

Equation 7.13.4-B provides the flexural stiffness relationship that was computed for this girder cross-section. This cumulative exponentially modified Gaussian equation relates K to M through six variables that define the shape of the curve. Figure 7.13.4-A graphically presents the relationship. Note how the stiffness of the cross-section does not begin to decrease until the moment has increased well above the cracking moment. This behavior is due to the cracking spacing behavior and post-cracking load carrying ability of UHPC as discussed earlier in this chapter.

(7.13.4-B)

$$K = E \left[I_{uncr} + \frac{b}{2} \left[1 + \operatorname{erf} \left(\frac{M - c}{d\sqrt{2}} \right) - \left(\frac{e}{|e|} + \operatorname{erf} \left(\frac{M - c}{d\sqrt{2}} - \frac{d}{e\sqrt{2}} \right) \right) \exp \left(\frac{d^2}{2e^2} + \frac{c - M}{e} \right) \right] \right]$$

with: K = flexural stiffness of girder cross-section, k-in.²

M = live plus dead load moment on girder cross-section, k-in.

E = 8100 ksi

I_{uncr} = 52400 in.⁴

b = -60300

c = 20730

d = 583

e = 22900

Figure 7.13.4-B presents the results of a comparison between the analytical deflection or rotation calculated using Equation 7.13.4-B and the experimentally observed behavior.

The results of this comparison are displayed for the six monitored deflections and the two rotations for each of the 122 observational steps that comprise the girder test. The mean value of the predicted-to-observed ratio is also presented. This figure shows that the predicted deflections and rotations are within 5% of the experimental values throughout nearly the entire test.

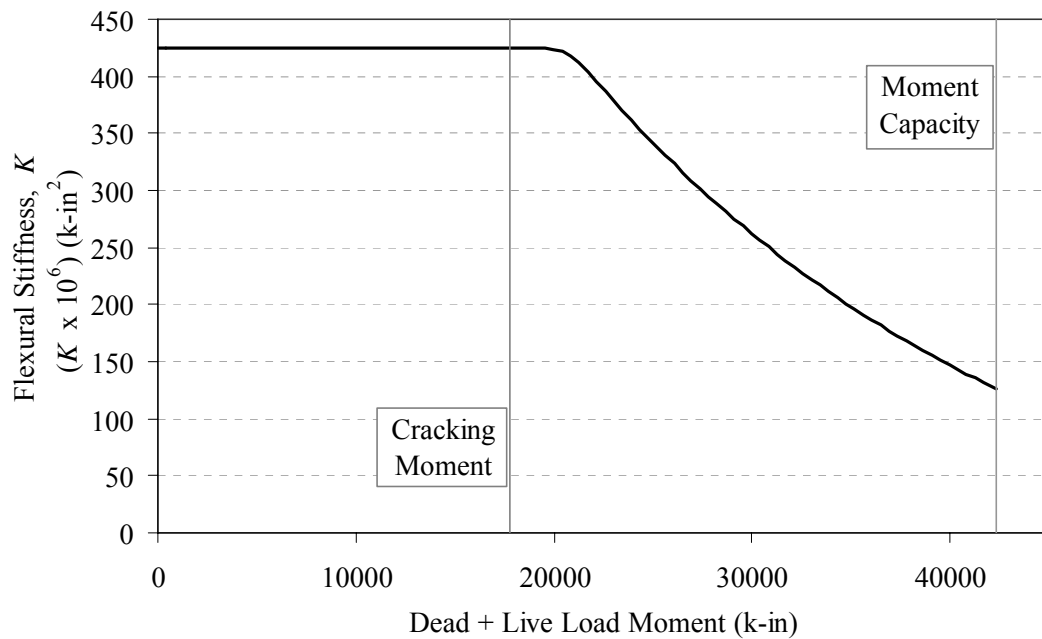


Figure 7.13.4-A: Flexural stiffness of an AASHTO Type II girder

Figures 7.13.4-C through 7.13.4-F provide graphical representations of the accuracy of the flexural stiffness model. Figure 7.13.4-C presents the experimentally observed midspan deflection results and the analytical values. Figure 7.13.4-D focuses on the deflection results at the load points, and Figure 7.13.4-E focuses on the deflection at the quarter points. Finally, Figure 7.13.4-F presents the experimental and analytical results for the rotation at the ends of the girder. In all cases, note the accuracy with which the analytical model corresponds to the experimentally observed behaviors.

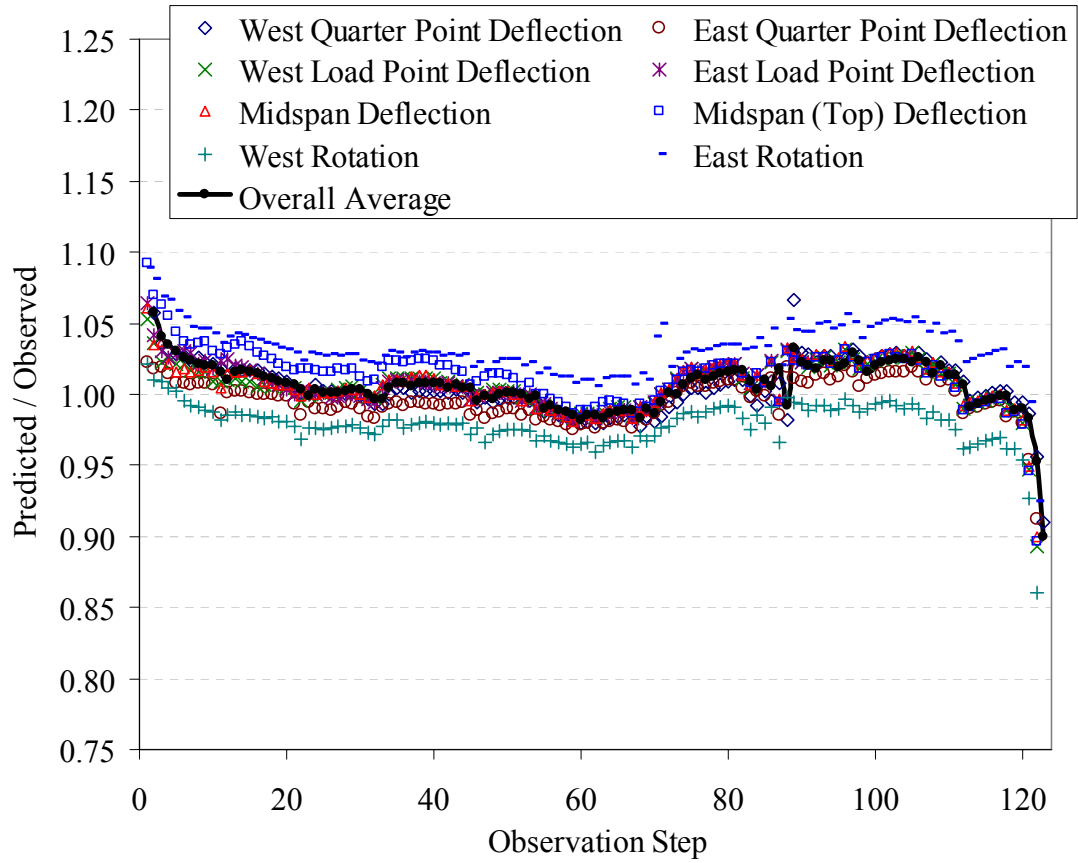


Figure 7.13.4-B: Ratio of predicted deflections and rotations to experimental results

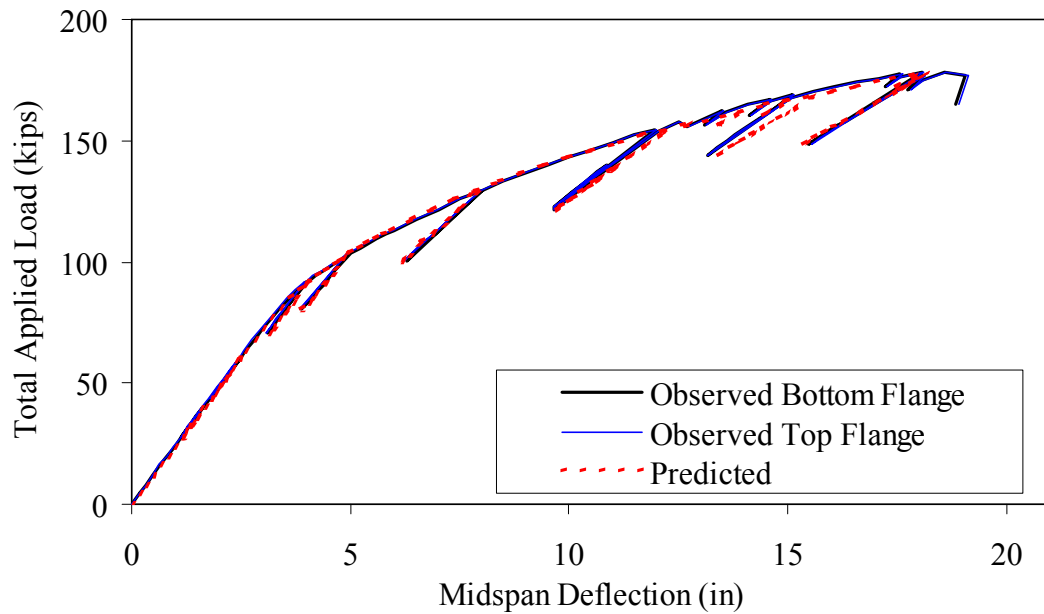


Figure 7.13.4-C: Predicted and observed midspan deflection results

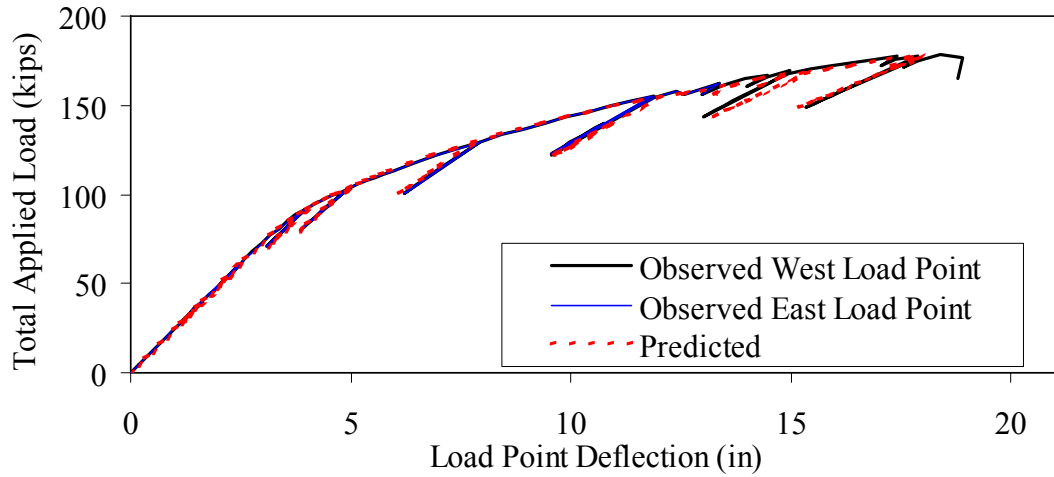


Figure 7.13.4-D: Predicted and observed load point deflection results

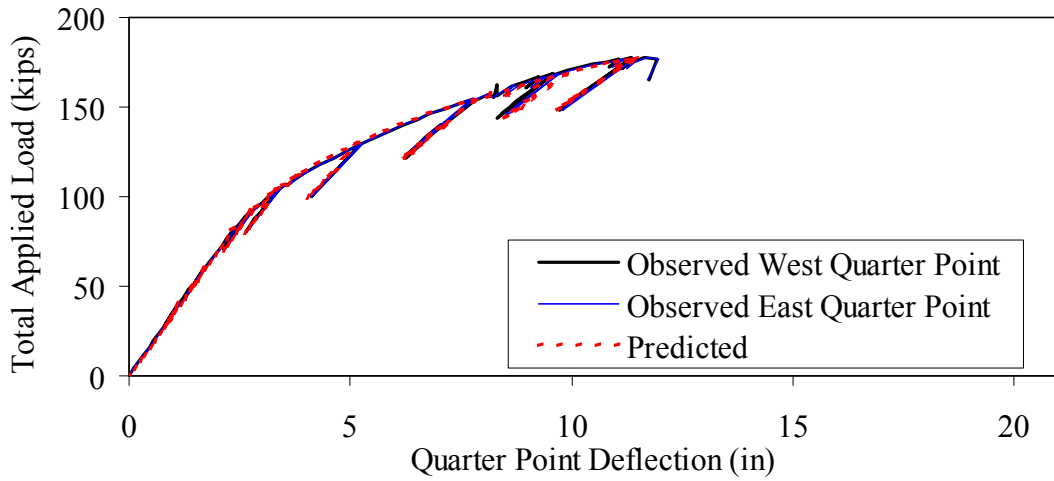


Figure 7.13.4-E: Predicted and observed quarter point deflection results

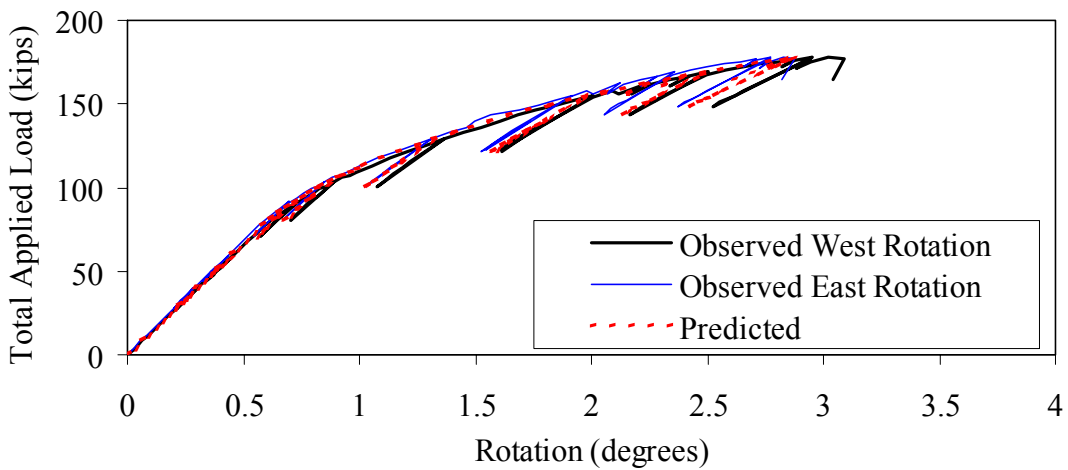


Figure 7.13.4-F: Predicted and observed end rotation results

7.13.5 Uniaxial Stress-Strain Model of Girder Flexural Behavior

The effective structural use of UHPC requires knowledge of its uniaxial stress-strain behavior. An analytical derivation of the uniaxial stress-strain response of the UHPC was obtained from the experimental results of the flexural testing of Girder 80F. This section presents the basis of this derivation and the derived stress-strain response.

The testing and instrumentation setup for Girder 80F was presented in Chapter 5, and the test results were presented in Chapter 6. One principle component of these results was the strain profile on the midspan cross-section of the girder. This strain profile was determined based on bonded strain gage readings in uncracked regions of the cross-section on both faces of the girder. Plane sections are assumed to remain plane in this analysis; therefore, the strain profile results were then extrapolated to determine both the strains at the top and bottom of the cross-section and the location of the neutral axis. Figure 7.13.5-A shows these results for each load step throughout the test. The experimental results also included the moment applied to midspan of the girder throughout the test and the composite stiffness of the girder as derived in Section 7.13.4. Finally, an approximation of the compressive stress-strain response of UHPC was derived in Section 7.10.

The state of strain in the girder at the initiation of flexural loading must be known to complete this analysis. Prior to the application of flexural live load, the only stresses at midspan are caused by the prestress force and the dead load. An analysis was completed to determine the stresses in the UHPC and the prestressing strands. The basic

assumptions in this analysis included that plane sections within the cross-section remain plane and that strain compatibility between the strands and the concrete is maintained. The prestressing force and dead load were applied to the girder when its compressive strength was at least 10 ksi and its modulus of elasticity was 5000 ksi. The prestressing losses discussed in Section 7.12 were then applied after the modulus of elasticity increased to 6000 ksi. The compressive stresses in the concrete at the initiation of the Girder 80F test were determined to be 1.0 ksi at the top of the midspan cross-section and 1.5 ksi at the bottom of the midspan cross-section. The stresses in the strands ranged from 122.2 ksi in the top flange strands to 118.9 ksi in the lowest bottom flange strands.

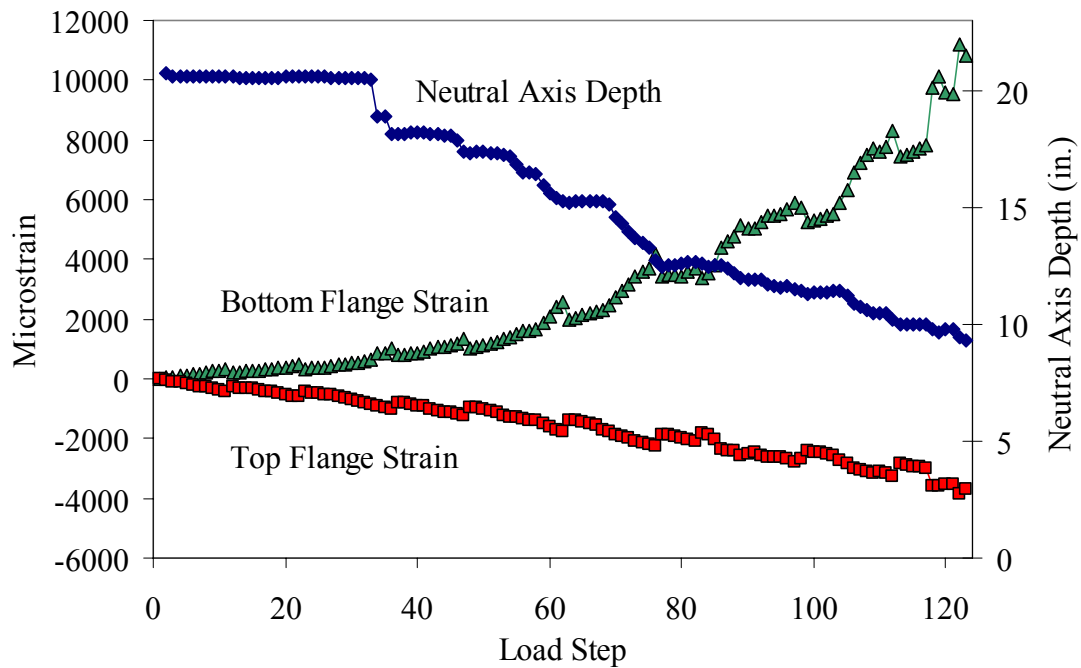


Figure 7.13.5-A: Experimental strain profile results for midspan of Girder 80F

These concrete and strand stress values were then transformed into equivalent strain values on the cross-section. This transformation assumed linear elastic behavior with 8100 ksi and 28500 ksi as the moduli of elasticity for the UHPC and the prestressing strands, respectively. Thus, the linear strain profile on the cross-section at the Girder 80F test's initiation included 123 microstrain of compression at the top of the girder and 190 microstrain of compression at the bottom. The strain in the top prestressing strands was 4287 microstrain, and the four layers of strands in the bottom flange had strains of 4192, 4185, 4178, and 4170 from top to bottom, respectively.

These results provide the basis for the analysis that was completed to determine the full uniaxial stress-strain behavior of UHPC. The analytical procedure included the following steps. First, the midspan cross-section of the girder was discretized into 72 concrete slices and 5 prestressing strand slices parallel to the neutral axis. The strain on each of these slices at every load step throughout the test was then calculated based on the observed strain profiles. A complete uniaxial stress-strain response for the UHPC was then assumed. Using this stress-strain response and assuming that the prestressing strand behaved linear elastically, the stresses on the cross-section at each load step were calculated. Note that this analysis initially focused on the loading steps throughout the test and ignored the unloading and reloading steps.

The summation of the stresses in the concrete and the strands were then compared with one another to ensure that the internal forces on the cross-section were in equilibrium at every load step. The assumed UHPC uniaxial stress-strain response was repeatedly

modified, and the calculations were recomputed until the internal forces on the cross-section were sufficiently coincident. Figure 7.13.5-B shows the uniaxial stress-strain response that was derived through this analytical technique. Figure 7.13.5-C shows the force in the concrete, the force in the strands, and the ratio of the two values for each load step. On all loading steps, the concrete and strand forces are within 7% of one another. This result is considered sufficiently accurate given the experimental variability inherent in the test results that are the basis for these calculations.

Figure 7.13.5-B is composed of four separate curves. Each curve defines a portion of the behavior. In compression, the UHPC follows the relationship defined in Section 7.10 with a modulus of elasticity of 8100 ksi. The initial tensile behavior of UHPC is considered to be linear elastic with an 8100 ksi modulus of elasticity. The post-cracking behavior of UHPC is defined by the red curve in Figure 7.13.5-B, with an initial modulus of elasticity of 5000 ksi. The final portion of the behavior is the tensile transition zone during the initial cracking of the concrete. This transition, highlighted in green on Figure 7.13.5-B, allows the UHPC to transform from an uncracked, elastic material into a significantly cracked material that is still capable of carrying tensile loads.

Note that the UHPC has to carry 3.0 ksi of tensile stress before the cross-section becomes sufficiently cracked to cause the stress-carrying capacity to decrease. This value is well above the tensile cracking strength that was determined in the UHPC material property characterization testing, because those tests focused on first cracking while the girder test focused on sufficient cracking to change global behaviors. Small-scale tensile tests tend

to limit the load path redundancy thus allowing initial crack(s) to grow longer and wider prior to other cracks forming. Full-scale prestressed girders offer redundancy through two means. First, the prestressing strands tend to help maintain tight cracks. Second, the large scale of the girder eliminates the localized stiffness effects caused by single cracks on prism flexure specimens.

To complete this analysis, the unloading and reloading behaviors of UHPC were investigated. Similar to most structural materials, after UHPC undergoes inelastic deformation, subsequent unloading and reloading of the concrete causes it to behave linear elastically with a reduced modulus of elasticity. This continues until new strain levels are attained. In this analysis, UHPC not experiencing peak tensile or compressive strains was assumed to behave linear elastically with a stiffness equal to the secant modulus of elasticity of the peak strain ever attained. This assumption was used both in tension and compression. For the post-cracking tensile behaviors, shown by the red curve in Figure 7.13.5-B, the origin for the secant modulus was shifted to the location where the red curve is shown to intersect the x-axis. In the tensile cracking transition region, the secant moduli were calculated just before and after the transition region. The secant values in the transition region were then linearly interpolated from these end values.

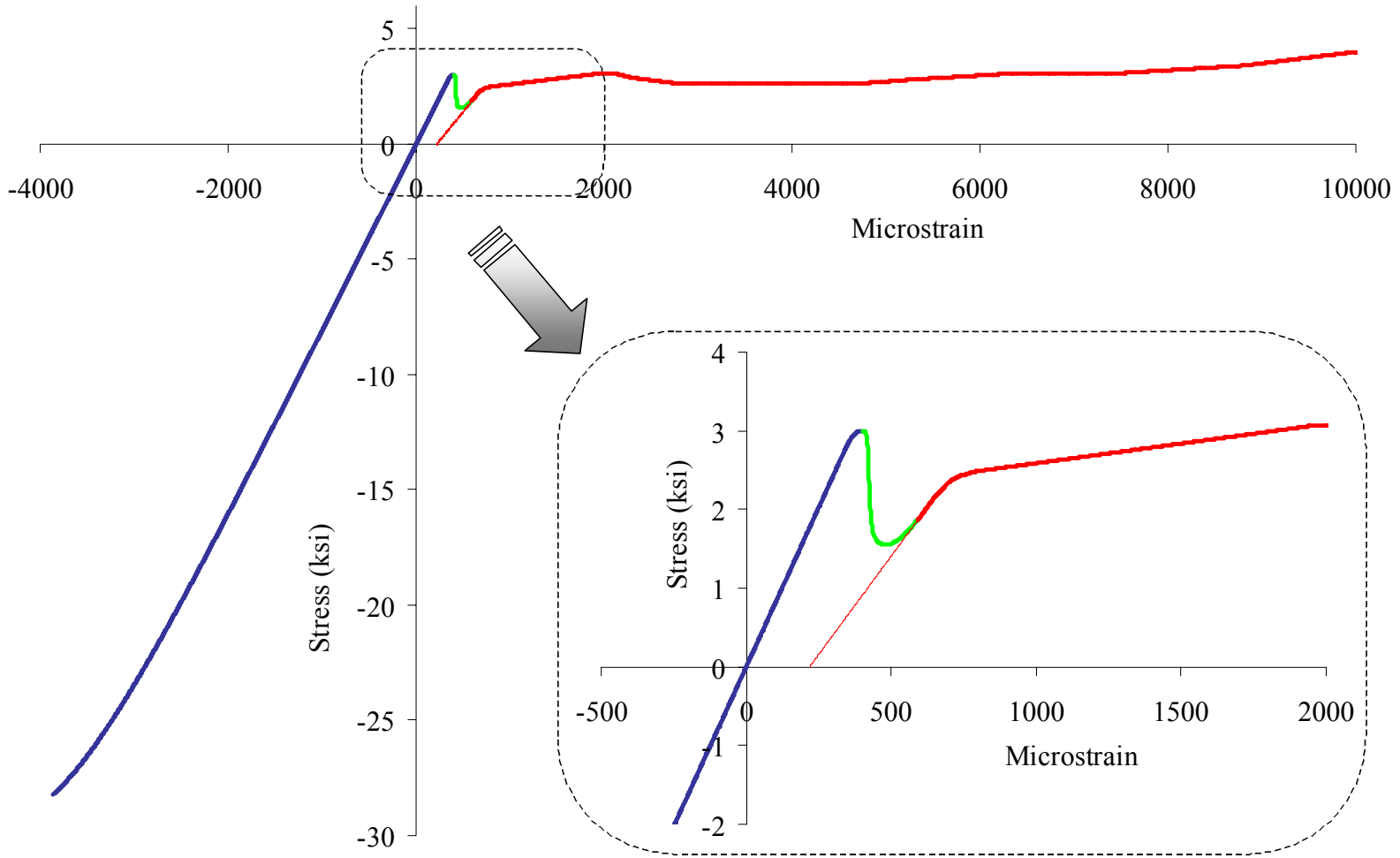


Figure 7.13.5-B: Analytically derived uniaxial stress-strain behavior of UHPC

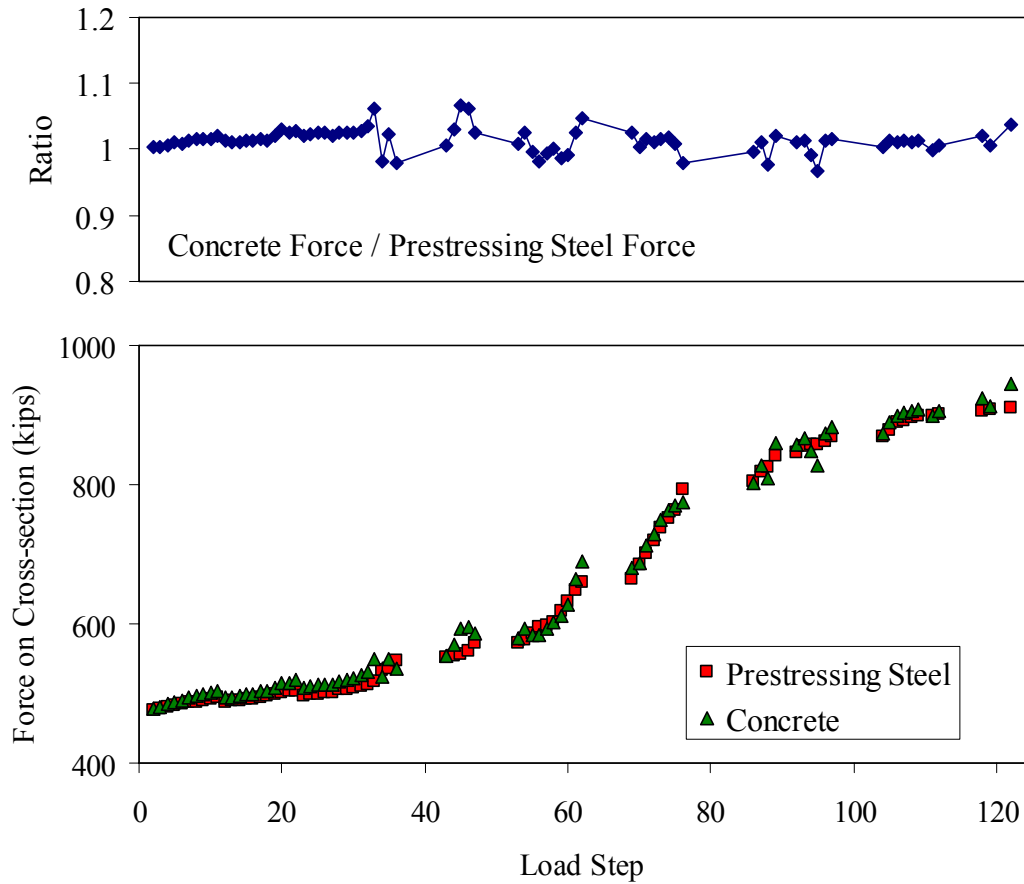


Figure 7.13.5-C: Summation of forces on cross-section during loading steps

The results of this analysis are presented in Figure 7.13.5-D. This figure shows the experimentally captured external moments that were applied to the midspan cross-section. The figure also shows the internal moments on the cross-section caused by the assumed stress-strain response at every load step. The results are quite accurate until the final load steps of the test. At this point, the model tends to overestimate the internal moment, which is understandable for two reasons. First, the experimentally determined strain profile on the cross-section is least accurate at these high loads when the cross-

section is significantly cracked and the neutral axis has moved closer to the top flange. Second, the method used to determine the uniaxial stress-strain response builds on itself throughout the test. Therefore, more accuracy is built into the lower tensile and compressive strain ranges than can be expected in the higher strain ranges.

The final portion of this analysis focuses on determining the stiffness exhibited by the UHPC throughout its uniaxial behavior. In Section 7.13.4, the stiffness of this UHPC AASHTO Type II cross-section was determined for the range of applied moments encountered in this test. Thus, the total stiffness of the midspan cross-section, as analyzed in this section of the report, should add up to the stiffness determined in Section 7.13.4. Figure 7.13.5-E presents the results from Section 7.13.4 and the stiffness results from this analysis. The UHPC stiffness on the loading branch in compression and in tension prior to cracking was defined by the tangent modulus of elasticity. The stiffness was defined by the secant modulus of elasticity during unloadings and reloadings, and after cracking. This method of determining the moment of inertia of the UHPC flexural section provides very accurate results, with only a slight underestimation of the stiffness after cracking has occurred, as shown in Figure 7.13.5-E.

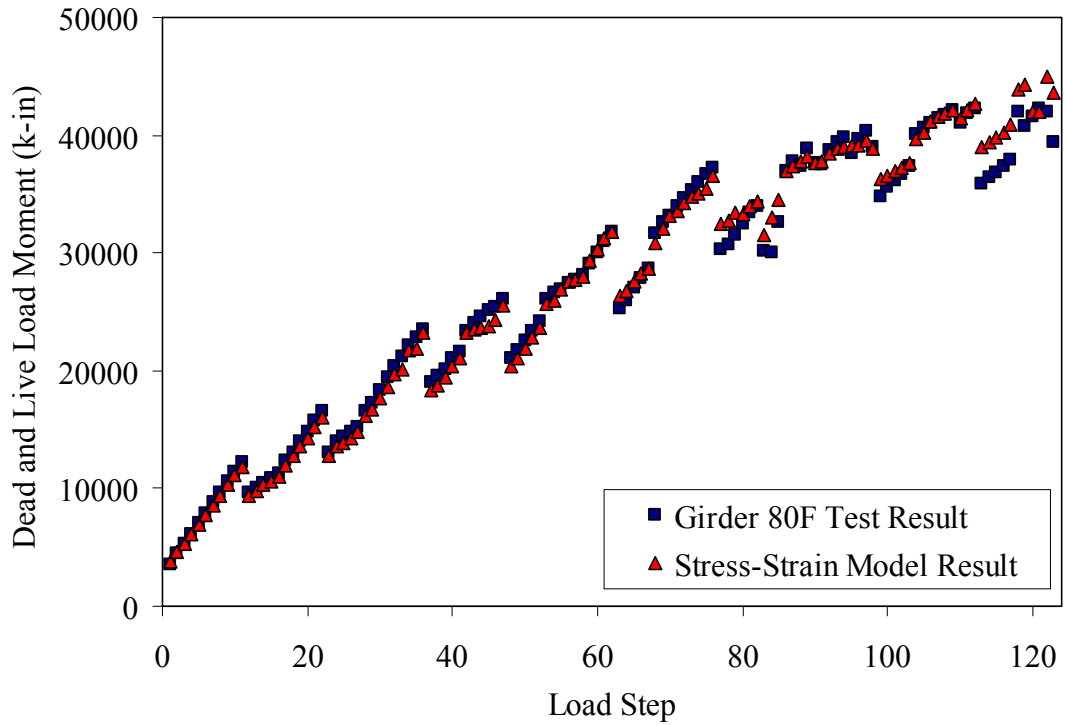


Figure 7.13.5-D: External and internal moments on midspan cross-section

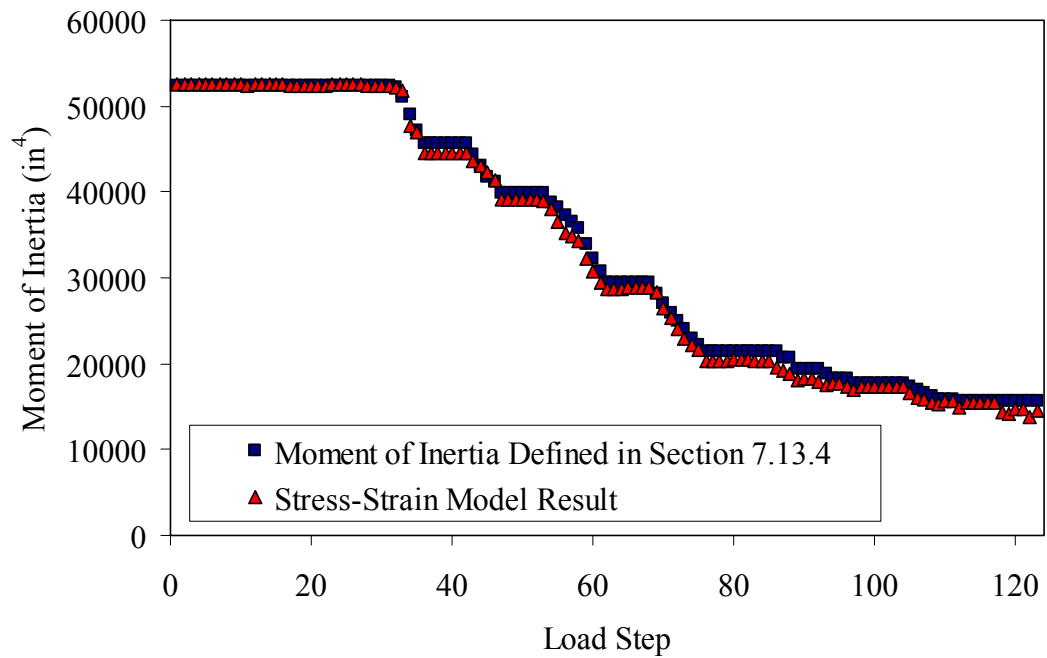


Figure 7.13.5-E: Internally and externally determined moment of inertia

7.14 Shear Behavior of Prestressed UHPC Girders Containing No Mild Steel

Three AASHTO Type II prestressed UHPC girders were failed in shear as part of this research program. The results of these tests were presented in Chapter 6. This section combines the results from these three tests. First, the shear capacity results are compared with the predicted capacity calculation results. Second, the shear cracking behavior of UHPC is discussed. The final part of this section focuses on a truss model developed to explain the behaviors observed in one particular shear test.

7.14.1 Predicted vs. Actual Global Behavior

The primary goal of the three full-scale shear tests was to determine the shear capacity of prestressed UHPC girders. To summarize the results presented in Chapter 6, Girder 28S had a shear capacity of 384 kips and failed due to a preexisting horizontal crack at the base of the web. Girder 24S had a shear capacity of 502 kips and failed due to diagonal tension in the shear region. Girder 14S had a shear capacity of 438 kips and failed due to a combination of diagonal tension and strand slip. These results indicate that the shear capacity of a 36-in. deep prestressed concrete girder can be as high as 500 kips without any standard shear reinforcement. Under a normal loading condition, in which strand slip might be expected, a shear capacity of more than 400 kips can still be expected.

Predicting the shear capacity of these UHPC girders can be attempted through the use of standard structural design procedures. However, because UHPC exhibits strengths well beyond the limits of most structural design codes, those code provisions cannot necessarily predict the shear behavior of UHPC girders. Most codes predict the shear

capacity of prestressed concrete girders by dividing the shear resistance into three terms. These terms include the contributions from the concrete, the mild reinforcing steel, and the prestressing strands. Because these UHPC girders contained no mild steel and no draped strands, the only relevant term is the concrete resistance to shear forces.

For comparative purposes, an AASHTO Type II girder, similar to those discussed in this report, was analyzed to determine its shear resistance. This prestressed girder was composed of 8 ksi concrete and contained #4 stirrups at a 4-in. spacing. According to the AASHTO Standard Bridge Design Specification, this girder would have exhibited a nominal shear capacity of approximately 250 kips, with half of the capacity coming from the concrete and half from the stirrups. Although this level of shear capacity is significant for this depth of girder, it also illustrates the high level of shear capacity achieved with the UHPC girders.

The Association Française de Génie Civil (AFGC) *Interim Recommendations for Ultra High Performance Fibre-Reinforced Concretes* (2002) is one design aid that does directly address the contribution of fiber reinforcement to shear capacity. In this document, the ultimate shear strength of the cross-section is defined as the composed portions contributed by the concrete, the standard steel reinforcement, and the fiber reinforcement. For the UHPC girders tested in this study, the concrete contribution to the shear capacity, V_{Rb} , is given by Equation 7.14.1-A. In this equation, $\gamma_E \gamma_b$ is a safety factor defined to equal 1.5. The compressive strength is f_c' , b_0 is the web width, and z is the lever arm at the ultimate moment. All measurements are in metric units. The lever arm is assumed to

equal the distance from the center of the compression block to the center of the strands, or 26.5 in. for these girders. Thus, the design value for the concrete contribution to the shear capacity is 51 kips. Alternatively, because this equation is being used to model experimentally observed behaviors, setting the factor of safety terms to equal 1.0 results in a concrete contribution to the shear capacity of 77 kips.

$$V_{Rb} = \frac{0.24}{\gamma_E \gamma_b} \sqrt{f'_c} b_0 z \quad (7.14.1-A)$$

The fiber contribution, V_f , within the AFGC recommended provisions is defined by Equation 7.14.1-B. The variable S is the area of the shear plane being considered. This variable is assumed to equal 90% of the web width multiplied by the depth to the centroid of the prestressing strands. β_u is the angle of the compression struts in the shear area as measured from the horizontal. The assumption that the angle is 40 degrees is a conservative estimate of the angle based on the prestressed concrete girder behavior. The variable γ_{bf} defines a factor of safety that is set equal to 1.3. Finally, σ_p defines the average residual tensile stress carried by the fibers across a shear crack from cracking until a limiting strain value is achieved. This value is normally based on experimental tension test results. In this case, based on the results presented in Chapter 3 and in Sections 7.1 and 7.13, the residual tensile stress will be assumed to be 1.0 ksi. Thus, the design value for the fiber contribution to the UHPC shear capacity is 156 kips. Alternatively, setting the factor of safety terms again to 1.0 results in a fiber contribution to the shear capacity of 170 kips.

$$V_f = \frac{S\sigma_p}{\gamma_{bf} \tan \beta_u} \quad (7.14.1-B)$$

These girders contain no mild steel reinforcement and the prestressing strands are not draped; therefore, the concrete and fiber contributions are the only two items relevant to determining the shear capacity. In total, the AFGC recommendations indicate that the ultimate design shear capacity of the AASHTO Type II prestressed girders tested in this study is 207 kips. Eliminating the factor of safety terms produces the true AFGC estimate of the shear capacity, which is 247 kips. Although this method of estimating the shear capacity of UHPC girders is more rigorous than many shear capacity calculations, the method still clearly significantly underestimates the shear capacity of these UHPC girders.

7.14.2 Cracking Behavior

The shear cracking of the UHPC girders during the shear tests is again indicative of the structural cracking behaviors associated with UHPC. First, this section discusses the cracking behaviors observed during the shear tests. Then the cracking behavior of Girder 24S is analyzed to determine the effective prestress force applied to the girder.

Girders 24S and 14S both exhibited diagonal web shear cracking that eventually led to the failure of the girders. Girder 24S first exhibited shear cracking at a shear load of 254 kips. The cracking initiated in the portion of the shear span closer to the load point, because this location experienced both high shear stresses and larger flexural forces. The angle of the shear cracks at this location was approximately 35 degrees from the

horizontal. Girder 14S first exhibited shear cracking at a shear load of 205 kips. Again, shear cracking initiated in the web close to the load point with an angle of 38 degrees from the horizontal.

The number of shear cracks in both girders increased as the shear load increased. Initially, the cracks were spaced approximately 1 in. apart throughout the web from the load point to the bearing. As the test progressed, the crack spacing decreased as more cracks appeared until the crack spacing had decreased to 0.25 in. or less in some locations.

As presented in Chapter 5, Girder 24S failed when the fibers bridging a highly stressed shear crack began to pull out. In this girder, the loss of tensile capacity across the shear crack resulted in immediate failure because the shear forces could not be redistributed around the crack. The cracking and eventual fiber pullout across a crack in Girder 14S resulted in a different type of failure. In this girder, the shear capacity and girder stiffness decreased simultaneously as the fibers pulled out and the strands slipped, thus allowing for a slow decrease in shear capacity until over one-fourth of the shear load had been shed.

The first cracking behavior of a prestressed girder is indicative of both the tensile cracking strength and the level of prestress applied to the girder. The method used to test Girder 24S resulted in the prestressing strands fully transferring their stress into the girder outside of the highly stressed shear region. The analysis of this girder enabled the

verification of the prestress force and tensile cracking strength values that were discussed previously. Shear and flexural strains at cracking on an element in the web of this girder, located under the rosette strain gage closest to the load point, indicate that 161 microstrain of tension caused cracking. If the tensile cracking strain of UHPC is assumed to be 200 microstrain, the effective prestress force on this girder would be 455 kips, which was determined in Section 7.12. Note that a 200 microstrain tensile cracking strain would correspond to an 8000 ksi modulus of elasticity with linear elastic behavior through cracking at 1.6 ksi. This tensile cracking behavior is consistent with the behaviors discussed in Section 3.1.

7.14.3 Simplified Model of UHPC Girder Shear Failure

The girder shear behaviors observed during the testing of Girders 24S and 14S indicate that the shear behavior of a UHPC I-girder containing no mild steel shear reinforcement is less complex than is normally associated with a concrete girder. For example, determination of the shear capacity of a concrete girder could involve the estimation of the capacity provided by the concrete alone, the capacity provided by the mild steel reinforcement alone, and the capacity that results from the interaction of the mild steel reinforcement to enhance the concrete capacity. The terms associated with concrete behavior are normally difficult to ascertain and are frequently approximated through empirical relationships. Observations from the UHPC girder tests indicate that the shear behaviors of a UHPC girder as failure is approached are significantly less complicated and lend themselves to basic modeling and approximation procedures.

The descriptions of the failure of Girder 24S, in particular the photographs shown in Figure 6.2.2-H, clearly illustrate that the failure of this girder was caused by diagonal tensile forces in the highly stressed shear region of the girder. Because this UHPC girder contained no mild steel, this tensile failure of the concrete was not influenced by reinforcing bars bridging the cracks. Also, because UHPC has a very fine granular structure, it is not anticipated that any significant level of aggregate interlock could be present in a UHPC girder. All indications—including the observations of many tightly spaced cracks parallel to the eventual tensile failure plane—lead to the conclusion that simply determining the vertical component of the tensile stress capacity over the expected shear failure plane would lead to the shear capacity of the girder.

This simple analytical procedure is conceptually equivalent to the fiber contribution to shear capacity (detailed in the AFGC recommended provisions and discussed in Section 7.14.1). In the AFGC design procedure, the fiber contribution to the shear capacity is composed of terms representing the average tensile capacity of UHPC at failure, the angle of the failure plane relative to the girder, and a partial depth of the cross-section. Algebraic manipulation shows that the AFGC equation actually estimates the shear failure plane area, multiplies it by the average estimated tensile stress over the failure plane, and converts the result into a vertical component that is useful for shear calculations.

Thus, the knowledge of two girder specific properties and one material property allow for the estimation of the shear capacity of the girder. During design, the angle of the failure

plane can be estimated based on the level of prestress in the girder. The area of the failure plane is more difficult to estimate. However, it should be able to be bounded based on the thickness of the web, the height of the web and web transitions, and the angle of the failure plane. Finally, the average tensile stress exhibited by UHPC prior to fiber pullout must be estimated based on prior knowledge of the material behavior.

Test results from Girders 24S and 14S can be used to illustrate the capabilities of this simple analytical procedure. The failure plane angles in these two girders were measured to be 28 and 25 degrees from the horizontal, respectively. The peak shear loads carried by these girders prior to the fiber pullout were 500 and 438 kips, respectively. The depth of the cross-section that the failure plane traverses can be estimated to be between the depth of the web, 15 in., and the AFGC recommended depth, 28 in. Observed shear cracking behaviors during the tests indicate that most diagonal tensile shear loads were carried by the girders within the web and a small part of the web transitions. Thus, for this analysis the depth of the failure plane is assumed to be 19 in. By assuming this depth of failure plane over the width of the web at the failure plane angles mentioned above, the geometry of the failure surface has been defined. Using these values, the average tensile stress in Girder 24S is determined to be 2.3 ksi. In Girder 14S the value is determined to be 1.8 ksi.

These average tensile stress values prior to fiber pullout are reasonable approximations of UHPC behavior based on results presented elsewhere in this report. The tensile stress-strain behavior derived in Section 7.13.5 and presented in Figure 7.13.5-B is of greater

relevance for this discussion. In that analysis of the flexural loading of a prestressed girder, the figure shows that the average tensile stress prior to fiber pullout was over 2.5 ksi. Because the shear regions in Girders 24S and 14S were not supplementally reinforced by prestressing strands like the bottom flange of a prestressed girder, it is understandable that the average stress across the failure plane might be lower prior to fiber pullout. Regardless, this analytical procedure clearly provides a reasonable interpretation of shear failure behavior based on sound engineering principles without reverting to empirical relationships.

7.14.4 Strut-and-Tie Model of Girder 28S Failure

The fiber reinforced concrete matrix is capable of carrying and dispersing both tensile and compressive loads. Therefore, in general, truss modeling of UHPC behavior is likely to be less useful than truss modeling on normal or high performance concrete behavior. Thus, the tension ties that are a major part of most truss models become significantly less relevant with UHPC.

However, the final failure of Girder 28S involved crushing of the web concrete and tensile rupture of the top flange. These behaviors were not expected in a girder shear test, which lead to the development of a truss model to explain the global behavior at failure. Recall that this girder test included the development of a shearing plane along the base of the web in the highly stressed shear region.

Figure 7.14.4-A displays the truss system that was developed to model the failure of Girder 28S. In this figure, the brown dashed lines indicate compression struts while the solid green lines indicate tension ties. The design of this model includes a complete delamination of the web from the bottom flange within the highly stressed shear region, which ensured that no forces were able to transfer across this boundary.

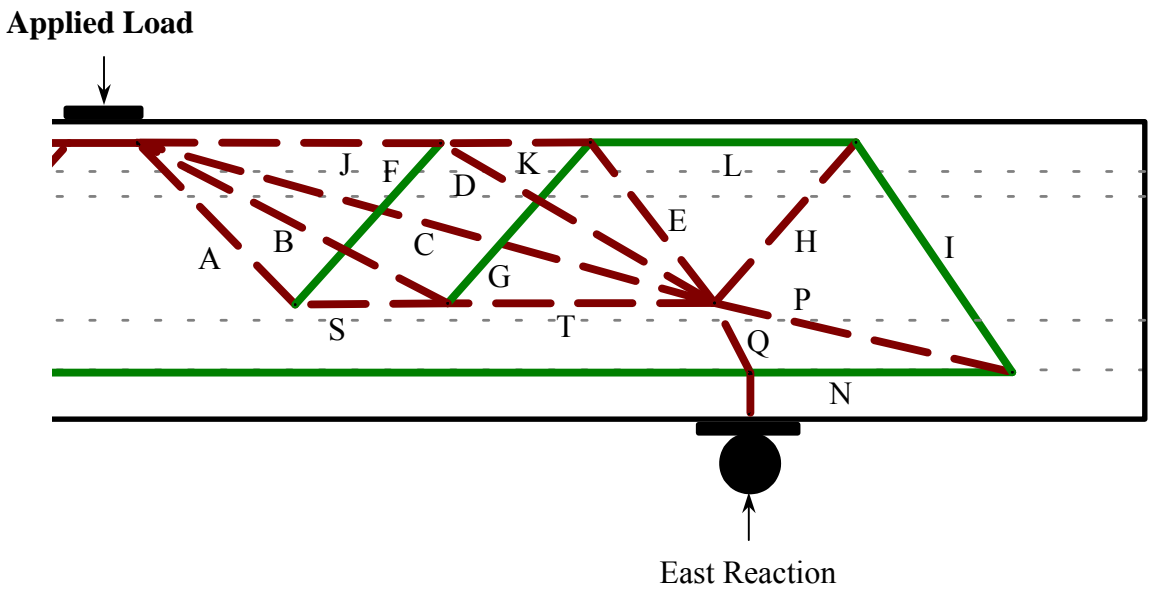


Figure 7.14.4-A: Truss model for failure of Girder 28S

At failure, the applied load on this girder was 500 kips, with 384 kips being carried by the east support. Given this loading, the forces in kips in the compression struts of the truss model include: A = -249, B = -359, C = -76, D = -327, E = -235, H = -234, J = -470, K = -35, P = -785, Q = -541, S = -334, and T = -805. The forces in the tension ties include: F = 240, G = 247, I = 216, L = 272, and N = 643.

Although truss models provide an upper bound to the solution, an examination of this answer indicates that it is a reasonable solution. In particular, a detailed analysis shows that the node connecting seven compression struts just above the bearing is the critical node. As was observed in the girder test, the compression forces shown in the struts would create a compression failure of this 28 ksi UHPC at this node. This model also reasonably predicts the subsequent tensile failure of the top flange above the bearing. The tension tie shown in Figure 7.14.4-A carries 272 kips. This load is large enough to cause tensile cracking of the UHPC top flange and to initiate fiber pullout leading to strain localization in the strands and strand rupture.

CHAPTER 8

DESIGN PHILOSOPHY FOR UHPC BRIDGE GIRDERS

8.1 Introduction

The experimental research and associated analytical analyses undertaken in this research program provide significant insight into the potential structural behavior of UHPC bridge girders. The design of prestressed concrete I-girders normally focuses on flexural and shear behaviors. The results of this research program indicate that the flexural and shear behaviors of prestressed I-girders that are composed of UHPC can be modeled through straightforward analytical procedures. Therefore, rational design of UHPC I-girders based on these same analytical principles is possible. This chapter presents a rational design philosophy for prestressed UHPC I-girders.

8.2 Flexure

The flexural behavior of an AASHTO Type II UHPC girder has been extensively discussed in this report. The behavior of this girder from initial elastic loading through failure was analyzed to determine the contribution of the UHPC to the overall flexural behaviors of the girder. Figure 7.13.5-B provides the analytically determined uniaxial stress-strain response of UHPC within the girder during the test. With this knowledge, the flexural design for other prestressed I-girders is possible.

The design of a prestressed UHPC I-girder for flexure requires only two factors. First, a conservative approximation of the UHPC's uniaxial stress-strain response must be

applied to the cross-section. Second, the occurrence of the expected flexural behaviors must be ensured. A primary factor must be taken into consideration in an I-girder to ensure the expected UHPC behavior: Sufficient prestressing strands or mild steel reinforcement must exist in the primary flexural tensile regions so that cracks in the UHPC remain tightly closed and closely spaced. Without sufficient gross reinforcement restraining the tensile flexural regions, individual cracks will begin to widen as the fibers pull out, and the tightly spaced cracking, shown in Figure 6.1-H, will probably not occur.

Determining a sufficiently conservative approximation of UHPC uniaxial stress-strain behavior depends on the application and on the prescribed design limits. In a situation where cracking of the girder is not allowed at service loads, the girder can easily be designed using normal design procedures with the known modulus of elasticity and tensile cracking strength of UHPC. In a situation where a minimal amount of cracking will be allowed at service loads, a post-cracking uniform tensile stress capacity will need to be assumed. Finally, for the ultimate load state, a full compressive and tensile stress-strain response will be required. This response will include an effective tensile strain that causes fiber pullout, a limiting tensile capacity relevant at any strain below the fiber pullout strain, and a limiting compressive strength.

A conservative uniaxial stress-strain response for UHPC could be described by the following three conditions. First, the UHPC could be assumed to behave linear elastically in compression up to 0.85 times the compressive strength. Second, in tension, the UHPC could be assumed to behave in a rigid-plastic fashion at a conservative percentage of the

post-cracking tensile capacity at strains below the tensile pullout strain. Third, based on the results presented in this report, sample values could include 24 ksi for the compressive strength, 1.5 ksi for the tensile capacity, and 0.007 for the limiting tensile strain. Figure 8.2-A graphically presents this sample stress-strain behavior.

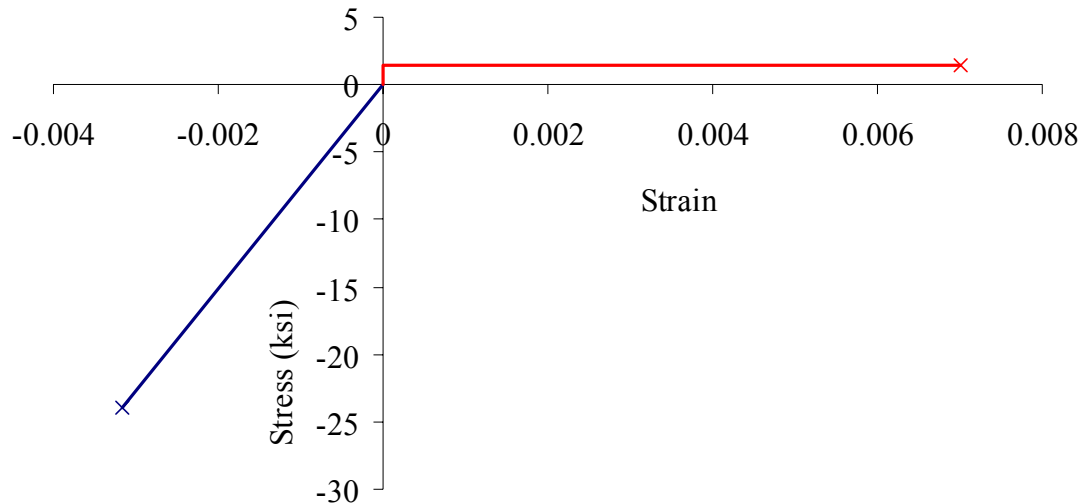


Figure 8.2-A: Sample uniaxial stress-strain behavior for I-girder flexural design

Determining the flexural capacity of a UHPC I-girder using a stress-strain response such as the one shown in Figure 8.2-A can be completed using basic mechanics of materials concepts. A number of iterations on the neutral axis depth and on the limiting strain condition will likely be needed before a final solution is reached.

8.3 Shear

The shear behavior of prestressed UHPC I-girders was also extensively discussed in this report. Three AASHTO Type II prestressed girders that did not contain any mild steel shear reinforcement or any draped prestressing strands were tested to determine their

shear capacity. The shear capacities exhibited by these girders were very large in comparison to normal AASHTO Type II girders. The behaviors were also very consistent with the mechanics of materials concepts of the flow of tensile and compressive forces in the shear region of a bridge girder.

A basic design philosophy, based on these results, is proposed to aid in the shear design of UHPC girders. The results presented in Section 7.14 indicate that a reasonable estimate of the shear capacity can be determined by assuming that all shear forces are carried by diagonal tension and compression in the web of the girder. Given the high compressive strength of UHPC, the limiting value will be the post-cracking tensile stress capacity. The shear capacity of a UHPC girder can be conservatively estimated with the area of the web as a variable and an approximated angle of the diagonal tensile failure plane in the girder. A conservative estimate of the average tensile stress capacity of UHPC must be known prior to the fiber pullout.

The analyses discussed in Section 7.14 indicate that the average tensile strengths in the unreinforced webs of two AASHTO I-girder were 1.8 ksi and 2.3 ksi. In both cases, conservatively large shear areas were assumed so that the average tensile strength determined was minimized. Regardless, a conservative estimate of the available average tensile strength of UHPC could be set at a reasonable percentage of the observed strengths. From this value, the shear failure plane area required can be determined, which leads directly to the necessary dimensions of the girder web.

To ensure that the expected shear behaviors can occur, the girder must be detailed to allow for tight crack spacing and small crack widths in the highly stressed shear region. Therefore, to ensure this cracking behavior, the shear region must be restrained by the top and bottom flanges of the girder. Additionally, draped prestressing strands that pass through highly stressed shear regions will also likely help to retard crack growth. However, even with these details, the crack restraining actions in the web will not be as efficient as the ones that occur in the bottom flange of a prestressed girder. Thus, the tensile stress and strain capacities, discussed in Section 8.2, are not expected to be applicable in this situation.

Finally, determining the state of stress in the girder web under prestressing and dead loads is important when designing a prestressed girder for shear. The significant compressive forces in the web could possibly delay the onset of tensile cracking and the eventual tensile fiber pullout behaviors.

CHAPTER 9

CONCLUSIONS AND FUTURE RESEARCH

9.1 Introduction

Ultra-High Performance Concrete (UHPC) is a new type of concrete that exhibits properties of enhanced strength, durability, and long-term stability. The objective of this research was to evaluate the potential use of UHPC in highway bridge girders. This objective was achieved by characterizing UHPC material behaviors through small-scale specimen testing and by characterizing structural behaviors through full-scale girder testing.

The research included two experimental phases and one analytical phase. The experimental phases focused on determining the material and structural behaviors of UHPC. Over 1000 individual specimens were tested to determine the material characterization of UHPC. The tests determined the compressive and tensile behaviors, the long-term stability, and the durability of UHPC. The full-scale bridge girder testing was conducted on AASHTO Type II prestressed girders. One flexure test on an 80-ft span girder and three shear tests on shorter span girders were conducted. These girders did not contain any mild steel reinforcement; therefore, the UHPC carried all secondary (i.e., shear, temperature, shrinkage) tensile forces. The analytical phase of this research combined, analyzed, and elaborated on the results from the experimental phases. This phase included developing predictor equations for basic properties of UHPC and

developing a rational philosophy for the flexure and shear design of prestressed UHPC I-girders.

The conclusions of this study are presented in Section 9.2. A brief discussion of ongoing and potential future research topics follows in Section 9.3.

9.2 Conclusions

The following conclusions are based on the research presented in this report. For clarity, the conclusions have been grouped into three sections, focusing on study-wide conclusions, highway bridge girder specific conclusions, and material characterization specific conclusions.

9.2.1 General

The following conclusions focus on the overall body of work presented in this report:

1. UHPC displays significantly enhanced material properties compared with normal and high performance concrete.
2. UHPC is a viable substitute for normal concrete and HPC in prestressed I-girders.
3. UHPC I-girders can be designed to more efficiently carry flexure and shear forces. A conservative estimate of the full UHPC tensile and compressive stress-strain behavior could be used to predict the flexural capacity of an I-girder. A conservative estimate of the post-cracking tensile capacity could be

used to predict the diagonal tensile capacity of UHPC in the shear region of a girder.

9.2.2 Highway Bridge Girders

The following conclusions focus on UHPC highway bridge girders:

1. The placing of UHPC in an I-girder formwork can be completed very rapidly with little need for supplemental vibration. UHPC was observed to be virtually self-placing. The ability of UHPC to be reinforced internally by fiber reinforcement allows for the reduction or elimination of most mild steel reinforcement, which greatly simplifies the I-girder formwork preparation. Without taking any special precautions to release the formwork during setting, no shrinkage cracks were observed in the girders.
2. The shear capacity of UHPC AASHTO Type II girders that did not contain any mild steel shear reinforcement or any draped prestressing strands were between 380 and 500 kips. Traditional shear failure of the girder web, without any strand slippage, occurred in one girder at 500 kips. Two other girders failed at lower loads due to strand slippage and to horizontal debonding of the web from the bottom flange, which resulted from a preexisting defect.
3. The live load flexural capacity of a UHPC AASHTO Type II girder containing twenty-four 0.5-in. prestressing strands was 38700 k-in. This increased flexural capacity compared with normal concrete and HPC is primarily the result of the sustained post-cracking tensile capacity of UHPC.

4. The failure of bridge girders composed of UHPC was observed to be precipitated by the pull out of fibers that were bridging tension cracks in the concrete. The flexural failure of an AASHTO Type II girder occurred when the UHPC at a particular cross-section began to lose tensile capacity due to fiber pullout. This loss of the UHPC tensile capacity necessitated the transfer of those internal flexural tensile forces onto the prestressing strands. This transfer then resulted in the rupture of the prestressing strands. The traditional shear failure of a similar girder was also caused by the loss of tensile capacity of the UHPC due to fiber pullout. In this loading configuration, the girder could not redistribute the tensile shear forces through any other load path, thus the girder rapidly lost all load carrying capacity. A different girder's shear failure in combination with strand slip demonstrated that fibers tend to pull out gradually over a short time frame and that, in the presence of an alternate load path, the girder can continue to maintain some load carrying capacity.
5. UHPC that is subjected to large tensile strains will exhibit tightly spaced cracking in a restrained region of a structural member. Crack spacing as small as one-eighth inch was observed during the structural testing of bridge girders. The tensile flange of a prestressed girder allows for the very tight crack spacing due to the prestressing strands ensuring tight cracks and allowing for the redistribution of some local strain irregularities. The web region of an I-girder is sufficiently restrained by the top and bottom flanges to exhibit relatively tight crack spacing, but the web region spacing is not as tight as occurs in the tension flange under flexural loading.

6. The development length of 0.5-in., 270-ksi low relaxation prestressing strands in UHPC is less than 37 in. The AASHTO Type II girder shear tests indicate that in a heavily distressed shear region, the prestressing strands will rupture after only minimal slip if they are embedded at least 37 in. into the UHPC.

9.2.3 Material Property Characterization

The following conclusions focus on the material property characterization of UHPC:

1. Steam-based treatment of UHPC tends to significantly enhance its material properties. Three steam-based treatments—Steam, Delayed Steam, and Tempered Steam—were investigated and compared with UHPC that was not subjected to a curing treatment after casting. In general terms, Steam treatment increases UHPC's compressive strength by 53% to 28 ksi, increases its modulus of elasticity by 23% to 7600 ksi, decreases its creep coefficient from 0.78 to 0.29, and virtually eliminates long-term shrinkage. Steam treatment also decreases chloride ion penetrability to a negligible level and significantly enhances abrasion resistance. The enhancements of material properties affected by the Delayed Steam and Tempered Steam treatments are similar to those of the Steam treatment but of a slightly lesser magnitude.
2. UHPC exhibits very high compressive strengths, regardless of the curing treatment applied. The average 28-day compressive strengths of Steam, Delayed Steam, Tempered Steam, and Air treated UHPC were found to be 28, 24.8, 24.8, and 18.3 ksi. The compressive strength of Steam treated UHPC was found to have stabilized by the completion of the curing treatment. Thus,

Steam treated UHPC can reach its full compressive strength within 4 days after casting.

3. The mixing time and rheological properties of fresh UHPC are influenced by the concrete mixer design, the ambient environmental conditions in the mixer, and the elapsed time since blending of the premix. A 1934 vintage pan mixer was successfully used to mix the UHPC; however, the inability of this mixer to impart significant energy into the mix resulted in extended mixing times. Low humidity within the mixer and in the mix room can result in stiffer UHPC. Older UHPC premix requires more mixing to achieve the correct rheological properties, likely due to the agglomeration of fine particles in the premix during storage.
4. The set time of UHPC is significantly delayed compared with normal concrete; final set does not occur until 12 to 24 hours after casting. This time to set could also be longer depending on the admixtures and on other constituents in the mix.
5. Once setting has initiated, UHPC gains compressive strength very rapidly. If maintained at normal laboratory temperatures, UHPC compressive strength will increase to over 10 ksi by 2 days after setting. Subsequently, the rate of strength gain will decrease; 14 ksi will be reached by 10 days after setting.
6. The compressive strength of UHPC is not affected by the specimen geometry used to determine the result. Cylinders with 2-in., 3-in., and 4-in. diameters were tested according to ASTM C39, and 2 in. and 100 millimeter cubes were tested according to ASTM C109. The testing was conducted for two batches

of Steam treated UHPC and for one batch of Air treated UHPC. In all cases, the compressive strength results did not vary by more than 8% from the 3 in. cylinder control result. However, the 2 in. cubes and cylinders did tend to exhibit a larger standard deviation. The minimal preparation requirements for a cube specimen and the similarity of results mentioned above make the 100 mm cube a viable specimen geometry for UHPC compressive strength determination.

7. The curing conditions present during and just after the setting of UHPC can significantly affect the final properties of the concrete. In the Air treated case, concrete cylinders that were stripped as final set was being reached exhibited 25% lower 28-day compressive strengths compared with those stripped 1 day after setting was complete. A 30% difference was observed in the Steam treated case. These strength differences are likely due to the relatively more permeable nature of UHPC at earlier ages combined with the very low moisture content in the UHPC. This low moisture content results in a loss of water to the surrounding atmosphere and thus reduced hydration of the concrete.
8. The tensile strength of UHPC, both before and after tensile cracking, is significantly higher than the strength that occurs in normal concrete. Four test methods were implemented to capture the tensile strength of UHPC. The combined results of these tests indicate that the tensile cracking strength of UHPC is approximately 1.3 ksi after the steam-based curing treatment and approximately 0.9 ksi without any treatment. Qualitatively, UHPC was

observed to exhibit similar levels of tensile strength after cracking; however, in general, these tests were unable to indicate specific post-cracking strengths.

9. The ASTM C496 split cylinder tension test, modified to capture first cracking, provides the clearest indication of the tensile cracking strength of UHPC.

Through the use of a hydraulically controlled test machine and minimal instrumentation, the tensile cracking strength of UHPC can be obtained. Other tensile tests require more extensive instrumentation, specialization of specimen geometry, and more sophisticated loading equipment.

Unfortunately, the split cylinder test is not useful for determining the post-cracking tensile stress capacity, because the biaxial state of stress applied to the cylinder does not accurately mimic the conditions that are normally associated with tensile regions in a structural member.

10. The modulus of rupture defined by the ASTM C1018 prism flexure test overestimates the tensile cracking strength of UHPC by approximately 60%. This result was confirmed through the completion of this test on 2-in. square cross-sections with 6, 9, 12, and 15-in. spans, and on 3 in. by 4 in. cross-sections with a 12-in. span.

11. The ASTM C1018 prism flexure test provides a clear means of comparing the post-cracking tensile behavior of various fiber-reinforced concretes. UHPC, regardless of curing treatment, performed exceptionally well according to the toughness indices defined by this test. For example, the I_{20} toughness index normally ranges from 1 to 25 for fiber-reinforced concretes. In UHPC, the I_{20} results ranged from 28 to 32. Although these results cannot be directly

reinterpreted to apply to full-scale structural members, they do indicate that UHPC can continue to carry significant tensile loads after cracking.

12. UHPC displays durability properties that are significantly beyond those normally associated with concrete. Regardless of the curing treatment, the ASTM C666 relative dynamic modulus was at least 95% of the original value after more than 600 freeze-thaw cycles. UHPC exhibited no scaling under the ASTM C672 test, even after undergoing approximately 200 cycles. The chloride ion penetrability as measured by ASTM C1202 was below 50 Coulombs for UHPC that had undergone the steam-based treatment, and was 360 Coulombs for Air treated UHPC 28 days after casting. The Air treated UHPC results dropped to 76 Coulombs by 56 days after casting. UHPC was found to be innocuous to alkali-silica reaction.
13. Exposing cracked UHPC split cylinders to an aggressive environment did not result in any noticeable decrease in the peak tensile load carrying capacity. Tight cracks, as might be observed in a highly stressed tensile flexural region of an I-girder, were created by loading cylinders in a split cylinder configuration. These cracks were on the order of 0.0002 in. wide. A cracked face of the cylinder was then ponded with a sodium chloride solution as specified in AASHTO T259. After 90 days of ponding, the cylinders were tested for peak split cylinder tensile strength. The peak load carrying capacity of either Steam or Air treated UHPC did not have a discernable decrease after cracking, thus indicating that the sodium chloride solution did not enter the cracks and did not cause the fiber reinforcement to deteriorate.

14. UHPC exhibits shrinkage behaviors that are somewhat different from those of normal concrete. In total, UHPC tends to exhibit approximately 800 microstrain of shrinkage as measured from casting through 1 year. However, shrinkage initiation is affected by the delayed set times associated with UHPC, and the majority of the shrinkage occurs in a short time frame just after the concrete has set. Unrestrained shrinkage rates of over 60 microstrain per hour were observed during the period of rapid strength gain just after setting. Without any curing treatment, UHPC will continue to shrink at an ever decreasing rate. Steam treatment accelerates the shrinkage to such an extent that the entirety of the shrinkage occurs during the two-day treatment, and the UHPC is then stabilized against further shrinkage. Also, the total shrinkage in Steam treated UHPC tends to be slightly higher than the asymptotic shrinkage approached by Air treated UHPC.
15. Large compressive stresses on relatively low strength UHPC can cause significant short-term creep. This situation is akin to the stressing of prestressed girders. Eight to thirteen ksi compressive strength UHPC was loaded to compressive stresses between 60% and 90% of the strength. During the 30 minutes following the load application, the UHPC exhibited 30-minute creep coefficients between 0.32 and 0.85. UHPC loaded to over 90% of its compressive strength failed under the sustained load. The creep that occurred over this short load duration indicates that the total long-term creep of UHPC loaded at this compressive strength would be much higher than that observed in the long-term creep testing.

9.3 Ongoing and Future Research

The findings from this report suggest a number of potential topics for future research:

1. Develop optimized bridge girders that take advantage of the material properties of UHPC. These bridge girders should use the tensile and compressive capacities of UHPC, while also enhancing the design life of the bridge as a whole by eliminating many of the less durable components of a normal bridge.
2. Fabricate full-scale, optimized UHPC bridge girders to resolve problems associated with casting slender concrete members with fiber reinforced concrete.
3. Develop a practical test to quantitatively determine the post-cracking uniaxial tensile behavior of UHPC.
4. Conduct full-scale flexure and shear testing to verify the design philosophies presented in this report.

The research program discussed herein has already been extended to encompass a portion of the topics listed above.

REFERENCES

- Acker, P., "Micromechanical Analysis of Creep and Shrinkage Mechanisms," in Ulm, F.-J., Z.P. Bazant, and F.H. Wittman (eds.) "Creep, Shrinkage, and Durability Mechanisms of Concrete and Other Quasi-Brittle Materials," *Proceedings of ConCreep-6@MIT*, Elsevier, London, 2001, pp. 15-25.
- Acker, P., "Why Does Ultra High-Performance Concrete (UHPC) Exhibit Such a Low Shrinkage and Such a Low Creep?" *Autogenous Deformation of Concrete*, ACI SP-220, 2004, pp. 141-154, Detroit, MI: American Concrete Institute.
- Acker, P., and M. Behloul, "Ductal[®] Technology: A Large Spectrum of Properties, A Wide Range of Applications," *Proceedings of the International Symposium on Ultra High Performance Concrete*, Kassel, Germany, September 13-15, 2004, pp. 11-23.
- Aldea, C., S. Shah, and A. Karr, "Permeability of Cracked Concrete," *Materials and Structures*, V. 32, pp. 370-376.
- American Association of State Highway and Transportation Officials, *AASHTO Standard Specifications for Highway Bridges*, 15th ed., 1992.
- American Association of State Highway and Transportation Officials, *AASHTO LRFD Bridge Design Specifications*, 2002.
- AASHTO T106, "Standard Method of Test for Compressive Strength of Hydraulic Cement Mortar (Using 50 mm or 2 in. Cube Specimens)," In American Association of State Highway and Transportation Officials, *Standard Specifications for Transportation Materials and Methods of Sampling and Testing*, Washington, D.C., 2000.
- AASHTO T132, "Standard Method of Test for Tensile Strength of Hydraulic Cement Mortars," In American Association of State Highway and Transportation Officials, *Standard Specifications for Transportation Materials and Methods of Sampling and Testing*, Washington, D.C., 2000.
- AASHTO T161, "Standard Method of Test for Resistance of Concrete to Rapid Freezing and Thawing," In American Association of State Highway and Transportation Officials, *Standard Specifications for Transportation Materials and Methods of Sampling and Testing*, Washington, D.C., 2000.
- AASHTO T259, "Standard Method of Test for Resistance of Concrete to Chloride Ion Penetration," In American Association of State Highway and Transportation Officials, *Standard Specifications for Transportation Materials and Methods of Sampling and Testing*, Washington, D.C., 2000.

- AASHTO T260, “Standard Method of Test for Sampling and Testing for Chloride Ion in Concrete Raw Materials,” In American Association of State Highway and Transportation Officials, *Standard Specifications for Transportation Materials and Methods of Sampling and Testing*, Washington, D.C., 2000.
- AASHTO T277, “Standard Method of Test for Electrical Indication of Concrete’s Ability to Resist Chloride Penetration,” In American Association of State Highway and Transportation Officials, *Standard Specifications for Transportation Materials and Methods of Sampling and Testing*, Washington, D.C., 2000.
- American Concrete Institute, *Building Code Requirements for Structural Concrete*, ACI 318, 1995.
- ASTM C39, “Standard Test Method for Compressive Strength of Cylindrical Concrete Specimens,” American Society for Testing and Materials Standard Practice C39, Philadelphia, Pennsylvania, 1994.
- ASTM C78, “Standard Test Method for Flexural Strength of Concrete (Using Simple Beam with Third-Point Loading),” American Society for Testing and Materials Standard Practice C78, Philadelphia, Pennsylvania, 1994.
- ASTM C109, “Standard Test Method for Compressive Strength of Hydraulic Cement Mortars (Using 2-in. or [50-mm] Cube Specimens),” American Society for Testing and Materials Standard Practice C109, Philadelphia, Pennsylvania, 1998.
- ASTM C157, “Standard Test Method for Length Change of Hardened Hydraulic-Cement Mortar and Concrete,” American Society for Testing and Materials Standard Practice C157, Philadelphia, Pennsylvania, 1993.
- ASTM C227, “Standard Test Method for Potential Alkali reactivity of Cement-Aggregate Combinations (Mortar-Bar Method),” American Society for Testing and Materials Standard Practice C227, Philadelphia, Pennsylvania, 1997.
- ASTM C230, “Standard Test Method for Flow Table for Use in Tests of Hydraulic Cement,” American Society for Testing and Materials Standard Practice C230, Philadelphia, Pennsylvania, 1998.
- ASTM C457, “Standard Test Method for Microscopical Determination of Parameters of the Air-Void System in Hardened Concrete,” American Society for Testing and Materials Standard Practice C457, Philadelphia, Pennsylvania, 1998.
- ASTM C469, “Standard Test Method for Static Modulus of Elasticity and Poisson’s Ratio of Concrete in Compression,” American Society for Testing and Materials Standard Practice C469, Philadelphia, Pennsylvania, 1994.

- ASTM C496, “Standard Test Method for Splitting Tensile Strength of Cylindrical Concrete Specimens,” American Society for Testing and Materials Standard Practice C496, Philadelphia, Pennsylvania, 1990.
- ASTM C512, “Standard Test Method for Creep of Concrete in Compression,” American Society for Testing and Materials Standard Practice C512, Philadelphia, Pennsylvania, 1987.
- ASTM, “Standard Test Method for Resistance of Concrete to Rapid Freezing and Thawing,” American Society for Testing and Materials Standard Practice C666, Philadelphia, Pennsylvania, 1997.
- ASTM C672, “Standard Test Method for Scaling Resistance of Concrete Surfaces Exposed to Deicing Chemicals,” American Society for Testing and Materials Standard Practice C672, Philadelphia, Pennsylvania, 1992.
- ASTM C944, “Standard Test Method for Abrasion Resistance of Concrete or Mortar Surfaces by the Rotating Cutter Method,” American Society for Testing and Materials Standard Practice C944, Philadelphia, Pennsylvania, 1995.
- ASTM C1018, “Standard Test Method for Flexural Toughness and First-Crack Strength of Fiber-Reinforced Concrete (Using Beam With Third-Point Loading),” American Society for Testing and Materials Standard Practice C1018, Philadelphia, Pennsylvania, 1997.
- ASTM C1202, “Standard Test Method for Electrical Indication of Concrete’s Ability to Resist Chloride Ion Penetration,” American Society for Testing and Materials Standard Practice C1202, Philadelphia, Pennsylvania, 1997.
- ASTM C1260, “Standard Test Method for Potential Alkali reactivity of Aggregates (Mortar-Bar Method),” American Society for Testing and Materials Standard Practice C1260, Philadelphia, Pennsylvania, 1994.
- ASTM C1437, “Standard Test Method for Flow of Hydraulic Cement Mortar,” American Society for Testing and Materials Standard Practice C1437, Philadelphia, Pennsylvania, , 2001.
- Association Française de Génie Civil, *Interim Recommendations for Ultra High Performance Fibre-Reinforced Concretes*, 2002.
- Behloul, M., K.C. Lee, and D. Etienne, “Seonyu Ductal® Footbridge,” In *Concrete Structures: The Challenge of Creativity*, FIB Symposium 2004 Proceedings, April 26-28, Avignon, France: Association Française de Génie Civil, 6 pp.
- Blais, P.Y., and M. Couture, “Precast, Prestressed Pedestrian Bridge – World’s First Reactive Powder Concrete Structure,” *PCI Journal*, Sept.-Oct. 1999, pp. 60-71.

- Boulay, C., and A. Colson, "A Concrete Extensometer Eliminating the Influence of Transverse Strains on the Measurements of Longitudinal Strains," *Materials and Structures*, V. 14, No. 79, 1981, pp. 35-38, (in French).
- Boulay, C., P. Rossi, and J.-L. Tailhan, "Uniaxial Tensile Test on a New Cement Composite Having a Hardening Behaviour," in di Prisco, M., R. Felicetti, and G.A. Plizzari, Eds., *Fiber Reinforced Concretes – BEFIB 2004, Proceedings of the Sixth International RILEM Symposium*, 2004, pp. 61-68.
- Builelaar, P., "Heavy Reinforced Ultra High Performance Concrete," *Proceedings of the International Symposium on Ultra High Performance Concrete*, Kassel, Germany, September 13-15, 2004, pp. 25-35.
- Carpinteri, A., and B. Chiaia, "Embrittlement and Decrease of Apparent Strength in Large-Sized Concrete Structures," *Sadhana*, V. 27, No. 4, August 2002, pp. 425-448.
- Cavill, B., and Chirgwin, G., "The World's First RPC Road Bridge at Shepherds Gully Creek, NSW," *Proceedings of the Fifth Austroads Bridge Conference*, Hobart, Australia, May 2004.
- Chanvillard, G., and S. Rigaud, "Complete Characterization of Tensile Properties of Ductal® UHPFRC According to the French Recommendations," *Proceedings of the 4th International RILEM Workshop on High Performance Fiber Reinforced Cement Composites (HPFRCC4)*, Ann Arbor, Michigan, June 15-18, 2003, 14 pp.
- De Larrard, F., A. Belloc, S. Renwez, and C. Boulay, "Is the Cube Test Suitable for High Performance Concrete?" *Materials and Structures*, V. 27, No. 174, 1994, pp. 580-583.
- Hajar, Z., A. Simon, D. Lecointre, and J. Petitjean, "Construction of the First Road Bridges Made of Ultra-High-Performance Concrete," *Proceedings, 2003 International Symposium on High Performance Concrete*, Orlando, Florida, October 2003, 18 pp.
- Hegger, J., D. Tuchlinski, and B. Kommer, "Bond Anchorage Behavior and Shear Capacity of Ultra High Performance Concrete Beams," *Proceedings of the International Symposium on Ultra High Performance Concrete*, Kassel, Germany, September 13-15, 2004, pp. 351-360.
- Horszczaruk, E., "Abrasion Resistance of High Strength Fiber-Reinforced Concrete," in di Prisco, M., R. Felicetti, and G.A. Plizzari, Eds., *Fiber Reinforced Concretes – BEFIB 2004, Proceedings of the Sixth International RILEM Symposium*, 2004, pp. 257-266.

- Kakizaki, M., *Effect of Mixing Method on Mechanical Properties and Pore Structure of Ultra-High Strength Concrete*, Katri Report No. 90, Kajima Corporation, Tokyo, 1992, 19 pp.
- Li, V., “Engineered Cementitious Composites (ECC) – Tailored Composites Through Micromechanical Modeling,” *Fiber Reinforced Concrete: Present and Future*, Ed. N. Banthia, Canadian Society of Civil Engineers, 1997, 213 p.
- Li, V.C., H.-C. Wu, M. Maalej, and D.K. Mishra, “Tensile Behavior of Cement-Based Composites with Random Discontinuous Steel Fibers,” *Journal of American Ceramic Society*, V. 79, No. 1, Jan. 1996, pp. 74-78.
- Li, Z., F. Li, T.P. Chang, and Y. Mai, “Uniaxial Tensile Behavior of Concrete Reinforced with Randomly Distributed Short Fibers,” *ACI Materials Journal*, V. 95, No. 5, Sept.-Oct. 1998, pp. 564-574.
- Morris, A.D., and G.G. Garrett, “A Comparative Study of the Static and Fatigue Behavior of Plain and Steel Fibre Reinforced Mortar in Compression and Direct Tension,” *International Journal of Cement Composites and Lightweight Concrete*, V. 3, No. 2, 1981, pp. 73-91.
- Nanni, A., “Splitting-Tension Test for Fiber Reinforced Concrete,” *ACI Materials Journal*, V. 85, No. 4, Jul.-Aug. 1988, pp. 229-233.
- Neville, A.M., *Properties of Concrete, Fourth and Final Edition*, John Wiley & Sons, Inc., New York, 1996.
- Petroski, H.J., and R.P. Ojdrovic, “The Concrete Cylinder: Stress Analysis and Failure Modes,” *International Journal of Fracture*, V. 34, 1987, pp. 263-279.
- Phillips, D.C., and B.S. Zhang, “Direct Tension Test on Notched and Unnotched Plain Concrete Specimens,” *Magazine of Concrete Research*, V. 45, No. 162, 1993, pp. 25-35.
- Popovics, S., *Strength and Related Properties of Concrete*, John Wiley & Sons, Inc., New York, 1998.
- Rapoport, J., C.-M. Aldea, S.P. Shah, B. Ankenman, and A. Karr, “Permeability of Cracked Steel Fiber-Reinforced Concrete,” *ASCE Journal of Materials in Civil Engineering*, V. 14, No. 4, Jul.-Aug. 2002, pp. 355-358.
- RILEM, TC 162-TDF, “Test and Design Methods for Steel Fibre Reinforced Concrete – Recommendations: Uni-axial Tension Test for Steel Fibre Reinforced Concrete,” *Materials and Structures*, V. 34, Jan.-Feb. 2001, pp. 3-6.

- Rossi, P., "High Performance Multimodal Fiber Reinforced Cement Composites (HPMFRCC): The LCPC Experience," *ACI Materials Journal*, V. 94, No. 6, Nov.-Dec. 1997, pp. 478-483.
- Russel, B.W., and N.H. Burns, "Static and Fatigue Behavior of Pretensioned Composite Bridge Girders Made with High Strength Concrete," *PCI Journal*, V. 38, No. 3, May-June 1993, pp. 116-128.
- Saito, M., and S. Imai, "Direct Tensile Fatigue of Concrete by the Use of Friction Grips," *ACI Journal*, V. 80, No. 5, 1983, pp. 431-438.
- Semioli, W.J., "The New Concrete Technology," *Concrete International*, Nov. 2001, pp. 75-79.
- Steinberg, E., and A. Lubbers, "Bond of Prestressing Strands in UHPC," *Proceedings, 2003 International Symposium on High Performance Concrete*, Orlando, Florida, October 2003, 15 pp.
- Stiel, T., B. Karihaloo, and E. Fehling, "Effect of Casting Direction on the Mechanical Properties of CARDIFRC[®]," *Proceedings of the International Symposium on Ultra High Performance Concrete*, Kassel, Germany, September 13-15, 2004, pp. 481-493.
- Tawfig, K., "Cracking and Shear Capacity of High Strength Concrete Bridge Girders," FL/DOT/RMC/612(1)-4269, Jan. 1995, 145 pp.
- Tawfig, K., "Cracking and Shear Capacity of High Strength Concrete Bridge Girders Under Fatigue Loading," FL/DOT/RMC/612-7896, Nov. 1996, 124 pp.
- Timoshenko, S., and J.N. Goodier, *Theory of Elasticity, 2nd Edition*, McGraw-Hill Book Company, New York, 1951.
- USBR 4914, "Procedure for Direct Tensile Strength, Static Modulus of Elasticity, and Poisson's Ratio of Cylindrical Concrete Specimens in Tension," United States Department of Interior, Bureau of Reclamation, 1992.
- Wang, Y., V.C. Li, and S. Backer, "Experimental Determination of Tensile Behavior of Fiber Reinforced Concrete," *ACI Materials Journal*, V. 87, No. 5, Sept.-Oct. 1990, pp. 461-468.
- Zhang, J., H. Stang, and V. Li, "Experimental Study on Crack Bridging in FRC Under Uniaxial Fatigue Tension," *Journal of Materials in Civil Engineering*, ASCE, V. 12, No. 1, Feb. 2000, pp. 66-73.
- Zheng, W., A.K.H. Kwan, and P.K.K. Lee, "Direct Tension Test of Concrete," *ACI Materials Journal*, V. 98, No. 1, Jan.-Feb. 2001, pp. 63-71.

CURRICULUM VITAE

Benjamin Allen Graybeal is a research engineer employed by PSI, Inc. as a contractor for the Federal Highway Administration's Turner-Fairbank Highway Research Center. Since 2001, his work has focused on structural concrete research including characterization of structural materials and large scale structural testing of bridges and bridge members. From 1998 to 2001, he worked at Turner-Fairbank as a research engineer focusing on the nondestructive evaluation of highway structures.

While at Turner-Fairbank, Mr. Graybeal has presented research findings on topics ranging from Ultra-High Performance Concrete to visual inspection of highway bridges to automated inspection of steel welds. He has authored ten proceedings papers and presented results at equally many national and international conferences.

Mr. Graybeal is a Professional Engineer in the State of Virginia.

Mr. Graybeal received his Bachelor of Science in Civil Engineering from Lehigh University in May of 1996. He earned a Master of Science in Structural Engineering from the same school in May of 1998. His Master's thesis, titled "Confinement Effectiveness of High Strength Spiral Reinforcement in Prestressed Concrete Piles", focused on the full scale testing of spirally reinforced columns and the development of a rational design procedure for the proportioning of the reinforcement. The present report was completed for his doctoral dissertation at the University of Maryland, with anticipated graduation in May 2005.